



Department of Physics

Modeling Solar Cosmic Ray Transport within the Ecliptic Plane

A PhD Thesis submitted for the
degree of *Doctor of Science* (Dr. rer. nat.)
by Dipl. Systemwiss. Florian Lampa

Osnabrück, February 23, 2011

Supervisor, First reviewer:

Prof. Dr. May-Britt Kallenrode

Universität Osnabrück
Fachbereich Physik
Barbarastraße 7
49069 Osnabrück

Second reviewer:

Prof. Dr. Philipp Maaß

Universität Osnabrück
Fachbereich Physik
Barbarastraße 7
49069 Osnabrück

Abstract

Since six decades the understanding of interplanetary propagation of solar flare accelerated, energetic charged particles in the inner heliosphere has not yet achieved sufficient closure. The essential mechanisms acting on these charged particles, which perform helical orbits along the large-scale magnetic field lines as probes, have already been identified. However, in particular the impact of the three-dimensional, small-scale magnetic fluctuations on the particles' trajectories has not yet been fully understood. These superimposed disturbances are expected to interact with the charges via resonance principle – leading to both field-aligned scattering and diffusive cross-field displacements of the particles' guiding center.

Since numerical solutions and known theoretical formulations have failed to verify the measurements so far, Ruffolo's equation – which is a special formulation of the Fokker-Planck equation – is applied to take account of the current knowledge about field-parallel transport; The partial differential equation is extended to a two-dimensional model within the ecliptic plane by a spatial diffusion term perpendicular to the field. We assume an idealized Archimedean field neither with polarity changes nor large-scale disturbances such as traveling magneto-hydrodynamic shock waves or magnetic clouds.

The transport equation is solved numerically by finite differences. For typical ratios of perpendicular to parallel diffusion coefficient as deduced from theory, various fits have been found in good agreement with multi-spacecraft measurements. Some events and the occurrence of observed sudden flux drop-outs suggest that scattering on magnetic field irregularities significantly varies from one flux tube to another. In addition to the already existing, but sparse set of particle observations at different positions, once the current solar minimum has passed by, a new set will be available from the recently launched STEREO satellites.

Zusammenfassung

Die interplanetare Ausbreitung von hochenergetischen, geladenen Teilchen, die innerhalb der inneren Heliosphäre durch solare Flares freigesetzt werden, ist auch nach 6 Jahrzehnten astrophysikalischer Forschung nicht ausreichend verstanden. Die wichtigsten, auf diese geladenen Partikel wirkenden Mechanismen wurden bereits erfasst: Solare energiereiche Teilchen breiten sich wie Testteilchen spiralförmig entlang der großskali-gen Magnetfeldlinien aus. Dennoch ist insbesondere der Einfluss der drei-dimensionalen, kleinskaligen Magnetfeld-Fluktuationen auf die Teilchenpfade noch nicht vollständig ver-standen. Man vermutet, dass diese überlagerten Störungen via Resonanzprinzip mit den Ladungen wechselwirken, was sowohl zu feldparalleler Streuung als auch diffusiven, senkrechten Verschiebungen der Trajektorien führen kann.

Da bisherige theoretische Betrachtungen die Beobachtungen nicht im ausreichenden Maß verifizieren konnten, wird die Ruffolo-Gleichung verwendet – eine spezielle For-mulierung der Fokker-Planck Gleichung – um das aktuelle Wissen um feld-parallelen Transport zu berücksichtigen; die partielle Differentialgleichung ist mittels eines additiven räumlichen Diffusionskoeffizienten in feldsenkrechter Richtung zu einem zwei-dimensio-nalen Model ausgebaut worden (die Ekliptikalebene repräsentierend). Es wird ein ide-alisiertes, archimedisches Spiralfeld angenommen, in dem es weder Polaritätswechsel noch Störungen wie z.B. laufende magneto-hydrodynamische Shockwellen oder mag-netische Wolken gibt.

Die Transport-Gleichung wird mittels Finiter Differenzen numerisch gelöst. Mittels typi-scher, aus der Theorie stammender Verhältnisse zwischen senkrechtem und parallelem Diffusionskoeffizienten sind als Ergebnis eine Vielzahl von Fits ermittelt worden, die in guter Übereinstimmung mit dem simultanen Messungen zweier Raumfahrzeuge sind. Einige Teilchen-Ereignisse und das Auftreten abrupter Einbrüche in den Flüssen niederen-ergetischer Protonen lassen vermuten, dass sich die Streueigenschaften des interpla-netaren Mediums deutlich von einer Flußröhre zur nächsten ändern können. Neben der bereits vorhandenen, aber nicht sehr umfangreichen Datensammlung von Teilchen-beoachtungen an verschiedenen Positionen wird es demnächst zusätzliches Datenma-terial von den STEREO-Satelliten geben, zumal das aktuelle solare Minimum in Kürze durchlaufen sein wird.

Contents

1. Introduction	9
2. Energetic Particles in the Inner Heliosphere	11
2.1. Charged particles in electromagnetic fields	11
2.1.1. Single particle motions	11
2.1.2. Magnetohydrodynamics (MHD)	15
2.2. Solar structure and its magnetic field	19
2.3. Sources of solar energetic particles	22
2.4. Interplanetary propagation of SEPs	24
2.4.1. SEP motion along the average interplanetary magnetic field	24
2.4.2. Resonance scattering	27
2.4.3. Changes to momentum	31
2.4.4. Measurands	32
3. Modeling in 2-D	35
3.1. Conventional modeling of solar energetic particle transport	35
3.2. An extended and modified model version	37
3.2.1. Model equation	39
3.2.2. Choice of the grid	43
4. Numerics in Non-equidistant Grids	51
4.1. Basics of the Finite-Difference Method	51
4.1.1. Consistency of finite differences	51
4.1.2. Stability	52
4.1.3. Summarized approximation method	53
4.2. Transport along an IMF line (s-transport)	55
4.3. Transport in pitch-cosine	60
4.4. Adiabatic deceleration (momentum-transport)	61
4.5. Transport perpendicular to the IMF	63
4.5.1. Consistency	64
4.5.2. Stability	67
4.6. Initial and boundary conditions	69
5. Simulation Assumptions	73
5.1. SEP injections and boundary conditions	73
5.2. Assumptions regarding field-parallel transport	74
5.3. Strength and variability of the perpendicular diffusion coefficient κ_{\perp}	75
5.3.1. Does cross-field transport depend on rigidity?	77
5.4. The standard scenario	79
6. Validation and Tests	81
6.1. Field-parallel Transport	81

6.2. Field perpendicular transport	83
6.3. Azimuthal vs. perpendicular cross-field transport	87
6.4. Introduction of solar wind effects	88
6.5. Spatial resolution	90
7. Model Results	95
7.1. A parameter study	95
7.1.1. Plots in the ecliptic plane	95
7.1.2. Cross-field profiles	98
7.1.3. Intensity-time and anisotropy-time profiles	100
7.2. Observations	106
7.2.1. Intensities varying with connection to the flare site	106
7.2.2. Fitting both intensity- and anisotropy profiles	110
7.2.3. Diffusion as the big leveler vs. sudden flux dropouts	121
8. Conclusions and Outlook	125
A. Appendix	127
A.1. Physical quantities and acronyms	127
A.2. Program details	128
A.2.1. Structure	128
A.2.2. Installation	131
A.2.3. Parallelization	133
A.3. User interfaces	135
A.4. Numerically solved flux tubes	138
A.5. Various intensity-time profiles for ~ 0.5 MeV electrons	140

1. Introduction

The main issue of this PhD thesis will be to investigate the propagation of solar energetic particles (SEPs) in the inner heliosphere - an area covering about three astronomical units (AU) around the Sun. SEPs mainly consist of charged particles as electrons, protons and α -particles – their energies range in the MeV domain. Neutral atoms and molecules are not present since the hard electromagnetic radiation (e.g. X-rays) ionizes all matter. Moreover, ionization occurs by heating to such high temperatures that the random kinetic energy of the molecules exceeds the ionization energy.

First indirect evidences of charged particles were found in 1911-12 by balloon flights in the Earth's atmosphere (Gockel, 1911; Hess, 1912). But the particles causing these charges have their origin beyond the heliosphere (galactic cosmic rays, GCRs). Three decades later, the SEPs (also called “solar cosmic rays”) could be detected indirectly by ground-based neutron monitors (Forbush, 1946): Very high-energetic particles, sometimes emitted during solar events, interact with atmospheric molecules/ atoms, which themselves are split into smaller pieces. Each of them still has sufficient energy to interact with other components. The process continues and is termed an “atmospheric cascade”. If the primary cosmic ray that started the cascade has an energy above 500 MeV, some of its secondary byproducts (including neutrons) will reach ground level where they can be detected by neutron monitors. Correlations of the neutron counting rates to the largest solar outbursts (ground level events, GLEs) showed, that these charged particles hitting the upper atmosphere originate from the Sun. Solar energetic particles form the solar component of cosmic rays. They are accelerated in the upper solar corona as well as in interplanetary space. SEPs are not allowed to be confused with the continuously outward streaming *solar wind* plasma. This plasma is less energetic. As part of the solar corona (the Sun's atmosphere), it is accelerated (heated up) and, as a consequence, a hydrodynamic expansion (Parker, 1958) into space occurs. Solar wind speeds vary between 300 km s^{-1} and 800 km s^{-1} . Near the heliomagnetic equator, the solar wind propagates more slowly than in polar regions and is directed radially outward. On its way out, the solar wind shapes the local magnetic field structure of the Sun because the plasma energy density is higher than the field's energy density (frozen-in magnetic fields, Alfvén, 1976, and references therein). Since the Sun rotates with a sidereal period of about 27 days, the base of each field line frozen into the solar wind plasma is carried westward - forming an Archimedean spiral.

The interplanetary magnetic field (IMF) is one of the essential parts to describe the propagation of SEPs: Once they have been accelerated, the charged particles mainly propagate along the magnetic field lines – guided by the Lorenz force, which keeps them on helical orbits. The particle's velocity components are mainly field-parallel aligned as seen in the anisotropies (Fisk and Axford, 1969; Jokipii, 1966). Other transport mechanisms as well as small-scale disturbances in the IMF have already been identified, too. Besides convection along the IMF lines, there are scattering on magnetic irregularities, focusing in the diverging IMF as well as adiabatic deceleration (cooling) of the expanding particles, and convection due to the solar wind.

Interplanetary transport of SEPs has been regarded essentially as spatially one-dimensional: particles gyrate around the interplanetary magnetic field and are scattered back and forth along it at magnetic field inhomogeneities. But some observations in the early past, that also looked beyond the field lines particles have been injected on, have suggested that solar cosmic rays were transported oblique to the field. An estimate about the efficiency of cross-field transport is not as easy as it seems: Energetic particles do not form a homogeneous bulk but are manifold and temporally variable in many ways. Thus, energetic particles in interplanetary space must have their origin in different sources. But these sources of acceleration do not necessarily take place in the upper corona – moreover they are not expected to be implicitly located at confined, point-like areas either. An observer remote from the source will detect particles, which represents a mixture of both interplanetary transport- and acceleration processes such as traveling interplanetary shock waves. This makes the interpretation of the satellite data difficult.

It will be the purpose of this work to adopt the knowledge about interplanetary transport and to incorporate it into a two-dimensional model of solar particle transport in the ecliptic plane. The model will be extended by momentum transport, so that acceleration processes such as traveling shocks can be introduced.

As an introduction into space and plasma physics, Chapter 2 will provide the basic requirements about plasmas in interplanetary space to understand the following modeling approaches. Chapter 3 start with the illustration of former modeling approaches. The Ruffolo's equation is extended by additional terms within the modeled ecliptic plane. The resulting partial differential equation (PDE) is subsequently solved numerically by a Finite Difference scheme (see Chapter 4). Chapter 5 presents the modeling assumptions concerning in particular the mean free paths and the ratio of perpendicular to parallel diffusion. Without any physical context, Chapter 6 is dedicated to the validation the numerical code and to the comparison of its output with the outputs of the preceding numerical model. Parameter studies are used in the first part of Chapter 7 to check the plausibility of different propagation scenarios as well as the interpretation of field fluctuations as described by a pitch-angle diffusion coefficient. Finally, solutions have been fitted to the observed intensity- and anisotropy-time-profiles to obtain the scattering conditions (mean free paths or diffusion coefficients) in interplanetary space (see Chapter 7). Conclusions and possible new arising questions about interplanetary propagation of SEPs will illuminated in Section 8. The appendix A collects various numerical model details, including the user interfaces and the applied method of parallelization.

2. Energetic Particles in the Inner Heliosphere

With increasing distance from the Earth, the neutral components of matter, known in aggregate states “solid”, “liquid” and “gaseous” become rare, whereas the ionized matter dominates. Space is therefore dominated by plasmas, the fourth state of matter.

But the variety of different plasma constituents seems to pose a big challenge in describing their propagation in interplanetary space. In situ observations of the solar wind showed that the interplanetary medium was rather turbulent and permeated by sizable fluctuations of the plasma flow and density and of the magnetic field. The fluctuations occur on all observed spatial and temporal scales. The charged particles are introduced into a preexisting field, which exert a force on them. The force will be different for electrons and protons, so currents will develop. The currents will modify the magnetic field. Thus, finding a solution to the resulting transport equations is somewhat complicated. This chapter will be addressed to this issue, which can be solved to both dense plasmas, such as the solar wind, and to solar energetic particles (SEPs), respectively.

2.1. Charged particles in electromagnetic fields

Compared to matter on Earth, densities of plasmas and solar energetic particles in the heliosphere are very low. Particles are not expected to interact with each other - neither by direct collisions nor by Coulomb forces (an exception from this, of course, is the dense interior of the Sun and its largest planets).

2.1.1. Single particle motions

Under these almost vacuum conditions, external electromagnetic fields can not induce fields into these conglomerate of charged particles. The permeability μ and the permittivity ϵ are both equal one: the medium can be neither magnetized nor polarized.

Positive and negative charges are nearly equal, at least in larger scales of the Debeye-length (see Section 2.1.2).

SEPs are much more energetic than the solar wind particles, but their energy density is much too low to modify the fields through which they pass. This makes them to ideal probes for studying the interplanetary magnetic field \mathbf{B} .

The amount of SEPs is highly variable from event to event – ranging from “not distinguishable” from background plasma up to intensity increases by a few orders of magnitude. Every solar energetic particle, charged by q , will be affected by the Lorentz force:

$$\mathbf{F}_L = q \cdot \mathbf{v} \times \mathbf{B} \equiv m \frac{d\mathbf{v}}{dt} . \quad (2.1)$$

It acts perpendicular to the field as well as perpendicular to the particles's speed \mathbf{v} . Thus, there is no energy gain within the magnetic field. In a presence of a static, homogeneous magnetic field, charges perform a uniform circular orbit within a plane perpendicular to

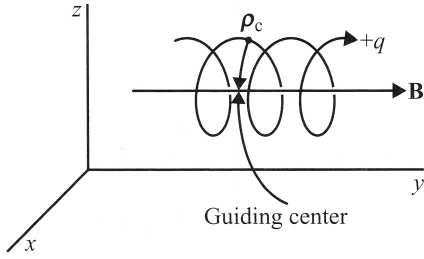


Figure 2.1.: The motion of a charged particle in a static magnetic field (Gurnett and Bhattacharjee, 2005, p. 25).

\mathbf{B} (gyration), while they move constantly forward along the field. The resulting trajectory describes a helix around the field line (Figure 2.1). The direction of motion depends on the particle's charge: Positively charged particles rotate in the left-hand sense with respect to the magnetic field. The radius of the particle orbit, the Larmor radius r_L , can be obtained from either solving the partial differential equation (2.1) directly or from the perpendicular component of the Lorentz force, which is equivalent to the centrifugal force. Thus, (2.1) can be written:

$$m \frac{v_\perp^2}{r_L} = |q| v_\perp B .$$

The radius is given by:

$$r_L = \frac{mv_\perp}{|q|B} . \quad (2.2)$$

It is identical to the cyclotron radius ρ_c , as mentioned in the Figure 2.1. Since v_\perp is constant, the Larmor radius is also constant. Because of $\omega = \frac{v}{r_L}$, the cyclotron frequency of this harmonic oscillator is

$$\omega = \frac{|q|B}{m} . \quad (2.3)$$

The instantaneous center of the rotation is called the *guiding center*, which moves with constant velocity along the field for a static uniform field. The concept of guiding centers will also be useful for describing motion in non-uniform fields (Section 2.4).

Pitch angle

The pitch-angle α denotes the inclination of the particle's trajectory with respect to the magnetic field; it is given by the ratio between the velocity components perpendicular and parallel to \mathbf{B} :

$$\tan(\alpha) = \frac{\mathbf{v}_\perp}{\mathbf{v}_\parallel} . \quad (2.4)$$

Its projection into the field direction is

$$\mu = \cos(\alpha) , \quad (2.5)$$

which is the so-called “pitch-cosine”. This quantity plays an important role in describing a single charged particle in interplanetary space. Under some constraints, the particle's

motion can be split up into field-parallel motion of the gyro-center and the gyro-motion. The pitch-cosine represents the projection factor of the particle's position vector and velocity onto the gyro-center's field line (see Section 2.4.1 for more details). Moreover, the μ notation has been found reasonable in terms of a theoretical formulation of diffusive processes (see Section 2.4.2).

Magnetic rigidity

Magnetic rigidity P [V] describes the resistance of a charged particle to change its direction in a magnetic field:

$$P = \frac{p_{\perp}}{q}. \quad (2.6)$$

p_{\perp} is the momentum component perpendicular to \mathbf{B} and, again, q denotes the particle's charge. Combined with (2.2), the Larmor radius is directly related to the magnetic rigidity by $r_L = P/B$: Particles of identical rigidity always propagate along identical orbits as long as the magnetic field configuration is static or is changing slowly (adiabatically) compared to the particle's motion. The direction of motion is determined by the charge sign. Theoretical studies about solar cosmic ray propagation (Hasselmann and Wibberenz, 1970, and references therein) predict, that SEPs of different rigidities are differently affected by magnetic field fluctuations – leading to different mean free paths. Observations on the other hand, suggest λ to be independent of rigidity (Kallenrode, 1993b). Thus, this issue is still unsolved.

Magnetic moment

A charged particle moving in a circular orbit with radius r_L and gyration time T_c gives rise to a ring current $I = q/T_c = q\omega_c/(2\pi)$. In analogy to electric currents within conductor loops, an angular momentum develops – trying to align the encircled conductor loop layer perpendicular to the magnetic field.

The magnetic moment is defined by:

$$\mathbf{M} = I A \mathbf{n} \quad , \text{ in } [\text{Am}^2]. \quad (2.7)$$

The normal vector \mathbf{n} of the area A is directed opposite to the external field. The scalar form of the magnetic momentum is given by:

$$M = \frac{|q|\omega_c}{2\pi} \cdot \pi r_L^2 = \frac{mv_{\perp}^2}{2B} = \frac{W_{kin,\perp}}{B}, \quad (2.8)$$

using the definition of the Larmor radius (2.2) and the cyclotron frequency (2.3).

The angular momentum

$$\mathbf{L} = mr_{\mathbf{L}} \times \mathbf{v}_{\perp} = mr_L v_{\perp} \mathbf{e}_{\mathbf{L}} \quad (2.9)$$

is connected to the magnetic moment via

$$M = \frac{mv_{\perp}^2}{2B} \stackrel{(2.3)}{=} \frac{v_{\perp}^2 |q|}{2\omega} \stackrel{(2.9)}{=} \frac{|q|L}{2}. \quad (2.10)$$

The vectorial description yields:

$$\mathbf{M} = \frac{q\mathbf{L}}{2} = \frac{1}{2}q\mathbf{r}_{\mathbf{L}} \times \mathbf{v}_{\perp} = -W_{kin,\perp} \frac{\mathbf{B}}{B^2} \quad (2.11)$$

Indeed, \mathbf{M} is always anti-parallel to \mathbf{B} . Moreover, with no electric fields at present, it is also a conservation quantity – like the kinetic energy – as long as \mathbf{B} is kept constant or is just changing slowly compared to the gyro-motion (*adiabatic invariants*, see next Section 2.1.1 and also 2.4.1).

Adiabatic Invariants

In a nearly periodic system with slowly varying parameters – such as the external magnetic fields – the *action integral*

$$J = \oint pdq \quad (2.12)$$

is an *adiabatic invariant* (Goldstein, 1959). p and q denote the generalized momentums and coordinates, respectively. This constant of motion provide a powerful tool to describe motions of charged particles in weakly and slowly varying fields. For gyro-motion, three types can be identified (see also e.g. Northrop, 1963):

First, the field changes only slowly during one gyration. The corresponding action integral in polar coordinates is:

$$J = 2\pi m\omega_c r_L^2 . \quad (2.13)$$

Except for some multiplicative constants, it is the same as the constancy of the magnetic moment: $J = 4\pi mM/|q|$.

The second invariant says that the field only varies weakly on a scale comparable with the distance traveled along the field by the particles. The action integral for parallel motion can be written:

$$J = m \oint v_{\parallel} ds , \quad (2.14)$$

where the integration is along the magnetic field between two points of vanishing v_{\parallel} . The parallel velocity in (2.14) can be determined from the energy conservation equation

$$E_{kin} = E_{kin,\parallel} + E_{kin,\perp} = \frac{1}{2}mv_{\parallel}^2 + \frac{1}{2}mv_{\perp}^2 \Leftrightarrow MB_m = \frac{1}{2}mv_{\parallel}^2 + MB , \quad (2.15)$$

so that

$$J = \sqrt{2Mm} \int_a^b \sqrt{B_m - B(s)} ds . \quad (2.16)$$

Since M is a constant according to the first invariant, the second adiabatic invariant is equivalent to requiring that the integral

$$\int_a^b \sqrt{B_m - B(s)} ds \quad (2.17)$$

has to be a constant, where a and b are two points of vanishing v_{\parallel} . We will address some applications in inhomogeneous magnetic fields in Section 2.4.

The third invariant (flux invariant), states that magnetic flux enclosed by the drift orbit is constant. To proof the result, we only consider orbits near the axis of symmetry. According to Faraday's law, a temporally changing magnetic field produces an azimuthal, non-conservative electric field:

$$\int_C \mathbf{E} d\mathbf{l} = - \int_S \frac{\partial \mathbf{B}}{\partial t} dt . \quad (2.18)$$

The integral is evaluated along the drift contour C . In axial symmetry and in a weakly varying radial magnetic field near the axis, the integrals can be evaluated and show that

$$2\pi RE = -\frac{dB}{dt}(\pi R^2)$$

or

$$E = -\frac{R}{2} \frac{dB}{dt}.$$

The azimuthal electric field produces a radial ($\mathbf{E} \times \mathbf{B}$)-drift, given by

$$v_E = \frac{E}{B} = -\frac{R}{2B} \frac{dB}{B}.$$

Since $v_E = dR/dt$ it follows that

$$2\frac{dR}{R} = -\frac{dB}{B}.$$

Direct integration of the above equation shows that the magnetic flux inside the drift orbit is constant:

$$\Phi_B = \pi R^2 B.$$

In an adiabatically varying magnetic, axially symmetric field, the particle always stays on the surface of the drift orbit. This area is called a *flux tube*. Magnetic flux through the surface of a flux tube remains constant, independent of the surface's position. Frozen-in magnetic fields (Section 2.1.2) can be explained by this.

The partial differential equation (2.1) would reveal a theoretical model to describe particle transport in the interplanetary magnetic field (IMF), if it is combined with solar wind effects, namely the convection with the solar and adiabatic deceleration (cooling) in the expanding solar wind (see Section 2.4). But note that the definitions, as mentioned above, were made in homogeneous and slowly varying fields under very idealized conditions. They are found adequate to describe particle propagation, but these approaches are complicated by the nature of the field: the nominal Archimedean spiral field is disturbed by fluctuations (waves and turbulence), the passage of transient disturbances such as magnetic clouds and interplanetary coronal mass ejections (CMEs) and, at least beyond 1 AU, corotating interaction regions. Besides these features, one has to take into account the different acceleration mechanisms, which might vary in time and space as well (Section 2.3).

2.1.2. Magnetohydrodynamics (MHD)

The preceding section began with the discussion of individual particle motions, but plasma in general consists of a collection of particles. The macroscopic properties of a large number of particles, such as density, temperature and pressure, can be described in terms of averages over small spatial volumes. The size of these regions and the time scales of interest have to be chosen properly in order to have statistically relevant values. They have to be larger than the microscopic particle motions: For example, the spatial scales of interest have to be large with respect to the gyro-radius (2.2) and *Debye length* λ_D . Within a gas containing both ions and electrons, λ_D describes the distance from an isolated, charged particle, where its electrostatic potential does not significantly influence

its surroundings anymore (note that λ_D depends on density). Time scales of interest are long compared with the times of single particles, e.g. the periods of the cyclotron motion $T = 2\pi/\omega$ (2.3) and the inverse plasma frequency. The average properties are governed by the basic conservation laws for mass, momentum, and energy in a fluid. The influence of electric and magnetic fields as well as currents will be added – forming the equations of *magnetohydrodynamics* (MHD).

Phase-space density

To carry out a statistical description of plasma, describing the properties of the plasma and its motion (*kinetic theory*), it is convenient to introduce a six-dimensional space, called the *phase space*. It consists of three position coordinates x , y and z , and the velocity coordinates v_x , v_y and v_z . The average number density of particles in a small volume element of phase space is called *phase space density* or *distribution function*:

$$dN = f(\mathbf{r}, \mathbf{v}, t) d^3r d^3v \quad d^3r = dx dy dz \quad d^3v = dv_x dv_y dv_z. \quad (2.19)$$

The average value of any dynamical quantity (bulk velocity, number density, pressure e.g.) can be computed by taking the integral over the distribution function.

Kinetic equations

The evolution of distribution function (2.19) in phase space is described by a differential equation, called the *Boltzmann equation*. Its derivation requires that forces \mathbf{F} on charged particles are the same for all particles in a given phase space volume element. These external, long-range forces originate from collective effects of a large number of particles. According to the Newton's law on a single particle (fixed values for \mathbf{v} and \mathbf{r}) it follows that each particle has its own, unique trajectory in phase space. The trajectories do not intersect, thus all of the particles within the volume element $d\mathbf{r}^3 d\mathbf{v}^3$ at time t are mapped into the corresponding volume element $d\mathbf{r}'^3 d\mathbf{v}'^3$ at time $t' = t + \Delta t$. The number of particles in the “new” volume element yields

$$f\left(\mathbf{v} + \frac{\mathbf{F}}{m}\Delta t, \mathbf{r} + \mathbf{v}\Delta t, t + \Delta t\right) d\mathbf{r}'^3 d\mathbf{v}'^3.$$

Small-range interactions are neglected, thus particles are not expected to change velocity within the time interval Δt . Consequently, the particle number in the volume element $d\mathbf{r}^3 d\mathbf{v}^3$ has been completely shifted to the new volume element by changing its position to $\mathbf{r}' = \mathbf{r} + \mathbf{v}\Delta t$ and by being exposed to the external force(s) $\mathbf{v}' = \mathbf{v} + \frac{\mathbf{F}}{m}\Delta t$. The difference of particle numbers between the volume elements in primes and without primes is zero:

$$\left[f\left(\mathbf{v} + \frac{\mathbf{F}}{m}\Delta t, \mathbf{r} + \mathbf{v}\Delta t, t + \Delta t\right) - f(\mathbf{v}, \mathbf{r}, t) \right] = 0. \quad (2.20)$$

Dividing (2.20) by Δt and forming $\Delta t \rightarrow 0$, we get the total differential of f :

$$\frac{\partial f}{\partial t} + \mathbf{v} \frac{\partial f}{\partial \mathbf{r}} + \frac{\mathbf{F}}{m} \frac{\partial f}{\partial \mathbf{v}} = 0, \quad (2.21)$$

which is the Boltzmann equation describing the evolution of the distribution function in phase space (incompressible fluid according to Liouville's theorem). In interplanetary space plasmas, the external forces are described by the Lorentz force. Inserting into

the Boltzmann equation gives rise to the *Vlasov* equation (Vlasov, 1938). By introducing collisions, particles might be lost or added during time interval Δt . As a consequence, a collision term $(\partial f / \partial t)_c$ is added to the right hand side of (2.21).

Short-range interactions between particles (e.g. collisions) give rise to the *Fokker-Planck equation*. Trajectories of individual particles in phase space can not be predicted, although their initial positions are known. The collisions under consideration are expected to lead to only a small change in the particle's state. Thus, there is no direct mechanical analogy to Brownian motion, where particles even reverse the direction of motion after being hit once by another particle.

Formally, the stochastic process of collisions can be described by averaging over sufficient number of particles (cf. Subsection 2.1.2). Then, collective behavior can be determined: The probability function $\Psi(\mathbf{v}, \Delta v)$ is defined as the probability that a particle of velocity \mathbf{v} after many collisions in time interval Δt has changed to $\mathbf{v} + \Delta \mathbf{v}$:

$$f(\mathbf{r}, \mathbf{v}, t) = \int f(\mathbf{r}, \mathbf{v} - \Delta \mathbf{v}, t - \Delta t) \Psi(\mathbf{v} - \Delta \mathbf{v}, \Delta \mathbf{v}) d(\Delta \mathbf{v}). \quad (2.22)$$

Small angular changes are considered only, thus $|\Delta \mathbf{v}| \ll |\mathbf{v}|$. Consequently, we are allowed to expand the product $f \cdot \Psi$ to second order by Taylor:

$$\begin{aligned} f(\mathbf{r}, \mathbf{v}, t) &= \int \left[f(\mathbf{r}, \mathbf{v}, t - \Delta t) \Psi(\mathbf{v}, \Delta \mathbf{v}) - \Delta \mathbf{v} \cdot \frac{\partial(f\Psi)}{\partial \mathbf{v}} \right] d(\Delta \mathbf{v}) \\ &\quad + \int \left[\frac{\Delta \mathbf{v} \Delta \mathbf{v}}{2} \odot \frac{\partial^2(f\Psi)}{\partial \mathbf{v} \partial \mathbf{v}} \right] d(\Delta \mathbf{v}). \end{aligned} \quad (2.23)$$

Since, by definition, the probability function can be normalized by

$$\int \Psi d(\Delta \mathbf{v}) = 1,$$

(2.23) simplifies to:

$$f(\mathbf{r}, \mathbf{v}, t) = f(\mathbf{r}, \mathbf{v}, t - \Delta t) - \frac{\partial(f\langle \Delta \mathbf{v} \rangle)}{\partial \mathbf{v}} + \frac{1}{2} \frac{\partial}{\partial \mathbf{v} \partial \mathbf{v}} \odot (f\langle \Delta \mathbf{v} \Delta \mathbf{v} \rangle). \quad (2.24)$$

The averages of $\Delta \mathbf{v}$ and $\Delta \mathbf{v} \Delta \mathbf{v}$ over all possible changes $d(\Delta \mathbf{v})$ are given by

$$\langle \Delta \mathbf{v} \rangle = \int \Psi \Delta \mathbf{v} d(\Delta \mathbf{v}) \quad \text{and} \quad \langle \Delta \mathbf{v} \Delta \mathbf{v} \rangle = \int \Psi \Delta \mathbf{v} \Delta \mathbf{v} d(\Delta \mathbf{v}). \quad (2.25)$$

The difference of the distribution function at times $t + \Delta t$ and t

$$\left(\frac{\partial f}{\partial t} \right)_{coll} = \frac{f(\mathbf{r}, \mathbf{v}, t) - f(\mathbf{r}, \mathbf{v}, t - \Delta t)}{\Delta t} \quad (2.26)$$

is equivalent to the collision term, as it has been introduced in (2.21). According to (2.24) this is equivalent to:

$$\left(\frac{\partial f}{\partial t} \right)_{coll} \Delta t = - \frac{\partial}{\partial \mathbf{v}} \cdot (f\langle \Delta \mathbf{v} \rangle) + \frac{1}{2} \frac{\partial^2}{\partial \mathbf{v} \partial \mathbf{v}} \odot (f\langle \Delta \mathbf{v} \Delta \mathbf{v} \rangle). \quad (2.27)$$

The collision term can also formally be described by a diffusion tensor/ coefficient D :

$$\left(\frac{\partial f}{\partial t} \right)_{coll} \Delta t = - \nabla_{\mathbf{v}} \cdot (D \cdot \nabla_{\mathbf{v}} \cdot f). \quad (2.28)$$

Inserting $(\partial f / \partial t)_{coll}$ into the Boltzmann equation (2.21), we finally get the Fokker-Planck-equation:

$$\frac{\partial f}{\partial t} + \mathbf{v} \frac{\partial f}{\partial \mathbf{r}} + \frac{\mathbf{F}}{m} \frac{\partial f}{\partial \mathbf{v}} - \frac{\partial}{\partial v} \left(\frac{D \partial f}{\partial \mathbf{v}} \right) = 0 \quad (2.29)$$

Since plasma densities in interplanetary space are low, changes in the SEPs' velocity are expected not to be due to particle-particle collisions, but due to interactions between charges and some fluctuating part of the ambient magnetic fields (Section 2.4.2). We will resume this formal description when the focus is taken on modeling solar energetic particles in the inner heliosphere.

Frozen-in principle

If the kinetic energy density of the particle distribution is much larger than the magnetic field strength, the particle's velocity field is prescribed. The magnetic field does not influence the charged particles, and the field is swept away from the bulk of particles. The relative strength of particle's to the field's energy density is determined by the ratio

$$\Xi = \frac{B^2/2\mu_0}{mv^2/2} = \frac{\text{magnetic field energy density}}{\text{kinetic energy density}} .$$

It is equivalent to plasma- β , which gives the ratio of gas dynamic pressure and magnetic pressure. To illustrate, what happens for $\Xi \ll 1$ within a medium of high conductivity, we assume a magnetic field $\mathbf{B}(\mathbf{r}, t_0)$ at a time t_0 in a prescribed velocity field $\mathbf{u}(\mathbf{r}, t)$. The magnetic flux through a surface S , enclosed by a curve C is $\Phi = \oint_S \mathbf{B} d\mathbf{S}$. Following the motion of the plasma of high kinetic energy density, the magnetic flux changes due to the time-varying magnetic field, and due to the field lines entering or leaving surface S . A trajectory of the surface through time and space leads to a cylinder with mantle surface M (see Figure 2.2). The change of magnetic flux is given by:

$$d\Phi = \Phi_2 - \Phi_1 = dt \int_S \frac{\partial \mathbf{B}}{\partial t} d\mathbf{S} + \int_M \mathbf{B} d\mathbf{S}_M , \quad (2.30)$$

with surface element $d\mathbf{S}_M = \mathbf{u} \times dl dt$ (dl as the path element along curve C). (2.30) yields:

$$\frac{\partial \Phi}{\partial t} = \int_S \frac{\partial \mathbf{B}}{\partial t} d\mathbf{S} + \int_C \mathbf{B} \cdot \mathbf{u} \times dl . \quad (2.31)$$

Using the Stoke's theorem, the last term in (2.31) can be written as:

$$\int_C \mathbf{B} \cdot \mathbf{u} \times dl = - \int_C \mathbf{u} \times \mathbf{B} \cdot dl = - \int_S \nabla \times (\mathbf{u} \times \mathbf{B}) d\mathbf{S} . \quad (2.32)$$

Inserting this expression into (2.31), we get

$$\frac{\partial \Phi}{\partial t} = \int_S \left[\frac{\partial \mathbf{B}}{\partial t} d\mathbf{S} - \nabla \times (\mathbf{u} \times \mathbf{B}) \right] d\mathbf{S} . \quad (2.33)$$

Replacing the $(\mathbf{u} \times \mathbf{B})$ -term by Ohm's law and $\partial \mathbf{B} / \partial t$ by Faraday's law, we finally get

$$\frac{\partial \Phi}{\partial t} = - \int_S \nabla \times \mathbf{j} \frac{1}{\sigma} d\mathbf{S} = - \int_C \frac{1}{\sigma} \mathbf{j} \cdot dl . \quad (2.34)$$

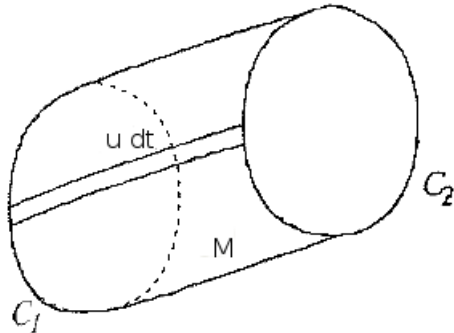


Figure 2.2.: The temporal evolution of the magnetic flux through a curve C moving with the fluid from time t to time $t + dt$ (Kallenrode, 2004, p. 67).

In case of high conductivity, σ converges to infinity. According to (2.34), $\partial\Phi/\partial t$ converges to zero. Thus, the magnetic field is *frozen into* the plasma and carried away with speed \mathbf{u} . As we will see later on, the interplanetary solar magnetic field frozen into the solar wind plasma is the prime example of the application of this concept (Section 2.2).

To sum it up, this section provides the theoretical framework to formally describe plasmas either as single particle motion or as a fluid, but neglecting additional changes in momentum due to different acceleration processes in interplanetary space.

2.2. Solar structure and its magnetic field

Originally, the solar wind was generated by the Sun. The Sun mainly consists of ionized hydrogen, which is fused to α -particles in the solar core under huge pressure and temperatures (Eddington, 1926). The released energy needs thousands of years till it finally reaches the solar surface, passing the radiative core by radiation and then being transported by convection until it finally reaches the top of the convection zone: the photosphere. Here, the fusion energy is released as electromagnetic radiation. The upper atmosphere is heated up to a million degrees – not just owing to the radiation, but also owing to energies, that are stored within the magnetic field (Dwivedi, 2003, p. 156). These high temperatures lead to an unstable atmosphere of ionized particles that is blown away as the solar wind. This plasma mainly consists of electrons, protons and α -particles. As a medium of high conductivity, it carries the magnetic fields out into the heliosphere (principle of “frozen-in” magnetic fields, see previous section). The magnetic fields are generated by rotating, highly conductive fluids in the hot interior of the Sun. In such a magneto-hydrodynamic dynamo (MHD-dynamo, Proctor and Gilbert (1994), p. 79, and references therein), part of the current induced into the circuit loop than is fed back into the system to support the static field. Despite this self-stabilizing mechanism, polarity reversals are observed approximately every 11 years. It is called the “solar cycle”, which defines the period between two consecutive minima of solar activity.

The magnetic field is carried with the radially outward streaming solar wind. The base of each field line is shifted westward according to the Sun’s rotation (sidereal rotation of about 27 days, angular frequency of $\omega_\odot = 0.0103 \text{ km s}^{-1}$). An Archimedean spiral is

formed (Parker spiral, see Figure 2.3). Its polarity is uniform over large angular regions and then abruptly changes sign (sector boundaries).

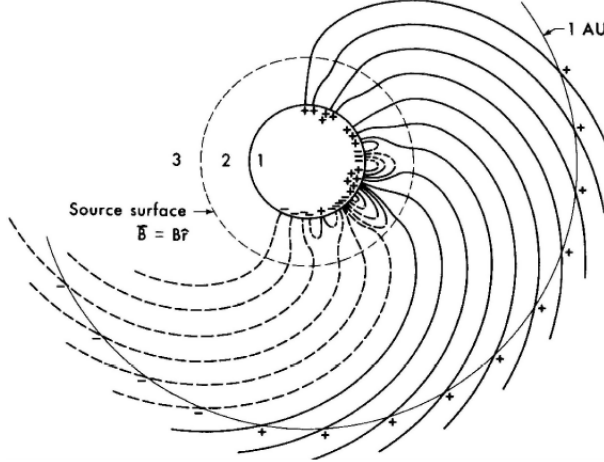


Figure 2.3.: Interplanetary magnetic field (IMF) shaped as an Archimedean spiral (reprinted from Schatten et al., 1976)

Thus, according to the Gaussian law for magnetic fields (Maxwell, 1865), the net magnetic flux is still zero (no magnetic monopoles).

Gauss's law in spherical coordinates yields:

$$\nabla \cdot \mathbf{B} = \frac{1}{r^2} \frac{\partial}{\partial r} (r^2 B_r) = 0 . \quad (2.35)$$

Thus, the magnetic flux through the spherical shells is conserved and the radial component of the field decreases as

$$B_r = B_0 \left(\frac{r_0}{r} \right)^2 .$$

In the frame of reference of the rotating Sun, the solar wind plasma has an apparent component in the direction of the solar longitude φ : $V_{sw,\varphi} = -\omega_\odot r$. Then the magnetic field stretched out along the path of plasma flowing from the fixed source in this coordinate system has components related by

$$\frac{B_\varphi}{B_r} = \frac{V_{sw,\varphi}}{V_{sw,r}} = \frac{-\omega_\odot r}{v_{sw}} .$$

Thus, the longitude component of the field is given by

$$B_\varphi(r) = -\frac{\omega_\odot r}{v_{sw}} = -B_0 \frac{\omega_\odot r_0}{v_{sw}} \frac{r_0}{r}$$

The overall magnetic field strength finally yields:

$$B(r) = B(r_0) \frac{1}{r^2} \sqrt{1 + \left(\frac{\omega_\odot \sin \theta r}{v_{sw}} \right)^2} \quad (2.36)$$

with $\theta \in [0^\circ, 180^\circ]$ as the heliographic latitude.

The spiral angle Ψ with

$$\Psi = \frac{1}{\sqrt{1 + \left(\frac{\omega_{\odot} \sin(\theta)r}{v_{sw}}\right)^2}} ; \theta \text{ as inclination of the ecliptic plane ,} \quad (2.37)$$

defines the angle between the magnetic field direction and the radius vector from the Sun.

In the rest frame of the Sun, a plasma parcel at time t can be found at the position $\varphi = \omega_{\odot}t + \varphi_0$ and $r = v_{sw}t + r_0$. Setting the initial position to zero and eliminating the time in both equations, we get the equation for the Archimedean spiral

$$\varphi(r) = \frac{\omega_{\odot} \sin(\theta)r}{v_{sw}} .$$

Parameterized in terms of radius r , the position vector in Cartesian coordinates is given by

$$\mathbf{r}(r) = r \begin{pmatrix} \cos(\omega_{\odot} \sin(\theta)r/v_{sw}) \\ \sin(\omega_{\odot} \sin(\theta)r/v_{sw}) \end{pmatrix} ,$$

with ω_{\odot} being negative to indicate, that \mathbf{r} moves clockwise.

The arc length along a field line is given by

$$s(r) = \int \left| \frac{\partial \mathbf{r}(r)}{\partial r} \right| dr = \int \sqrt{1 + \left(\frac{\omega_{\odot} \sin(\theta)r}{v_{sw}}\right)^2} dr , \quad (2.38)$$

which can be substituted by the spiral angle $\tan(\Psi) = \omega_{\odot} \sin(\theta)r/v_{sw}$:

$$s(\Psi) = \frac{1}{2} \frac{v_{sw}}{\omega_{\odot}} \left(\Psi \sqrt{\Psi^2 + 1} + \ln(\Psi + \sqrt{\Psi^2 + 1}) \right) .^1 \quad (2.39)$$

The number of polarity changes depends on solar activity. The magnetic field sectors are separated by a neutral line. During solar minimum (upper left panel of Figure 2.4) it is roughly aligned with the solar equator, while with increasing activity, the neutral line becomes wavy and extends to higher latitudes. In the right panel of Figure 2.4, it would extend outwards through the tips of the helmet streamers: its extension into interplanetary space is called the heliospheric current sheet (HCS). The slow solar wind with speeds ranging between 250 km s^{-1} and 400 km s^{-1} originates from those regions, whereas fast solar wind flows of speed between 400 km s^{-1} and 800 km s^{-1} originates in the coronal holes close to the solar poles, where open field lines are observed.

Closed, coronal loops, structures as filaments and prominences can be observed within less than two solar radii. They are covered by the virtual source surface (Figure 2.4), where field lines are almost radial (perpendicular to the source surface). Beyond that layer, the solar corotation winds up the field lines – leading to an Archimedean spiral field.

As a consequence of the *overexpansion of the solar wind* (Smith et al., 1978) energetic particles originating at the poles (open field line) can also escape along the heliospheric current sheet. Therefore, satellite observations within the neutral layer are scientifically interesting.

¹ $\ln(\Psi + \sqrt{\Psi^2 + 1}) = \sinh^{-1}(\Psi)$ inverse hyperbolic sine

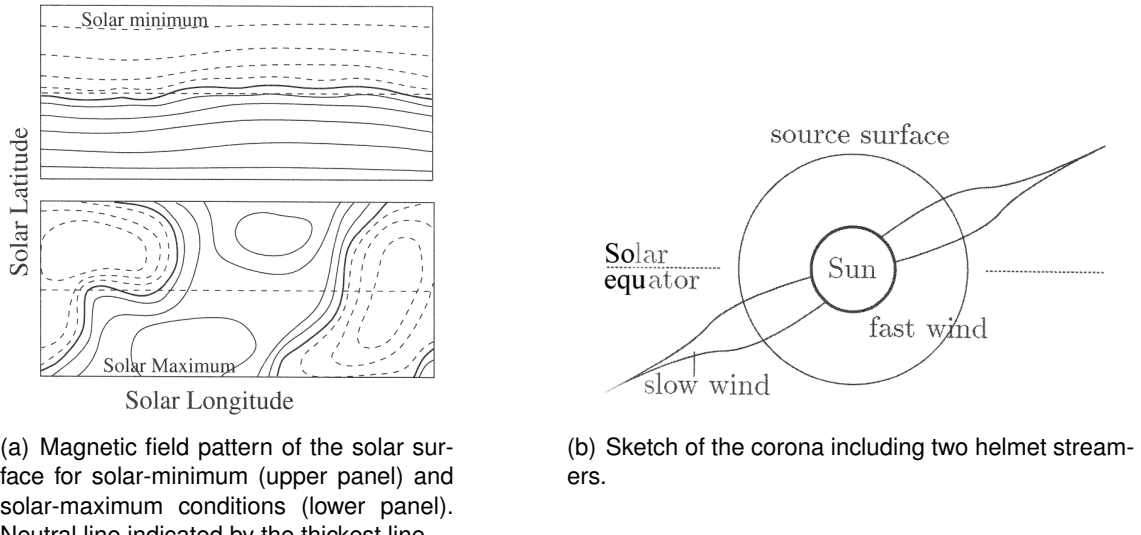


Figure 2.4.: The solar source surface and the magnetic field structure beyond (Kallenrode, 2004, p. 145, 148).

2.3. Sources of solar energetic particles

Solar energetic particles (SEPs) have different sources which might vary in time and space as well. They are related to the solar magnetic field, sunspots, and filaments. The energy of these particles has originally been stored in the field. The outburst of energy is accompanied by the release of a variety of electromagnetic radiation, providing information about the acceleration mechanisms.

Solar flare particles are separated into two categories: *impulsive* and *gradual* flares (see e.g. Kallenrode, 2003; Pallavicini et al., 1977) – nevertheless the transition between both is smooth, and some events show properties and dynamics lying in between.

Impulsive events last some minutes or up to an hour. High charge states of Fe or Si indicate that plasma has been heated up to very high temperatures. Some particle distributions are enriched in heavy ions, in particular in $^{3}\text{He}/^{4}\text{He}$ (Reames et al., 1988), Fe/C and Fe/O. The so-called “selective heating” process can be explained by particles being accelerated in closed magnetic loops in the corona. These particles in turn excite electromagnetic waves which accelerate particles on neighboring, open field lines. Consequently, the particles can escape into space. The selective character can be explained by the fact that different types of waves are absorbed by different particles (based on wave-particle resonance principle, see also Section 2.4.2). Waves of specific modes do not leave the closed loops because these waves have been absorbed by the most common plasma species in the lower corona (e.g. H and ^{4}He). These species themselves are captured within the closed loops and can not escape on adjacent, open field lines. But the other types of waves can reach open field line areas, where the minor constituents then are accelerated.

Other particles might be released by a rearrangement of small, compact loop structures. Filled with charged particles, these filaments can be stable for a few solar rotations, since the magnetic pressure (having the tendency to smooth out gradients in the magnetic field strength, Baumjohann and Treumann, 1986) prevents the arcades from falling down to the photosphere. The motion of the magnetic field lines anchoring the filament

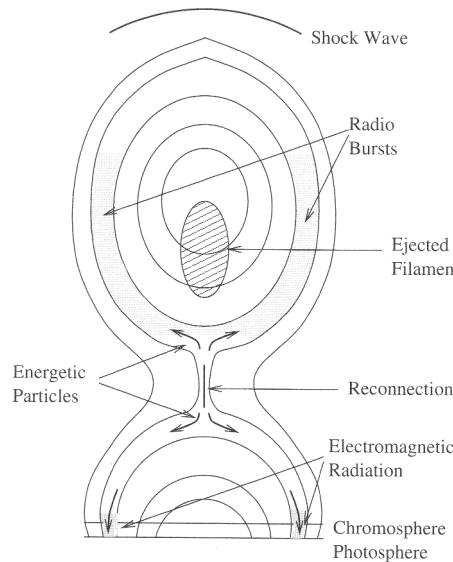


Figure 2.5.: Simplified model of a large, eruptive flare (Kallenrode, 2004, p.192).

or a slow rise of the filament due to buoyancy can lead to *reconnection* at the X-point (see Figure 2.5). At this point, field lines of opposite polarity meet. Within the neutral line, a current flows perpendicular to the drawing plane, shifting the flux tube towards the neutral line. As the distance decreases, the current density increases, and may pass the current density the plasma can carry. Consequently, the current becomes unstable, the frozen-in approximation (Alfvén, 1976) breaks down at the X-point. The anti-parallel field lines merge and magnetic tension leads to a sudden shortening of the lines. The energy of the terminated neutral line is converted to high-speed tangential flows. The filament above, contained closed magnetic field structures (magnetic clouds, Burlaga, 1991) will be ejected into space. If these structures reveal spatially small scale structures and short-time acceleration process as described above, both selective heating and the small loops are related to impulsive events.

Gradual flares can last hours, based on hard X-rays, microwaves (and other) measurements. If the magnetic field energy, transformed into kinetic energy, is large enough, a CME can be ejected whose speeds are higher than the Alfvén speed, leading slow or intermediate MHD shock waves (Gosling, 1992). They show typical abrupt changes in the plasma density, speed, plasma temperature and in the magnetic field strength. In addition to flares and CME, they can even accelerate energetic particles beyond the lower corona on their way out. The theory of shock acceleration (Jones and Ellison, 1991; Pizzo, 1985; Stone and Tsurutani, 1985) suggests, that they are very efficient in distributing the SEPs along the shock front, leading to a considerable spread in longitude and latitude (up to 180° , larger than the driving CME). That is why flare accelerated particle events without those spatially extended features reveal a good magnetic connection between the observer and the flare site. Shocks gradually and preferably accelerate protons since these particles can not escape the shock as easily as the faster electrons.

Flares and CMEs can occur together, but neither a flare nor a CME is a necessary criterion to trigger the other one. Despite of different acceleration mechanisms, SEP events should consist of both flare and shock accelerated particles, since the particle's kinetic

energy has originally been stored in the magnetic field. Therefore, cases of only flare accelerated and only shock accelerated particles are the limiting cases (Kallenrode, 2003). The composition of these different acceleration processes makes it very difficult for a single observer to interpret what the sources were and how particles were accelerated from the start of flare/CME up to the spacecraft. In this work, the focus is on SEP events, where shock acceleration can be excluded, according to the plasma and magnetic field data. The transport model, as it is presented here, already includes other momentum changing mechanisms. Thus, it is ready to be extended by particle acceleration at traveling shock fronts in the near future.

2.4. Interplanetary propagation of SEPs

Magnetic fields in the interplanetary space can be smooth or turbulent. It is assumed that to first order, that magnetic small-scale disturbances are superimposed on the IMF, which itself varies only weakly on the temporal and spatial scales of the gyration: The particle motion can be described by the concept of the *adiabatic invariants* (see Section 2.1.1). One of the consequences is that the magnetic moment (2.8) does not change while the SEPs propagate through interplanetary space.

2.4.1. SEP motion along the average interplanetary magnetic field

Apart from small scale disturbances, the interplanetary magnetic field does not reveal a homogeneous structure. Particles leaving the Sun are exposed to a diverging field, especially close to the Sun, where the IMF lines are almost radial. Thus, particle motion does not seem to be as trivial. But observations confirm that these charged particles mainly propagate along the average magnetic field lines. The observer has to be magnetically connected to the source region, where SEPs have been released during an impulsive, point-like flare. Anisotropies in the heliosphere (at 1 AU radial distance to the Sun) suggest that the high energetic particles' speeds are almost field-parallel aligned (low pitch-angles) (Fisk and Axford, 1968; Jokipii, 1966). Other Arguments for field-parallel transport are those based on azimuthal intensity gradients (Krimigis et al., 1971).

Consequently, it is assumed that, under those strict constraints, at least for some species of SEPs, the particle's gyro-centers move with speed v_{\parallel} parallel to the IMF lines.

Additionally, SEPs are convected with the solar wind (Parker, 1965), which is more evident for those particles having speeds of the same order of magnitude as the solar wind. The radially outward streaming solar wind can cause additional anisotropy in the distributions. Beyond a few tenth of an AU, cosmic rays are shifted oblique to the field, skewing the distributions relative to the average magnetic field. This process is also called the "Compton-Getting effect" (Compton and Getting, 1935).

But the question remains how, in general, the gyro-motion of SEPs can be described formally in a converging/ diverging magnetic field. Since the spatial scales of the particle's motion in interplanetary space are much smaller than the curvature of the magnetic field, cross-field displacements of the guiding center due to the magnetic field curvature can be neglected. Traverse field gradients – also causing an additional drift – are neglected, although they are immanent e.g. within the heliospheric current sheet (within regions of opposite polarity). Therefore, an axially symmetric field is assumed for which it is convenient to use cylindrical coordinates, with ρ representing the radius from the symmetry

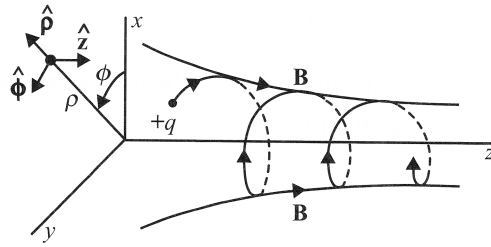


Figure 2.6.: Charged particle in magnetic mirror field, given in cylindrical coordinates z , ρ , and Φ (Gurnett and Bhattacharjee, 2005, p.39).

axis, Φ representing the azimuthal angle around the symmetry axis, and z representing the position along the symmetry axis (see Figure 2.6).

According to Maxwell's equation $\nabla \cdot \mathbf{B} = 0$, increasing magnetic field strength along the field line z implies the convergence of field lines:

$$\nabla \cdot \mathbf{B} = \frac{1}{\rho} \frac{\partial}{\partial \rho} (\rho B_\rho) + \frac{\partial B_z}{\partial z} = 0. \quad (2.40)$$

Integrating once with respect to ρ , assuming $\partial B / \partial \Phi = 0$ (axis symmetry), and $\partial B_z / \partial z$ being independent of ρ , gives:

$$B_\rho = -\frac{1}{2} \left(\frac{\partial B_z}{\partial z} \right) \rho, \quad (2.41)$$

or in Cartesian coordinates:

$$B_x = -\frac{1}{2} \left(\frac{\partial B_z}{\partial z} \right) x \quad \text{and} \quad B_y = -\frac{1}{2} \left(\frac{\partial B_z}{\partial z} \right) y. \quad (2.42)$$

Charged particles, entering this region of converging field lines, are described by:

$$m \frac{dv_z}{dt} = F_z = q[v_x B_y - v_y B_x]. \quad (2.43)$$

If the magnetic field varies sufficiently slowly compared to the gyro-motion frequency (first adiabatic invariant), the transverse motion is nearly circular around the field with

$$x = \rho_c \sin \omega_c t, \quad y = \frac{q}{|q|} \rho_c \cos \omega_c t$$

and

$$v_x = \omega_c \rho_c \cos \omega_c t, \quad v_y = -\frac{q}{|q|} \omega_c \rho_c \sin \omega_c t. \quad (2.44)$$

Inserting (2.42) and (2.44) into (2.43), we get

$$F_z = -\frac{\partial B_z}{\partial z} \left(\frac{|q|}{2} \omega_c \rho_c^2 \right) = -M \frac{\partial B}{\partial z}, \quad (2.45)$$

which is the equation for the force on a magnetic moment in an inhomogeneous magnetic field. The charged particle tends to be repelled from the region of strong magnetic field (mirror effect).

The constancy of the magnetic moment can be shown by computing the time derivative of the Lorentz force in azimuthal (field-perpendicular) direction. The force is given by

$$F_\Phi = qv_z B_\rho . \quad (2.46)$$

The rate of change of the perpendicular kinetic energy $W_{kin,\perp}$ is computed from the rate at which work is done by the azimuthal force,

$$\frac{dW_{kin,\perp}}{dt} = v_\Phi F_\Phi = qv_\Phi v_z B_\rho .$$

Substituting (2.41) for B_ρ and noting that $v_\Phi = -(q/|q|)v_\perp$, the above equation becomes

$$\frac{dW_{kin,\perp}}{dt} = |q|v_\perp v_z \left(\frac{\partial B_z}{\partial z} \right) \frac{\rho}{2} .$$

The perpendicular energy changes with position, but nevertheless, the total kinetic energy remains constant, because the $\mathbf{v} \times \mathbf{B}$ acts perpendicular to the particle's velocity vector. If we use the Larmor radius r_L (2.2) instead of ρ , the above rate of change can be written

$$\frac{dW_{kin,\perp}}{dt} = \frac{W_{kin,\perp} v_z}{B} \left(\frac{\partial B_z}{\partial z} \right) . \quad (2.47)$$

We next show that the magnetic moment is a constant of the motion. The time derivative of M is given by

$$\frac{dM}{dt} = \frac{d}{dt} \left(\frac{W_{kin,\perp}}{B} \right) = \frac{1}{B} \frac{dW_{kin,\perp}}{dt} - \frac{W_{kin,\perp}}{B^2} \left(\frac{\partial B}{\partial t} \right) . \quad (2.48)$$

Substituting expression (2.47) for $dW_{kin,\perp}/dt$, and $dB/dz = v_z(\partial B/\partial z)$, we obtain:

$$\frac{dM}{dt} = \frac{W_{kin,\perp} v_z}{B^2} \left(\frac{\partial B_z}{\partial z} \right) - \frac{W_{kin,\perp} v_z}{B^2} \left(\frac{\partial B}{\partial z} \right) = 0 ,$$

or $M = \text{constant}$.

Let us now extend the small local region to interplanetary dimensions by changing z to s , the distance along the field line, v_z to v_{\parallel} , the parallel component of velocity, and B_z to B , the magnetic field strength. The equation of parallel motion (2.45) becomes:

$$m \frac{dv_{\parallel}}{dt} = -M \frac{\partial B}{\partial s} . \quad (2.49)$$

Since $dv_{\parallel}/dt = v_{\parallel} dv_{\parallel}/ds$ and noting that M is a constant, the above equation can be integrated once, yielding:

$$\frac{d}{ds} \left(\frac{1}{2} m v_{\parallel}^2 + MB \right) = 0 , \quad (2.50)$$

which implies that

$$\frac{1}{2} m v_{\parallel}^2 + MB = MB_m . \quad (2.51)$$

M and B_m are constants. (2.51) can be interpreted as an energy conservation equation for a particle of mass m moving in the effective potential $MB(s)$.

As we have seen before, the overall particle's motion is governed by the field-parallel motion of the gyro-center and the gyro-motion, as it is seen in the first and second term of (2.51), respectively. In diverging fields (magnetic field strength decreases), the loss of the gyration energy is compensated by increasing drift energy (termed as *focusing*). Charged particles that have started within a helical orbit, are transformed into a more field-aligned motion - the pitch angle tends to zero. With increasing solar distance, for example, a pitch angle of about 90° will be transformed to 0.7° at the Earth's orbit.

On the other hand, converging fields lead to subsequent conversion of drift energy into gyro-motion energy, and sometimes, even to a change in the direction of motion relative to the IMF: The ratio between the pitch-angle and the magnetic field strength at two different locations is calculated according to the magnetic moment M :

$$\frac{v^2 \sin(\alpha)^2}{B_1} = \frac{v^2 \sin(\alpha_m)^2}{B_m}. \quad (2.52)$$

A moving charge at location 1 will undergo a reversal in the direction of motion at the mirror point (indicated by the index m), if condition

$$\mu_1 = \sqrt{1 - \frac{B_1}{B_m}}. \quad (2.53)$$

is fulfilled. SEPs having larger pitch-cosines pass the mirror point, whereas particles with lower values are mirrored earlier. Energetic particles can be trapped between two mirroring points, thus the adiabatic invariants can be applied to the Earth's radiation belts (Van Allen and Frank, 1959), or to solar filaments, e.g. single mirroring effects can be observed in terms of magnetic clouds (Burlaga, 1991) and corotating interaction regions (Mazur et al., 2002).

2.4.2. Resonance scattering

Even though the IMF provides a preferential direction on large spatial scales, measurements reveal magnetic field fluctuations on different scales, indicating different source and modes of turbulence (see Figure 2.4.2). These disturbances can be described by a power density spectrum, given by a power law

$$f(k_{\parallel}) = C \cdot k_{\parallel}^{-q}, \quad (2.54)$$

with k_{\parallel} being the wave number parallel to the field, q the slope, and the parameter C denoting the level of turbulence. The spectrum plotted versus the frequency shows some domains of different slopes. Below $5 \cdot 10^{-6}$ Hz, large scale structures – such as magnetic field sectors (see Section 2.2) – in the magnetic field lasting several days or more, and the solar wind expansion, are responsible for that mode of disturbances. Both processes involve sources of turbulences on smaller scales. The frequency range between $5 \cdot 10^{-6}$ Hz and 10^{-4} Hz covers meso-scale fluctuations, which are associated with flux tube structures originating in the photospheric super-granulation. The granules are considered to be signs of the convection cells in the solar convective layer.

The dissipation range above 1 Hz is attributed to turbulence on the smallest scales, they are expected to be caused by cyclotron waves, ion-acoustic waves, and Whistlers (see e.g. Baumjohann and Treumann, 1986).

The inertial range between 10^{-4} Hz and 1 H is of high interest. These disturbances are mainly caused by Alfvén-waves. These waves are transversal waves propagating parallel

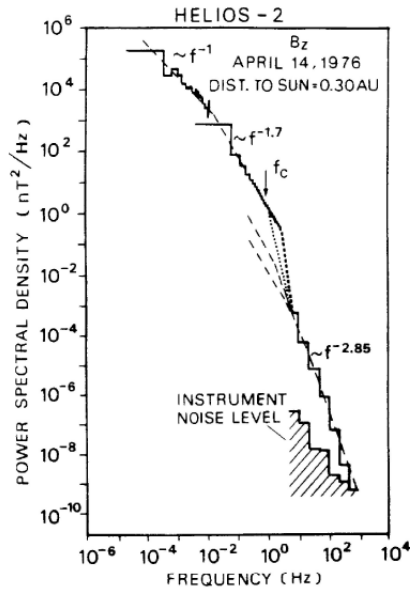


Figure 2.7.: Power-density spectrum, reprinted from Denskat et al. (1983).

to the IMF (the wave vector is aligned $\mathbf{k} \parallel \mathbf{B}_0$). The fluctuating quantities are the magnetic field and the current density. The restoring force behind these disturbances is called *magnetic tension*: Within a curved magnetic field, a force develops with the tendency to shorten the lines (in analogy with an elastic string). But in space, the resulting waves and its propagation propagation properties depend on the plasma charge density ρ_0 and the magnetic field alone. The waves are non-dispersive: disturbance moving faster than the Alfvén speed $v_a = B_0 / \sqrt{\rho_0 \mu_0}$ can drive shocks.

These Alfvén-waves are said to be responsible for scattering SEPs in interplanetary space. Indeed, in situ observations of SEPs accelerated in impulsive flares look like diffusive curves (Roelof, 1969a): The classical three-dimensional diffusion equation has the solution

$$N(t) = \frac{N_0}{4\pi Dt^{3/2}} \exp\left(-\frac{r^2}{4Dt}\right),$$

with N as the particle number, D as the isotropic diffusion coefficient and r as the radial distance from the source site (defined formally as a δ -function). Time-series measurements (see Figure 2.8 for example) qualitatively give evidence to diffusive processes when they pass a locally fixed observer in space: The intensities reveal a rapid increase up to a pronounced maximum. Once the maximum intensity at the observer's location has been reached, the particle numbers fall again, but much more slowly than it has grown in the initial phase. Moreover, a second phenomenon supported the diffusion approach: the modulation of galactic cosmic rays (GCRs, see e.g. Diehl et al., 2002). They uniformly and isotropically enter the heliosphere from outside with very high energies extending up to 10²⁰ electron volts. Neutron monitor counting rates showed a solar cycle variation, which was just opposite to that of indicators of solar activity. Obviously, GCR are hindered by some kind of diffusive process to pass freely the inner heliosphere (see Roelof (1969b), p. 117–118).

Densities in space are small, and since the fluctuating quantities (described by Alfvén waves) are said to be responsible for the particle scattering, theories have been intro-

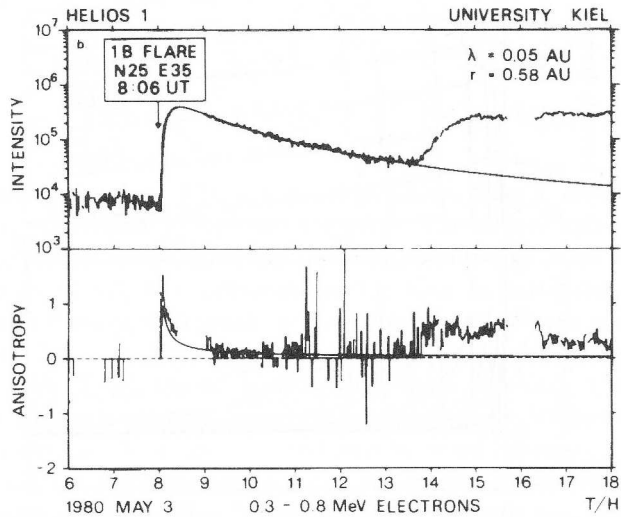


Figure 2.8.: Time-intensity- (upper panel) and Anisotropy-time profiles of an electron event. The solid lines are related to a fit with a transport model (Kallenrode et al., 1992).

duced that describe direct interactions between the fluctuating part of the magnetic field and the solar energetic particles.

It is now common sense that each interaction would result into just a small deviation of the particle's direction of motion, which can be described by diffusion in pitch-cosine space:

$$\frac{\partial}{\partial \mu} \left(\kappa(\mu) \frac{\partial f}{\partial \mu} \right) .$$

The pitch-angle-diffusion coefficient (PADC) $\kappa(\mu)$ is related to the field parallel mean free path (Hasselmann and Wibberenz, 1968; Jokipii, 1966):

$$\lambda_{||} = \frac{3}{8} v \int_{-1}^{+1} \frac{(1 - \mu^2)^2}{\kappa(\mu)} d\mu , \quad (2.55)$$

with v being the particle's speed.

On larger scales than the gyro motion, $\lambda_{||}$ leads to one-dimensional-diffusion along the magnetic field lines, but it should be noted that the free mean path denotes the distance traveled before the particle's pitch-angle has been reversed by 90° , and not the free path between two consecutive pitch-angle scatterings.

The shape of the pitch-angle diffusion coefficient is governed by the assumptions of the *quasi-linear theory* (QLT) (Jokipii, 1966). As we will see, the remaining transport processes (Section 2.4.1) and adiabatic deceleration (Section 2.4.3) can be modeled by a partial differential equation, which will even provide closed analytical solutions for a very simplified parameter set (constant quantities for the solar wind- and particle speed, vanishing focusing in homogeneous fields, neglecting momentum processes).

The stochastic wave-particle-interaction as an example of a non-linear process, are not widely understood, although there already exists a well-developed mathematical description. Based on perturbation theory, those collisionless interactions are considered to first order only. Effects of second order or even higher are neglected. Quantities such as phase space density $f = f_0 + f_1$ or the magnetic field strength $\mathbf{B} = \mathbf{B}_0 + \mathbf{B}_1$ are split into

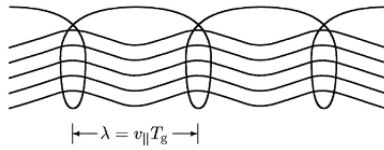


Figure 2.9.: Resonance scattering (Kallenrode, 2004, p. 233).

a slowly evolving part (the adiabatic invariants must be still fulfilled, see Section 2.1.1), and a fluctuating part (indicated by the index 1). The ensemble averages of the fluctuating linear terms vanish: $\langle f_1 \rangle = 0$ and $\langle B_1 \rangle = 0$

Wave-particle interactions can be explained by the *resonance principle*: An interaction takes place if the particle motion along the field are in resonance with the field fluctuations' wavelengths (Jokipii, 1966).

The waves propagate parallel to the interplanetary magnetic field \mathbf{B}_0 and the fluctuations are symmetric around the wave vector (*slab-model*). In Figure 2.9 the resonance case is briefly sketched: It occurs if the free mean path length λ_{\parallel} exactly corresponds to the path length of the gyro-center within one gyration:

$$\lambda_{\parallel} = v_{\parallel} \cdot T_c ,$$

with T_c being the gyration period.

The strength of interaction is defined by the power-density spectrum (2.54).

A clear separation between the slowly evolving (on the left-hand side) and fluctuating parts has been done, when the *Vlasov*-equation

$$\frac{\partial f_0}{\partial t} + \mathbf{v} \nabla f_0 + \frac{q}{m} \mathbf{v} \times \mathbf{B}_0 \cdot \frac{\partial f_0}{\partial \mathbf{v}} = -\frac{q}{m} \left\langle (\mathbf{E}_1 + \mathbf{v} \times \mathbf{B}_1) \frac{\partial f_1}{\partial \mathbf{v}} \right\rangle \quad (2.56)$$

has been introduced. It considers non-interacting particles (the right hand side of equation 2.56), thus, in contrast to the Fokker-Planck equation, short-range, local interactions as direct collisions between particles or Coulomb interactions between the charges are not involved.

Solutions can be found, if the particle's properties, such as magnetic rigidity (2.6) and the fluctuations are known via the power law (2.54). Based on the power-density-spectrum, one can derive the shape of the PADC by the assumption of slab turbulence:

$$\kappa(\mu) = A ((1 - sign(\mu)\sigma)|\mu|^{q-1} + H) (1 - \mu^2) . \quad (2.57)$$

The constant amplitude A describes the absolute level of magnetic field fluctuations. The polarization of the magnetic field fluctuations σ indicate the amount of left and right polarized wave modes. The power law index q is a measure of the deviation from isotropic scattering and is related to the power spectrum of magnetic field fluctuations $f(k_{\parallel}) \propto k_{\parallel}^{-q}$. For $q = 1$, diffusion acts uniformly on SEPs; with increasing q a resonance gap around $\mu = 0$ develops. It can be refilled by parameter H to simulate non-linear corrections.

For $q \geq 2$ the gap become too wide – leading to a decoupling: particles can not reverse direction.

Note that the dependency of the PADC $\kappa(\mu)$ on the magnetic field fluctuations is not completely understood (see Dröge, 1993). Matthaeus et al. (2003) introduced a more generalized theory about scattering particles at magnetic irregularities (including 2D turbulence). They considered the transverse complexity of the magnetic field and combined both scattering according to the slab model as well as diffusive loss terms towards neighboring field lines - the non-linear guiding center theory (NLGC). Besides these approaches, it will be one of the purposes for the future, to get new insights into the multi-dimensional scattering conditions in interplanetary space.

2.4.3. Changes to momentum

On their way out, energetic particles are exposed to a continuously decreasing magnetic field strength (2.36). If the temporal change is small compared to the gyration period of the SEP, the value of the magnetic moment (2.8) will be conserved – it is an *adiabatic invariant* as it is seen Section 2.1.1. An slowly decreasing magnetic field B involves falling momentum of the gyration motion. This cooling tends to be most effective beyond a few tens of an AU, where focusing in diverging fields is less dominant, and where the particle distributions become isotropic due to scattering on field irregularities. Consequently, there are significant abundances of particles having speed components in field perpendicular direction (and p_{\perp}), which will subsequently be reduced by this *betatron effect*.

Another cooling effects emerges from the fact, that the scattering centers (frozen into the outward streaming solar wind), gradually get separated from each other as the solar wind expands. Thus, energetic charged particles loose energy (inverse Fermi-effect Webb and Gleeson, 1975). Thus, this kind of “adiabatic deceleration” becomes most effective with increasing radial distance from the Sun.

Observations of SEP events have shown, that the SEP energy spectra follow a power law. The omnidirectional intensity (see Section 2.4.4) is related to the particles’s energy via

$$I_0(E) \propto \left(\frac{E}{E_0} \right)^{-\gamma},$$

with the power-law index γ ranging between approximately 2 and 4 (Ruffolo, 1994). But it should be noted that this assumption is a crude simplification: Numerical simulation runs using the Ruffolo transport equation (1994) have confirmed, that the spectra might vary in time and radial distance (Hatzky and Kallenrode, 1999). If the source particle distribution is assumed to follow a spectrum as mentioned above, the spectra on a double logarithmic scale become increasingly softer with increasing radial distance from the Sun (see also Hatzky, 1996, p. 132). Because of the negative slope, more particles of a certain energy are removed from the observer’s site than it would be without the cooling process. As a result, the spectrum’s slopes becomes convex towards lower energies, whereas the high energy domain remains almost unchanged. If solar wind effects are neglected, a similar effect (but temporally delayed and weaker) on the spectra was also found – owing to the later arrival of the low energy particles. Observations suggest that spectra must even follow a broken power law, with slopes differing with respect to different acceleration mechanisms in the lower corona. Accompanying shocks significantly affect the spectrum, since they differently accelerate energetic particles with different momentum (see e.g. Gosling et al., 1981).

2.4.4. Measurands

Differential intensity: It is defined as the number of particles with energies in the domain $[E + dE]$, crossing an area dA at location \mathbf{x} , coming from direction \mathbf{n} and covering the solid angle $d\Omega$ within the time period dt :

$$I(\mathbf{x}, E, \mathbf{n}, t) dE d\Omega dA dt \quad [I] = \frac{\text{number of particles}}{\text{MeV} \cdot \text{s} \cdot \text{sr} \cdot \text{cm}^2}$$

It is a directly measurable quantity, nevertheless it only can be approximately determined due to the finite aperture of the detector telescope.

Averaging over all directions \mathbf{n} results in the

omnidirectional intensity

$$I_0(\mathbf{x}, E, t) = \frac{\int \int I(\mathbf{x}, E, \mathbf{n}, t) d\Omega}{\int \int d\Omega} = \frac{1}{4\pi} \int \int I(\mathbf{x}, E, \mathbf{n}, t) d\Omega, \quad (2.58)$$

which is equivalent to the differential intensity in case of isotropic angular distributions.

According to the equation of continuity, the intensity is related to the differential particle density $U_E(\mathbf{x}, E, t)$ (number of particles within the energy domain $[E, E + dE]$ at location \mathbf{x} in volume element dx^3) via

$$U_E(\mathbf{x}, E, t) = \frac{1}{v} \int \int I(\mathbf{x}, E, \mathbf{n}, t) d\Omega \quad ; v \text{ particle's speed} .$$

In anisotropic distributions, a net flux of particles into a preferable direction \mathbf{s}_0 exists, denoted by the particle stream density

$$\mathbf{S}_E(\mathbf{x}, E, t) = \int \int I(\mathbf{x}, E, \mathbf{n}, t) \mathbf{n} d\Omega ,$$

with $\mathbf{n} d\Omega = -\mathbf{s}_0$ being the detector's line of sight. Since charged particles mainly propagate along the average magnetic field due to the Lorentz force (2.1), and since stochastic processes (see Section 2.4.2 and Hatzky, 1996, p. 14) are supposed to be responsible for uniform distributions in the azimuth φ , the distributions are assumed to be *gyrotropic* (symmetric along the magnetic field line direction \mathbf{e}_B). Consequently, the distributions depend on pitch-angle α only, and the particle stream density is reduced to

$$\mathbf{S}_E(\mathbf{x}, E, t) = 2\pi \int_{-1}^{+1} I(\mathbf{x}, E, \mu, t) \mu d\mu \mathbf{e}_B .$$

The pitch-cosine projects all quantities onto the field line at location \mathbf{x} .

To get a measure for a directed flux with respect to the particle's density, the vectorial quantity *anisotropy* \mathbf{A} has been introduced:

$$\mathbf{A}(\mathbf{x}, E, t) = \frac{3}{v} \frac{|\mathbf{S}_E|}{U_E} \mathbf{s}_0 .$$

For the gyrotropic case, the anisotropy simplifies to

$$\mathbf{A}(\mathbf{x}, E, t) = 3 \frac{\int_{-1}^{+1} I(\mathbf{x}, E, \mu, t) \mu d\mu}{\int_{-1}^{+1} I(\mathbf{x}, E, \mu, t) d\mu} .$$

In case of a rotating spacecraft (such as the *Helios* satellites), an angular distribution can be measured. Because of a specific alignment of the telescope relatively to the gyration axis of the SEPs, the observed latitudes ϑ correspond to the pitch-angles. Unfortunately, the intensity at *Helios* are averaged over 45° (8 sectors), only. Particle energies can just be associated to bins of broad domains. The differential intensity, measured by the two *Helios* spacecraft, exclusively depends on $\mu = \cos(\alpha)$ and a corresponding energy interval. In order to get an analytical description of $I(\mu)$, the intensity was fitted by Legendre-polynomials to fourth order (Green, 1992):

$$I(\mu) = \sum_{n=0}^{\infty} g_n P_n(\mu) \quad \text{with } g_n = \frac{2n+1}{2} \int_{-1}^{+1} I(\mu) P_n(\mu) d\mu .$$

The Legendre polynomials P_n form an orthogonal basis, thus the calculated Legendre coefficients are uniquely determined (Bronstein et al., 1993). Note that polynomials of even higher order would not give additional information about the pitch-angle distributions as long as only 8 detection sectors are used.

The zeroth coefficient describes the isotropic part of the pitch-angle distribution - the omnidirectional intensity.

The remaining coefficients - divided by g_0 - correspond to the *anisotropies* $|A|$ of n -th order:

$$|A_n| = \frac{g_n}{g_0} . \quad (2.59)$$

The first order anisotropy corresponds to the one as derived above. By definition, anisotropy is said to be negative if the particle flux is opposite to magnetic field polarity, positive, if both are parallel. As Hatzky already stated, a comparison of different pitch-angle distributions (PADs) on the basis of μ only (without Legendre polynomial approximation), might lead to misinterpretations, because anisotropy of first order does not reveal complete, unique picture of the PAD. A vanishing first-order anisotropy, for example, indicates a zero net particle flux. But this quantity does not necessarily implies vanishing particle speeds: It only states that, e.g., the Sun inward and the Sun outward particle flux cancel each other.

3. Modeling in 2-D

As it has already been mentioned in Section 2.4, solar energetic particles are expected to mainly follow the field-lines of the interplanetary magnetic field (IMF). An exception of this were studies of Sturinsky et al. (2006) who build a simple, isotropic three-dimensional diffusion model – or Parker (1965) who assumed a radial stream direction. As it has already been illustrated in Section 2.4.2, these approaches were not applicable with respect to the assumed scattering mechanisms.

There was no doubt that these particles undergo “focusing” at the diverging field while they are escaping from the Sun. In addition, their motion is governed by diffusion. Whereas early studies suggested that this process can be described by simple spatial diffusion (see Parker, 1958), later studies showed that diffusion is based on interactions between particles and magnetic field fluctuations, that are superimposed on the background field.

3.1. Conventional modeling of solar energetic particle transport

Thus, the particle’s motion is governed by multiple processes in an often strongly fluctuating field. An integration of a resulting equation of motion would require a Monte Carlo (MC) approach to take into account the different phase relations between particles and waves. Alternatively, the stochastic aspects can be accounted for by averaging over a sufficient number of particles, giving rise to a Fokker-Planck equation (2.29).

Besides other authors such as Roelof (1969a), the effectively one-dimensional transport was described by Ruffolo’s Equation (1994). Limiting to just the essential terms, Ruffolo gets:

$$\begin{aligned} \frac{\partial F(t, s, \mu', p')}{\partial t} = & \\ & \frac{\partial}{\partial s} \left(\left[\mu' v' + \left(1 - \frac{(\mu' v')^2}{c^2} \right) v_{sw} \sec \Psi \right] F(t, s, \mu', p') \right) \\ & + \frac{\partial}{\partial \mu'} \left(v' \frac{1 - \mu'^2}{2L(s)} F(t, s, \mu', p') - \kappa_\mu(s, \mu') \frac{\partial F(t, s, \mu', p')}{\partial \mu'} \right) \\ & \frac{\partial}{\partial p'} \left(p' v_{sw} \left[\frac{\sec \Psi}{2L(s)} (1 - \mu'^2) + \cos \Psi \frac{\partial}{\partial r} (\sec(\Psi)) \mu'^2 \right] F(t, s, \mu', p') \right) \\ & = Q(s_0, t, \mu', p'), \end{aligned} \quad (3.1)$$

where F denotes the distribution function:

$$F(t, s, \mu', p') = \frac{d^3 N}{ds d\mu' dp'} \quad (\text{number of particles inside a given flux tube}).$$

It depends on time t , distance s along the Archimedean magnetic field spiral, pitch cosine μ' and particle's momentum p' . The primes indicate that the two latter quantities are measured in the solar wind frame including solar corotation. The observer inside the ecliptic plane with an inclination of $\theta \approx 90^\circ$ always stays on the same field line and the solar wind vector will be transformed to

$$\mathbf{v}_{sw}^c = v_{sw} \mathbf{e}_r + \sin(\theta) \omega_\odot r \mathbf{e}_\varphi$$

such that it is aligned parallel to the spiral field lines.

The fixed frame used by Roelof – whose transport equation is given by simply ignoring the solar wind effects ($v_{sw} = 0$) in (3.1) – and the solar wind frame by Ruffolo will be revealed in detail when we introduce an extended, slightly modified version of (3.1).

F itself denotes a linear density (density of particles inside a flux-tube per unit length), related to the phase-space density f by $F = A(r) \cdot f$ (Ng and Wong, 2005), with $A(r)$ being the cross section of the flux tube at the corresponding radial distance r . F depends on momentum and not on energy; thus a power law spectrum in energy in space-phase density reads $I(E) \propto E^{-\gamma'}$, for the distribution function the spectrum reads $F(p) \propto p^{-\delta'}$ with $\delta' = 2\gamma'$ in the non-relativistic case.

The transport equation (3.1) denotes a special case of the Fokker-Planck equation because it describes the temporal change in the distribution function as the particles propagate along the lines of an inhomogeneous field, as they change pitch-angle, and as they are scattered in momentum space (termed as “adiabatic deceleration” which is described formally in Section 3.2.1).

The term in s corresponds to the second term of the Fokker-Planck equation (2.29), and consists of two parts: propagation of particles with their field-parallel speed component $v'_\parallel = v'\mu'$ in the corotating solar wind frame and the convection of particles with the solar wind v_{sw} . The product $v_{sw} = v_{sw} \sec(\Psi)$ gives the component of the solar wind speed parallel to the IMF in the corotating solar wind frame, with Ψ being the angle between the radial direction and the Archimedean magnetic field spiral at the radial distance r . In this frame of reference, the “transformed” speed can exceed the speed of light beyond a certain radial distance. To avoid this unphysical quantity, the damping relativistic correction term $1 - (\mu'v')^2/c^2$ has been introduced.

The third term of the Fokker-Planck equation (2.29) can be re-identified by the focusing term $\partial_\mu(v'(1 - \mu'^2)F(\mu'))/2 L(s)$ which described changes in pitch-angle α (2.4) as a consequence of diverging field lines. The particle's speed \mathbf{v} is transformed gradually into field-parallel motion when it is exposed to decreasing magnetic field strength (see also Section 2.4.1). According to Newton's law the corresponding force in field parallel direction yields

$$F = m \cdot \frac{\partial v_\parallel}{\partial t} = m \cdot \mathbf{v} \cdot \frac{\partial}{\partial t}(\mu(t)) \Leftrightarrow \frac{F}{m} = v \cdot \frac{\partial \mu}{\partial t}. \quad (3.2)$$

Moreover, because of $v_\parallel = \mu v$, the derivative in velocity $\partial F/\partial v_\parallel$ becomes

$$\frac{\partial F}{\partial v_\parallel} = \frac{\partial F}{\partial(\mu v)}. \quad (3.3)$$

Inserting (3.2) and (3.3) into the third term of the Fokker-Planck equation gives

$$\frac{F}{m} \frac{\partial F}{\partial v_\parallel} = v \cdot \frac{\partial \mu}{\partial t} \cdot \frac{\partial F}{\partial(\mu v)} = \frac{\partial \mu}{\partial t} \frac{\partial F}{\partial \mu}. \quad (3.4)$$

The change in pitch-angle depends on the change in the magnetic field strength B , as the particle follows the current field line. Consequently, $\partial_t \mu$ is described by

$$\frac{\partial \mu}{\partial t} = \frac{\partial \mu}{\partial B} \frac{\partial B}{\partial s} \frac{\partial s}{\partial t}. \quad (3.5)$$

For single particle motions in a mirroring field in Section 2.4.1, we have already derived the condition

$$\mu = \sqrt{1 - \frac{B}{B_s}} \quad , \text{ see (2.53)} .$$

Its derivative in terms of B is

$$\frac{\partial \mu}{\partial B} = \frac{1}{2} \left(1 - \frac{B}{B_s}\right)^{-1/2} \cdot \left(-\frac{1}{B_s}\right) . \quad (3.6)$$

Replacing $\partial_B \mu$ in (3.5), combined with $B_s = B/(1 - \mu'^2)$, we get the final result

$$\frac{\partial \mu}{\partial t} = \frac{1}{2} \left(1 - \frac{B}{B_s}\right)^{-1/2} \cdot \left(-\frac{1}{B_s}\right) \frac{\partial B}{\partial s} \cdot v\mu = -\frac{1}{2\mu} \frac{1 - \mu^2}{B} \frac{\partial B}{\partial s} \cdot v\mu , \quad (3.7)$$

where $L(s) = B(s)/(\partial B(s)/\partial s)$ denotes the *focusing length*. The latter quantity tends to infinity for a homogeneous field, which makes the overall term vanish for this special case.

Different changes in pitch-angle are due to pitch-angle scattering as described by the pitch-angle diffusion coefficient (PADC) $\kappa_\mu(s, \mu')$ (2.55). The parallel mean free path $\lambda_{||}$ is related to small angle wave-particle interactions via (2.55). In the geometry of an Archimedean spiral, $\lambda_{||}$ is connected to the radial mean free path λ_r by

$$\lambda_r = \lambda_{||} \cos^2 \Psi. \quad (3.8)$$

Changes in momentum, as shown in the forth line of (3.1), are due to the expansion of the solar wind (adiabatic deceleration, betatron effect) and the “inverse Fermi effect” (see Section 2.4.3 and 3.2.1).

The last term in (3.1) gives a particle source, depending on time t , position s_0 , pitch-cosine μ' , and momentum p' .

It should be noted that the partial differential equation (3.1) does not represent the complete transport equation by Ruffolo. Some terms have explicitly been excluded, since these physical processes play a minor role. As an example, the solar wind convection can cause an anisotropy in the distribution of the fixed frame (*Compton-Getting effect*, Section 2.4.1).

3.2. An extended and modified model version

Intensity- and anisotropy-profiles measured by satellite in interplanetary space have to be interpreted carefully since the observation site and the acceleration sites in general are remote from each other. The observed data is a result of both acceleration mechanisms at different locations and subsequent interplanetary transport.

In most studies, the interplanetary transport was treated essentially one-dimensional along the magnetic field lines. SEP events were assumed to be spherically symmetric, that is to say that source particles would be injected symmetrically around the flare

side. As a consequence, all computed intensity-time profiles of any location are subject to a factor of normalization proportional to the total number of particles injected onto that field line (Zhang, Qin and Rassoul, 2009).

Indeed, observations of field-aligned anisotropies suggest that particles stream essentially along the magnetic field line (Fisk and Axford, 1968; Jokipii, 1966). According to the quasi-linear theory (cf. Section 2.4.2), perpendicular diffusion coefficient is usually much smaller than parallel diffusion coefficient. Palmer (1982) made the highest estimate for $\lambda_{\perp}/\lambda_{\parallel}$ of about 1/10 (see also Section 5.3).

However, observations show that perpendicular diffusion could be considerably large relative to parallel diffusion (Dwyer et al., 1997; Zhang et al., 2003). Evaluating SEP time-profiles observed by multiple spacecraft show, that these measurement at different locations must be somehow related, and that they have the same source.

McKibben et al. (2003) and later studies used multi-spacecraft measurements of SEP events to illustrate that the particle fluxes measured at very different locations often reach an equal level in the decay phase of large SEP events, independent of the events source on the Sun. These observations in protons, but also heavy ions and energetic electrons give evidence for a uniform filling of the inner heliosphere with invariant spectra and vanishing gradients (called “reservoirs” by Roelof et al., 1992, see also McKibben et al., 2003). Events observed by IMP at 1 AU and Ulysses ranging between 2 and 2.8 AU with magnetic footpoints almost opposite on the Sun and at widely different latitudes show similar intensity-profiles (McKibben et al., 2001). Interpretations include particle trapping behind the shock (Reames et al., 1996) or the filling of a magnetic bottle formed by an earlier coronal mass ejection (CME) (Reames, Barbier, Rosenvinge, Mason, Mazur and Dwyer, 1997). Since invariant spectra can also be observed in small impulsive electron events without an accompanying (or preceding) shock/CME (Kallenrode, 2005) as well as up to high latitudes (Dalla et al., 2003) their coupling to special plasma structures such as magnetic clouds or shocks is not necessary. Instead, they also can be explained considering the heliosphere as a leaky particle reservoir (McKibben et al., 2001) at least 50 AU³ in size (Patterson and Armstrong, 2003) with an intensity decay time of about three days (MacLennan et al., 2003). A possible filling mechanism is transport of particles both parallel and perpendicular to the field from a localized, but not necessarily punctual, source.

The SEP fluxes in the initial phase, however, can be very different by several orders of magnitude, depending on where the spacecraft is located relatively to the solar source.

Currently there is no consensus on the mechanisms for the formation of solar energetic particle reservoirs. McKibben (1972) and McKibben et al. (2003) suggested an effective cross-field diffusion to distribute the particles uniformly, while Roelof et al. (1992) and Reames, Kahler and Ng (1997) involved some kind of diffusion barrier produced by interplanetary coronal mass ejections or shocks to contain the particles long enough for them to distribute uniformly through normal diffusion and adiabatic cooling. However, none of these theories have gone through detailed model calculation to reproduce the observed properties.

Another hint for cross-field transport comes the continuous spread of type III radio bursts that indicates that the 2 - 50 keV electrons responsible for these bursts must be transported across the field lines in interplanetary space (Cane and Erickson, 2003).

The theoretical re-analysis of three-dimensional magnetic field turbulence show that non-linear effects could cause large perpendicular diffusion (Matthaeus et al., 2003; Qin, 2007; Shalchi et al., 2004).

Using pure slab geometry (assuming Alfvén waves), comparisons between the numerical

solutions to mfps and PADCs determined from the fluctuations yield a discrepancy by up to a factor of 10 (e.g. Bieber et al. (1994), and references therein). In addition, the standard QLT predicts an increase of λ with rigidity while the observations suggest λ to be independent of rigidity.

Obviously, the dynamics of the fluctuating parts of the field - interacting with the energetic particles - are still not well understood. The introduction of additional cross-field losses might explain the discrepancy. This allows to formulate constraints on the interpretation of one-point in-situ measurements of magnetic field turbulence from particle data to gain a better understanding on the nature of this turbulence. In addition, new possibilities as well as limitations in data interpretation could be identified. Thus, besides slab turbulence affecting field-parallel propagation, the first step would be to find a formal description of cross-field transport, and to incorporate it into already existing modeling approaches.

3.2.1. Model equation

The choice of the transport model depends on what should be modeled. In case of the Roelof's Equation, we are limited to high energetic particles where solar wind effects do not affect particles significantly. But, we will only document the features of the Ruffolo's equation (1994) since both are identical, if solar wind effects are neglected.

This is, how the modified, cross-field-including version of the Ruffolo equation looks like:

$$\frac{\partial F(t, s_{\parallel}, s_{\perp}, \mu', p')}{\partial t} = \quad (3.9)$$

$$\frac{\partial}{\partial s_{\parallel}} ([\mu' v' + v_{sw} \cos \Psi] F(t, s_{\parallel}, s_{\perp}, \mu', p')) \quad (3.10)$$

$$+ \frac{\partial}{\partial \mu'} \left(v' \frac{1 - \mu'^2}{2L(s)} F(t, s_{\parallel}, s_{\perp}, \mu', p') - \kappa_{\mu}(s, \mu') \frac{\partial F(t, s_{\parallel}, s_{\perp}, \mu', p')}{\partial \mu'} \right) \quad (3.11)$$

$$\frac{\partial}{\partial p'} \left(p' v_{sw} \left[\frac{\cos \Psi}{2L(s_{\parallel}, s_{\perp})} (1 - \mu'^2) + \cos \Psi \frac{\partial}{\partial r} (\cos(\Psi)) \mu'^2 \right] F(t, s_{\parallel}, s_{\perp}, \mu', p') \right) \quad (3.12)$$

$$+ \frac{\partial}{\partial s_{\perp}} (v_{sw,\perp}(s_{\perp}) F(t, s_{\parallel}, s_{\perp}, \mu', p')) - \frac{\partial}{\partial s_{\perp}} \left(\kappa_{\perp}(s_{\parallel}, s_{\perp}, \mu) \frac{\partial F}{\partial s_{\perp}} \right) \quad (3.13)$$

$$= Q(s_{\perp,0}, t, \mu', p') . \quad (3.14)$$

All unchanged terms – except for (3.12) and (3.13) – have already been described in Section 3.1. What obviously changed is that we have added a spatial diffusion term in azimuthal/ perpendicular direction $\kappa_{\perp}(s_{\parallel}, s_{\perp}, \mu)$ as well as an convection term in s_{\perp} .

This extension by an extra diffusion term is formally reasonable since Roelof and Ruffolo start from the assumption that acceleration in interplanetary space does not change the particle's energy but only the direction of motion. The scattering process then is described as a random walk of the velocity vector on a sphere in velocity space. Inserted into a Fokker–Planck equation, this assumption leads to a transport equation with a simple solution for the undisturbed magnetic field \mathbf{B}_0 independent of location and a more complex one for $\mathbf{B}_0 = \mathbf{B}_0(\mathbf{r})$. In the simple model, spatial diffusion perpendicular to the field is inhibited efficiently – as a result but not as a prerequisite of the model. The model for $\mathbf{B}_0 = \mathbf{B}_0(\mathbf{r})$ is simplified to the commonly-used Roelof equation under the assumption that the squared product $(\omega T)^2$ of the gyration period (2.3) ω and the typical time scale

T of propagation is large and thus $\lambda_{\perp}/\lambda_{\parallel} \ll 1$. The assumptions underlying Ruffolo's transport equation are fulfilled as long as low ratios are chosen¹.

In fact, all changes are a consequence of both a change in the frame of reference and additional transport in the field-perpendicular direction. We will focus on these changes in the following subsections – each section treating one of the transport processes in s_{\parallel} , s_{\perp} , μ' and p' .

Field-parallel transport

In Ruffolo's approach, the observer is corotating with the Sun. Thus, the observer is always connected to the same field line. Consequently, the local observer detects a solar wind which is always aligned parallel to the IMF. v_{sw}^c inevitably grows till infinity because the azimuthal component increases linearly with the radial distance (see also Parker, 1958). This is why the relativistic correction term $1 - (\mu'v')^2/(c^2)$ has been established. The driving force behind this “artificial” approach is the lack of adjacent field lines: Owing to the projection, the solar wind velocity is insured to be always field-aligned and that the observer stays on the central field line (CFL). That is also the reason why pitch-angle distributions in the solar wind frame are assumed to be conserved as long as we are neglecting focusing effects.

However, including additional perpendicular transport, and thus extending to a two-dimensional geometry, we gave up the unphysical corotation approach and split the local solar wind velocity v_{sw} into one component parallel to the IMF

$$\mathbf{v}_{sw,\parallel} = v_{sw} \cos(\Psi) \mathbf{e}_s$$

and another which is perpendicular to the IMF:

$$\mathbf{v}_{sw,\perp} = v_{sw} \sin(\Psi) \mathbf{e}_{\perp}.$$

Thus, for the field-parallel part of the transport equation (3.1), we get alternatively:

$$\frac{\partial F(t, s_{\parallel}, s_{\perp}, \mu', p')}{\partial t} = \frac{\partial}{\partial s_{\parallel}} ([\mu'v' + v_{sw} \cos \Psi] F(t, s_{\parallel}, s_{\perp}, \mu', p')) . \quad (3.15)$$

The relativistic correction factor has been omitted since the solar wind does not exceed v_{sw} : The new frame of reference is “convected” with the parallel component of radially outward streaming solar wind. Its implications on pitch-cosine and momentum transport are discussed in the following subsections. The parallel particle speed in the rest frame of the Sun is $\mu v = \mu'v' + v_{sw} \cos \Psi$. Note that this transformation would not work without explicit splitting.

¹In the unrealistic case of $\lambda_{\perp}/\lambda_{\parallel} > 1/10$, the particle's motion would not be effectively one-dimensional. Thus, the Ruffolo and Roelof equation would be obsolete, and a simple two-dimensional diffusion model would be a better choice for a first approach on 2D transport.

Pitch-cosine transport

The μ' -transport term remains unchanged in its structure. The focusing length L and the PADC κ_μ must be determined with regard to different spatial coordinates $(s_{\parallel}, s_{\perp})$.

$$\begin{aligned} \frac{\partial F(t, s_{\parallel}, s_{\perp}, \mu', p')}{\partial t} = \\ \frac{\partial}{\partial \mu'} \left(v' \frac{1 - \mu'^2}{2L(s_{\parallel}, s_{\perp})} F(t, s_{\parallel}, s_{\perp}, \mu', p') - \kappa_\mu(s_{\parallel}, s_{\perp}, \mu') \frac{\partial F(t, s_{\parallel}, s_{\perp}, \mu', p')}{\partial \mu'} \right) \end{aligned} \quad (3.16)$$

The positive side effect of the splitting of the solar wind into the field-parallel part $v_{sw,\parallel}(s) = v_{sw} \cos(\Psi(s))$ and an exactly perpendicular part $v_{sw,\perp}(s) = v_{sw} \sin(\Psi(s))$ is, that pitch-angle distributions are conserved during field-parallel- or field-perpendicular advection. But it should be noted that the superposition again would lead to additional anisotropy, as it is described by the Compton-Getting effect (Compton and Getting, 1935).

Perpendicular transport

As already done by Lampa (2006) and in more advanced studies by Lampa and Kallenrode (2009), we introduced a second spatial coordinate s_{\perp} to accommodate perpendicular transport in the plane of the ecliptic. The diffusion coefficient $\kappa_{\perp}(s_{\parallel}, s_{\perp}, \mu)$ is exclusively defined on the basis of spatial gradients (classical diffusion) and might vary in space and pitch-cosine as well:

$$\frac{\partial F(t, s_{\perp})}{\partial t} = \frac{\partial}{\partial s_{\perp}} (v_{sw,\perp}(s_{\perp}) F(t, s_{\perp})) - \frac{\partial}{\partial s_{\perp}} \left(\kappa_{\perp}(s_{\parallel}, s_{\perp}) \frac{\partial F(t, s_{\perp})}{\partial s_{\perp}} \right). \quad (3.17)$$

s_{\parallel} , μ' and p' in (3.17) have been omitted because these variables are kept constant to find a numerical solution (see Section 4.1.3). The modeled SEPs are additionally convected with the solar wind, as denoted by the perpendicular component $v_{sw,\perp}(s_{\perp})$ in the first derivative of (3.17). Formally, this PDE describes the same type of equation as the one for transport in pitch-angle.

Adiabatic deceleration

If changes due to momentum are involved, the Fokker-Planck equation (2.29) is expanded by the term

$$-\frac{\partial}{\partial p'} \left(\frac{\Delta p'}{\Delta t} F(p') \right). \quad (3.18)$$

The time derivative $\dot{p}' = \Delta p'/\Delta t$ in the frame of the field-aligned solar wind covers various effects of adiabatic deceleration – among them are two of major impact on the particle distribution. The first one results from the fact that the magnitudes of SEP velocities v' in the moving reference frame are conserved because solar energetic particles are expected to interact with the superposed small-scale irregularities frozen into the solar wind. On the other hand, focusing preserves v , as it has already been shown in (3.7). The combination of scattering in the moving frame and focusing in the fixed frame systematically

decreases v' . The second effect emerges as particles streaming outward along the field line experience decaying solar wind velocities (only the field-aligned component of \mathbf{v}_{sw} is considered). Ruffolo (1994) derived an explicit formula in the framework of focused transport which includes this kind of deceleration and the solar wind convection – under the assumption that the small- and large-scale structures of the IMF remain stationary. The first rate of deceleration can be calculated in a straightforward way:

$$\dot{v}' = \frac{dv'}{d\mu} \Big|_{v'=v} \frac{d\mu}{dt}, \quad (3.19)$$

with

$$\frac{d\mu}{dt} = \frac{v}{2L(s)} (1 - \mu^2)$$

as the focusing term in the fixed frame (3.7). v' expressed in terms of μ gives:

$$v'(\mu) = \sqrt{v_\perp'^2 + v_\parallel'^2} = \sqrt{(1 - \mu^2)v^2 + (\mu v - v_{sw,\parallel})^2}.$$

Its derivative with respect to μ yields

$$\frac{dv'}{d\mu} = \frac{1}{2} \frac{1}{\sqrt{(1 - \mu^2)v^2 + (\mu v - v_{sw,\parallel})^2}} (-1) 2vv_{sw,\parallel} = -\frac{vv_{sw,\parallel}}{v'},$$

and therefore

$$\frac{dv'(\mu)}{d\mu} \Big|_{v'=v} = -v_{sw,\parallel}.$$

Inserting into (3.19), we get

$$\dot{v}' = -\frac{v'v_{sw}}{2L(s)} (1 - \mu'^2) \quad \text{or} \quad \dot{p}' = -\frac{p'v_{sw}}{2L(s)} (1 - \mu'^2). \quad (3.20)$$

This equation is identical to the one as derived from Ruffolo (1994), Equation (4), but the solar wind component parallel to an Archimedean spiral field was considered. In literature, this rate of change in momentum is termed “adiabatic focusing” or *betatron effect* as described phenomenologically in the basics Section 2.4.3.

To formally shed light on the second, above-mentioned physical effect, consider particles streaming outward from point A to B along the field line. On their way, they experience decaying solar wind velocities. Assuming $p_{\parallel A}$ to be constant and neglecting terms of order $(v_{sw,\parallel}/c)^2$, we get

$$p'_{\parallel,A} = p_{\parallel A} - \frac{E}{c^2} v_{sw,\parallel,A} \quad \text{and} \quad p'_{\parallel,B} = p_{\parallel B} - \frac{E}{c^2} v_{sw,\parallel,B}.$$

The momentum difference between point A and B is

$$\Delta p'_{\parallel} = -\frac{E}{c^2} v_{sw} (\Delta \cos(\Psi)).$$

In the Parker spiral, with Δs being the distance between A and B , and Δt being the travel time, we get

$$\Delta p'_{\parallel} = -\frac{E}{c^2} v_{sw} \left(\frac{d}{ds} \cos(\Psi) \right) v_{\parallel} \Delta t \quad ; \quad \Delta s = v_{\parallel} \Delta t$$

$$\Leftrightarrow \dot{p}'_{\parallel} = \lim_{\Delta t \rightarrow 0} \frac{\Delta p'_{\parallel}(t)}{\Delta t} = -p_{\parallel} v_{sw} \left[\frac{dr}{ds} \frac{d}{dr} (\cos(\Psi(r))) \right] = -p_{\parallel} v_{sw} \left[\cos(\Psi(r)) \frac{d}{dr} (\cos(\Psi(r))) \right]$$

$$\Leftrightarrow \dot{p}'_{\parallel} = -p_{\parallel} v_{sw} \left[\frac{1}{\sqrt{1 + \left(\frac{\omega_{\odot} r}{v_{sw}} \right)^2}} \cdot \left(-\frac{r \left(\frac{\omega_{\odot}}{v_{sw}} \right)^2}{(1 + (\frac{\omega_{\odot} r}{v_{sw}})^2)^{\frac{3}{2}}} \right) \right] = -p_{\parallel} v_{sw} \left[-\frac{r \left(\frac{\omega_{\odot} r}{v_{sw}} \right)^2}{\left(1 + \left(\frac{\omega_{\odot} r}{v_{sw}} \right)^2 \right)^2} \right]$$

In order to examine differential convection alone, p'_{\perp} is fixed. Since $p_{\parallel} v_{sw} \approx p'_{\parallel} v_{sw}$ to first order in $(v_{sw,\parallel}/c)$ – according to Equation (6) in Ruffolo (1994) – the second order rate of deceleration is:

$$\dot{p}' = \frac{p'_{\parallel}}{p'} \dot{p}'_{\parallel} = -p' v_{sw} \left(\cos(\Psi) \frac{d}{dr} (\cos(\Psi)) \right) \mu'^2 \quad (3.21)$$

The term differs from the former one by the last cosine of Ψ , since another transformation of the solar wind has been made. Under the assumption of isotropic distributions of solar cosmic rays and a radial field, (3.21) simplifies to

$$\langle \dot{p}' \rangle = -\frac{p'}{3} \nabla \mathbf{v}_{sw}, \quad (3.22)$$

which has been used in many studies of cosmic ray transport (e.g. Parker, 1965). Finally, the momentum dependent part of Fokker-Planck equation (3.18) with (3.20) and (3.21) becomes:

$$\frac{\partial F(t, \mu', s, p')}{\partial t} = \frac{\partial}{\partial p'} \left(p' v_{sw} \left[\frac{\cos(\Psi)}{2L(s)} (1 - \mu'^2) + \cos \Psi \frac{\partial}{\partial r} (\cos(\Psi)) \mu'^2 \right] F(t, \mu', s, p') \right). \quad (3.23)$$

For the sake of completeness, it should be emphasized that, in contrast to the betatron effect, the inverse Fermi-effect can cool SEPs propagating perpendicular to the field – in particular around 1 AU, since changes of the field-perpendicular component of the solar wind speed are maximum there. If both field-parallel and perpendicular solar wind effect are considered, it can be denoted as *inverse Fermi-effect* (Section 2.4.3).

3.2.2. Choice of the grid

We adopted both the Roelof's Equation and the Ruffolo's Equation to accommodate cross-field transport in the inner heliosphere. The differential terms are discretized by finite differences (see Chapter 4), thus the spatial domain of the ecliptic has to be discretized, too: An appropriate grid has to be defined.

Azimuthal Transport

The original one-dimensional code works on equidistant grid points along the magnetic field line with step size Δs . Expanding this approach to two dimensions combined with azimuthally aligned cross-field trajectories, leads to concentric rings which get closer and closer to each other with increasing radial distance (see also Lampa and Kallenrode, 2009). Thus particles are shifted in the azimuthal direction by

$$ds_{\perp}(r) = rd\varphi. \quad (3.24)$$

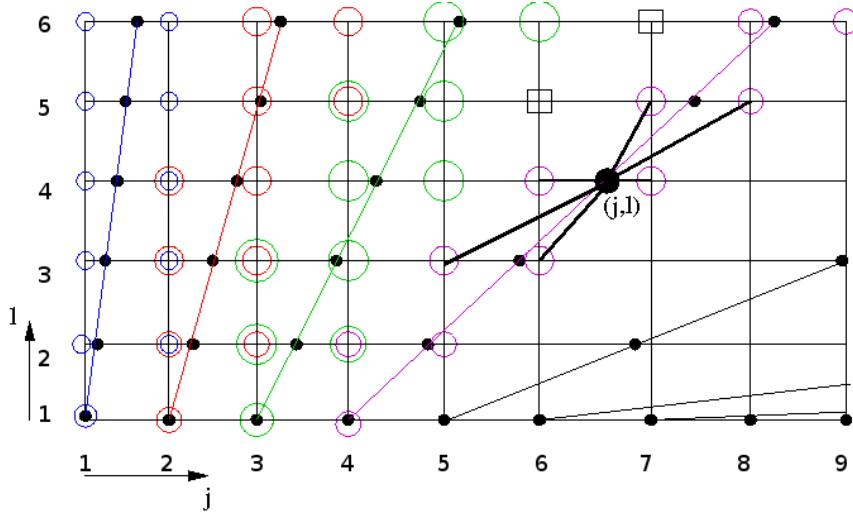


Figure 3.1.: Perpendicular paths in a grid of azimuthal cross-field transport ($\Delta s = \text{const.}$).
The resulting numerical scheme would be inaccurate since the topology is not squared – some of the grid points do not contribute to the transport.

But in this spatially fixed frame, these trajectories are just “roughly” perpendicular to the IMF very close to the Sun (within a radius of a few tens of an AU).

Consequently, the first step was to find a scheme that would realize perpendicular transport without changing the grid architecture. The idea was to calculate the intersection between the perpendicular path with the neighboring field line. In general, these intersections are not expected to hit a neighboring grid point exactly (indicated by the black filled circles in Figure 3.1). Based on these “virtual grid points”, a weighting factor could be established. During cross-field transport, it determines the fractions of particles that are assigned to the left neighboring grid points (on the same field line like the intersection point) and to the neighboring right points (these are equally colored in Figure 3.1). So, basically, the fluxes in westward/ eastward direction are split into 2 components.

Despite this splitting, we can still realize perpendicular transport as essentially one-dimensional - denoted by the point (j, l) in the Figure: The classical diffusion finite difference (FD) needs three neighboring grid point to approximate the second derivative. Here, due to the splitting, six points are involved for each virtual grid point. As an example, we have marked these inter-point-relationships at point (j, l) . This would lead to an equation system that – in matrix form – would have six diagonals (six grid points are involved as seen in Figure 3.1), but just under the assumption that the numerical values ξ of the distribution function are properly arranged within the solution vector v^n .

Example for the magenta colored curve:

$$\mathbf{A}v^{n+1} = v^n \quad \text{with } v^n = (\xi_{9,6}, \xi_{8,6}, \xi_{8,5}, \xi_{7,5}, \xi_{7,4}, \xi_{6,4}, \xi_{6,3}, \xi_{5,3}, \xi_{5,2}, \xi_{4,2}, \xi_{4,1})^T$$

The sequence of indexes for v^n has to be computed before the numerical scheme starts. The sequence differs with respect to different perpendicular curves. If we hit the grid points exactly, the resulting matrix \mathbf{A} would be tri-diagonal. The equation could be solved in linear runtime. In case of the six-point-scheme, the effort doubles.

In a slightly modified approach, we do not try to solve the complete scheme within a single time step, but split into an azimuthal part and a part hitting the neighboring (right) point.

Unfortunately, sometimes and especially at larger radial distances from the Sun and for large azimuthal distances $\Delta\varphi$, this fails completely, since the azimuthal part and/or the neighboring part is missing. Starting at point (5, 1) for example, point (5, 2) in azimuthal direction does not account for cross-field transport.

Coming back to the first approach, another artifact can be observed – denoted by the squares: Further out, where the perpendicular curves tend to point in radial direction, some grid points are never hit, thus there exists no perpendicular transport. On the other hand, there are grid points which are considered twice (or even higher in eastern direction). These cells dry out by trend, although the net flux is kept in balance by the weighting factors. The reason is that the next time step can not be computed for all perpendicular curves simultaneously. We have to prioritize a curve over another.

Consequently, the next step was to realize exact perpendicular transport in the plane of the ecliptic, where a grid point exactly hits the neighbor during the cross-field shift.

Exact Perpendicular Transport

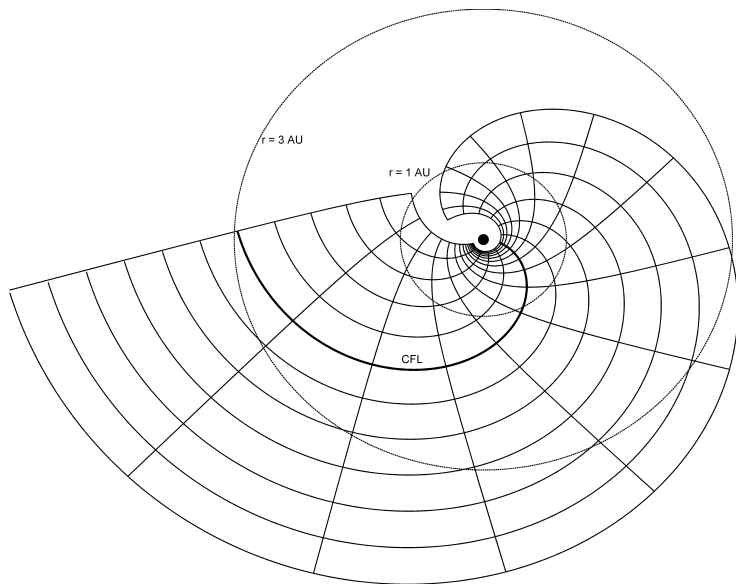


Figure 3.2.: IMF and perpendicular curves for azimuthal distances of $d\varphi = 20^\circ$.

The question now is how to calculate a grid consisting of both the fictitious Archimedean field lines and the curves perpendicular to it.

The intersections “field line – perpendicular trajectory” can be found by looking at the local geometry in Figure 3.3: The dotted curves of lower density indicate two field lines within the ecliptic plane, originating at the Sun S . The intersection point A of the densely dotted, perpendicular curve is known by construction. The following intersection point B can be found by calculating the slope triangle in point $(r_0, 0)$:

$$\frac{rd\varphi}{dr} = \frac{\cos(\Psi(r))ds_\perp}{\sin(\Psi(r))ds_\perp},$$

where ds_\perp denotes an infinitesimal deviation in field-perpendicular direction. Simplifying

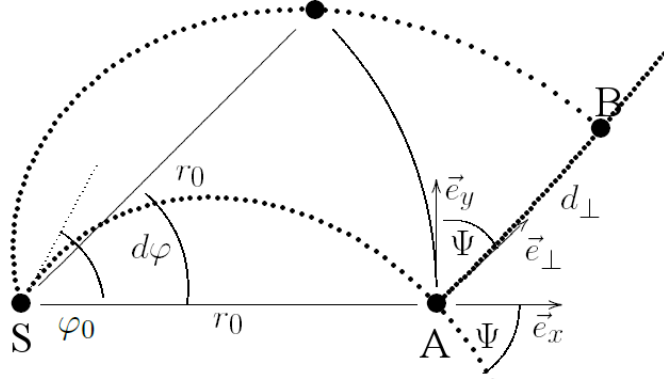


Figure 3.3.: Local geometry in the Archimedean field

the upper equation yields:

$$\frac{rd\varphi}{dr} = \frac{1}{\tan(\Psi(r))}.$$

Since $\tan(\Psi(r)) = \omega_\odot \sin(\theta)r/v_{sw}$ according to the definition of the Archimedean spiral angle (2.39), we finally get an equation which depends solely on φ and r_\perp . It is separable into

$$\frac{1}{r^2}dr = \frac{\omega_\odot \sin(\theta)}{v_{sw}}d\varphi \quad (3.25)$$

and can be solved by taking the integral over the equation as a whole:

$$r_\perp(r_0, \varphi) = \frac{r_0}{1 - \frac{\omega_\odot r_0 \sin(\theta)\varphi}{v_{sw}}}. \quad (3.26)$$

Thus, we are able to express the radius in terms of φ only. The corresponding position vector is

$$\mathbf{r}_\perp(r_0, \varphi) = r_\perp(r_0, \varphi) \begin{pmatrix} \cos(\varphi(r)) \\ \sin(\varphi(r)) \end{pmatrix}, \quad (3.27)$$

which starts at position $(r_0, 0)$ in the Cartesian coordinate system as defined in Figure 3.3. The footpoint A lies on the field line

$$\mathbf{r}_{\parallel}(\varphi) = \frac{v_{sw}\varphi}{\omega_\odot} \begin{pmatrix} \cos(\varphi(r) + \varphi_0) \\ \sin(\varphi(r) + \varphi_0) \end{pmatrix} \quad ; \quad \varphi_0 = \frac{\omega_\odot \sin(\theta)r_0}{v_{sw}}.$$

Note that, because of the rotational symmetric geometry, all other field lines and perpendicular trajectories can be built by simply rotating by a multiple of $\Delta\varphi$:

$$\mathbf{r}_{\perp,\parallel}(\varphi + n\Delta\varphi) = \mathbf{D}_{n\Delta\varphi} \mathbf{r}_{\perp,\parallel}(\varphi),$$

$$\text{with rotation matrix } \mathbf{D}_{n\Delta\varphi} = \begin{pmatrix} \cos(n\Delta\varphi) & -\sin(n\Delta\varphi) \\ \sin(n\Delta\varphi) & \cos(n\Delta\varphi) \end{pmatrix}.$$

The Archimedean field lines are defined for all φ , but the perpendicular trajectories end asymptotically in radially outward directed lines (see Figure 3.2). That is the reason why (3.27) – starting at $\varphi = 0$ is only valid for longitudes $\varphi \in [0, \frac{v_{sw}}{\omega_\odot \sin(\theta)r_0}]$.

Using Pythagoras' theorem, one can easily derive the arc length of the perpendicular curves needed to compute the distances between the field lines:

$$ds_\perp = \sqrt{dx^2 + dy^2} = \sqrt{\left(\frac{dx(r_0, \varphi)}{d\varphi}\right)^2 + \left(\frac{dy(r_0, \varphi)}{d\varphi}\right)^2} d\varphi.$$

With $x(r_0, \varphi) = r_\perp(r_0, \varphi) \cos(\varphi)$ and $y(r_0, \varphi) = r_\perp(r_0, \varphi) \sin(\varphi)$, ds_\perp can be reformulated according to the azimuth φ :

$$ds_\perp = \sqrt{\left(\frac{dr(\varphi)}{d\varphi}\right)^2 + (r(\varphi))^2} d\varphi = \sqrt{\left(\frac{r_\perp(\varphi)^2 \omega \sin(\theta)}{v_{sw}}\right)^2 + r_\perp(\varphi)^2} d\varphi.$$

A step size along a curve (or arc length) perpendicular to the IMF implies a change in azimuth of $\Delta\varphi$, which is denoted by the longitudinal distance between two neighboring field lines.

For simplicity (and without loss of generality) we assume that the perpendicular trajectories are drawn in the ecliptic plane with $\theta \approx 90^\circ$. We can integrate the expression above:

$$\Delta s_\perp(r_0, \Delta\varphi) = \int_{\varphi(r_0)}^{\varphi(r_0) + \Delta\varphi} \sqrt{\left(\frac{r_\perp(\varphi)^2 \omega}{v_{sw}}\right)^2 + r_\perp(\varphi)^2} d\varphi.$$

This is the perpendicular distance between two field lines. The integration path starts at radius r_0 , positive values in φ indicate westward (anti-clock-wise) and negative values eastward direction.

$$ds_\perp(r_0, \Delta\varphi) = \frac{v_{sw}}{\omega_\odot \chi(r_0, \varphi)} \left[-\chi(r_0, \varphi) \log \left(2 \left(-\chi(r_0, \varphi) + \sqrt{(r_0^2 \omega_\odot^2 + \chi(r_0, \varphi)^2)} \right) \right) - \sqrt{\chi(\varphi)^2 + r_0^2 \omega_\odot^2} \right]_{\varphi(r_0)}^{\varphi(r_0) + \Delta\varphi} \quad (3.28)$$

with

$$\chi(r_0, \varphi) = r_0 \varphi \omega_\odot - v_{sw}.$$

By doing so, we have overcome the problem from Jahns (2007) who actually found adequate perpendicular distances $ds_\perp(r) = rd\varphi/(1 + \tan(\Psi(r))^2)$ by linear approximation. As it is seen in Figure 3.4, $ds_\perp(r)$ is underestimated to the west of the corresponding field line in the Jahns' approach, and overestimated when going westward – owing to the linear approach.

Very close to the Sun $ds_\perp(\varphi(r))$ increases almost linearly with $ds_\perp \propto rd\varphi$ (indicated by the dotted line), since the field lines are aligned in radial direction (well in agreement with azimuthal transport and the Jahn's approach). The values coincide beyond a few AU as well, due to the concentric rings forming field lines whose corresponding perpendicular

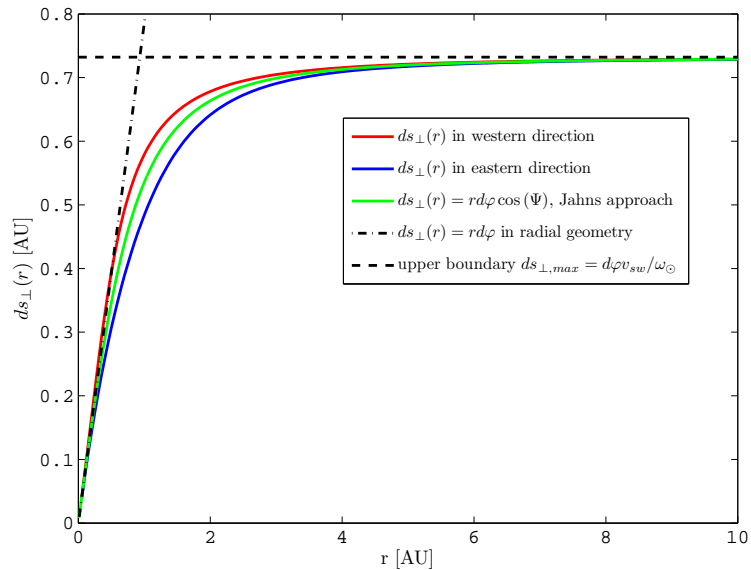


Figure 3.4.: Perpendicular distance $\Delta s_{\perp}(r)$ between two neighboring field lines for $\Delta\varphi = 45^\circ$ (angular distance between 2 field lines.)

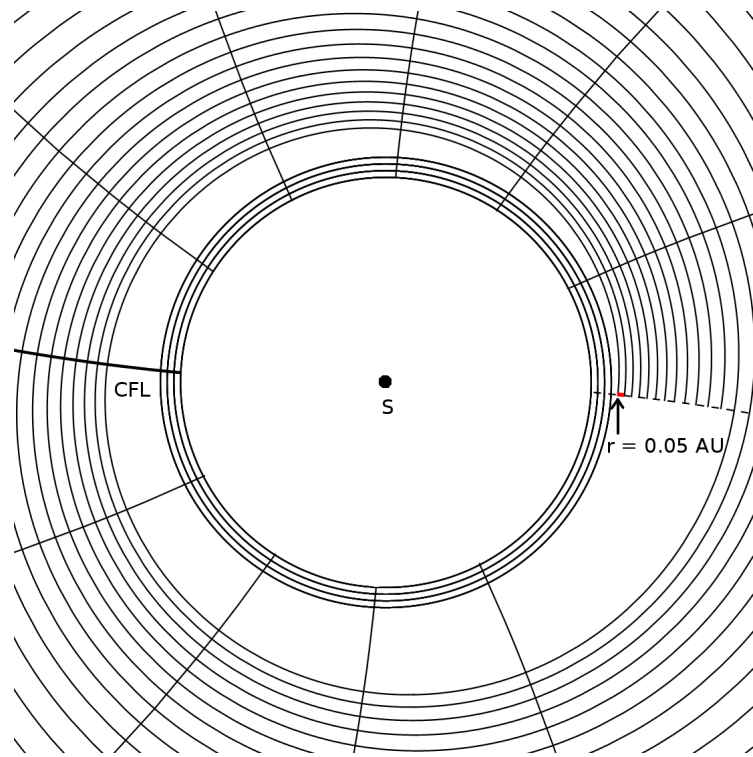


Figure 3.5.: The hybrid grid as a combination of both concentric rings close to the Sun and perpendicular trajectories.

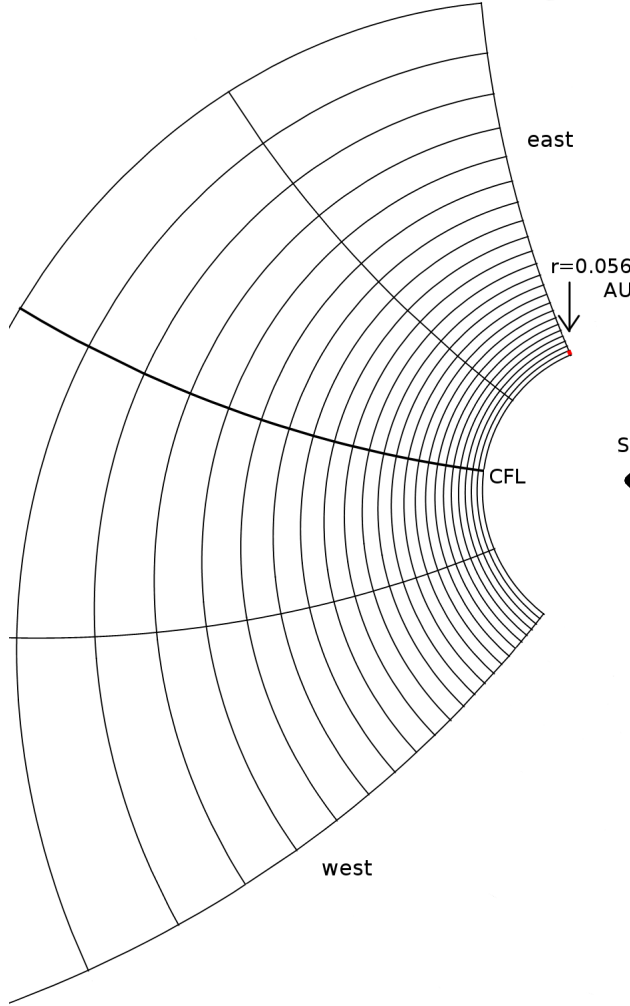


Figure 3.6.: Reducing the azimuthal extent of the perpendicular grid.

curves are directed in the radial direction. For these geometrical reasons, $ds_{\perp}(r)$ reaches asymptotically the upper boundary $\Delta s_{\perp,\max} = \Delta\varphi v_{sw}/\omega_{\odot}$.

During the time ΔT , a field line has been wound up once by

$$\Delta\varphi = \omega_{\odot}\Delta T.$$

At the same time, it has been shifted in radial direction by the increment

$$\Delta r = v_{sw}\Delta T.$$

Since $\Delta r = \lim_{r \rightarrow \infty} \Delta s_{\perp}(r) = \Delta s_{\perp,\max}$ we finally get the maximal perpendicular distance as mentioned above.

The values of this current approach and the one of Jahn differ the most at 1 AU (the Earth's orbit) where the spiral angle is $\Psi \approx 45^\circ$. These differences seem to be not that much – especially for $\Delta\varphi \rightarrow 0$. But local errors sum up when the perpendicular paths are calculated incrementally, by going from one field line to the neighboring one, calculating the intersections of the perpendicular curve and the neighboring field line.

Since we know about the intersections between the field lines and their perpendicular counterparts, as expressed by $r_{\perp}(r_0, \varphi)$ in (3.26), we can compute the field parallel distance between two intersection points: The neighboring radii, denoted by

$$r_{\perp}(r_0, \varphi_n) \text{ and } r_{\perp}(r_0, \varphi_{n+1}) \text{ with } \varphi_{n+1} = \varphi_n + n\Delta\varphi ; n \in \mathbb{N},$$

are transformed into the corresponding arc length along the field line by applying (2.39) and then taking the difference. For a fixed position, the parallel step sizes $\Delta s_{\parallel}(r)$ are even smaller than $\Delta s_{\perp}(r)$ – as it also can be seen in Figure 3.2. In the numerics section 4.2 at (4.21), it will be shown that very low values of Δs_{\parallel} enlarge the computation time of the numerical model significantly.

This negative effect can be weakened by introducing some restrictions to the grid. Probably the most effective technique would be a “hybrid” approach, which combines both the features of the purely azimuthal grid and the perpendicular grid (see Figure 3.5). The very inner region below $r = 0.05$ AU is replaced by concentric rings. The distance between two neighbouring rings is given by the smallest Δs_{\parallel} (red colored line, indicated by an arrow in Figure 3.5). If that region of concentric rings had been covered by perpendicular trajectories, Δs_{\parallel} would be significantly smaller. A negative, secondary effect are very large step sizes in the transition region between the azimuthal and perpendicular domain. The hybrid approach has not been implemented yet, but at least one feature can already be applied: The more the inner boundary is shifted Sun outward, the larger the step sizes will be. Unfortunately, by doing so, the domain close to the Sun will not be covered anymore. In order to still simulate close to the Sun and simultaneously have adequate step sizes, we could reduce the azimuthal extent around the CFL instead, as indicated in Figure 3.6. The smallest step sizes are found at the eastern boundary. The less we are forced to go westward, the larger are the step sizes. Note that this is the most useful method if it is a priori known that no significant particle populations reach the outer boundary within the simulation period.

To sum up, Ruffolo’s equation has been applied within the plane of ecliptic by introducing a second spatial coordinate s_{\perp} perpendicular to the field. The frame of reference has been changed to the field-parallel component of the solar wind speed. The resulting grid is used in the following chapter to solve the transport equation numerically.

4. Numerics in Non-equidistant Grids

The goal is to build a numerical scheme that can adequately approximate the solution of the transport equation (3.9). As we know, an exact analytical solution is possible under very strong simplifications only see also (see also Hatzky, 1996; Lampa, 2006). Fortunately, we are able to adopt (at least in some parts) the Finite Difference (FD) schemes which have been applied to Roelof's (1969a) and later also to Ruffolo's equation (1994) on equally spaced grids by Wong (1982), Schlüter (1985), Ruffolo (1994), Hatzky (1996) and others.

4.1. Basics of the Finite-Difference Method

The infinite set of values in the continuous solution F is represented by a finite set of values ξ referred to as the discrete solution. For simplicity, we consider first the case of a function ξ of two variables t and x (time and space coordinate). Given a set of points $x_i; i = 1, \dots, I$ and $t_n; n = 1, \dots, N$ in the domain of $F(t,x)$, the numerical solution is represented by a discrete set of function values $\{\xi_{n,i}; i = 1, \dots, I; n = 1, \dots, N\}$ that approximate F at these points, i.e., $\xi_{n,i} \approx F(t_n, x_i)$. For a better comprehension, the points are assumed to be equally spaced within the domain with constant step sizes $\Delta t = t_{n+1} - t_n; n = 1, \dots, N - 1$ and $\Delta x = x_{i+1} - x_i; i = 1, \dots, I - 1$.

4.1.1. Consistency of finite differences

The construction of the numerical scheme involves the replacement of the differential terms by the corresponding finite difference (FD) terms. The latter ones can be build by using Taylor expansions around the point t_n or x_i . For instance, the forward difference approximation gives to $\xi_{i+1} \approx F(x_i + \Delta x)$ using $N+1$ terms of a Taylor expansion around x_i is given by

$$\begin{aligned}\xi_{i+1} &= \xi_i + \partial_x F(x)|_{x=x_i} \Delta x + \partial_{xx} F(x)|_{x=x_i} \frac{\Delta x^2}{2} + \dots \\ &\quad + \frac{\partial^n}{\partial x^n} F(x)|_{x=x_i} \frac{\Delta x^n}{n!} + \frac{\partial^{n+1}}{\partial x^{n+1}} F(x^*)|_{x=x_i} \frac{\Delta x^n}{(n+1)!}.\end{aligned}\quad (4.1)$$

The last term is called the *remainder* with $x_i \leq x^* \leq x_{i+1}$, and represents the error in the approximation if only the first n terms in the expansion are considered. Although the expression (4.1) is exact, the position x^* is unknown.

Putting ξ_i on the left side of (4.1) and dividing by Δx , we obtain the forward difference approximation of $\frac{\partial F}{\partial x}|_{x=x_i}$:

$$\frac{\partial F}{\partial x}\Big|_{x=x_i} = \frac{x_{i+1} - x_i}{\Delta x} + \epsilon_i,$$

where ϵ_i is given by

$$\epsilon_i = -\frac{\Delta x}{2} \partial_{xx} F(x^*) + O((\Delta x)^2).$$

Alternative approximations such as the backward and centered FD approximations (Chatot, 2002, p.6), would be also mathematically equivalent to the forward difference term: The approximations converge towards the derivative as $\Delta x \rightarrow 0$. But since Δx is finite, the numerical solutions of different FD converge differently towards the exact solution, which is indicated by the truncation error ϵ_i .

The truncation error is defined as the difference between the exact value and its numerical approximation. This term depends on Δx but also on F and its derivatives. The *order* of a finite difference approximation in terms of the step size is defined as the power p such that

$$\lim_{\Delta x \rightarrow 0} (\epsilon / \Delta x^p) = \gamma \neq 0, \text{ where } \gamma \text{ is a finite value. This is often written as } \epsilon_i = O(\Delta x^p).$$

For instance, the forward difference approximation gives $\epsilon_i = O(\Delta x)$ and it is said to be first-order accurate ($p = 1$).

If we apply this method to the centered finite difference approximation, we find that, for constant Δx , their errors are

$$\frac{\partial F}{\partial x} \Big|_{x=x_i} = \frac{x_{i+1} - x_{i-1}}{2\Delta x} - \frac{\Delta x^2}{12} \partial_{xxx} F(x^*) \quad \rightarrow \quad \epsilon_i = O(\Delta x^2).$$

The ϵ_i will be separately computed for each variable, keeping the other variable t constant. In the overall numerical scheme, the truncation errors for each FD will be added, e.g. $\epsilon_i^n = \epsilon_i + \epsilon^n$.

The resulting scheme has to be *consistent* which means that the truncation error ϵ_i^n (difference between the differential and its discretized terms) with respect to independent variable x_i and time t_n has to converge towards zero if the corresponding step sizes go to zero.

4.1.2. Stability

Having a stable numerical scheme requires that inherent, initial perturbations of the FD scheme are not allowed to grow arbitrarily high. The discrete solutions ξ_i^n have to be bounded within the domain:

$$\xi_i^n \leq C(\Delta t, \Delta x, \xi_0(t = t_1, 0), \xi_1(t, x = x_1), \xi_2(t, x = x_I)) \quad \forall i = 1, \dots, I. \quad (4.2)$$

The constant boundary C depends on the step sizes as well as the initial value ξ_0 and the boundary conditions ξ_1, ξ_2 . The inequality (4.2) originally comes from the treatment of the FDE as a *Cauchy problem* (Samarskij, 2001, p. 384). Assuming that the discrete solution is separable with respect to the time, the scheme can be rewritten as a linear equation system $\xi^{(n+1)} = \mathbf{A}\xi^{(n)}$ that iteratively describes the temporal evolution of $\xi_i; i = 1, \dots, I$ from t_n to t_{n+1} . Special requirements to \mathbf{A} , n -times application of the linear equation system, starting at $t = t_1$ and a proper choice of the norm would give an estimate of the upper boundary, denoted by (4.2).

If a limiting upper boundary is needed according to the maximum norm $\|\xi_i^n\|_{max} = \max_i |\xi_i|$, this would lead to the application of the *maximum principle* (Samarskij, 2001, p. 258), which is equivalent special properties of the matrix \mathbf{A} . We will come back to the details of stability analysis in the following sections, especially in Section 4.5.2. Matrix eigenvalues analysis in this context would be an alternative approach, but there are more involved.

Another norm under consideration is the euclidean norm

$$\|\xi_i^n\|_2 = ((\xi_1^n)^2 + (\xi_2^n)^2 + \cdots + (\xi_I^n)^2)^{1/2} .$$

Unfortunately, because of its averaging nature, highly frequent parts of ξ – high values of single components $\xi_i^{(n)}$ according to amount – will be damped, which might lead to unreasonable, high or even negative discrete solutions.

The stability of FD schemes for hyperbolic and parabolic PDEs under the Euclidean norm can be analyzed by the *Von Neumann* (or Fourier) method. It can only be applied to linear homogeneous FD equations or systems, as it is based on the superposition of wave modes. The idea behind the method is the following: The analytical solutions of e.g. the model diffusion equation $\partial_t F(t, x) - b \partial_{xx} F(t, x) = 0$ can be found in the form

$$F(t, x) = \sum_{m=0}^{\infty} \sum_{l=0}^{\infty} g_m \exp(\beta_m t) \exp(ik_l x) ;$$

with wave numbers k_n and frequency β_m of mode m , as it shown e.g. in (Chattot, 2002, p.54). This solution involves a Fourier series in space and an exponential decay in time since $\beta_m \leq 0$. Here we have included the complex version of the Fourier series, $\exp(ik_l x) = \cos(k_l x) + i \sin(k_l x)$ with the imaginary unit $i = \sqrt{-1}$, because this considerably simplifies later algebraic manipulations. To analyze the growth of different Fourier modes as they evolve under the numerical scheme we can consider each mode separately, namely

$$F_{m,l}(t, x) = g_m \exp(\beta_m t) \cdot \exp(ik_l x) .$$

A discrete version of this equation is $\xi_j^{(n)} = g_m \exp(\beta_m t_n) \exp(ik_l x_j)$. We can use, without loss of generality and in case of equally spaced grid points, $x_j = j \Delta x$ and $t_n = n \Delta t$ to obtain

$$\xi_j^{(n)} = g_m^n \exp(\beta_m n \Delta t) \cdot \exp(ik_l j \Delta x) = \exp(\beta_m \Delta t)^n \cdot \exp(ik_l j \Delta x) .$$

The term $\exp(ik_l j \Delta x) = \cos(k_l j \Delta x) + i \sin(k_l j \Delta x)$ is bounded and, therefore, any growth in the numerical solution will arise from the complex amplitude raised to the n -th power g_m^n . Each Fourier mode is treated separately: The linearity of the equations insures that, if the numerical scheme is stable for each mode, it will be stable for any superposition of modes. Putting the complex Fourier mode into the FD equation and dividing by $g_m^n \exp(\beta_m n \Delta t)$ yields the amplification factor g_m . The numerical method will be stable and the numerical solution $F_i^{(n)}$ will be bounded with $n \rightarrow \infty$ respectively, if $|g_m| \leq 1$. Stability analysis, using the Von Neumann method, of implicit as well as explicit diffusion scheme can be found in literature or e.g. in Lampa (2006).

Then, if both characteristics (consistency and stability) are fulfilled, the PDE is said to be *convergent* according to the Lax's equivalent-theorem (see Richtmyer and Morton, 1967).

4.1.3. Summarized approximation method

Within the overall numerical scheme, the distribution function F depending on momentum p_k and pitch-cosine μ_i at location $(s_{\parallel,j}, s_{\perp,l})$ at time t_n will be denoted by its numerical value $\xi_{j,l,i,k}^n$.

The time derivative will be discretized by the forward difference

$$\frac{\partial F}{\partial t} \Big|_{t=t_n} = \frac{\xi^{n+1} - \xi^n}{\Delta t} + O(\Delta t), \quad (4.3)$$

which is accurate to first order in constant step size Δt . Additionally, if all terms in a partial differential equation (PDE) can be linearized (as it is done in this study), the resulting difference scheme can be expressed by a matrix form – even if ξ depends on more than one independent variable (see Samarskij, 2001). The operator $\mathbf{A}^{(n+1)}$ with all entries according to time t_{n+1} has to be limited by a finite upper boundary (this always true for linear PDEs) and $\mathbf{A}^{(n)}$ has to be at least *diagonal dominant*. Consequently, the inverse of $\mathbf{A}^{(n)}$ exists and the next time step can be executed by solving the linear equation system. In general, the system matrix $\mathbf{M} = (\mathbf{A}^{(n)})^{-1} \mathbf{A}^{(n+1)}$ will not be “well shaped”. There will exist many entries beyond the main diagonal and they are not expected to uniformly fill the secondary diagonals with non-zero values. There would be many clusters of non-zero values and the system matrix would not be symmetric.

The Gaussian elimination method will be in the order of $O(m^2)$ - with $m = l_s \cdot l_\mu \cdot l_z \cdot l_p$ being the row/ column number of \mathbf{M} . The l variables correspond to the number of grid points within the s_{\parallel} , μ , s_{\perp} , and p domain. Comparing to the computational possibilities at present, this leads to an unacceptable runtime. But apart from that, one would probably fail at taking the hurdle to invert $\mathbf{A}^{(n)}$. The diagonal dominance is a strong stability restriction as we will see later on.

So, again, we adopted the numerical scheme described by Hatzky (1996). Its basis is an enhanced fractional time step and time splitting method (e.g. Marchuk, 1975) – also known under *summarized approximation method* (see Samarskij, 2001) - which allows to treat transport in each independent variable separately, reducing this multi-dimensional problem to a chain of one-dimensional problems. As nomenclature, all properties, that do not change during a specific transport, are not indicated. For instance, in case of pitch-angle transport, all spatial variables and momentum will be left out, and the numerical representant of F reads ξ_i^n . Splitting in two half steps and arranging each separate, pairwise occurring scheme in s_{\parallel} , s_{\perp} , μ and p in a symmetric manner increases overall approximation in time to second order. In simple words: During each time step, spatial s_{\parallel} -transport is advanced by half a step, pitch-angle transport is advanced by half a step, perpendicular transport is advanced by half a step, momentum transport happens in two half steps, perpendicular transport is advanced by the second half a step, pitch-angle transport is advanced by the second half step and finally spatial s_{\parallel} -transport is advanced by the second half step.

The difference operator for the μ -transport e.g. is written $L_\mu(t, s_{\parallel}, s_{\perp}, \mu, p)$ and the other four are accordingly defined. The overall consistency and stability of the overall scheme

$$L(t, s_{\parallel}, s_{\perp}, \mu, p) =$$

$$\begin{aligned} & \frac{1}{2} L_{s_{\parallel}}(t, s_{\parallel}, s_{\perp}, \mu, p) + \frac{1}{2} L_{\mu}(t_n, s_{\parallel}, s_{\perp}, \mu, p) + \frac{1}{2} L_{s_{\perp}}(t, s_{\parallel}, s_{\perp}, \mu, p) + \frac{1}{2} L_p(t, s_{\parallel}, s_{\perp}, \mu, p) \\ & + \frac{1}{2} L_p(t, s_{\parallel}, s_{\perp}, \mu, p) + \frac{1}{2} L_{s_{\perp}}(t, s_{\parallel}, s_{\perp}, \mu, p) + \frac{1}{2} L_{\mu}(t_n, s_{\parallel}, s_{\perp}, \mu, p) + \frac{1}{2} L_{s_{\parallel}}(t, s_{\parallel}, s_{\perp}, \mu, p) \end{aligned}$$

is determined by the sum of stability criteria and consistencies for each separate difference scheme in t , s_{\parallel} , s_{\perp} , μ and p .

To have symmetric a scheme, which is split into two temporal half-steps, allows each transport process to be nearly equally represented in the overall framework. But note that the first executed transport is always more dominant than the others.

Whereas the simplified, azimuthal grid is based on a constant step size Δ_s along the magnetic field line (see Section 3.2.2), we now have to take care of possible restrictions using varying step sizes. The numerical grid is based on the geometry we have defined in Section 3.2.2.

Building an expanded model on a distorted grid forces the developer to pay attention to the correct assignment of array indexes. Unlike the former 2-D model (Lampa and Kallenrode, 2009), one single step in the cross-field direction results in both a change in azimuth and radial distance. In order to make the architecture more clear, the schematic spatial grid in Figure 4.1 might help to get an overview. Note that this grid just describes the topology, and not exact distances between two neighboring points. This depends strongly on the radial distance.

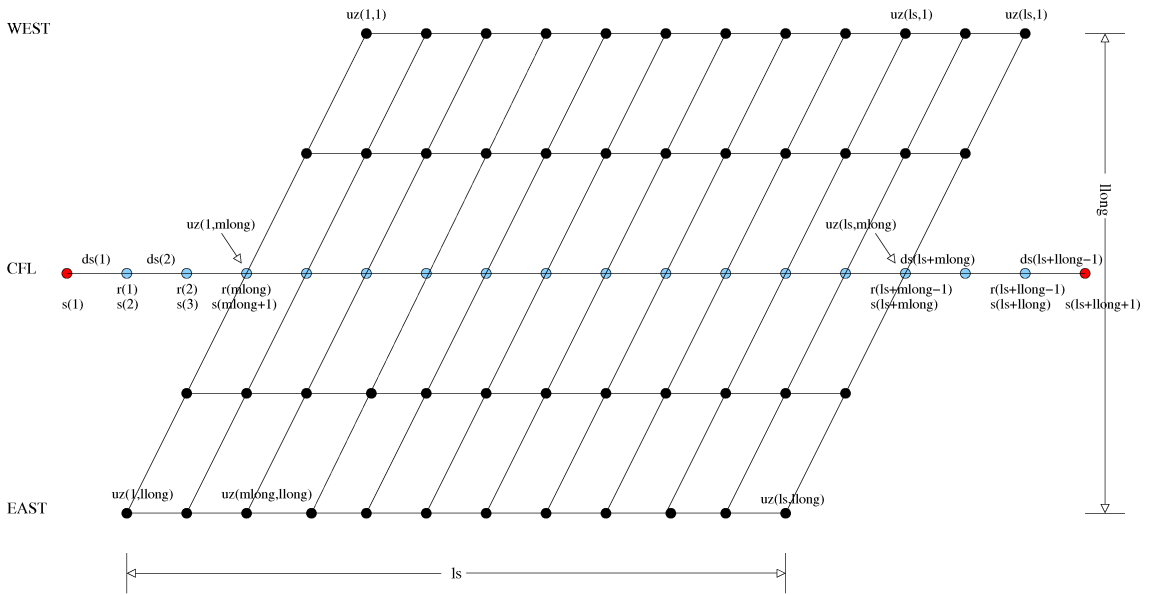


Figure 4.1.: Schematic grid including some variables of the numerical model *nperpgref*. The field lines are aligned horizontally.

The simulated particles are injected on the footpoint of the *central field line* (CFL) via a delta-function, or even more extended symmetrically around the CFL (see Section 4.6). The footpoints are located at $s_{\perp,ml}$ with $ml = \lfloor l_z/2 + 1 \rfloor$. Note that – according to the notation in Figure 4.1 – the CFL does not start at s_1 but at s_{ml} .

Summing up, this subsection provides a short introduction into solving partial differential equations numerically via finite differences – in particular for varying step sizes. The summarized approximation method is applied for this multi-dimensional problem.

4.2. Transport along an IMF line (s-transport)

The second order finite difference scheme, that has been derived by Lax-Wendroff (Anderson et al., 1984), will be maintained in its structure for field-parallel transport. Hatzky already illustrated that this second order accurate FD scheme combined with a monotonized-centered flux-limiter (van Leer, 1977) would be the best choice. According to the

Courant-Friedrichs-Levy (CFL) stability condition

$$\gamma = \max_{j,i} |v_{j,i}| \frac{\Delta t}{\Delta s_{\parallel}} \leq 1 , \quad (4.4)$$

the step sizes are chosen such that the scheme works exactly for the fastest particles. We preferred this scheme over the first-order-upwind scheme as well as over the flux-corrected transport (numerical artefacts/ terraces at strong gradients for $\gamma << 1$). But we have to address the question whether the varying step sizes pose additional problems/restrictions to the numerical code.

As we remember, the *Lax-Wendroff-scheme* was built by making a Taylor expansion around a certain point in time t_n and by replacing the resulting time derivatives by the corresponding space derivatives which are defined by the hyperbolic differential equation itself:

$$\frac{\partial F}{\partial t} + v \frac{\partial F}{\partial s_{\parallel}} = 0 \quad ; \quad v \text{ particle speed .} \quad (4.5)$$

Again, let ξ_j^n be the numerical value of the analytical, PDE solving function F at point $(t_n, s_{\parallel,j})$. The Taylor expansion around t_n yields:

$$\xi(t + \Delta t, s_{\parallel,j}) = F(t, s_{\parallel,j}) + \Delta t \partial_t F(t_n, s_{\parallel,j}) + \frac{1}{2} \Delta t^2 \partial_{tt} F(t_n, s_{\parallel,j}) + O(\Delta t^3) .$$

Replacing the time derivatives using equation (4.5) and ignoring higher order terms we get another formulation of the advection equation

$$\frac{\partial F}{\partial t} = -v \frac{\partial F}{\partial s_{\parallel}} + \frac{\Delta t^2}{2} \frac{\partial^2 F}{\partial s_{\parallel}^2}, \quad (4.6)$$

which has already been solved numerically for equispaced step sizes Δs_{\parallel} . The additional diffusion terms prevents the numerical solution to be smeared out less with time than without the diffusion term (numerical diffusion, see e.g. Roach, 1982). The first derivative in s is chosen to be the centered finite-difference approximation and the second derivative is set to be the conventional second order difference scheme well known in terms of a numerical solution of the one-dimensional heat equation. Hatzky (1996) and others already incorporated the case of spatially varying velocities.

The final result can be found at p. 54:

$$\xi_j^{n+1} = \xi_j^n - (\gamma_{j+1/2} \xi_j^n - \gamma_{j-1/2} \xi_{j-1}^n) - \eta_{j+1/2} (\xi_{j+1}^n - \xi_j^n) + \eta_{j-1/2} (\xi_j^n - \xi_{j-1}^n) , \quad (4.7)$$

with $\gamma_{j+1/2} = v_{j+1/2} \frac{\Delta t}{\Delta s_{\parallel}}$ and $\eta_{j+1/2} = \frac{1}{2} \gamma_{j+1/2} (1 - \gamma_{j+1/2})$.

This scheme is second order accurate and saves monotony (Roe, 1986), or in other words: spatial distributions of ξ do not change local slope sign during the entire simulation. Of course, exceptions from the monotony feature are additional sources such as modeled traveling shocks or SEPs originating from a different flare/ CME that is not magnetically connected to the observer's field line. Resuming the numerics, we can also state that the stability criterion is identical to the one in case of the much simpler Eulerian scheme (Courant-Friedrichs criterion, for short: CFL).

This scheme prevents particles to get lost out of the system by applying the *control volume approach* (Roach, 1982) which insures that all particles leaving a certain cell are completely transported to one or more neighboring cells.

The scheme mentioned above does not work anymore when spatial step sizes become variable. With regard to the calculated IMF grid we are dealing with increasing step sizes as particles are transported from the Sun outwards along the local field line and as particles are swept westward along a perpendicular path respectively.

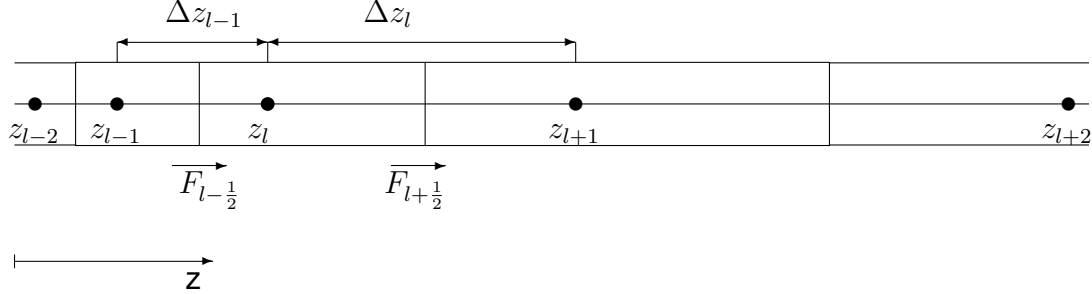


Figure 4.2.: Grid structure in both field-parallel (s_{\parallel}) and field-perpendicular (s_{\perp}) direction.

Based on the grid, as denoted by Figure 4.2, the following scheme can be applied to variable particle speeds and step sizes as well:

$$\xi_j^{n+1} = \xi_j^n - \Delta t \left[\left(v_{j+1/2} \frac{\xi_{j+1}^n + \xi_j^n}{2} - v_{j-1/2} \frac{\xi_j^n + \xi_{j-1}^n}{2} \right) / \left(\frac{\Delta s_{\parallel,j-1} + \Delta s_{\parallel,j}}{2} \right) \right] + \frac{\Delta t^2}{2} \left[\left(v_{j+1/2}^2 \frac{\xi_{j+1}^n - \xi_j^n}{\Delta s_{\parallel,j}} - v_{j-1/2}^2 \frac{\xi_j^n - \xi_{j-1}^n}{\Delta s_{\parallel,j-1}} \right) / \left(\frac{\Delta s_{\parallel,j-1} + \Delta s_{\parallel,j}}{2} \right) \right] \quad (4.8)$$

Again, we made an adoption of the control volume approach. Unknown values at the cell boundaries (here: particle velocity) were calculated by arithmetic means.

The first term in square brackets (4.8) numerically describes the advective in- and outputs F at cell $s_{\parallel,j}$.

$$v_{\parallel}(s_{\parallel}) \frac{\partial f}{\partial s_{\parallel}} \Big|_{s_{\parallel}=s_{\parallel,j}} \approx \frac{F_{j+1/2} - F_{j-1/2}}{\frac{\Delta s_{\parallel,j-1} + \Delta s_{\parallel,j}}{2}} \quad \text{with} \quad F_{j+1/2} = v_{\parallel,j+1/2} \frac{\xi_{j+1}^n + \xi_j^n}{2}. \quad (4.9)$$

Remember that this centered finite difference approximation is not accurate to second order but to first order only. Its consistency can be proven by putting the exact, Taylor-expanded solution $F(s_{\parallel})$ into the FD in place of the approximated solution:

$$\frac{v_{\parallel,j+1/2} \frac{\xi_{j+1}^n + \xi_j^n}{2} - v_{\parallel,j-1/2} \frac{\xi_j^n + \xi_{j-1}^n}{2}}{\frac{\Delta s_{\parallel,j-1} + \Delta s_{\parallel,j}}{2}} = \frac{F(s_{\parallel,j})}{\Delta s_{\parallel,j-1} + \Delta s_{\parallel,j}} (v_{\parallel,j+1/2} - v_{\parallel,j-1/2}) \quad (4.10)$$

$$+ \frac{v_{\parallel,j-1/2} \Delta s_{\parallel,j-1} + v_{\parallel,j+1/2} \Delta s_{\parallel,j}}{\Delta s_{\parallel,j-1} + \Delta s_{\parallel,j}} \frac{\partial F}{\partial s_{\parallel}} \quad (4.11)$$

$$+ \frac{1}{2} \frac{v_{\parallel,j-1/2} \Delta s_{\parallel,j-1}^2 + v_{\parallel,j+1/2} \Delta s_{\parallel,j}^2}{\Delta s_{\parallel,j-1} + \Delta s_{\parallel,j}} \frac{\partial^2 F}{\partial s_{\parallel}^2} \quad (4.12)$$

$$+ O(\Delta s_{\parallel,j-1}^3 + \Delta s_{\parallel,j}^3).$$

It should be noted that particle velocities $v_{\parallel}(s_{\parallel})$ and $\Delta s_{\parallel}(s_{\parallel})$ have to be continuously differentiable functions in s_{\parallel} . $v_{\parallel,j-1/2}$ and $v_{\parallel,j+1/2}$ become identical when the cell boundaries converge asymptotically.

The limiting values can be determined by also making a Taylor expansion for the velocities around $s_{\parallel,j}$, neglecting terms higher than first order:

$$v_{\parallel,j+1/2} = v_{\parallel,j} + \frac{\Delta s_{\parallel,j}}{2} \left. \frac{\partial v_{\parallel}(s_{\parallel})}{\partial s_{\parallel}} \right|_{s_{\parallel}=s_{\parallel,j}} \quad \text{and} \quad v_{\parallel,j-1/2} = v_{\parallel,j} - \frac{\Delta s_{\parallel,j-1}}{2} \left. \frac{\partial v_{\parallel}(s_{\parallel})}{\partial s_{\parallel}} \right|_{s_{\parallel}=s_{\parallel,j}} .$$

The first term on the right-hand site of (4.10) becomes:

$$\frac{F(s_{\parallel,j})}{\Delta s_{\parallel,j-1} + \Delta s_{\parallel,j}} (v_{\parallel,j+1/2} - v_{\parallel,j-1/2}) = \frac{1}{2} F(s_{\parallel}) \left. \frac{\partial v_{\parallel}(s_{\parallel})}{\partial s_{\parallel}} \right|_{s_{\parallel}=s_{\parallel,j}} \quad (4.13)$$

Analogous to this term, the following two terms (4.11) and (4.12) are further approximated to:

$$\frac{v_{\parallel,j-1/2} \Delta s_{\parallel,j-1} + v_{\parallel,j+1/2} \Delta s_{\parallel,j}}{\Delta s_{\parallel,j-1} + \Delta s_{\parallel,j}} \left. \frac{\partial F(s_{\parallel})}{\partial s_{\parallel}} \right|_{s_{\parallel}=s_{\parallel,j}} = v_{\parallel}(s_{\parallel}) \left. \frac{\partial F(s_{\parallel})}{\partial s_{\parallel}} \right|_{s_{\parallel}=s_{\parallel,j}} \quad (4.14)$$

$$+ \frac{\Delta s_{\parallel,j-1}^2 + \Delta s_{\parallel,j}^2}{\Delta s_{\parallel,j-1} + \Delta s_{\parallel,j}} \left. \frac{\partial v_{\parallel}(s_{\parallel})}{\partial s_{\parallel}} \frac{\partial F(s_{\parallel})}{\partial s_{\parallel}} \right|_{s_{\parallel}=s_{\parallel,j}} \quad (4.15)$$

and

$$\frac{1}{2} \frac{v_{\parallel,j-1/2} \Delta s_{\parallel,j-1}^2 + v_{\parallel,j+1/2} \Delta s_{\parallel,j}^2}{\Delta s_{\parallel,j-1} + \Delta s_{\parallel,j}} \left. \frac{\partial^2 F(s_{\parallel})}{\partial s_{\parallel}^2} \right|_{s_{\parallel}=s_{\parallel,j}} = \frac{1}{2} \frac{\Delta s_{\parallel,j-1}^2 + \Delta s_{\parallel,j}^2}{\Delta s_{\parallel,j-1} + \Delta s_{\parallel,j}} v_{\parallel}(s_{\parallel}) \left. \frac{\partial^2 F(s_{\parallel})}{\partial s_{\parallel}^2} \right|_{s_{\parallel}=s_{\parallel,j}} \quad (4.16)$$

$$+ \frac{1}{4} \frac{\Delta s_{\parallel,j-1}^3 - \Delta s_{\parallel,j}^3}{\Delta s_{\parallel,j-1} + \Delta s_{\parallel,j}} \left. \frac{\partial v_{\parallel}(s_{\parallel})}{\partial s_{\parallel}} \frac{\partial^2 F(s_{\parallel})}{\partial s_{\parallel}^2} \right|_{s_{\parallel}=s_{\parallel,j}} \quad (4.17)$$

To achieve a consistent FD approximation, spatial changes of the particles' velocity have to be small compared to the local step size $\Delta s_{\parallel}(s_{\parallel})$. According to (2.38) the step size Δs_{\parallel} is related to the corresponding radial change via

$$dr = \sqrt{1 + \left(\frac{\sin \theta \omega_{\odot} r}{v_{sw}} \right)^2} ds_{\parallel}(r) = \frac{1}{\cos(\Psi(r))} ds_{\parallel}(r) .$$

We therefore get:

$$\begin{aligned} \frac{d}{ds_{\parallel}}(v_{\parallel}(s_{\parallel})) &= \frac{d}{ds_{\parallel}} \left(v'_{\parallel} + v_{sw} \cos(\Psi(s_{\parallel}(r))) \right) \\ \Leftrightarrow \cos(\Psi(r)) \frac{d}{dr} (v_{\parallel}(s_{\parallel}(r))) &= \cos(\Psi(r)) \frac{d}{dr} \left(v'_{\parallel} + v_{sw} \cos(\Psi(r)) \right) . \end{aligned}$$

For $v_{sw} = 400 \text{ km s}^{-1}$ and a solar angular frequency of $\omega_{\odot} = 0.0103 \text{ h}^{-1}$ within the plane of ecliptic, the particles's speed in the rest frame of the Sun changes by

$$\left| \frac{dv_{\parallel}(s_{\parallel}(r))}{ds_{\parallel}(r)} \right| = \left| -\cos(\Psi(r))^4 (\omega_{\odot} r)^2 \frac{1}{v_{sw}} \right| << 0.0024 . \quad (4.18)$$

The upper boundary corresponds the maximum rate of change at about $r = 1$ AU, where the spiral angle yields 45° . The value is below the size of the step sizes, thus there are more inaccuracies due to the grid resolution than due to differential solar wind convection. The average value within $r = 10$ AU is 6.19825E-04, which is at least one order of magnitude better than the average rate of change in the solar wind frame including corotation. Consequently, the terms (4.13), (4.15) and (4.17) can be neglected. The remaining terms give rise to the truncation error of the first term in (4.8)

$$\begin{aligned}\epsilon_j &= \frac{v_{\parallel,j+1/2} \frac{\xi_{j+1}^n + \xi_j^n}{2} - v_{\parallel,j-1/2} \frac{\xi_j^n + \xi_{j-1}^n}{2}}{\frac{\Delta s_{\parallel,j-1} + \Delta s_{\parallel,j}}{2}} - \left. \frac{\partial}{\partial s_{\parallel}} (v_{\parallel}(s_{\parallel}) F(s_{\parallel})) \right|_{s_{\parallel}=s_{\parallel,j}} \\ &+ \frac{1}{2} \frac{\Delta s_{\parallel,j-1}^2 + \Delta s_{\parallel,j}^2}{\Delta s_{\parallel,j-1} + \Delta s_{\parallel,j}} v_{\parallel}(s_{\parallel}) \left. \frac{\partial^2 F(s_{\parallel})}{\partial s_{\parallel}^2} \right|_{s_{\parallel}=s_{\parallel,j}} + O(\Delta s_{\parallel,j-1}^2 + \Delta s_{\parallel,j}^2),\end{aligned}$$

indicating that the finite difference is accurate to first order.

The same procedure is applied to the FD term representing the second derivative in (4.8). Formally, it is identical to the FD scheme which approximately solves the diffusive transport in perpendicular direction. Thus, the approximation of the second derivative will be analyzed in Section 4.5. We limit ourselves to the resulting FD equation, whose second finite difference also has a first-order accuracy. As a consequence, the truncation error of the complete FD (4.8) is given by the summation of the errors of both finite differences.

Arranging the FD scheme as in Hatzky and adding the flux limiter, we get:

$$\xi_j^{n+1} = \xi_j^n - (\gamma_{j+1/2} \xi_j^n - \gamma_{j-1/2} \xi_{j-1}^n) - \eta_{j+1/2} (\xi_{j+1}^n - \xi_j^n) \Phi(\theta_{j+1/2}) + \eta_{j-1/2} (\xi_j^n - \xi_{j-1}^n) \Phi(\theta_{j-1/2}), \quad (4.19)$$

(4.20)

with $\gamma_{j+1/2} = v_{\parallel,j+1/2} \frac{2\Delta t}{\Delta s_{\parallel,j-1} + \Delta s_{\parallel,j}}$, $\eta_{j+1/2} = \frac{1}{2} \gamma_{j+1/2} (1 - \frac{v_{\parallel,j+1/2} \Delta t}{\Delta s_{\parallel,j}})$, and the flux-limiter:

$$\Phi(\theta_j) = \max \left(0, \min \left(2\theta_j, \frac{1+\theta_j}{2}, 2 \right) \right) \quad \text{with } \theta_j = \frac{\xi_j - \xi_{j-1}}{\xi_{j+1} - \xi_j}.$$

Φ became necessary because solutions of the Lax-Wendroff method show some oscillations in the regions of strong gradients (van Leer, 1977). As in (4.7), $\gamma_{j+1/2}$ corresponds to the CFL number. Thus, the stability criterion for field-parallel transport is:

$$\frac{2\Delta t v_{j+1/2}}{(\Delta s_{\parallel,j-1} + \Delta s_{\parallel,j})} \leq 1.$$

In the distorted grid, the CFL number reaches its maximum at the inner boundary where step sizes are very small and particle speeds have their highest values in the field-parallel direction before being pitch-angle scattered and decelerated by the solar wind effects. The time step is set to

$$\Delta t = \frac{\Delta s_{\parallel,1} + \Delta s_{\parallel,2}}{2 \max_{p_k} v_1(p_k)}. \quad (4.21)$$

The numerical scheme works exact within the footpoint cell of the most eastern field line (see Figure 3.2) for the fastest particles, whereas the exactness is subsequently weakened towards the western direction.

4.3. Transport in pitch-cosine

This linear, parabolic convection-diffusion equation

$$\frac{\partial \xi}{\partial t} + \frac{\partial}{\partial \mu} (b(\mu) \xi) - \frac{\partial}{\partial \mu} \left(\kappa_\mu(\mu) \frac{\partial \xi}{\partial \mu} \right) = 0, \quad (4.22)$$

with

$$b(\mu) = \frac{1 - \mu^2}{2L(s)} \quad \text{and} \quad \kappa_\mu(\mu) = \frac{3}{4} \frac{1}{\lambda_{\parallel}(s)} \overline{\kappa_\mu}(\mu),$$

has been solved according to the following discretization:

The focusing term has been approximated by the central difference

$$\left. \frac{\partial}{\partial \mu} (b(\mu) \xi(\mu)) \right|_{\mu=\mu_i} \approx \frac{F_{i+1/2} - F_{i-1/2}}{\Delta \mu} \quad \text{with } F_{i+1/2} = b_{i+1/2} \frac{\xi_{i+1} + \xi_i}{2},$$

and the pitch-angle scattering term by the classical second order difference quotient:

$$\left. \frac{\partial}{\partial \mu} \left(\kappa_\mu(\mu) \frac{\partial \xi(\mu)}{\partial \mu} \right) \right|_{\mu=\mu_i} \approx \frac{w_{i+1/2} - w_{i-1/2}}{\Delta \mu} \quad ; \text{ with } w_{i+1/2} = a_{i+1/2} \frac{\xi_{i+1} - \xi_i}{\Delta \mu}.$$

Note that these discrete terms remain unchanged compared to the original code since we are still working on an equally spaced grid in μ . The focusing length $L(s)$ and κ_μ , which both have spatial dependencies, have to be computed with regard to the new grid. The truncation error still gives $\epsilon_i^{(n)} = O((\Delta \mu)^2)$ for the entire μ -transport.

We adopted the implicit, second order scheme since the stability criterion for an explicit scheme

$$\Delta t \leq \frac{1}{2} \frac{(\Delta \mu)^2}{\kappa_\mu(r, \mu)} \quad (4.23)$$

would be rather strict (Roach, 1982). Thus, the upper-mentioned difference quotients have been defined according to the next time step t_{n+1} . If the values of the PADC are explicitly discrete and have discontinuities (e.g. $\kappa_\mu(\mu)$ at $\mu = 0$ for $q = 1$ and $\sigma \neq 0$) – that is to say, they do not solve a continuous function $f : \mathbb{N} \rightarrow \mathbb{R}$ with $f(\mu_i) = \kappa_\mu(\mu_i)$, $\kappa_\mu(\mu_{i \pm 1/2}) = a_{i \pm 1/2}$ will be determined by the *Integro-interpolation*-method (Tichonov and Samarskij, 1961) or by linear interpolation.

Putting together all difference equations for all i , we get a system of linear equations whose system matrix reveals a tri-diagonal shape. The diagonal dominance has to be fulfilled for stability. This leads to an essential condition for the focusing length (Hatzky, 1996, p. 62):

$$L \geq \Delta \tau \left(1 + \frac{\Delta \mu}{2} \right). \quad (4.24)$$

Another restriction emerges from the fact that both μ -terms in the transport equation compete against each other: Close to the Sun, focusing dominates, whereas beyond a few tens of an AU pitch-angle scattering strongly affects the particle distributions. It has been calculated that

$$\max_i \left| \frac{b_{i+1/2}}{a_{i+1/2}} \right| \Delta \mu < 2 \quad , \rho_{i+1/2} = \frac{b_{i+1/2}}{a_{i+1/2}},$$

has to be fulfilled to be stable throughout the entire simulation.

Additionally, the consistency error $\epsilon_i^{(n)}$ might grow to infinity if $\kappa_\mu(\mu) \rightarrow 0$. In literature, this has been paraphrased as *singular perturbed problem* (Grossmann and Roos, 1994, p. 341).

The parameter

$$\bar{\chi}(\rho_{i+1/2}) = \rho_{i+1/2} \coth \rho_{i+1/2} \quad \text{with } \rho_{i+1/2} = \frac{b\Delta\mu}{2a_{i+1/2}} \quad (4.25)$$

has been introduced to fulfill the stability criterion (4.23) and also the problem of vanishing diffusion.

The modified scheme (for a specific $i \in \{0, 1, \dots, I\}$) is:

$$L_{\Delta\mu}\xi_i = \frac{b_{i+1/2}(\xi_{i+1} + \xi_i) - b_{i-1/2}(\xi_i + \xi_{i-1})}{\Delta\mu} - \frac{1}{(\Delta\mu)^2} [\tilde{\chi}_{i+1/2}a_{i+1/2}(\xi_{i+1} - \xi_i) - \tilde{\chi}_{i-1/2}a_{i-1/2}(\xi_i - \xi_{i-1})] . \quad (4.26)$$

This is a variant of the so called *IIjin-scheme* (Roos, 1994), which converges with second order, if diffusion is sufficient. Otherwise one order gets lost according to the maximum norm.

4.4. Adiabatic deceleration (momentum-transport)

Similar to the convection term in Section 4.2, adiabatic deceleration is described by a hyperbolic PDE:

$$\frac{\partial F}{\partial t} - \frac{1}{\tau_D} \frac{\partial}{\partial p'} (p' F) = 0 , \quad (4.27)$$

$$\text{with } \frac{1}{\tau_D} = v_{sw} \left[\frac{\cos(\Psi)}{2L(s_\parallel, s_\perp)} (1 - \mu'^2) + \cos(\Psi) \frac{\partial}{\partial r} (\cos(\Psi)) \mu'^2 \right] . \quad (4.28)$$

It can be solved numerically in equidistant momentum step sizes by performing the logarithmic transformation

$$\bar{F} = p' F \quad \text{and} \quad \bar{p}' = \ln \left(\frac{p'}{p'_0} \right) ,$$

which leads to a simpler equation:

$$\frac{\partial \bar{F}}{\partial t} - \frac{1}{\tau_D} \frac{\partial \bar{F}}{\partial \bar{p}'} . \quad (4.29)$$

The characteristics are linear curves in a semilogarithmic graph:

$$\bar{p}' + \frac{t}{\tau_D} = C_1 \quad ; C_1 \in \mathbb{R}_+ . \quad (4.30)$$

The step sizes $\Delta\bar{p}'$ in the moving frame increase in the half logarithmic scale due to the exponential grid:

$$p'_k = p'_0 \cdot \exp((k-1) \cdot \Delta\bar{p}') \quad k = 0, 1, \dots, l_p ,$$

with p'_0 as the lower boundary. The corresponding, relativistically calculated particle velocities are

$$v'_k = \frac{1}{\sqrt{\left(\frac{m_0}{p'_k}\right)^2 + \frac{1}{c^2}}} , \quad (4.31)$$

with rest mass m_0 and speed of light c . \bar{F} can re-transformed by applying the natural exponential function to the characteristics equation (4.30). The result

$$p' \exp\left(\frac{t}{\tau_D}\right) = C_2 , \quad C_2 \in \mathbb{R}_+ ,$$

can be put into (4.29), which finally leads to

$$F(t, p') = \exp\left(\frac{t}{\tau_D}\right) F_0\left(p' \exp\left(\frac{t}{\tau_D}\right)\right) ,$$

or

$$F(t, \bar{p}') = \exp\left(\frac{t}{\tau_D}\right) F_0\left(\bar{p}' + \frac{t}{\tau_D}\right) ,$$

once momentum has been transformed logarithmically. Solutions for the subsequent time $t + \Delta t$ can now be computed from the states at time t :

$$F(t + \Delta t, \bar{p}') = \exp\left(\frac{\Delta t}{\tau_D}\right) F\left(t, \bar{p}' + \frac{\Delta t}{\tau_d}\right) .$$

As initial condition, a power law spectrum in momentum

$$F_0(p') = B \left(\frac{p'}{p'_0}\right)^{-\delta'}$$

is assumed, which – in semilogarithmic scale – relates to

$$F_0(\bar{p}') = B \exp(-\delta' \bar{p}') .$$

Thus again, we can apply the upwind scheme combined with the flux limiter method. It should be favored instead of the flux-corrected transport, since the Courant-Friedrichs-Levy number (CFL)

$$\gamma(s_{\parallel}, s_{\perp}, \mu) = \frac{\Delta t}{|\tau_D(s_{\parallel}, s_{\perp}, \mu')| \Delta \bar{p}'} \ll 1$$

is far below 1 because of the large τ_D values. So, overall stability can easily be fulfilled without such strict constraints to minimum step size $\Delta \bar{p}'$ as in case of the s transport. We adopt all the numerical details that have been discussed at the beginning of Section 4.2. Note that this scheme is also accurate to second order with

$$\epsilon_k = L_{\Delta p'} \xi_k - \frac{1}{\tau_D} \frac{\partial}{\partial p'} (p' F(p')) \Big|_{p'=p'_k} = O(\Delta p'^2) .$$

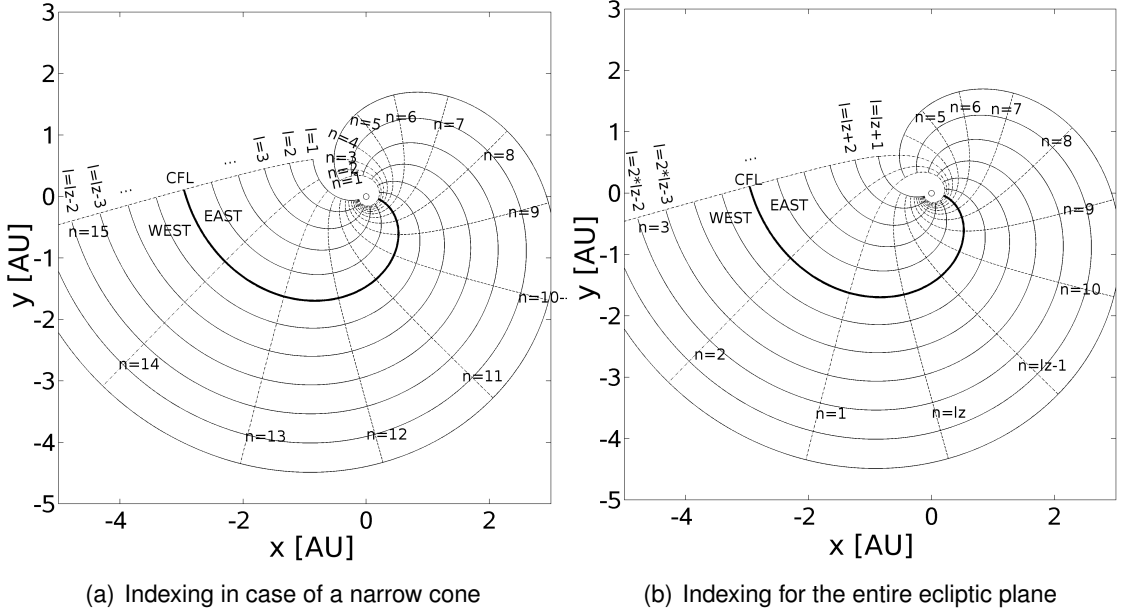


Figure 4.3.: Numerical grid of the ecliptic plane. Some array indices are inserted: n denotes the perpendicular curve, l represents a field line number.

4.5. Transport perpendicular to the IMF

We connected the grid points with the following grid indices: Figure 4.3 illustrates possible spatial grid constructions. In the left panel, the most western and the most eastern field line correspond to “right” and “left” reflecting boundary. It should be emphasized that a perpendicular displacement does not only involve a change in azimuth φ but also a change in the radial distance r . The indices l, j indicate an arbitrarily chosen point (or better: cell) in the ecliptic plane, and all of its neighbors are denoted by the index pair plus and/or minus 1. In the numerical code, all entities have been initialized according to Figure 4.1, for example $\xi_{j,l} = uz(j, l)$.

Formally, the FD scheme as presented here is based on the same PDE as the one for the s_{\parallel} -transport:

$$\frac{\partial F(s_{\perp})}{\partial t} + \frac{\partial}{\partial s_{\perp}} (v_{sw,\perp}(s_{\perp})F(s_{\perp})) - \frac{\partial}{\partial s_{\perp}} \left(\kappa_{\perp}(s_{\perp}) \frac{\partial F(s_{\perp})}{\partial s_{\perp}} \right) = 0, \quad (4.32)$$

with

$$v_{sw,\perp}(\Psi) = v_{sw} \sin(\Psi) \iff v_{sw,\perp}(r) = \frac{v_{sw}}{\sqrt{1 + (\omega_{\odot} \sin(\Theta) r v_{sw}^{-1})^2}}.$$

The perpendicular component of the solar wind $v_{sw,\perp}$ has its maximum close to the Sun where the solar-wind direction (radial) and magnetic field direction are approximately the same. Further out, the corotation has shaped the IMF such that the radially outward flowing solar wind is directed oblique to the field lines.

This part of the partial differential equation is a linear, parabolic convection-diffusion equation. But in contrast to Section 4.2 the diffusion in the dominant part of these two transport processes. Since κ_{\perp} is expected to be highly variable, the decision has been made to solve this equation implicitly.

4.5.1. Consistency

As nomenclature we adopted the labels defined in Section 4.2 but replaced s_{\parallel} by s_{\perp} in order to indicate that transport occurs in field-perpendicular direction.

The coordinate system for perpendicular transport (in s_{\parallel} and s_{\perp}) is set to be positive in western direction. This is also the direction of the field-perpendicular component of the solar wind flow. Thus, we set $v_{sw,\perp} \geq 0$, and also each corresponding numerical transport coefficient. Again, we used the control volume approach in order to determine the cell-crossing in- and outward fluxes.

Note that implicit solutions allow particles (at least a vanishing part of them) to propagate faster than it would be physically reasonable. We accepted this since we were able to construct a scheme which is stable for all step sizes and all propagation properties.

The first derivative in (4.32) has been approximated by the centered difference scheme in analogy to (4.9):

$$\frac{\partial}{\partial s_{\perp}} (v_{sw,\perp}(s_{\perp}) F(s_{\perp})) \Big|_{s=s_{\perp,j}} \approx L_{\Delta s_{\perp,j}}^c = \frac{F_{j+1/2} - F_{j-1/2}}{\frac{\Delta s_{\perp,j-1} + \Delta s_{\perp,j}}{2}} + O(\Delta s_{\perp,j}), \quad (4.33)$$

with the convection flux $F_{j+1/2} = v_{sw,\perp,j+1/2} \frac{\xi_{j+1} + \xi_j}{2}$.

The truncation error $\epsilon_j^{(n)}$, which is the derivative of the FD (4.33) from a possible analytical exact solution, indicates an accuracy to first order, namely $O(\Delta s_{\perp,j})$. We already derived the truncation error in Section 4.2:

$$\epsilon_c^{(j)} = L_{\Delta s_{\perp}^c} \xi_j - v_{sw,\perp}(s_{\perp}) \frac{\partial}{\partial s_{\perp}} F(s_{\perp}) \Big|_{s_{\perp}=s_{\perp,j}} = O(\Delta s_{\perp,j}). \quad (4.34)$$

We have a loss of precision of one order of magnitude in Δs_{\perp} – not just owing to the distorted grid but also owing to the varying solar wind velocity. Making all values constant would lead to the classical centered, second-order FD approximation (Chattot, 2002, p. 6).

The second term in (4.32) is approximated as follows:

$$\frac{\partial}{\partial s_{\perp}} \left(\kappa_{\perp}(s_{\perp}) \frac{\partial}{\partial s_{\perp}} F(s_{\perp}) \right) \Big|_{s_{\perp}=s_{\perp,j}} = \frac{F_{j+1/2} - F_{j-1/2}}{\frac{\Delta s_{\perp,j-1} + \Delta s_{\perp,j}}{2}} + O(\Delta s_{\perp,j}), \quad (4.35)$$

with the perpendicular diffusive flux across the cell boundary at $s_{\perp,j+1/2}$:

$$F_{j+1/2} = \kappa_{\perp}(s_{\perp}) \frac{\partial F(s_{\perp})}{\partial s_{\perp}} \Big|_{s_{\perp}=s_{\perp,j+1/2}} \approx \kappa_{\perp,j+1/2} \frac{\xi_{j+1} - \xi_j}{\Delta s_{\perp,j}}$$

It is indicated in (4.35) that we loose one order of magnitude in accuracy compared to the FD with constant step size. The truncation error can be derived by inserting the Taylor-expanded, analytical solution in place of ξ . But we have to be aware that both $\kappa_{\perp}(s_{\perp}(r))$ and $\Delta s_{\perp}(s_{\perp}(r))$ are continuously differentiable functions with respect to r . The arc length in field-perpendicular direction is given by the integration of the position vector \mathbf{r}_{\perp} (3.27) over the radius:

$$\Delta s_{\perp} = \int \sqrt{1 + \left(\frac{d\varphi(r)}{r} \right)^2} dr = \int \sqrt{1 + \frac{1}{(r\vartheta)^2}} dr ; \vartheta = \frac{\sin \theta \omega_{\odot}}{v_{sw}}.$$

The result $\Delta s_{\perp}(r)$ increases continuously with increasing radial distance:

$$s_{\perp}(r) = r \sqrt{1 + \left(\frac{v_{sw}}{\sin \theta \omega_{\odot} r} \right)^2} - \frac{v_{sw} \operatorname{arcsinh} \left(\frac{v_{sw}}{\sin(\theta) \omega_{\odot} r} \right)}{\sin(\theta) \omega_{\odot}}. \quad (4.36)$$

Since both Δs_{\perp} and κ_{\perp} (see Section 5.3) obviously are continuous functions in r , they can be approximated by a Taylor expansion around $s_{\perp,j}$. The Taylor expansions in westward and eastward direction are:

$$\kappa_{\perp,j+1/2} = \kappa_{\perp}(s_{\perp})|_{s_{\perp}=s_{\perp,j}} + \frac{\Delta s_{\perp,j}}{2} \frac{\partial \kappa_{\perp}(s_{\perp})}{\partial s_{\perp}} \Big|_{s_{\perp}=s_{\perp,j}}, \quad (4.37)$$

$$\kappa_{\perp,j-1/2} = \kappa_{\perp}(s_{\perp})|_{s_{\perp}=s_{\perp,j}} - \frac{\Delta s_{\perp,j-1}}{2} \frac{\partial \kappa_{\perp}(s_{\perp})}{\partial s_{\perp}} \Big|_{s_{\perp}=s_{\perp,j}} \quad \text{and} \quad (4.38)$$

$$\begin{aligned} F(s_{\perp,j+1}) &= F(s_{\perp,j}) + \Delta s_{\perp,j} F' + \frac{(\Delta s_{\perp,j+1})^2}{2} F'' + \frac{(\Delta s_{\perp,j+1})^3}{6} F''' \\ &\quad + \frac{(\Delta s_{\perp,j+1})^4}{24} F^{(iv)} + O((\Delta s_{\perp,j})^5), \end{aligned}$$

$$\begin{aligned} F(s_{\perp,j-1}) &= F(s_{\perp,j}) - \Delta s_{\perp,j-1} F' + \frac{(\Delta s_{\perp,j-1})^2}{2} F'' - \frac{(\Delta s_{\perp,j-1})^3}{6} F''' \\ &\quad + \frac{(\Delta s_{\perp,j-1})^4}{24} F^{(iv)} + O((\Delta s_{\perp,j-1})^5). \end{aligned}$$

If we insert all these terms into (4.35), we get:

$$L_{\Delta s_{\perp}}^d(s_{\perp,j}) = \frac{\partial \kappa_{\perp}(s_{\perp})}{\partial s_{\perp}} \frac{\partial F(s_{\perp})}{\partial s_{\perp}} \Big|_{s_{\perp}=s_{\perp,j}} \quad (4.39)$$

$$+ \kappa_{\perp}(s_{\perp}) \frac{\partial^2 F(s_{\perp})}{\partial s_{\perp}^2} \Big|_{s_{\perp}=s_{\perp,j}} \quad (4.40)$$

$$+ \frac{1}{2} \frac{\partial \kappa_{\perp}(s_{\perp})}{\partial s_{\perp}} \frac{\partial^2 F(s_{\perp})}{\partial s_{\perp}^2} \Big|_{s_{\perp}=s_{\perp,j}} \left(\frac{\Delta s_{\perp,j}^2 - \Delta s_{\perp,j-1}^2}{\Delta s_{\perp,j-1} + \Delta s_{\perp,j}} \right) \quad (4.41)$$

$$+ \frac{1}{6} \frac{\partial \kappa_{\perp}(s_{\perp})}{\partial s_{\perp}} \frac{\partial^3 F(s_{\perp})}{\partial s_{\perp}^3} \Big|_{s_{\perp}=s_{\perp,j}} \left(\frac{\Delta s_{\perp,j}^3 + \Delta s_{\perp,j-1}^3}{\Delta s_{\perp,j-1} + \Delta s_{\perp,j}} \right) \quad (4.42)$$

$$+ \frac{\kappa_{\perp}(s_{\perp})}{6} \frac{\partial^4 F(s_{\perp})}{\partial s_{\perp}^4} \Big|_{s_{\perp}=s_{\perp,j}} \left(\frac{\Delta s_{\perp,j}^3 + \Delta s_{\perp,j-1}^3}{\Delta s_{\perp,j-1} + \Delta s_{\perp,j}} \right) \quad (4.43)$$

$$+ \frac{1}{12} \frac{\partial \kappa_{\perp}(s_{\perp})}{\partial s_{\perp}} \frac{\partial^4 F(s_{\perp})}{\partial s_{\perp}^4} \Big|_{s_{\perp}=s_{\perp,j}} \left(\frac{\Delta s_{\perp,j}^3 - \Delta s_{\perp,j-1}^3}{\Delta s_{\perp,j-1} + \Delta s_{\perp,j}} \right) \quad (4.44)$$

$$+ O(\Delta s_{\perp,j-1}^2 + \Delta s_{\perp,j}^2)$$

Since step sizes in west- and eastward direction are different, some of the terms do not completely vanish, whereas they cancel out in case of constant step sizes Δs_{\perp} . Considering the limiting values

$$\lim_{\substack{\Delta s_{\perp,j-1} \rightarrow 0 \\ \Delta s_{\perp,j} \rightarrow 0}} L_{\Delta s_{\perp}}(s_{\perp,j}),$$

the two neighboring step sizes become asymptotically equal, and thus their difference tends to zero. Therefore, the terms (4.41) and (4.44) can be neglected.

Term (4.39) contains the spatial derivative of the diffusion coefficient, which itself is assumed to be at least linearly interpolated. κ_{\perp} is not allowed to grow faster along the perpendicular path than the corresponding step sizes. In absolute values, the factor $0.5\partial_{s_{\perp}}\kappa_{\perp}(s_{\perp})$ has to be in the same order of magnitude as $s_{\perp}(s)$ – otherwise κ_{\perp} would additionally contribute to the truncation error.

The derivative is given by:

$$\frac{\partial\kappa_{\perp}(s_{\perp}(r))}{\partial r} \frac{dr}{ds_{\perp}} = \left(1 + \left(\frac{v_{sw}}{\omega_{\odot}\sin(\theta)}\right)^2\right)^{-1/2} \frac{\partial\kappa_{\perp}(s_{\perp}(r))}{\partial r}.$$

To find out how the term evolves along s_{\perp} , we have solve the (4.36) numerically for fixed s_{\perp} . For relativistic electrons with $\kappa_{\perp}(r) \propto r^4$ (see also Section 5.3) and $v_{sw} = 400 \text{ km s}^{-1}$ within the plane of ecliptic, the gradient of the diffusion coefficient lies in the same order of magnitude as the step size, if we are confined to radial distances of at most 2 AU. Thus, with the estimates as made above, the FD approximates the differential term (4.40). The remaining terms (4.42) and (4.43) show squared step size dependencies. Consequently, the truncation error of the diffusive part is:

$$\epsilon_j^d = L_{\Delta s_{\perp}(r_j)}^d - \kappa_{\perp}(r_j)F''(r_j) + O(\Delta s_{\perp,j}^2) \quad (4.45)$$

is accurate to second order, but it may loose one order in case of strong gradients of the perpendicular diffusion coefficient.

The FD of the diffusive part (4.35) is also a result of the *Galerkin finite element method (FEM)* (Johnson, 1987; Peiro and Sherwin, 2005), which uses the integral formulation of the PDE as the starting point of the discretization process, denoted by

$$\frac{\partial}{\partial t} \int \left(F(t, s_{\perp})w(s_{\perp}) - \frac{\partial}{\partial s_{\perp}} \left[\kappa_{\perp}(s_{\perp}) \frac{\partial}{\partial s_{\perp}} F(t, s_{\perp}) \right] w(s_{\perp}) \right) ds_{\perp} = 0. \quad (4.46)$$

The additional weight functions $w(s_{\perp})$ define the type of the scheme. In general, the FEM are better suited than the FD methods to deal with complex geometries in multi-dimensional problems as the integral formulations do not rely in any special mesh structure. Moreover, it provides a more natural way of discontinuous source terms due to their reduced requirements on the regularly or smoothness of the solution.

As in the FD approximation, the region of interest will be discretized into $L - 1$ sub domains $\Omega_k = \{s_{\perp} : s_{\perp,k-1} \leq s_{\perp} \leq s_{\perp,k}\}$. The approximation solution is assumed to be represented by

$$\xi(t_n, s_{\perp}) = \sum_{k=1}^L \xi(t_n)N_k(s_{\perp}),$$

where the set of functions $N_k(s_{\perp})$ is known as the expansion basis. For the *Galerkin* FEM method these are equivalent to the weight functions in (4.46). We will impose that the weight functions $w(s_{\perp})$ are zero at the boundaries at each sub-domain. By integrating the diffusion term by parts, (4.46) becomes

$$\int_{s_{\perp,1}}^{s_{\perp,L}} \frac{dN_k}{ds_{\perp}}(s_{\perp}) \sum_{j=1}^L \xi_j \frac{dN_j}{ds_{\perp}}(s_{\perp}) ds_{\perp} = \int_{s_{\perp,1}}^{s_{\perp,L}} N_k(s_{\perp}) \partial_t F(t, s_{\perp}) \text{ for } k = 1, \dots, L-1. \quad (4.47)$$

This represents a linear system of $L - 1$ equations with $L - 1$ unknowns: $\{\xi_2, \dots, \xi_L\}$. The basis functions are set to have a compact support, meaning that their value and their derivatives are different from zero only on the elements containing the node k , for example,

$$N_k(s_\perp) = \begin{cases} \frac{s_\perp - s_{\perp,k-1}}{\Delta s_{\perp,k-1/2}} s_{\perp,k-1} < s_\perp < s_{\perp,k} \\ \frac{s_{\perp,k+1} - s_\perp}{\Delta s_{\perp,k+1/2}} s_{\perp,k} < s_\perp < s_{\perp,k+1} \end{cases}.$$

This means that the only integrals different from zero in (4.47) are

$$\begin{aligned} \int_{s_{\perp,k-1}}^{s_{\perp,k}} \frac{dN_k}{ds_\perp} \left(\xi_{k-1} \frac{dN_{k-1}}{ds_\perp} + \xi_k \frac{dN_k}{ds_\perp} \right) ds_\perp + \int_{s_{\perp,k}}^{s_{\perp,k+1}} \frac{dN_k}{ds_\perp} \left(\xi_k \frac{dN_k}{ds_\perp} + \xi_{k+1} \frac{dN_{k+1}}{ds_\perp} \right) ds_\perp \\ = \int_{s_{\perp,k-1}}^{s_{\perp,k}} N_k \partial_t F(t, s_\perp) ds_\perp + \int_{s_{\perp,k}}^{s_{\perp,k+1}} N_k \partial_t F(t, s_\perp) ds_\perp \end{aligned}$$

The right-hand side can be evaluated using a simple integration rule like the trapezoidal rule:

$$\left(\frac{\Delta s_{\perp,k-1}}{2} + \frac{\Delta s_{\perp,k}}{2} \right) \partial_t F(t, s_\perp).$$

Inserting the basis functions and its derivatives and putting $\partial_t F(t, s_\perp)$ on one side alone, we finally get the FD term for the diffusive part, which is identical to the one derived on the basis of Taylor series approximation.

The FD scheme in s_\perp is incorporated within the summarized approximation method, where the time derivative is represented by the first-order forward difference scheme. Thus, the overall truncation error is a sum of all single truncation errors (4.34) and (4.45):

$$\frac{\xi_j^{n+1} - \xi_j^n}{\Delta t} = L_{\Delta s_\perp}^c + L_{\Delta s_\perp}^d + O(\Delta t, \Delta s_{\perp,j}). \quad (4.48)$$

4.5.2. Stability

As part of the summarized approximation and time-splitting method (the time derivative has been replaced by the first-order, one sided FD), we decided to solve the scheme implicitly. This has already done for the pure diffusive transport (Laasonen scheme). Laasonen (1949) illustrated that the scheme works stable for all choices of step sizes and all magnitudes of κ_\perp . Even in case of very small convective flux (compared to the diffusive one), the scheme can be applied without any stability problems.

In contrast to the pure diffusive transport, the additional advective term can lead to oscillations. This is in contraction to the analytical solution where all transport parameters/coefficients are set to be constant. This might lead to physically unreasonable negative phase-space density. If the FDs are chosen as described above, this three-point approximation leads to linear equation system as follows:

$$\mathbf{A}\mathbf{y}^{n+1} = \mathbf{y}^n \quad (4.49)$$

with

$$\mathbf{y}^n = (\xi_{m,1}^n, \xi_{m,2}^n, \xi_{m,3}^n, \dots, \xi_{m,l_z-1}^n, \xi_{m,l_z}^n)^T \quad \forall m \in [1, l_s] \quad (\text{for each perp. curve}) .$$

The entry $\xi_{m,2}$ corresponds to the numerical value of the distribution function F at location (r_{l_z-l+m}, φ_l) at time $t = t_n$. The coefficient matrix is in tri-diagonal shape – the main and the two neighboring diagonals are filled with non-zero values.

An inner row of the coefficient matrix \mathbf{A} can be written as:

$$\begin{aligned} a_{j+1} &= \frac{\Delta t v_{sw\perp,j+1/2}}{\Delta s_{\perp,j-1} + \Delta s_{\perp,j}} - \frac{2\Delta t \kappa_{\perp,j+1/2}}{\Delta s_{\perp,j}(\Delta s_{\perp,j-1} + \Delta s_{\perp,j})} \\ a_j &= 1 + \frac{\Delta t(v_{sw\perp,j+1/2} - v_{sw\perp,j-1/2})}{\Delta s_{\perp,j-1} + \Delta s_{\perp,j}} + \frac{2\Delta t}{\Delta s_{\perp,j-1} + \Delta s_{\perp,j}} \left(\frac{\kappa_{\perp,j+1/2}}{\Delta s_{\perp,j}} + \frac{\kappa_{\perp,j-1/2}}{\Delta s_{\perp,j-1}} \right) \\ a_{j-1} &= -\frac{\Delta t v_{sw\perp,j-1/2}}{\Delta s_{\perp,j-1} + \Delta s_{\perp,j}} - \frac{2\Delta t \kappa_{\perp,j-1/2}}{\Delta s_{\perp,j}(\Delta s_{\perp,j-1} + \Delta s_{\perp,j})} \end{aligned}$$

Important for stability is that the system matrix \mathbf{A} is a *non-singular M-matrix* (see also Grossmann and Roos, 1994). It should be noted that this postulate corresponds to the one for stability under the maximum norm (maximum principle, see Richtmyer and Morton (1967) or Samarskij (2001) on p. 258–264). Numerical schemes of parabolic or hyperbolic PDEs, that are stable under the maximum norm, are even stable with respect to the *Von-Neumann* stability analysis, thus we limit ourselves to investigate the *M-matrix* properties.

This implies that matrix $\mathbf{A} = (a_{i,j})$ is either weakly column or weakly row-diagonal-dominant:

$$|a_{i,i}| \geq \sum_{j \neq i} |a_{i,j}| \quad ; i, j \in [0, 1, \dots, N] \quad ; \text{row-dominance in row } i .$$

The strict inequality must hold for at least one i .

Moreover, \mathbf{A} has to be *non-singular*:

$$\det \mathbf{A} \neq 0, \quad \mathbf{A}^- = (a_{ij}^-) \geq 0 \quad \text{and} \quad a_{ij} \leq 0 \quad \forall i \neq j$$

and an irreducible *L-matrix*:

$$a_{ii} > 0 \quad i \in \mathbb{N} \quad \forall \quad a_{ij} < 0 \quad \forall i \neq j$$

These conditions assure that \mathbf{A} can be inverted in order to get the F -values for the next time step.

Checking the diagonal dominance with regard to the matrix coefficients a_{j-1} , a_j and a_{j+1} , we can directly see that it is always fulfilled with $|a_{i,i}| - \sum_{j \neq i} |a_{i,j}| = 1 \quad i, j \in [0, 1, \dots, N]$.

Being an irreducible *L-matrix* requires that a_{l-1} and a_{l+1} have to be negative. But in the first row, we can not keep the condition when convection becomes more pronounced than

diffusion. If the simulations parameters are chosen that way, we are forced to introduce a limiting factor, which adds additional *artificial (numerical) diffusion*:

$$X_{j+1/2} = \rho_{j+1/2} \coth(\rho_{j+1/2}) \quad \text{with } \rho_{j+1/2} = \frac{v_{sw\perp,j+1/2} \Delta s_{\perp,j-1} + \Delta s_{\perp,j}}{4\kappa_{\perp,j+1/2}} \quad (4.50)$$

$$a_{j+1} = \frac{\Delta t v_{sw\perp,j+1/2}}{\Delta s_{\perp,j-1} + \Delta s_{\perp,j}} - \frac{2\Delta t \kappa_{\perp,j+1/2}}{\Delta s_{\perp,j}(\Delta s_{\perp,j-1} + \Delta s_{\perp,j})} X_{j+1/2}$$

$$a_j = 1 + \frac{\Delta t(v_{sw\perp,j+1/2} - v_{sw\perp,j-1/2})}{\Delta s_{\perp,j-1} + \Delta s_{\perp,j}} + \frac{2\Delta t}{\Delta s_{\perp,j-1} + \Delta s_{\perp,j}} \left(\frac{\kappa_{\perp,j+1/2} X_{j+1/2}}{\Delta s_{\perp,j+1/2}} + \frac{\kappa_{\perp,j-1/2} X_{j-1/2}}{\Delta s_{\perp,j-1/2}} \right)$$

$$a_{j-1} = -\frac{\Delta t v_{sw\perp,j-1/2}}{\Delta s_{\perp,j-1} + \Delta s_{\perp,j}} - \frac{2\Delta t \kappa_{\perp,j-1/2}}{\Delta s_{\perp,j}(\Delta s_{\perp,j-1} + \Delta s_{\perp,j})} X_{j-1/2}$$

In case of vanishing solar-wind convection, we have pure diffusive, stable transport, and X tends to 1. In case of increasing convection X increases and adds some additional diffusive flux.

4.6. Initial and boundary conditions

At the beginning of the simulation, and with inclusion of solar wind effects, all numerical values of the distribution function have been set to $\epsilon = 1E - 10$. The p' transport coefficients are very small compared to those of the other numerical values. Operations between these and vanishing particle numbers could lead to underflow errors. Consequently, we have chosen ϵ to be much larger than smallest absolute value of floating point numbers – which is about 10^{-23} for single precision (32-bit). Since all particle species are distributed uniformly by ϵ and since the overall mass of injected particles is many orders of magnitude higher than ϵ , this additional particle population can be related to the omnipresent background plasma in interplanetary space.

The source function Q in (3.9) is realized as time-varying inner boundary in the s -transport (Section 4.2). As first approximation, the injection is located at the footpoint of the central field line (CFL). The CFL itself is positioned in the middle of the grid at $\varphi = 0^\circ$ to avoid boundary effects. Alternatively, an extended source along the perpendicular curve can be applied as well ($n=1$, see blue-colored line in Figure 4.4). The source is incorporated in terms of field-parallel transport (s_{\parallel} -transport):

$$\xi_{1,l}^{n+1} = \xi_{1,l}^n - \frac{\Delta t(v\mu + v_{sw,\parallel,1/2})}{\Delta s_{\parallel,1,l}} \xi_{1,l}^n + \frac{\Delta t(v\mu + v_{sw,\parallel,3/2})}{\Delta s_{\parallel,1,l}} q(t_n, s_{\perp,l}) \quad (4.51)$$

$q(t_n, s_{\perp,l})$ has been scaled with respect to time and space. Thus, the total number of injected particles is kept constant and the temporal evolution is conserved even if the grid resolution and the time step size change.

Although we can not assure mass conservation for each energy bin, because of the momentum transport, we would like to prevent particles to get lost by other transport

processes. In order to have a *conservative* scheme for perpendicular transport, we introduced reflection for the diffusive part. The refraction coefficient ν (see also Lampa, 2006) is set to zero.

According to the *Neumann* boundary condition, we have set the diffusive fluxes to zero at $s_{\perp,1}$ and s_{\perp,l_z} :

$$\kappa_{\perp}(s_{\parallel}, s_{\perp}) \frac{\partial F(s_{\parallel}, s_{\perp})}{\partial s_{\perp}} \Big|_{s_{\parallel}=s_j, s_{\perp}=s_{\perp,1}} \approx \kappa_{\perp,j,1} \frac{\xi_{j,1} - \xi_{j,2}}{\Delta s_{\perp,j,1}} = 0 \quad , \forall j \in [1, l_s] ,$$

and

$$\kappa_{\perp}(s_{\parallel}, s_{\perp}) \frac{\partial F(s_{\parallel}, s_{\perp})}{\partial s_{\perp}} \Big|_{s_{\parallel}=s_j, s_{\perp}=s_{\perp,l_z}} \approx \kappa_{\perp,j,l_z} \frac{\xi_{j,l_z-1} - \xi_{j,l_z}}{\Delta s_{\perp,j,l_z}} = 0 \quad , \forall j \in [1, l_s] .$$

Since $\xi_1, \xi_2, \xi_{l_z-1}$ and ξ_{l_z} are not to supposed to be zero during simulation time, we have to demand that the coefficients

$$\frac{\kappa_{\perp,j,1}}{\Delta s_{\perp,j,1}} = 0 \quad \text{and} \quad \frac{\kappa_{\perp,j,l_z}}{\Delta s_{\perp,j,l_z}} = 0$$

vanish. Introducing reflection for SEPs would not be adequate because the particles are swept westward: Particles, that have been reflected at the most western boundary, would immediately be transported to the cell they originally came from. From the most eastern site, particles would not expected to be produced out of nothing. Thus the flux at that location will be zero. Numerical reflection would be redundant since there are no particles that could make a reversal in direction. In sum, we have set the convective fluxes to zero.

$$F_{j,1}^c = v_{sw,\perp,j,1} \frac{\xi_1 - \xi_2}{2} = 0 \quad \text{and} \quad F_{j,l_z}^c = v_{sw,\perp,j,l_z} \frac{\xi_{j,l_z-1} - \xi_{j,l_z}}{2} = 0$$

$$\Leftrightarrow v_{sw,\perp,j,l_z} = v_{sw,\perp,j,1}$$

The upper row in the system matrix for perpendicular transport yields (without II' in correction):

$$a_{j,1} = 1 - \frac{\Delta t v_{sw,\perp,j-1/2}}{\Delta s_{\perp,j-1} + \Delta s_{\perp,j}} + \frac{2\Delta t}{\Delta s_{\perp,j-1} + \Delta s_{\perp,j}} \left(\frac{\kappa_{\perp,j-1/2}}{\Delta s_{\perp,j-1}} \right) ,$$

$$a_{j,2} = -\frac{\Delta t v_{sw,\perp,j-1/2}}{\Delta s_{\perp,j-1} + \Delta s_{\perp,j}} - \frac{2\Delta t \kappa_{\perp,j-1/2}}{\Delta s_{\perp,j-1} (\Delta s_{\perp,j-1} + \Delta s_{\perp,j})} ,$$

and the lower row yields:

$$a_{j,l_z-1} = -\frac{\Delta t v_{sw,\perp,j-1/2}}{\Delta s_{\perp,j-1} + \Delta s_{\perp,j}} - \left(\frac{2\Delta t \kappa_{\perp,j-1/2}}{\Delta s_{\perp,j} \Delta s_{\perp,j-1}} \right) ,$$

$$a_{j,l_z} = 1 - \frac{\Delta t v_{sw,\perp,l_z+1/2}}{\Delta s_{\perp,j-1} + \Delta s_{\perp,j}} + \frac{2\Delta t}{\Delta s_{\perp,j-1} + \Delta s_{\perp,j}} \left(\frac{\kappa_{\perp,j-1/2}}{\Delta s_{\perp,j-1}} \right) .$$

Comparing to Section 4.5.2, the stability criterion holds even at the boundaries. It should be noted that the western boundary acts as an boundary reservoir whereas the most eastern areas get void. The particle accumulation can be overcome either by just simulating till the first particles reach the western boundary. Consequently, the model covering

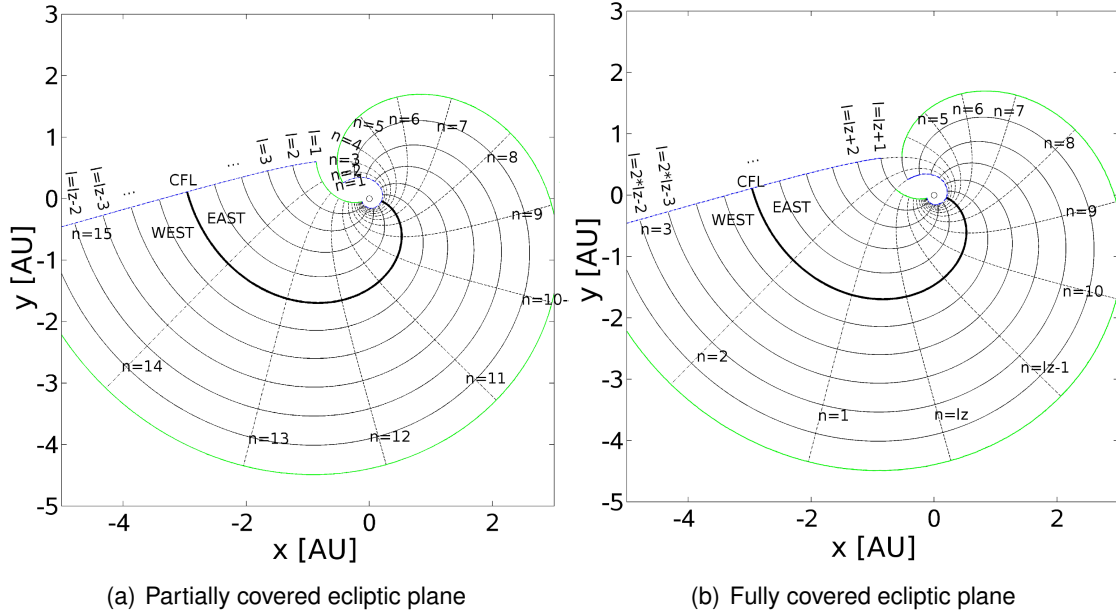


Figure 4.4.: Numerical grid of the ecliptic plane, including colored curvatures: Green lines indicate the boundary conditions for perpendicular transport, blue lines the initial and boundary conditions for field-parallel transport.

partially the ecliptic plane (see left panel in Figure 4.4) would be adequate. If the CFL is long enough – in the sense that it rolls up more than 360° – the original perpendicular curves can be elongated (e.g. curve number 1 combines with former number 13 in the left panel of Figure 4.4). The boundary segment, which is the closed to the Sun, shortens, if the footpoint of the CFL is shifted to smaller radial distances. Nevertheless, this segment is not expected to affect the simulation results significantly since most particles are swept out due to focusing before a recognizable spread in azimuth occurs, as it is evident in e.g. Figure 6.3.

5. Simulation Assumptions

First of all, all fits are based on a larger number of assumptions: (a) The large scale structure of the background medium is uniform (constant solar wind, no deviation from the Archimedean spiral); neither shocks and magnetic clouds nor corotating interaction regions influence the focusing length. (b) Scattering conditions are also assumed to be constant (conventionally, the radial particle mean free path λ_r is assumed to be constant in space and time). (c) In general, differences in scattering conditions between different flux tubes, as indicated e.g. in the sudden flux-drop outs or the propagation channels (see discussion in Chapter 7.2.3), are not considered. Such differences probably would be encountered by the observer due to the satellite's relative motion to the background medium, although at least from turbulence measurements it is not clear whether the medium is more structured as a checker board or in terms of streams (Stevens and Kasper, 2007; Zhang, Russell, Baumjohann, Jian, Balikhin, Cao, Wang, Blanco-Cano, Glassmeier, Zambelli, Volwerk, Delva and Vörös, 2009).

Some exceptions from the constancy of λ_r in azimuth were made to explain the observations during the crossing of sector boundaries and regions of different propagation properties (see Section 7.2.2).

5.1. SEP injections and boundary conditions

The injection function Q in (3.9) depends on location, time, pitch-cosine and momentum. The source term is made separable by

$$Q(s_{\perp,0}, t, \mu', p') = q_1(s_{\perp,0}) \cdot q_2(t) \cdot q_3(\mu') \cdot q_4(p') . \quad (5.1)$$

Numerically, Q has been realized as a time-varying inner boundary, which is equivalent to the footpoints of the modeled field lines (see Section 4.6). Concerning its spatial dependencies, it is not necessarily a point-like source term, but might be extended either described by the Gaussian distribution or a rectangular function (also expressed in terms of two Heaviside step functions). For program user information Section A.3 will give some insight.

The source particles are set to be isotropically distributed in the positive pitch-cosine. Other pitch-angle distribution do not considerably exhibit different results, since the strong focusing produces high, Sun outward-directed anisotropies.

The time evolution is either point-like as a Dirac delta function (also called δ -function) or a Reid-Axford profile (Reid, 1964):

$$q_2(t) \propto \frac{1}{t} \exp \left(-\frac{t_c}{t} - \frac{t}{t_L} \right) \quad (5.2)$$

with t_c being the coronal diffusion time and t_L the loss time. It should be noted that this is just a convenient and conventional parametrization. Both parameters in principle describe diffusive propagation from a point source through the corona combined with a loss of particles, but there is no evidence for such a process to occur in the corona.

Based on observational data, we adopted from Ruffolo (1994) the momentum spectrum that is expected to follow a power law according to

$$F(p') = F_0 \left(\frac{p'}{p'_0} \right)^{-\delta'}, \quad (5.3)$$

with $\delta' = 5$.

5.2. Assumptions regarding field-parallel transport

Various observations of SEP transport have shown, that particle propagation ranges from almost scatter-free (with free mean paths of the order of 1 AU) to strongly diffusive (with λ about 0.01 AU); for most events $\lambda_{||}$ is between 0.08 and 0.3 AU - termed as the *Palmer consensus range* (Bieber et al., 1994; Palmer, 1982). Although any scattering parameter derived from observations is model-dependent (Zhang et al., 2007), values of λ_r lying within the domain [0.01 AU, 1.0 AU] have been found to be plausible.

In this study, the spatial dependence of $\lambda_{||}$ is assumed such that the radial mean free path λ_r is constant. Support stems from earlier observations giving power law indices β for the radial dependence $\lambda_r \sim r^\beta$ ranging from 0 to 0.6 (Beeck et al., 1987; Hamilton, 1977; Zwickl and Webber, 1977). Without considering an explicit radial dependence, Wibberenz et al. (1992) and Müller-Mellin et al. (1993) argued from fits (using different one-dimensional propagation models) on particle events observed outside 3 AU for very similar local values of λ compared to observations inside 1 AU. These results suggest at most a slight increase of λ_r with radius. We will therefore adopt the earlier, successful approach of λ_r to be constant. As a consequence, the parallel mean free path $\lambda_{||}$ increases with increasing radial distance as

$$\lambda_{||}(r) = \lambda_r \sec^2 \psi. \quad (5.4)$$

The pitch-angle diffusion coefficient (PADC), defined in Section 2.4.2 as

$$\kappa_\mu(\mu) = A \left((1 - sign(\mu)\sigma) |\mu|^{q-1} + H \right) (1 - \mu^2), \quad (5.5)$$

is directly related to the free mean path by (2.55).

According to the quasi-linear theory (QLT) and the slab model of magnetic field fluctuations, the PADC is restricted to forms of $\kappa_\mu(\mu) \propto |\mu|^{q-1} (1 - \mu^2)$. Both left- and right-handed circularly polarized waves are assumed to be present equally, forming linearly polarized fluctuations ($\sigma = 0$). H is set zero, thus the filling of a possible gap around $\mu = 0$ is neglected.

In Figure 5.1, some shapes of the PADC are shown. A comparison between these theoretical predictions and the observed solar particle data, performed by Beeck and Wibberenz (1986), showed that the pitch-angle diffusion coefficient "has a minimum near 90° pitch angle" which is even more pronounced than in earlier studies by Bieber et al. (1980) where they predicted $q = 1.2$ and $H = 0$.

We chose $q = 1.6$ and $H = 0$ to realize damped scattering for low μ -values and compared the resulting numerical solution of (3.1) with the one using isotropic pitch-angle scattering

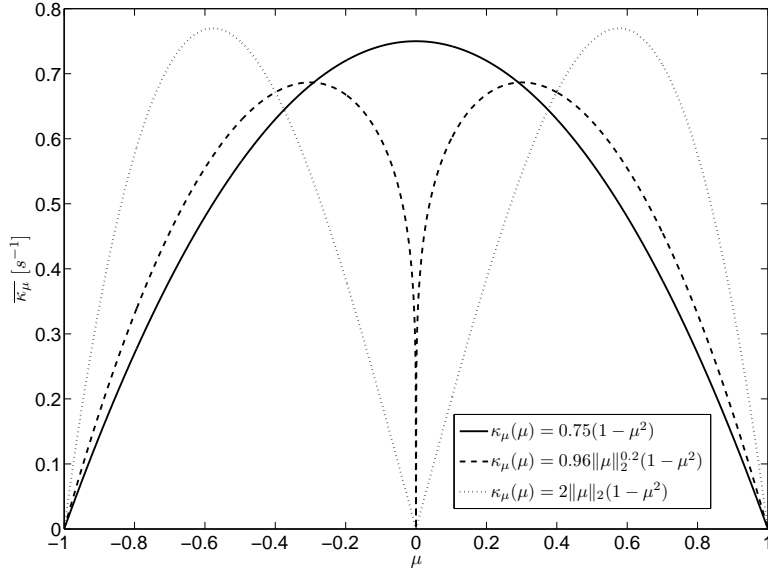


Figure 5.1.: Pitch-angle diffusion coefficients, normalized by (5.6)

($q = 1, H = 0$). The size of q as well as parameter H in (5.5) define how pronounced the minimum near $\mu \approx 0$ is. The PADC is normalized to 1 – termed $\bar{\kappa}_{\mu}(\mu)$ – using the formula

$$\bar{\kappa}_{\mu}(\mu) = \frac{1}{2}\kappa_{\mu}(\mu) \int_{-1}^{+1} \frac{(1 - \mu^2)^2}{\kappa_{\mu}(\mu)} d\mu \quad , \quad (\text{Schlüter, 1985}). \quad (5.6)$$

In contrast to Hatzky, we do not think that the factor 0.5 in (5.6) should be arbitrarily since it is the only normalization factor in order to set $\bar{\kappa}_{\mu}$ to 1 on an interval of $\mu = [-1, +1]$ – or in other words: Scaling in this way is necessary in order to make λ_{\parallel} and $\kappa_{\perp}(r)$ independent of the PADC's shape.

5.3. Strength and variability of the perpendicular diffusion coefficient κ_{\perp}

As already done by Lampa (2006) and in more advanced studies by Lampa and Kallenrode (2009), we introduced a second spatial coordinate s_{\perp} to accommodate perpendicular transport in the plane of the ecliptic. The diffusion coefficient $\kappa_{\perp}(s_{\parallel}, s_{\perp}, \mu)$ might vary in space and pitch-cosine μ , and is defined exclusively on the basis of spatial gradients (classical diffusion).

Although the mechanisms of perpendicular transport are still not well understood, Bieber et al. (2004b) suggested that the scattering conditions in field-parallel direction determine uniquely the perpendicular transport. But how to connect diffusive, small-angle scattering (Jokipii, 1966) with macro-scale spatial diffusion? According to the Fokker-Plank equation, each particle-wave interaction results in small angle changes that do not necessarily result in a reversal of the particles' speed v_{\parallel} . Classical spatial diffusion is based on the

Brownian motion, where a single particle-particle collision changes the particle's propagation direction considerably. The link between these macro-scale quantities – which is immanent in the mean free path λ_{\parallel} – and small-scale turbulence in μ has already been done in (2.55).

κ_{\perp} is suggested to depend on radial distance only, thus we limit ourselves to the radial coordinate r instead of $(s_{\parallel}, s_{\perp})$. Note that different $(s_{\parallel}, s_{\perp})$ could describe the same r . Since perpendicular diffusion occurs in one dimension alone, the parallel diffusion coefficient κ_{\parallel} and λ_{\parallel} are related as:

$$\kappa_{\parallel}(r) = \frac{1}{2}v\lambda_{\parallel}(r) . \quad (5.7)$$

To make $\kappa_{\perp}(r, \mu)$ dependent on $\kappa_{\parallel}(r)$, the factor γ has been introduced:

$$\kappa_{\perp}(r, \mu) = \gamma \kappa_{\parallel}(r) . \quad (5.8)$$

As suggested by Palmer (1982), we assume $\lambda_{\perp}/\lambda_{\parallel}$ to be constant with $\lambda_{\perp}/\lambda_{\parallel} \approx 1/10$ as the upper boundary at $r = 1$ AU. As an conservative estimate of the influence of perpendicular transport, values of $\lambda_{\perp}/\lambda_{\parallel}$ close to unity as suggested by Dwyer et al. (1997) and Zhang et al. (2003) are not considered. Since the numerical integration of particle trajectories in realistic 3D interplanetary magnetic field turbulence gives $\lambda_{\perp}/\lambda_{\parallel} \approx 0.02 - 0.04$ for the cross-field transport (Giacalone and Jokipii, 1999) – comparable to the ratio derived from the analysis of 2D turbulence Matthaeus et al. (2003) – we chose $\lambda_{\perp}/\lambda_{\parallel} \approx 1/50$ as the lower boundary. The ratios are fixed at 1 AU and, according to the Friedmann-Lemaître-Robertson-Walker metric scaled as r^2 .

Another confirmation for the squared radius dependence of κ_{\perp} comes from Zhang, Qin and Rassoul (2009), who stated that perpendicular diffusion is “inversely proportional to local magnetic field strength”. This is physically reasonable since perpendicular scattering is assumed to be very strong in isotropic distributions – which is the case at larger distances from the Sun.

Moreover, the theory of the graphical random walk of field lines suggests that perpendicular displacements are supposed to be of the order of magnitude of the gyro-radius $r_L = mv_{\perp}/(|q|B_0(r))$. Since $B_0(r) \propto r^{-2}$ for $r < 1$, this would lead to the r^2 dependency, too. Unfortunately, FLRW is based on field line displacements instead of spatial shifts of the particle's gyro-centers relatively to field line which is magnetically connected to the injection site. The field line meandering, as suggested by the FLRW, could not explain the fast azimuthal propagation and wide spread of SEPs in studies of Kallenrode (1993a).

In contrast to this work, Jokipii showed that the ratio between the perpendicular and the parallel diffusion coefficient derived from the Fokker-Planck equation is proportional to the inverse square to the mean magnetic field, yielding an even higher power in radial distance: $\kappa_{\perp} : \kappa_{\parallel} \propto r^4 \sec^2 \Psi$.

Nevertheless, several studies, based on observations and/or theory, supported the squared radius dependency of the λ_{\perp} -to- λ_{\parallel} -ratio.

Consequently, the perpendicular diffusion coefficient yields:

$$\kappa_{\perp}(r) = \gamma \frac{3 v^2 r^2}{16} \int_{-1}^{+1} \frac{(1 - \mu^2)^2}{\kappa_{\mu}(r, \mu)} d\mu , \text{ with } \gamma \in [0.02, 0.1] . \quad (5.9)$$

So far, we did not discuss the pitch-angle dependence of perpendicular transport. In case of pitch-angle independent transport of high energetic particles, as it has been realized in early studies in the ecliptic plane, the model resembles the Parker's Equation (Parker,

1965). Note that both models are similar but not equal since the Parker equation is based on spatial diffusion. Moreover, we also consider focusing in diverging magnetic fields from Roelof which significantly affects energetic particles very close to the Sun.

The μ -independence has two consequences: *i*) the particle's pitch angle is conserved during cross-field transport and *ii*) the likelihood of cross-field transport does not depend on pitch-angle.

Numerical simulations by Zhang, Qin and Rassoul (2009) have shown that even a μ -dependent κ_{\perp} would produce similar results: Perpendicular diffusion due to micro-scale turbulence becomes noticeable when particles have undergone "enough" pitch-angle scattering. This is the case when particles have already left the very inner heliosphere. In these regions (depending on λ_r), distributions are nearly isotropic and diffusion acts similarly on particles with different pitch-angles.

Although Zhang, Qin and Rassoul assumed that perpendicular scattering is very strong in isotropic distributions, we introduced some simple μ dependencies and made a comparison with isotropic scenarios (Section 5.3.1).

Numerically, $\kappa_{\mu}(s_{\parallel}, s_{\perp}, \mu)$ is incorporated via a splitting of the pitch-angle diffusion coefficient into a spatial-dependent and a pitch-cosine-dependent part:

$$\kappa_{\mu}(s_{\parallel}, s_{\perp}, \mu) = \kappa_{\mu}(s_{\parallel}, s_{\perp}) \cdot \bar{\kappa}_{\mu}(\mu), \quad (5.10)$$

with $\kappa_{\mu}(s_{\parallel}, s_{\perp}) = \kappa_r \cos^2(\Psi(s_{\parallel}, s_{\perp}))$ and the normalized pitch-angle diffusion coefficient $\bar{\kappa}_{\mu}(\mu)$ as defined in the previous Section 5.2.

5.3.1. Does cross-field transport depend on rigidity?

In Section 5.3, some assumptions about the variability and dependencies of κ_{\perp} were made on the basis of several studies. The still missing part is the validation of the dependencies in terms of the current model.

Whereas the total amount of perpendicular transport is determined as an average of the PADC over all pitch-angles $\mu = [-1, +1]$ (5.9), we thought about an explicit μ -dependence of κ_{\perp} as it has already been introduced in field-parallel direction.

For first estimates, we choose κ_{\perp} to be the following μ -dependent functions:

$$\bar{\kappa}_{\perp}(\mu) = 3\mu^2 \quad \text{and} \quad \bar{\kappa}_{\perp}(\mu) = \frac{3}{2}(1 - \mu^2)$$

Both κ_{\perp} s have been scaled in such that

$$\bar{\kappa}_{\perp}(\mu) = \kappa_{\perp}(\mu) / \left(\int_{-1}^{+1} \kappa_{\mu}(\mu) d\mu \right),$$

thus the total amount of diffusive flux is equal – whatever the shape of $\kappa_{\perp}(\mu)$ looks like.

The overall diffusion coefficient in perpendicular direction yields $\kappa_{\perp}(r, \mu) = \kappa_{\perp}(r)\bar{\kappa}_{\perp}(\mu)$ (separation approach). The total strength is incorporated implicitly in the radial term, as it is seen in (5.9).

At least the $(1 - \mu^2)$ -dependency has a plausible physical meaning. If κ_{\perp} is defined as in (5.9), combined with the assumption of λ_r to be constant, κ_{\perp} yields:

$$\kappa_{\perp}(r, \mu) = \kappa_{\perp}(r) \bar{\kappa}_{\perp}(\mu) \propto \frac{v^2(1 - \mu^2)r^2}{(\cos(\Psi))^2}. \quad (5.11)$$

$\kappa_{\perp}(r, \mu)$ can be interpreted in terms of *rigidity* P (2.6) as

$$\kappa_{\perp}(r, \mu) \propto \frac{P^2}{(\cos(\Psi))^2}, \quad (5.12)$$

where the spiral term solely originates from the assumption of a constant radial mean free path λ_r .

Several theories – among them the quasi-linear-theory (QLT) – suggested the parallel mean free path λ_{\parallel} to grow with increasing rigidity P (see Section 2.1.1). Instead of a continuous loss of particles from the observer's site in field-parallel direction, these losses could also be explained by enhanced cross-field transport, as it has been introduced here by (5.12).

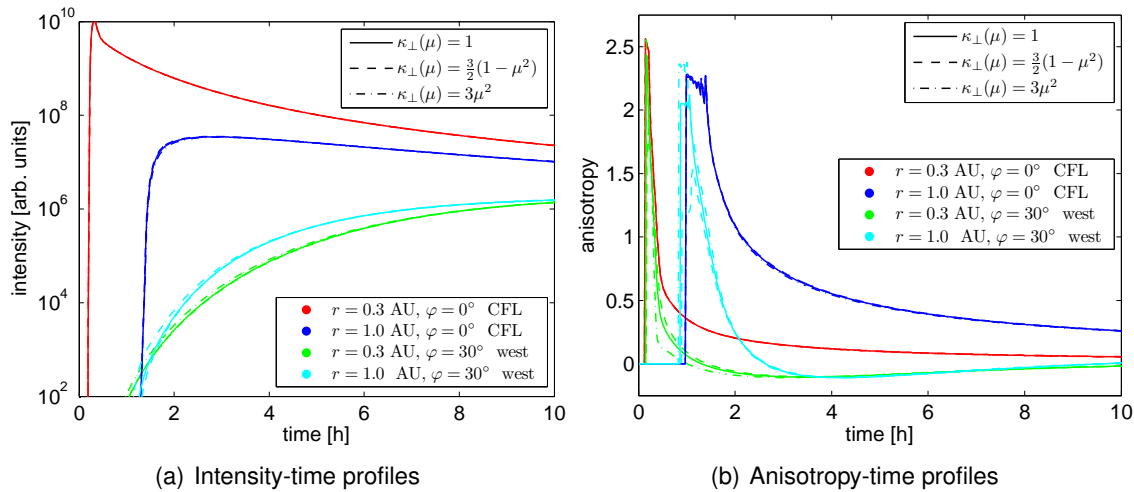


Figure 5.2.: Intensity-time profiles at different locations. The standard scenario was chosen, but $\kappa_{\perp} : \kappa_{\parallel}$ is set to 1/50. Three possible shapes for the μ -dependent part of the perpendicular diffusion coefficient were assumed: $\kappa_{\perp}(\mu) = 1$ (isotropic scattering, solid lines), $\kappa_{\perp}(\mu) = \frac{3}{2}(1 - \mu^2)$ (dashed lines) and $\kappa_{\perp}(\mu) = 3\mu^2$ (dot-dashed lines).

Some of the results can be seen in Figure 5.2. For illustration, 10 MeV protons with speed $v_p = 1 \text{ AU h}^{-1}$ were chosen because they are expected to be more sensitive to interplanetary scattering than relativistic electrons. Again, the impulsive and punctual injection takes place at the footpoint of the central field line (CFL) with particles being isotropically distributed in positive pitch-angle.

At first glance, one can state that the introduction of μ -dependent perpendicular transport does not affect the SEPs that much as adiabatic cooling does (see Section 6.4 for comparison). Deceleration as a consequence of the expanding solar wind leads to faster decay rates once the bulk of particles has passed the observer. Here, on the other hand, changes in omni-directional intensity and first-order anisotropy can be only observed in the very early phase of particle detection.

Within $r = 0.3 \text{ AU}$ at the CFL, no significant deviations can be observed. Since $\kappa_{\perp}(r)$ is suppressed by the scaling with r^2 , the cross-field loss of particles is marginal. At azimuthal distance $\varphi = 30^\circ$, the intensity is 4 orders of magnitude smaller than at the CFL. In case of $\kappa_{\perp} \propto 1 - \mu^2$ the diffusive flux is marginally higher than in case of isotropic diffusion, since the dominant particle population with $\mu \approx 1$ is favored. The other term

$\kappa_{\perp}(\mu) \propto \mu^2$ with the opposite effect in μ behaves neutral because there are no particles having a significant velocity component in field-perpendicular direction.

These changes can be better identified when looking at the anisotropies: For $\kappa_{\perp}(\mu) \propto \mu^2$, they are higher beyond the CFL than in terms of isotropic scattering, but they also decay faster.

The SEPs behave in the same manner (compared to $r = 0.3$ AU) at the radial distance $r = 1$ AU, even if the temporal evolution occurs on different scales.

The crucial feature, that causes these differences, is the pitch-angle distribution. Early in the event, the particles are highly isotropic – not just because of the injection profile but also by the pitch-angle focusing which keeps particles to be field-aligned within the first tenths of an AU. As they propagate outward, they subsequently undergo pitch-angle scattering which leads to isotropic distributions. This is the reason why the curves become identical 1 - 3 hours after the first SEPs have reached the observer.

But not only the “youth” of an event is important, but also the phase when the first particles arrive at the observer. This is why even at $r = 1$ AU, the profiles differ. Considering just a single energy band with no additional adiabatic deceleration, the first particles would be the ones that have a mostly field-aligned velocity component, and consequently they contribute to the highest anisotropies in the particle distribution. Note that even additional adiabatic cooling would not affect the results considerably since this would lead to changes in the decay phase (phase when the maximum of particles has already left the observer, see Section 6.4 for comparison).

Without the r^2 scaling, the curves would have the tendency to differ more within $r = 0.3$ AU. With the inclusion of the scaling and the nearly isotropic distributions beyond $r = 0.3$ AU, the effects of pitch-angle dependent cross-field transport are negligible at all observation points. The effects become more pronounced if the ratio of $\kappa_{\perp} : \kappa_{\parallel}$ increases, but are negligibly small compared to those of solar wind effects (see Section 6.4).

5.4. The standard scenario

To simplify the description of the various simulation runs in the two following Chapters 6 and 7, we define a set of parameters and assumptions that uniquely identifies a scenario - termed *standard scenario*.

variable	value	description
v	1 AU h^{-1}	particle's speed
λ_r	0.1 AU	mean free path in radial direction, related to 10 MeV protons with $v = 1 \text{ AU h}^{-1}$
γ	0.1	ratio perpendicular-to-parallel diffusion coefficient at 1 AU
s_{ini}	0.1 AU	injection position and footpoint of the CFL
v_{sw}	0.0096 h^{-1} AU	solar wind speed (corresponds to $v_{sw} = 400 \text{ km s}^{-1}$)
θ	1.5708 rad	helio-latitude (corresponds to $\theta = 90^\circ$; ecliptic plane $\theta \approx 83^\circ$)
$q_1(s_{\parallel,0}), q_2(t = \delta(s_{ini}) 0)$		source term

Table 5.1.: Standard scenario defining the default set of parameters. All quantities can be reviewed in the appendix A.1.

6. Validation and Tests

Validation of the numerics as a whole is impossible since it consists of a composition of separated and consecutively executed transport processes. The resulting data might be reasonable but we can not exclude that one single transport process still has some numerical inconsistencies or errors. Nevertheless, there are some general features that must be fulfilled during the entire simulation time.

First, particles are not allowed to be swept out of the system – except for the fact that we explicitly allow particles to leave the system, for example at the spatial boundaries in field-parallel as well as in perpendicular direction, or, as it realized for momentum transport, towards lower momenta.

Secondly, detection of negative particle populations would give evidence to erroneous Fortran code or to a violated stability criterion. Abrupt changes in intensities, oscillations in intensities or non-smooth surface plots within the ecliptic plane would also fit into this category.

Third, according to the model construction, particles are expected to be transported in a single bulk with a single center of mass which should be located in an area between the CFL and the radially outward directed tangent at the footpoint of the CFL.

A complete validation includes both a separate test of each transport process (see Section 6.1 and 6.2) and a comparison to already existing schemes. At least within the very inner heliosphere, where the IMF lines are almost radial, a comparison with the results of the azimuthal model introduced by Lampa and Kallenrode (2009) should give similar time- and azimuthal profiles (Section 6.3).

6.1. Field-parallel Transport

As it is illustrated in Section 4.2, the explicit Lax-Wendroff scheme works stable in the maximum norm even if step sizes along the field lines are not equidistant anymore. Unfortunately, the accuracy of the finite differences (FD) drops to one.

The corresponding code was tested by switching off all other schemes in μ , p and s_{\perp} . At different times, intensity- and anisotropy plots or data files were made in order to compare them with those of uniform step sizes. The solar wind speed was switched off to make the overall particles speed in the solar rest frame constant (see Figure 6.1).

Phase space density neither reaches negative values nor any oscillations as an indicator of violated stability conditions were observed. The total mass of particles remains constant, except for a very vanishing (0.1 %) fraction that gets lost due to rounding errors at transport coefficients $\gamma(s_j, \mu_i)$ and $\eta(s_j, \mu_i)$. These values are partially divided by very small step sizes Δs_j . The s -transport works exact for the fastest particles with $v_{max} = \mu_{max} v$. The truncation error $\epsilon_{j,i}$ vanishes, and at least these particles will be shifted exactly to the next following grid point.

As it is described in Section 5.1, particles are injected isotropically in the positive pitch-angle domain. Combined with a δ -injection in time, this results in 20 different field-parallel particle velocities, Figure 6.1 features 20 peaks in case of constant step sizes. With

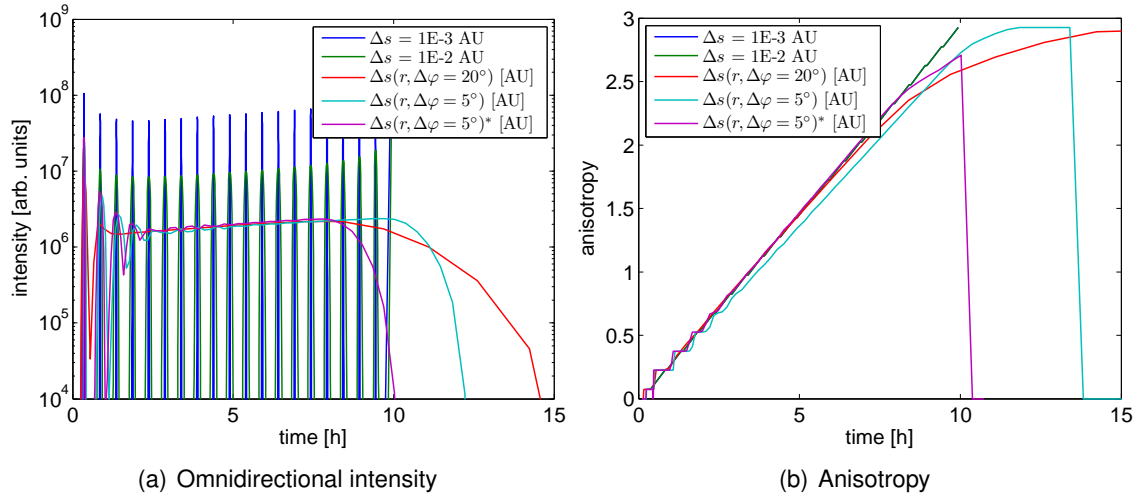


Figure 6.1.: Profiles along the magnetic field line for 10 MeV protons ($v = 1 \text{ AU h}^{-1}$) at time $t = 10.1$ hours: Only field-aligned advection is considered, solar wind and pitch-cosine transport is ignored, δ injection at $s_{ini} = 0.1 \text{ AU}$.

increasing step sizes, the green curve shows a pronounced broadening compared to the blue curve at a higher resolution. This results from a numerical dissipation and dispersion error in the first-order upwind-scheme (“numerical diffusion”, see Hatzky (1996), page 53). Even the anti-diffusive fluxes of the flux-limiter method can not prevent the gradients to be smeared out with time. In the current model, $\Delta s(s)$ grows and exceeds an order of magnitude with increasing s – compared to the innermost step size at the field line’s footprint. This is why the peaks disappear beyond $s = 1$ AU.

Some particles are transported faster out than it would be physically reasonable (beyond a radial distance of 10.2 AU). The original, numerical model stops advancing in space beyond that barrier (note that this is not the outer boundary), otherwise a fraction of SEPs would propagate faster than they actually are. This behavior can be also seen in the current model (see violet curves), but by default, the scheme considers all grid points because – in combination with enhanced perpendicular transport – especially the most eastern field lines could be filled with additional particle populations ahead of the propagation front.

If pitch-cosine transport is added besides advection along the IMF line, all profiles become very similar. The curves seem to be congruent for almost the entire path – except for the regions where the first particles arrive (see discussion above) and for the footpoints. The reason is that actually the injection is not peak-like in space but extended by $\Delta s(s_{ini})$ (with s_{ini} being the CFL footpoint's location). The source term as a time-varying inner boundary acts like an extended source in case of a coarse-meshed grid. Note that $\Delta s(s_j)$ itself depends both on s and $\Delta\varphi$.

The conclusion in terms of one-dimensional, field-aligned transport is that even with varying step sizes, the results are well in agreement with those of constant Δs . Because of the first-order accuracy, the results of the introduced scheme depend strongly on the grid resolution. It is recommended to work with adequately small Δs ($\Delta\varphi$) with $\Delta\varphi = 5^\circ$ and below – not because of the approximation error in the FDs but because of the focusing length (3.7) whose discrete values are overestimated for too large step sizes (for details see Section 6.5).

Outer boundary

We have two choices to overcome those effects emerging from the outer boundary at r_{out} . As in the conventional model we are able to allow particle to fully or partially leave the region under investigation. This can be done by making a change in the reflection coefficient which is 1 for full reflection and zero for complete passage into the outer space. We are mainly interested in particle behavior in the very inner heliosphere, which is up to the Earth's orbit (up to 1 AU). Particles that are backscattered significantly due to the outer boundary, could distort the results.

The outer boundary will be fixed beyond 5 AU radial distance, which is sufficient even for the fastest particles not to reach it during simulation time (for most computed scenarios). Larger values are not physically reasonable, because at these distances beyond the Jovian orbit, the assumption of Archimedean spirals certainly is no longer valid and corotating interaction regions will have formed.

This results from the growing step sizes in field-parallel and in perpendicular direction. A change in r_{out} does not involve a significant additional amount of grid points. Moreover – as we have seen in the Numerics chapter – time step sizes are chosen according to the stability criteria at the footpoints of the field lines. This is at $r_{ini} = 0.1$ AU as default, where the footpoints form the inner boundary. The minimum value lies at about 0.06 AU. Consequently, an extension of the ecliptic grid does not lead to a massive increase in computing time or in memory allocation.

6.2. Field perpendicular transport

Assuming that the perpendicular diffusion coefficient κ_{\perp} is constant (isotropic scattering) and that the source is impulsive, point-like injection of m_0 particles at location z_0 (in [AU])(δ -injection), an enclosed, analytical solution of the diffusion equation

$$\frac{\partial f}{\partial t} = \frac{\partial}{\partial z} \left(\kappa_{\perp}(s, z) \frac{\partial f}{\partial z} \right) \quad (6.1)$$

is possible. The area under consideration has to be infinite to both sides. It should be noted that – at least in this Section – f will be treated in units of linear density, since the transport is only governed by simple spatial diffusion in one dimension.

Then, both a Laplace-transform according to the time t and a Fourier transform according to the space can be applied (for details see Farlow, 2003).

Remember that the *Fourier transform* can be defined as

$$\mathcal{F}[f(z)] = \frac{1}{\sqrt{2\pi}} \int_{-\infty}^{+\infty} \exp(i\omega z) f(z) dz = F(\omega) , \quad (6.2)$$

under the assumption that the improper integral is bounded. Note that in literature, there is no unique definition for the Fourier transform. Definitions might differ in different scalings to the preceding factor and to ω .

If the first n derivatives of $f(z)$ exist, the following formula would help to apply the transform to Equation 6.1:

$$\mathcal{F}[f^{(k)}(z)] = (i\omega)^k \mathcal{F}[f(z)] \quad k = 1, \dots, n \quad (6.3)$$

The Laplace transform can be applied to continuous functions of exponential order c , if there exists a $M > 0$ and $c > 0$ in the sense that the inequality

$$|f(t)| \leq M \exp(c t)$$

is fulfilled for all $t \in [0, \infty[$.

According to the stability in the maximum norm, $f(t, z)$ is bounded between 0 and $m_0/dz(r)$ ($dz(r)$ is the width of the cell where the particles are injected) – given by the minimal values of the boundary conditions and the maximum value of the initial condition. Since all upper-bounded functions are automatically functions of exponential order zero, $f(z)$ can be Laplace-transformed without any constraints.

Definition of the Laplace transform for functions of exponential order c :

$$\mathcal{L}[f(t)] = \int_0^{+\infty} \exp(st) f(t) dt = L(s). \quad (6.4)$$

The integral is absolutely convergent, if $s > c$ (in this case: $s > 0$).

Theorem:

If the first n derivatives of $f(z)$ exist and these are all of exponential order c , the Laplace transform of the k th derivative of $f(t)$ gives for $s > c$:

$$\mathcal{L}[f^{(k)}(t)] = s^k \mathcal{L}[f(t)] - s^{k-1} f(0) - s^{k-2} f'(0) - \cdots - f^{(k)}(0) \quad k = 1, \dots, n. \quad (6.5)$$

The tools will help to get an enclosed solution to the heat conduction (6.1). Using the transformation $\tau(t) = \kappa_{\perp} t$, (6.1) can be rewritten:

$$\frac{\partial u}{\partial \tau} = \frac{\partial^2 u}{\partial z^2} \quad \in \Omega = [(z, \tau) | -\infty < z < +\infty, 0 \leq t < \infty] \quad (6.6)$$

with $u(z, \tau = 0) = \Gamma(z)$ being the initial condition. Concerning this diffusion problem, we have $\Gamma(x) = m_0 \delta(z)$, the *Dirac-δ-function*:

$$\delta(z) = \begin{cases} m_0 \delta(0) & \text{for } z = 0 \\ 0 & \text{for } z \neq 0 \end{cases}; \int_{-\infty}^{+\infty} \delta(z) dz = m_0; \int_{-\infty}^{+\infty} f(z) \delta(z) / m_0 dz = f(0).$$

The solution of (6.1) will be given by the solution of (6.6) by $f(z, t) = u(z, \kappa_{\perp} t)$.

First, the PDE (6.6) will be Laplace-transformed with respect to τ . The transformed value of $u(x, \tau)$ is defined as $U(x, s)$. Using (6.5), we get:

$$\partial_{xx} U(x, s) - s U(x, s) = \Gamma(z) \quad \text{with } \Gamma(z) = u(z, \tau = 0).$$

Now, the PDE will be Fourier-transformed with respect to the spatial variable z . The transformed function of $U(s, \tau)$ is called $V(\omega, s)$. Let $\Phi(\omega)$ be the transformed function of $\Gamma(z)$.

According to Equation (6.3), the upper equation yields:

$$-\omega^2 V(\omega, s) - s V(\omega, s) = \Phi(\omega) \Leftrightarrow V(\omega, s) = \frac{\Phi(\omega)}{\omega^2 + s}; .$$

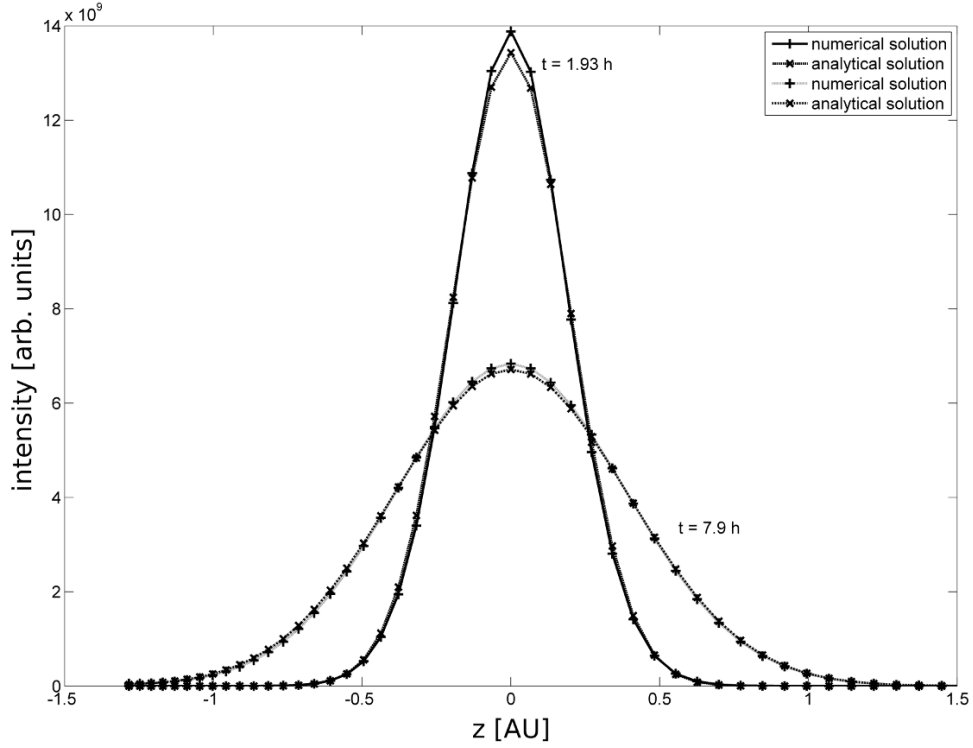


Figure 6.2.: One-dimensional diffusion profiles for varying step sizes along a cross-field path. Scenario settings: Isotropic diffusion with $D = 0.01 \text{ AU}^2 \text{ h}^{-1}$, δ -injection at ($z = 0, r_{inj} = 1.36$) AU, $d\varphi = 5^\circ$.

$V(\omega, s)$ will now be inversely transformed (Fourier and Laplace), starting with Laplace (transformation order can be arbitrarily):

$$\mathcal{L}^{-1}[V(\omega, s)] = \exp(-\omega^2\tau)\Phi(\omega)$$

Applying the Fourier transform, leads to:

$$u(x, \tau) = \frac{1}{\sqrt{2\pi}} \int_{-\infty}^{+\infty} \mathcal{L}^{-1}[V(\omega, s)] \cdot \exp(-i\omega s) d\omega = \frac{1}{\sqrt{2\pi}} \int_{-\infty}^{+\infty} \Phi(\omega) \cdot \exp(-i\omega s + \omega^2\tau) d\omega.$$

This is the general solution of PDE (6.6). Inserting the transformed initial condition of $\Gamma(z) = m_0\delta(z)$, we get as fundamental solution:

$$u(x, \tau) = \frac{m_0}{2\pi} \int_{-\infty}^{+\infty} \exp(-(i\omega z + \omega^2\tau)) d\omega = \frac{1}{\sqrt{\pi\tau}} \exp\left(-\frac{z^2}{4\tau}\right).$$

Reformulated in terms of f and assuming that the injection takes place at location z_0 instead, the solution gets its final shape by:

$$f(t, z) = \frac{m_0}{\sqrt{4\pi\kappa_\perp t}} e^{\frac{-(z-z_0)^2}{4\kappa_\perp t}} \quad t > 0, z \in [-\infty, +\infty]. \quad (6.7)$$

Comparing the numerical solutions with (6.7) implies that, during simulation time, no particles reach the outer boundaries. An adequate distance z_d between the injection location and the outer boundary can be defined, where just the fraction ϵ of the total mass m_0 has reached the boundaries after the time t_c (Lampa, 2006):

$$z_d = z_0 + \sqrt{-\ln(\epsilon \sqrt{4\pi\kappa_{\perp}t})} \frac{4\kappa_{\perp}t_c}{\epsilon} \quad \epsilon \in [0, 1]. \quad (6.8)$$

The computed diffusion profiles are expected to be similar to the analytical solution for $\epsilon \rightarrow 0$.

As numerical scheme, the implicit *Laasonen* scheme was chosen, since the diffusion coefficient is expected to be highly variable in the inner heliosphere. An explicit scheme like the *Crank-Nicolson-scheme* (Crank and Nicolson, 1947) would require the stability criterion

$$\frac{\kappa_{\perp}(r)\Delta t}{\Delta z(r)^2} \leq 1.$$

A $\kappa_{\perp}(r)$ scaled with the squared radius would grow faster than $\Delta z(r)^2$, thus the criterion will be violated beyond a certain radial distance. Moreover, the Laasonen scheme works properly even at strong gradients (e.g. at possible shock fronts, and in the early phase of an event at the injection location. As a consequence, the truncation error in t drops to the order of one.

Figure 6.2 illustrates two different kind of diffusion profiles, the first taken at $t \approx 2$ hours, and the other at $t \approx 8$ hours. The step sizes along the perpendicular curve grow in positive (westward) direction. They were computed according to an azimuthal resolution of $\varphi = 5^\circ$. The δ -injection occurred at $r_{inj} = 1.36$ AU and released a total mass of particle of $m_0 = 1E + 11/\Delta z(r_{inj})$. The diffusion coefficient was set to $\kappa_{\perp} = 0.01$ AU² h⁻¹.

Numerical solutions are indicated by crosses + while the exact solutions are denoted by diagonal crosses x. Each pair of profiles coincide perfectly except for the area around the injection location where the numerical f lies slightly under the exact solution. The reason is that the particles are injected numerically as an extended source with width $\Delta z(r_{inj})$. This is why these differences are pronounced in the early phase. Despite the fact that the step sizes vary with radial distance, we still get symmetrical profiles. No oscillations, that would cause negative linear densities, were observed. Thus the scheme is stable – even with other sets of parameters, that could violate the stability criterion for explicit schemes. Moreover, the total particles number $m_0 = \sum_{l=1}^{l_z} f(z_l)\Delta z_l$ stays constant. For $t \rightarrow \infty$, the z interval was uniformly filled with particles without any losses. Thus, even the total reflection at the outer boundaries works as it was expected.

Periodic boundary conditions were tested by plotting f along the complete perpendicular path. By the introduction of periodicity, segments of perpendicular paths, that were originally separated from each other, were sticked together (see Figure 4.4). The resulting profiles were smooth along the complete interval. Abrupt changes would have been an indicator that the array indexing failed.

Alternatively, the entire plane of ecliptic was checked with respect to smooth surfaces of intensity and anisotropy (see e.g. Figure 6.3 in the following Section 6.3).

6.3. Azimuthal vs. perpendicular cross-field transport

Time-profiles and spatial distributions are expected to be similar within 0.3 AU, since both grids are very similar and look like a radial magnetic field in that region. So, this Section is dedicated to a test of the complete model – but ignoring the solar wind effects.

We took the *standard scenario* which is defined as in Section 5.4 and chose $\Delta s = 0.001$ AU for the azimuthal model in order to have spatial resolutions of the same magnitude. But even a value for Δs , which is ten times larger, will not change the numerical results significantly – as we have already validated in Section 6.1. A first glance at a snapshot

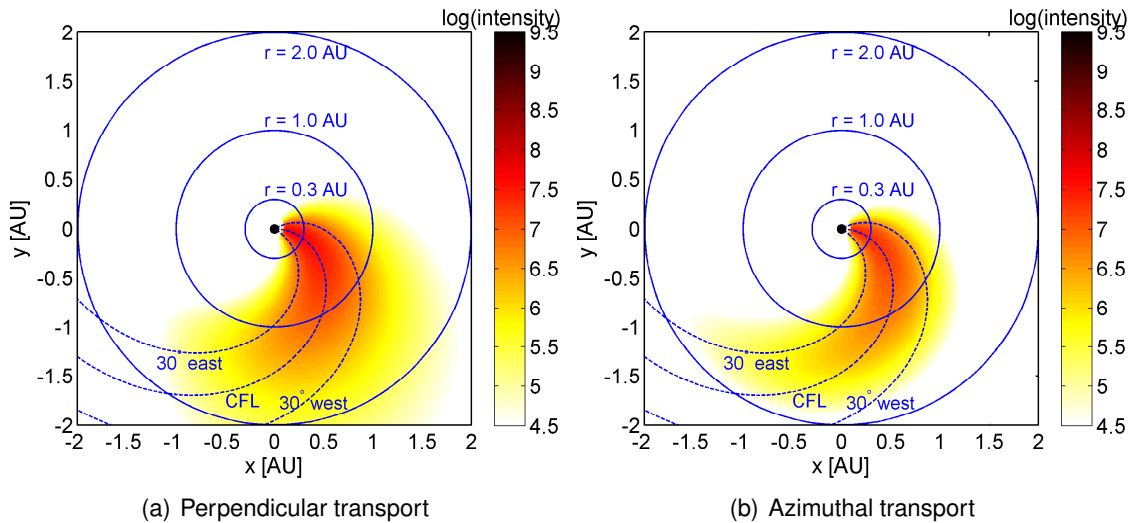


Figure 6.3.: Intensity-plots in the ecliptic plane at time $t = 5$ h in two different numerical grids. The simulation parameters have been chosen with respect to the standard scenario.

of the ecliptic plane (Figure 6.3) indicates that cross-field diffusion acts much stronger on particles in the perpendicular grid than in the azimuthal one, even though the diffusion coefficients themselves are the same. This underestimation in the former grid has already been mentioned by Lampa and Kallenrode (2009). Azimuthal displacements do not effectively separate particles from the CFL beyond 1 AU, since $\angle(e_\varphi, e_s)$ (cf. Figure 3.3) decreases with increasing radial distance.

At $r = 0.3$ AU, spatial distributions are almost identical. This can be seen even better when looking at the azimuthal profiles at the left panel of Figure 6.4. With increasing time, all profiles get levelled off: Particles are swept towards the flanks and tend to be distributed equally in space.

Both profiles (azimuthal and perpendicular) have in common that particles are displaced to both sides of the CFL in the same amount: The graphs are symmetric around the CFL, which is in good agreement with the assumption that the field has to be nearly radial within $r = 0.3$ AU.

Significant differences arise when we look at $r = 1.0$ AU: The azimuthal profiles seem to indicate that particles are not distributed as far as in the perpendicular ones (as seen in the 2D-profiles). Moreover, particles are obviously swept into western direction. The bulk center (maximum of particles) is located slightly to west, whereas the azimuthal profiles

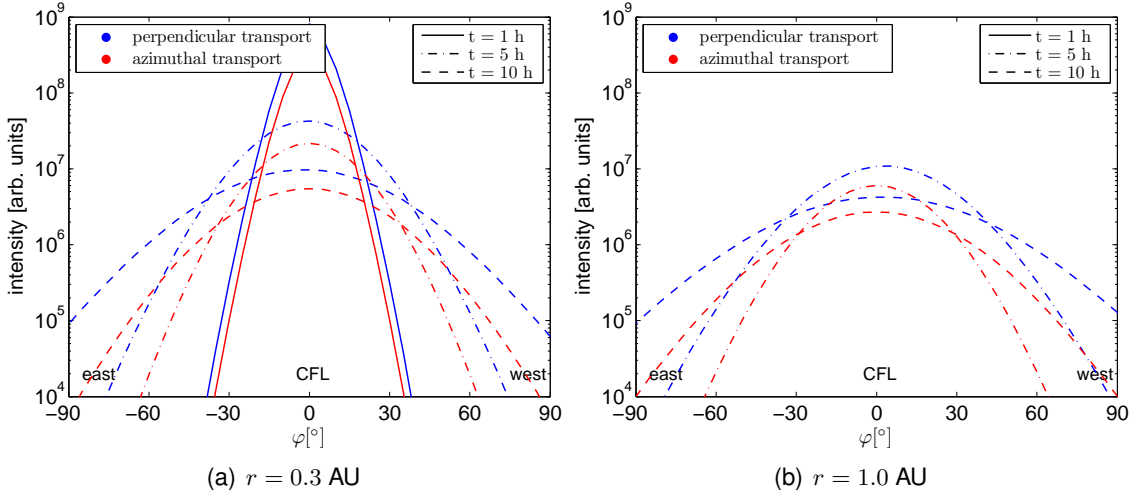


Figure 6.4.: Azimuthal variation of the omni-directional intensity

still show symmetric graphs. The reason is that particles at radial distance beyond 1 AU undergo a slight displacement in positive radial direction when they are swept westward. In eastward direction, the SEPs are slightly shifted towards the Sun. Thus, in situ measurements at a constant radial distance, the onset of the very first arriving particles as well as the maximum of particles is expected to be detected earlier on the western flank than on the opposite side if the CFL. This is clearly visible in the intensity-time-profiles (Figure 6.5).

The anisotropy-time profiles in both realizations of cross-field transport qualitatively show always the same behaviour, which is typically observed in impulsive SEP events: An abrupt rise very early in the event and gradual decrease towards zero in the following hours. But both grid architectures have in common, that the more we look azimuthally beyond the CFL the more the anisotropy falls and even changes to negative values. This decrease is even more pronounced in the western direction of the perpendicular grid. This can be explained by the fact that perpendicular diffusion coefficient κ_{\perp} is scaled with the squared radius:

Hours after the simulation start and within a few tenth of 1 AU, some of the neighboring field lines might not yet be filled with particles considerably, whereas the rest of the field line already shows significant particle populations. These particles are subsequently backscattered and reduce the net flux of particles streaming away from the Sun. If the amount of inward flux exceeds the outward flux, this results in negative anisotropies. Note that this happens beyond $\varphi \pm 60^\circ$ and weak cross-field diffusion. At larger radial distances, this negative anisotropy is not observed in the model.

6.4. Introduction of solar wind effects

Figure 6.6 demonstrates the time development of SEPs, when solar wind effects are involved. Remember that in contrast to Ruffolo's approach, the reference frame is the rest frame of the solar magnetic field, with μ and p measured in solar wind frame. The observer is located at a fixed field line, but the solar wind's orientation was not transformed by the additional corotation speed. Instead, solar wind particles flow radially outward with

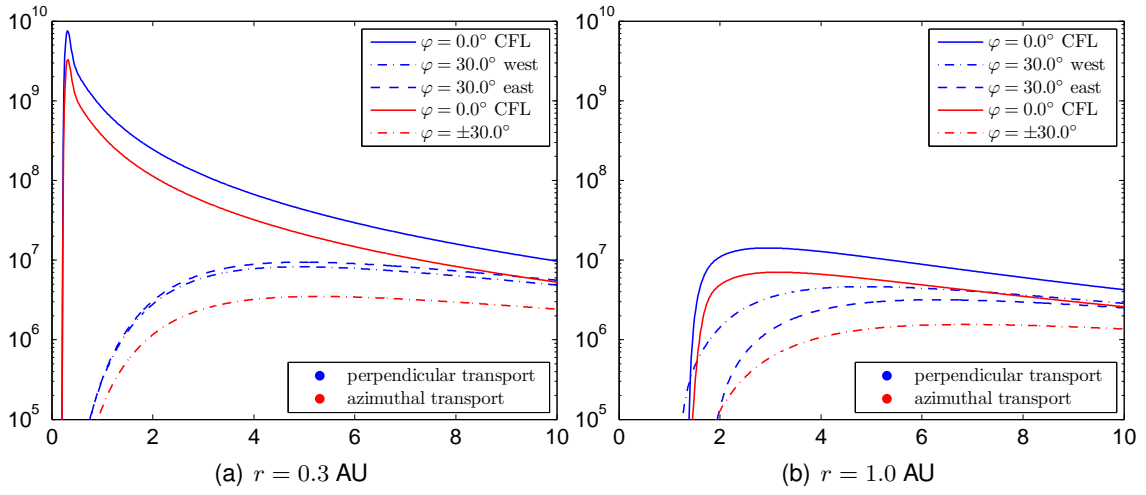


Figure 6.5.: Intensity-time-profiles at a constant radial solar distance, but different azimuthal distances

respect to the background field. Numerically, this advective flux was split into a field-parallel and field-perpendicular component. As a consequence, simulation results of the original Ruffolo-code can not directly be compared with those of this study. The data would be identical to the numerical model of the Roelof's Equation, if solar wind effects are switched off.

The output data of interplanetary transport with solar wind effects and without them was compared. When the SEP propagation was simulated without solar wind effects, the same model was used, but v_{sw} was set to zero and changes in momentum due to adiabatic cooling and the inverse Fermi-effect were neglected. The *standard scenario* was chosen (see Table 5.1).

If solar wind effects are considered (see the solid lines in Figure 6.6), the intensities rise earlier and show an earlier maximum. This behavior is more pronounced for the lowest energy bands, where the particle speeds are comparable to the solar wind speed. These shifted onsets are mainly due to field-parallel convection to the solar wind, while adiabatic deceleration does not affect the profiles significantly, since losses in a fixed energy band will be refilled by “cooled” particles from higher bands. This holds for monotonous falling energy spectra, of course. The onset shifts are even higher for larger radial distances: The solar wind had enough time to push particles further out. Note that the differences in the curves are less obvious than in the study of Hatzky and Kallenrode (1999); Ruffolo (1994). Ruffolo introduced the observer’s corotation, that artificially increases the field-parallel solar-wind speed $v_{\parallel}(r)' = v_{\parallel}(r) + \omega_{\odot}r \sec \Psi$.

Another fact is that intensities decay significantly faster than without solar wind effects. This is in good agreement with Hatzky and Kallenrode (1999). Changes in the particle distribution due to adiabatic deceleration are minimal compared to other interplanetary transport effects, but with increasing time and/or at larger radial distances, the change in momentum becomes noticeable: More particles of a certain energy are removed to lower energy bands than particles could be added from higher bands – owing to the energy spectrum. In the lower energy ranges, convection with the solar wind also contributes to the faster removal of particles from the observer’s position. But contrary to simulations in Hatzky and Kallenrode (1999), these particles do not just get lost in field-parallel direction:

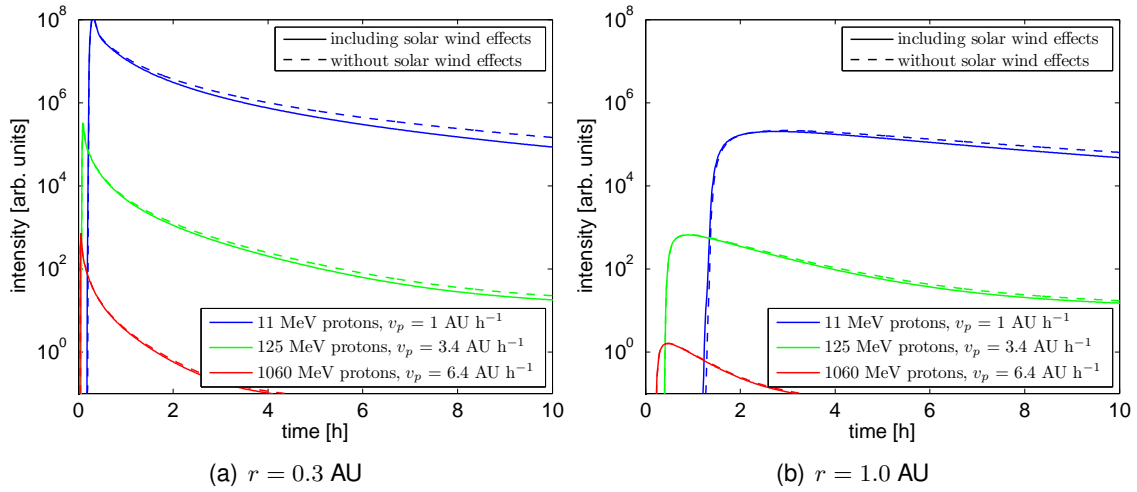


Figure 6.6.: Intensity-time profiles including (solid lines) and without (dashed lines) solar wind effects for different energies. The default parameter set was chosen according to the *standard-scenario*.

They were shifted to neighboring field lines in western direction. The central field line will not be adequately refilled from the opposite direction since the injection occurred at the CFL and the bulk of particles does not show the tendency to broaden or even shift its center to the east.

The same features can be observed in the first-order anisotropies (not shown here). At late times, they can even become negative since the main part of the particle distribution was convected across the observer. This leads to an inward directed intensity gradient and finally to a streaming of particles towards the Sun. The negative values are less pronounced than in earlier studies by Hatzky and Kallenrode (1999). The reason could be that the neighboring field lines still contribute enough particles streaming outward.

6.5. Spatial resolution of the grid and its impact on the numerical results

Before making any fits to the satellite observations, the crucial question has to be answered if and how the simulation results differ with different spatial resolutions. Note that this also incorporates a change in time step size, since the minimum step size in field-parallel direction is coupled with Δt via the stability criterion (4.21).

Again, the default parameter set according to the *standard scenario* is chosen, but neglecting the effects of the solar wind. As a first step, the focus was taken to pure field-parallel transport, including the particle's gyro center motion along the magnetic field line, focusing due to the diverging magnetic field and pitch-angle scattering. Four scenarios are compared with each other (see Figure 6.7), two of them are based on the original finite difference scheme for constant step sizes ($\Delta s = 0.001 \text{ AU}$, indicated by blue lines; and $\Delta s = 0.01 \text{ AU}$, indicated by the green lines). Scenarios 3 and 4 already incorporate variable step sizes along s , that have been computed with respect to an azimuthal resolution of $\Delta\varphi = 1^\circ$ (red lines) and $\Delta\varphi = 5^\circ$ (cyan lines) (see Section 3.2.2, (3.28)).

It is obvious that the time-profiles do not coincide for an observer at $r = 0.3 \text{ AU}$ as well as

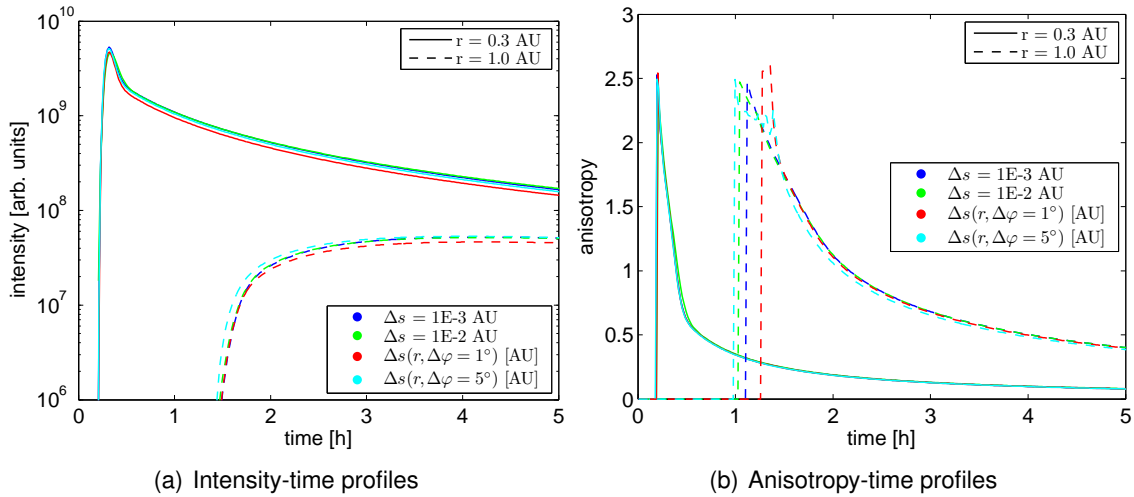


Figure 6.7.: Time profiles for pure field-parallel transport at different locations: Different grid resolutions were chosen: Constant step sizes $\Delta s = 0.001$ AU (blue lines) and $\Delta s = 0.01$ AU (green lines) as well as variable step sizes corresponding to $\Delta\varphi = 1^\circ$ (red lines) and 5° (cyan lines). The default parameter set was chosen according to the *standard-scenario*, but ignoring solar wind effects. Particles are 10 MeV protons with speed $v = 1$ AU h $^{-1}$.

1 AU. With increasing step size, as indicated in Figure 6.7, the test particles arrive later at the observer: the delays between the injection and the first arriving particles (illustrated best by a sudden rise in the anisotropies) is more pronounced at larger distances. Note that this is independent of the step size choice (constant or variable step sizes). Moreover, these delays can not be explained in terms of inaccuracies of the finite differences, in particular the observer's location: The delay between the two times of maximum anisotropy in non-equispaced grids (red and cyan curves) yields ≈ 0.25 hours – corresponding to a 0.25 AU distance between the maximum anisotropies. This is at least one magnitude higher than the step sizes at $r = 1$ AU ($\Delta s_{\perp}(r = 1AU, \Delta\varphi = 5^\circ) \approx 0.01$ AU; $\Delta s_{\perp}(r = 1AU, \Delta\varphi = 1^\circ) \approx 0.06$ AU).

The discrete solutions of the finite difference schemes do not considerably differ, but these differences are evident especially in the early phase of the event and along the propagation front. Larger step sizes can be best identified in the very fine structures of the time profiles, such as the anisotropy peaks. Note that vanishing particle numbers were cut off to defend anisotropies from statistical errors. What makes the difference in the example mentioned above, and in general, is the focusing length, which is expected to be highly variable within 0.3 AU. Due to numerical construction reasons combined with a fast decrease of the inverse focusing length (see Figure A.5), the pitch-angle-focusing term within the μ -scheme is overestimated for large spatial step sizes: Field-parallel transport and focusing are executed consecutively, but not at the same time: Once a particle was focused according to the local magnetic field structure, it will be shifted to next following grid point on the field line. If the jump becomes too large, this might also lead to a considerable change in the magnetic field, which was not taken into account when the focusing was applied in the previous time step. Note that these numerical effects emerge both in grids with constant and varying step sizes. For future studies (in case of constant step sizes along the field lines), it would be more adequate to determine the focusing

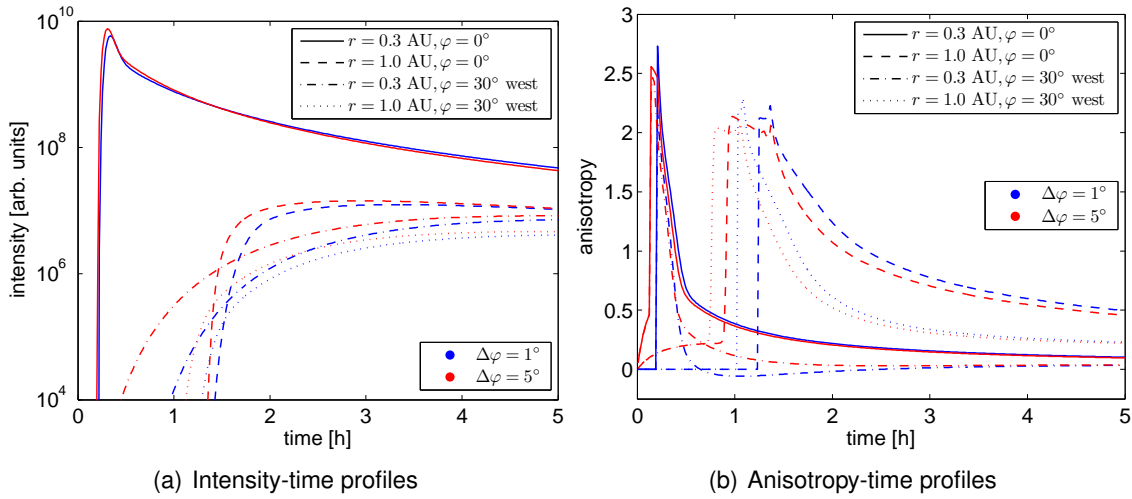


Figure 6.8.: Time profiles for different grid resolutions: 1° (blue lines) and 5° (red lines) at different locations. The default parameter set was chosen according to the *standard-scenario*, but ignoring solar wind effects. Particles are 10 MeV protons with speed $v = 1 \text{ AU h}^{-1}$.

length on the basis of average magnetic conditions between two neighboring grid points on a field line instead of a single point. The numerical grid of the current model is sufficient to represent the highly variable focusing length close to the Sun.

Pitch-angle focusing has strong influence on the simulation results, since it is the only transport process that dominates within a few tens of an AU. The other effects in interplanetary transport would lead to different results in the decay phase late in the event. Here, the results differ in very early phase (with five hours after the injection occurs), while the profiles become similar once this period has expired. It should be emphasized that these similar profiles are not a result of strong diffusion that levels out any gradients (see e.g. Figure 6.4). These studies showed that the profiles become similar for different spatial resolutions, but on different levels – depending on the observer’s location.

With additional cross-field diffusion and for small step sizes $\Delta\varphi$, the azimuthal profiles at fixed times reveal a stronger confinement of particles around the CFL (7.5° less within the first 5 hours for the current scenario). The difference lies in the same order of magnitude as the larger angular resolution of $\Delta\varphi = 5^\circ$. Therefore, it can be discussed in terms of inaccuracies of the numerical scheme. As long as the test particles are located within 0.3 AU, no significant spread in azimuth occurs - because of the r^2 scaling of the perpendicular diffusion coefficient, and because of the finer grid meshes.

The dominating contribution of pitch-angle focusing over scattering in μ become less significant, thus particles have the tendency to become isotropic earlier than in case of larger spatial step sizes. Therefore, particles need more time to escape to larger radial distances (see Figure 6.8). This has already been shown for the one-dimensional transport, but additional cross-field transport leads to even slightly higher time differences. For $\Delta\varphi = 5^\circ$ and $r = 1$ AU, the first particles arrive about 15 minutes earlier than in the 1D case: Especially beyond $r = 0.3$ AU, particles experience additional Sun outward directed displacements, when they are transported westward across the field lines, and when they are subsequently backscattered onto the CFL. It should be noted that just

a small fraction of the injected particles (approximately 0.1% of the maximum intensity) contributes to these differences.

In order to have reasonable onset times, it is recommended not to choose crude angular resolutions larger than $\Delta\varphi = 5^\circ$, since this would lead to significant differences from the highly resolved ($\leq 1^\circ$) solutions - as a result of both numerical focusing and cross-field-transport effects.

7. Model Results

Using the numerical model based on the Ruffolo's equation and the additional perpendicular diffusion, this section will be dedicated to the dynamics of cross-field transport. The propagation parameters, that have been introduced in one-dimensional transport, will be adopted as well as the estimate for the perpendicular diffusion coefficient (see Section 5.3). Parameter studies in Section 7.1 will illustrate the dynamics of the introduced 2-dimensional transport in the ecliptic plane. The resulting intensity- and anisotropy-time profiles will be validated with respect to the azimuthal spread of type III radio bursts (Section 7.2.1) as well as the multi spacecraft observations (Section 7.2.3).

7.1. A parameter study

The intent of this section is to estimate the possible influence of perpendicular transport, but not to fit energetic particle events. Scenarios with different parameter sets will be applied in order to illustrate how the particle spread evolves in space and time – depending on the parameter configuration. The results are checked with respect to plausibility and we will look for a physical explanation. A first impression about the dynamics of the two-dimensional transport without solar wind effects were already gained in Section 6.3 using the *standard scenario*.

The parameter sets are also based on the *standard scenario* (5.1), but the focus is taken on particle velocities of $v = 1, 3.4$ and 6.4 AU h^{-1} . The radial mean free path is set to the upper und lower boundary, which we have been declared to be plausible (Section 5.2). The ratio perpendicular to parallel diffusion strength is set to $1/10$ and $1/50$ at $r=1 \text{ AU}$, and scaled with r^2 . In sum, six scenarios have been computed.

7.1.1. Plots in the ecliptic plane

Combined effects of field-parallel and field-perpendicular transport can be illustrated best by looking at the ecliptic plane. The SEPs were injected as a δ -injection onto the field line originating at $\varphi = 0^\circ$. The local parallel particle mean free path is determined from $\lambda_r = 0.1 \text{ AU}$, the perpendicular mfp consequently is 0.01 AU at 1 AU , but scaled with r^2 .

On a logarithmic scale, Figure 7.1 shows the intensity for 10 MeV protons ($v = 1 \text{ AU h}^{-1}$) at different times ($t = 1 \text{ hour}$ in the first row, $t = 5 \text{ hours}$ in the second and $t = 10 \text{ h}$ in the last row). On the left, strong perpendicular diffusion was assumed, on the right the ratio was set to one fiftieth. It is evident that with increasing ratio, the spread of particles in azimuth is more pronounced – note just because of the scaling with $\gamma = 1/10$ or $1/50$. Beyond the Earth's orbit, the squared-radius-dependency of κ_\perp leads to a faster removal of SEPs from the CFL, whereas perpendicular diffusion close to the Sun is suppressed. The field lines shown in the figure are 30° apart. For this example, the area between the dashed field lines (around the CFL) is filled within an hour in case of strong perpendicular diffusion. Weak cross-field transport accordingly shows lower extents. Thus, enhanced perpendicular diffusion effectively removes more particles from the CFL. The gradients

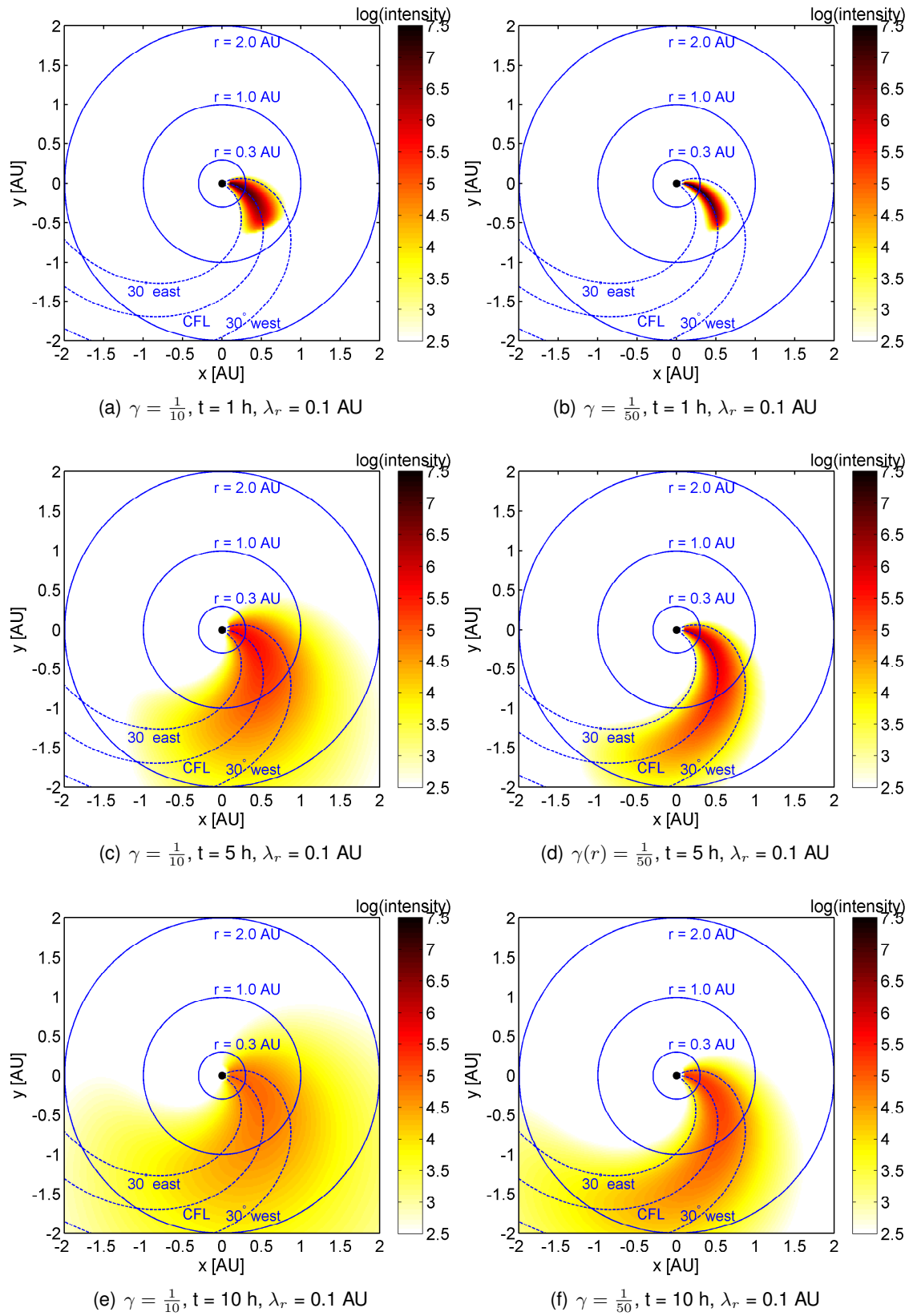


Figure 7.1.: Intensity (on a logarithmic scale) of SEPs ($v = 1$ AU h^{-1}) in the ecliptic plane.

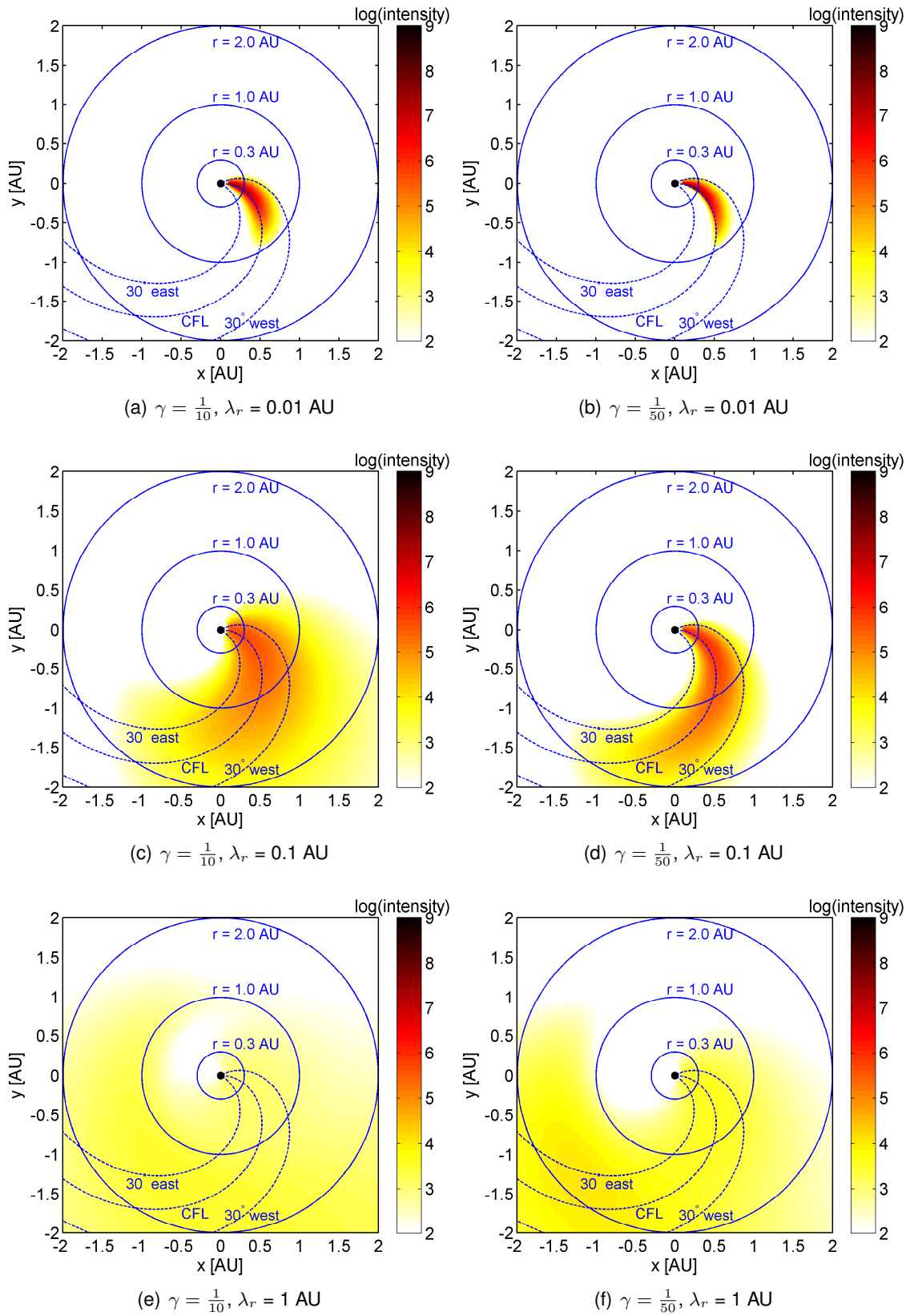


Figure 7.2.: Intensity-plots in the ecliptic plane at time $t = 5$ h for different scattering conditions.

in perpendicular direction are leveled off, and the front of the first arriving particles could not propagate as far as in the case of strong diffusion.

Moreover, the bulk center of particles shifts slightly westward as a consequence of the radially outward streaming solar wind. This can be seen more clearly in the cross-field profiles (see following Section 7.1.2).

So far, the model results are as expected, but what about different combinations of the ratio κ_{\perp} -to- κ_{\parallel} (denoted by γ) and the radial mean free path λ_r ? As an example, Figure 7.2 illustrates the spread of particles with $v = 1 \text{ AU h}^{-1}$. The snapshots were taken five hours after the injection, λ_r varies with 0.01, 0.1 and 1 AU and the diffusion ratio is $\gamma = 1/50, 1/10$. From top to bottom, λ_r increases by one order of magnitude in each row; the left panels were plotted with stronger perpendicular diffusion than the right ones. The middle row therefore corresponds to the middle row of Figure 7.1.

Discussing about the “horizontal dependencies” (strong vs. weak perpendicular diffusion), the same behavior can be observed as in 2D plots that illustrated the temporal evolution of particle transport for both $\gamma = 1/50$ and $1/10$. The new feature in this context is that the radial mean free path λ_r contributes to the overall strength of perpendicular transport. First, λ_r determines the strength of pitch-angle scattering along the field lines: Inserting the spatially dependent pitch-angle diffusion coefficient (PADC) (5.10) into (5.9) yields $\kappa_{\mu}(r) = 0.75 v \lambda_r^{-1} \cos(\Psi)^2$, which denotes the strength (“amplitude”) of the PADC. The smaller λ_r is, the more efficiently particles undergo pitch-angle scattering: Distributions that have originally been highly anisotropic due to the escape along open field lines and due to focusing effects, become consecutively more isotropic. This prevents particles from leaving the very inner heliosphere ($r < 0.3 \text{ AU}$), where the radially scaled perpendicular diffusion coefficient is not able to considerably shift particles in azimuthal direction. As can be seen in Panel (b) of Figure 7.2 for example, 10 MeV protons with $v = 1 \text{ AU h}^{-1}$ are still mainly confined to one AU although 5 hours since the injection have passed. Secondly, λ_r acts directly as a scaling factor in κ_{\perp} , since λ_r is assumed to be constant: $\kappa_{\perp} \propto \lambda_{\parallel} = \lambda_r \sec(\Psi)^2$.

The opposite case $\lambda_r = 1 \text{ AU}$, allows SEPs to propagate without significant pitch-angle scattering, so the fastest particles nearly reach 5 AU arc length along the CFL. Unfortunately, the SEPs are exposed to strong (radially scaled) cross-field diffusion much earlier than the ones described in the previous scenario.

Consequently, at fixed times, different combinations of $\kappa_{\perp} : \kappa_{\parallel}$ and λ_r lead to different shapes of the particle distributions. In the latter case ($\gamma = \frac{1}{50}$, $\lambda_r = 1 \text{ AU}$), the bulk center has been significantly shifted outward. The propagation front rather looks like a semi-circle, covering almost half of the ecliptic plane. The shape resembles a shock front. Normally, shocks are made responsible for this huge azimuthal spread of particles (180° within a few hours). Low- λ_r -distributions rather look like a tongue: they are more extended in field-parallel direction than perpendicular to it. Moreover, there appears to be no considerable peak of particles. The spatial gradients in field-parallel direction look smoother than in case of weak pitch-angle scattering: low λ_r -values and a cross-field diffusion coefficient, suppressed by the r^2 scaling, lead to a storage of particles within $r = 1 \text{ AU}$ and $\varphi \pm 30^\circ$, that could last up to ten hours after the injection.

7.1.2. Cross-field profiles

The azimuthal spread of particles can be better resolved by slices through the two-dimensional distributions for fixed times $t = 1, 5$ and 10 hours after the injection. Figure 7.3 shows the intensity on a logarithmic scale with the central field line being located

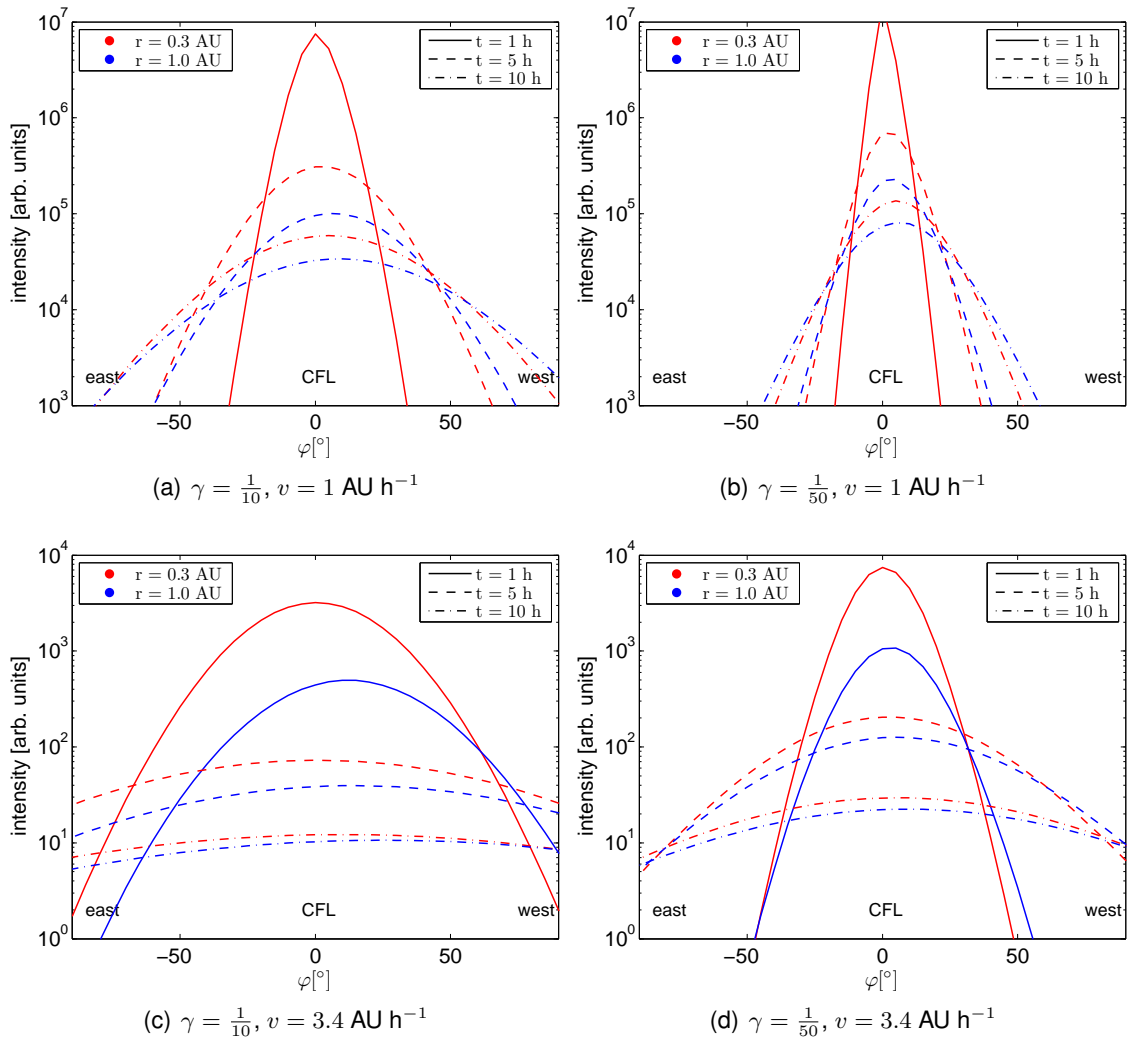


Figure 7.3.: Azimuthal profiles of omni-directional intensity for different times ($t = 1, 5$ and 10 hours) und medium pitch-angle scattering conditions ($\lambda_r = 0.1$ AU). The left-handed panels reveal stronger perpendicular diffusion than the right handed ones. For the first panel row, particle's speed is fixed at $v = 1$ AU h^{-1} , for the second at $v = 3.4$ AU h^{-1} .

at azimuthal distance $\varphi = 0^\circ$. Note that these snapshots were taken for fixed radial distances $r = 0.3$ and $r = 1$ AU, thus these profiles do not correspond to those of a certain perpendicular path. They become even more asymmetric beyond 0.3 AU than along a field-perpendicular path (see also Section 6.3). Again, the westward shift can be observed at $r = 1$ AU, since the solar wind convection occurs oblique to the field-line direction. Figure 7.3 confirms that the particle distribution moves slowly westward with increasing time. Moreover, these displacements do not depend on particle properties – which is not surprising since advection is solely influenced by the surrounding medium (solar wind plasma).

Perpendicular diffusion leads to a wider spread for *fast* particles than for *slow* particles, since κ_\perp is scaled with squared particle speed v (5.9). Thus, in contrast to the former, azimuthal model by Lampa and Kallenrode (2009), profiles of other particle species can not be obtained by a simple scaling with v .

Concerning the model results, we never observed a complete filling within $r = 0.3$ – independent of the diffusion parameter set. Pitch-angle focusing as well as the damped perpendicular diffusion prevents particles to be transported to the opposite site of the Sun.

Compared to the numerical results of the azimuthal model by Lampa and Kallenrode (2009), significant particle spread up to $\pm 30^\circ$ around CFL occurs at 0.3 AU within an hour for $\lambda_\perp/\lambda_\parallel \approx 1/10$. Within five hours significant particle spread over more than $\pm 60^\circ$ is observed even at 1 AU. The spread is slightly higher ($10 - 15^\circ$) since, due to geometrical reasons, the perpendicular transport in the former model is underestimated.

Nevertheless, particles still quickly fill a wide cone around CFL. For $\kappa_\perp/\kappa_\parallel = 1/50$ the particles are more closely confined to CFL, leading to higher intensities at $\varphi = 0^\circ$ and a slower azimuthal spread: significant filling of a cone of $\pm 40^\circ$ around CFL now requires five hours rather than one hour for 1 AU h^{-1} particles. All time scales are longer for slower and shorter for faster particles.

In particular at late times and strong perpendicular diffusion, combined with a large mean free path λ_r , the spatial gradients have the tendency to vanish.

The anisotropy-azimuth profiles show a decay towards the flanks, that can even reach negative values. We will discuss this feature in the following section.

7.1.3. Intensity-time and anisotropy-time profiles

The cross-field spread of particles leads to a continuous loss of particles from central field line. Consequently, during a SEP event the intensity decays faster than in Roelof's original model without perpendicular transport and also faster than in the former, azimuthal model by Lampa and Kallenrode (2009).

Figure 7.4 illustrates how the profiles of exact perpendicular transport and one-dimensional transport differ for otherwise identical parameter sets. Perpendicular transport also reveals a coherent peak at the CFL, but the intensity is lower and decays faster than in the case of one-dimensional transport. Moreover, the anisotropy is slightly higher. Thus, in order to cover the one-dimensional profile, a smaller mean free path λ_r and possibly a more gradual injection-time profile (with a long-lasting decay phase) would be required. The 2D model might help to overcome the magnitude problem of the quasi-linear theory (Bieber et al., 1994), where the mean free paths derived from theory always showed the tendency to be smaller than the fitted ones.

Early in the event, the anisotropy-time profiles occasionally show negative values for a time period of 30 minutes up to several hours once the bulk of particles has passed the

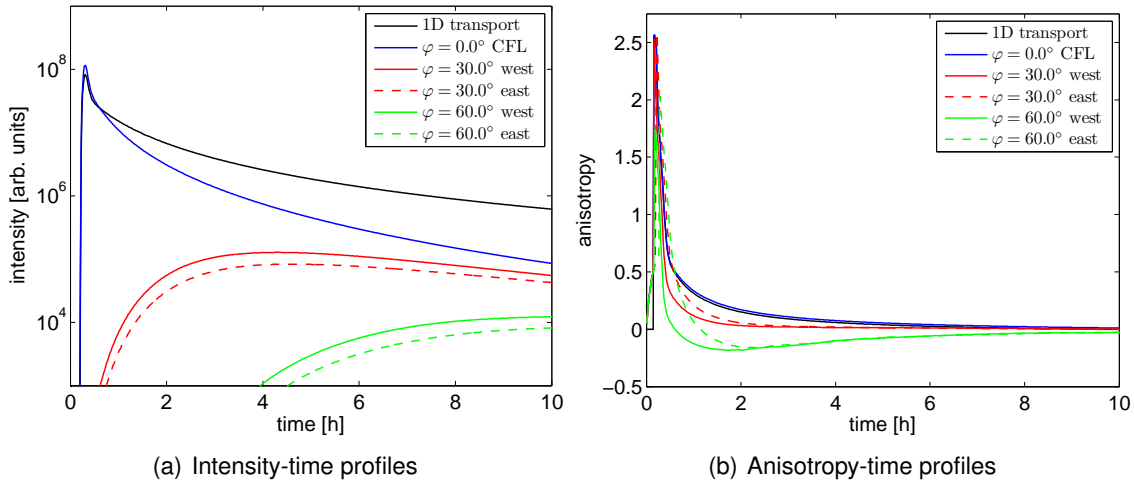


Figure 7.4.: Intensity- and anisotropy-time profiles at $r = 0.3$ AU, but different azimuthal distances. The default parameter (5.1) set without solar wind effects was chosen. The solid black curve denotes one-dimensional transport.

observer: This holds for field lines, that are separated by $\pm 60^\circ$ from the CFL (see panel (b) in Figure 7.4 or Figure 7.6) and beyond. All parameter combinations, that would lead to more cross-field further out than close to the Sun, could explain the numerical results. As it can be seen in the ecliptic plots (Section 7.1.1), the results can be reproduced for low particle speeds v , low ratios of $\kappa_\perp/\kappa_\parallel$ and high λ_r . Note that this effect should not be overestimated, since just small particle population contributes to the inward flux. The inward flux will probably vanish in the omnipresent background plasma in interplanetary space. It should be remarked, that another trigger for negative anisotropies are very strong, perpendicular displacements: The particles are gradually transported behind the Sun and back to the CFL. As a consequence, a second maximum in intensity occurs. The only scenario revealing these features within $r = 1$ AU, was for a mean free path of $\lambda_r = 6.3$ AU and $\kappa_\perp : \kappa_\parallel = 0.1$ for ~ 0.5 MeV electrons (see Figure A.11). Negative anisotropies can be seen for all field lines there. However, this scenario is rather unlikely and unreasonable because so far neither multi-spacecraft observations as e.g. (Palmer, 1982) nor theoretical results have given any indication for the mean free path to be $\lambda_r >> 1$ AU.

Besides negatives anisotropies there are also some azimuthal asymmetry that will be discussed below.

Figure 7.5 shows the omni-directional intensity-time profiles for an observer at radial distances of 0.3 AU on CFL and for azimuthal distances of 30° and 60° (panels “a” and “c”) as well as for $r = 1$ AU and the corresponding azimuthal distances (panels “b” and “d”). The ratio $\kappa_{\perp} - \kappa_{\parallel}$ was set to $\gamma = 1/10$ (panels “a” and “c”) and $1/50$ (panels “b” and “d”). Medium pitch-angle scattering conditions ($\lambda_r = 0.1$ AU) were assumed.

On the CFL, and compared to the solution without perpendicular transport, both weak and strong perpendicular transport almost reveal identical profiles with a coherent peak, but at a lower maximum intensity and with faster decaying intensities. This is the case for those particles, that have not yet undergone considerable pitch-angle scattering on their way to the observer – thus “spiking” profiles can be observed for < 100 MeV protons ($v \approx 3 \text{ AU h}^{-1}$) up to 0.3 AU and for proton energies above 100 MeV up to 1 AU . These

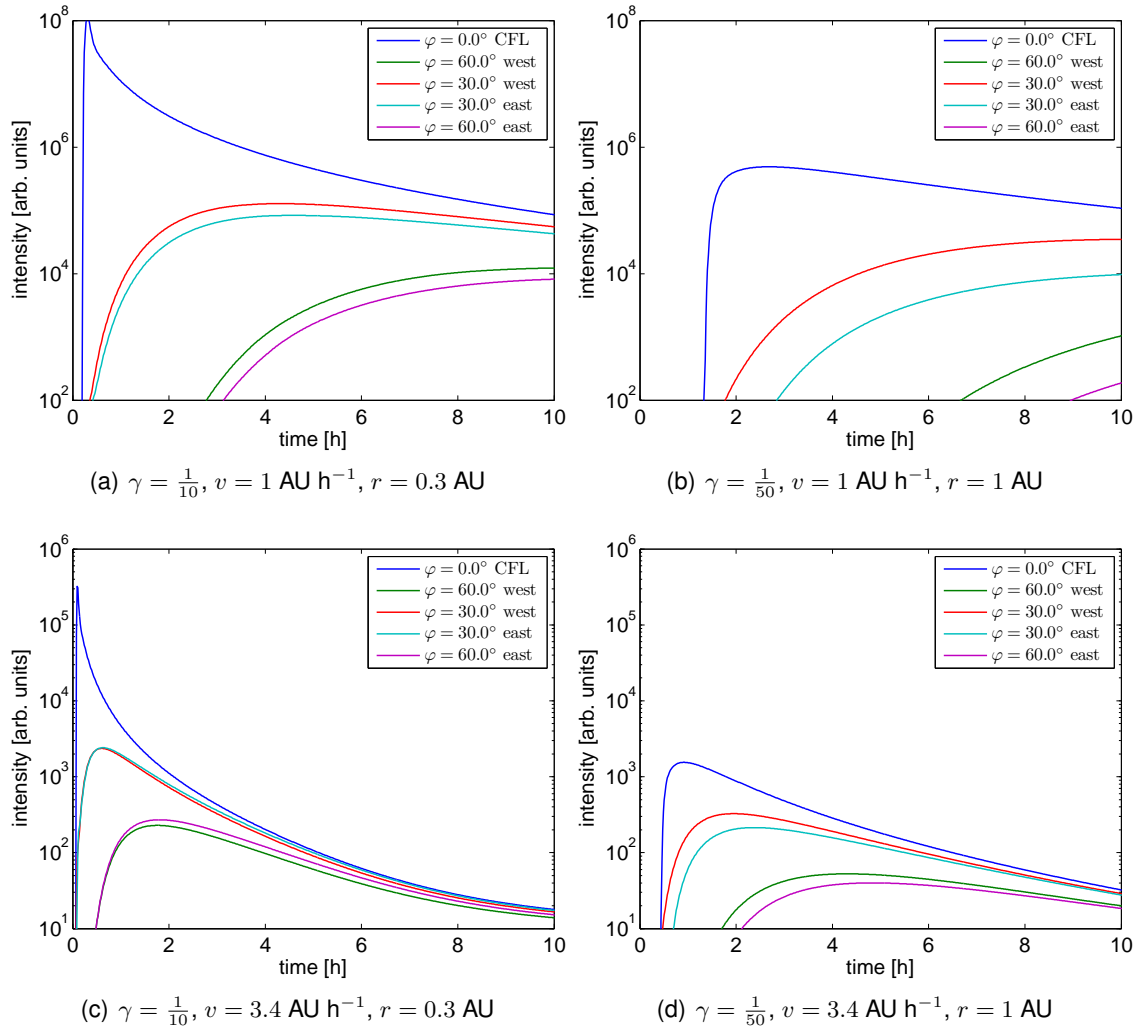


Figure 7.5.: Intensity-time profiles at $r = 0.3, 1 \text{ AU}$ and azimuthal distances $\varphi = 0^\circ, \pm 30^\circ, \pm 60^\circ$. For the first panel row, particle's speed is fixed at $v = 1 \text{ AU h}^{-1}$, for the second at $v = 3.4 \text{ AU h}^{-1}$. Medium pitch-angle scattering conditions ($\lambda_r = 0.1 \text{ AU}$) were assumed.

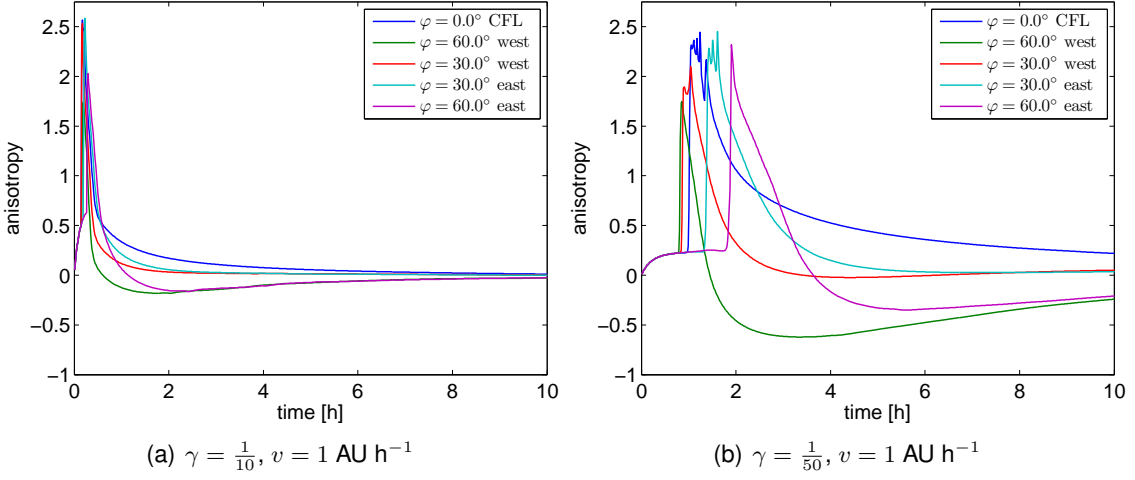


Figure 7.6.: Anisotropy-time profiles at $r = 0.3$ (left panel) and 1 AU (right panel) and azimuthal distances $\varphi = 0^\circ, \pm 30^\circ, \pm 60^\circ$. Parameters: $v = 1 \text{ AU h}^{-1}$, $\lambda_r = 0.1 \text{ AU}$, corresponding to intensity-time profiles in the top row of Figure 7.5.

spatial thresholds correlate with varying λ_r .

At $r = 0.3 \text{ AU}$, the plotted profiles beyond the CFL do not exhibit the coherent peak, instead profiles become more rounded. This is also true for larger radial distances, even on the CFL. Thus these profiles would not be described in terms of weak scattering but rather in terms of diffusive propagation. These differences compared to the CFL profile increase with increasing $\kappa_\perp/\kappa_\parallel$ as well as with increasing azimuthal and radial distance.

Again, the asymmetry in azimuth can be observed by comparing those profiles, where the observers are located symmetrically around the injection site (cf. panels (a) and (b) in Figure 7.5). The onset and the intensity maximum on the western flank occur earlier in the event, especially when the observer is located at $r = 1 \text{ AU}$. The temporal differences are even more evident in the anisotropy profiles. The delays stem from cross-field transport that provides radial displacements in particular beyond 0.3 AU . Despite these differences, all profiles at a fixed radial distance become continuously similar or even identical: Cross-field diffusion levels off all spatial gradients.

Figure 7.7 shows the intensity profiles on logarithmic scale for an observer at a radial distance of 0.3 AU (left panel) and 1.0 AU (right panel) with varying azimuthal distances of 0° (CFL), $\pm 30^\circ$ and $\pm 60^\circ$ for $\gamma = 0.1$. Compared to a scenario with a identical set of parameters, but $\gamma = 0.02$ (see Figure 7.8), one can state that in the presence of damped perpendicular diffusion, more particles are concentrated close to the CFL, thus in particular the profiles at $\varphi \pm 60^\circ$ show lower intensities. The time delays between the start of an impulsive flare and the time when the first arriving particles are detected, is considerably larger than in case of strong cross-field diffusion. The same holds for the maximum intensities. Qualitatively similar properties of cross-field transport are also found for low-energy particles, such as 10 MeV protons with speeds of about $v_p = 1 \text{ AU h}^{-1}$ (see e.g. again panels (a) and (b) in Figure 7.5). Obviously, the SEPs need additional time to perform diffusive cross-field transport.

If we fix the ratio of both diffusion coefficients at $\gamma = 0.1$ and decrease λ_r by the factor ten ($\lambda_r = 0.01$, strong pitch angle-scattering, see Figure 7.9), the decay phases last longer and the overall profiles become more rounded – compared to Figure 7.7. The latter

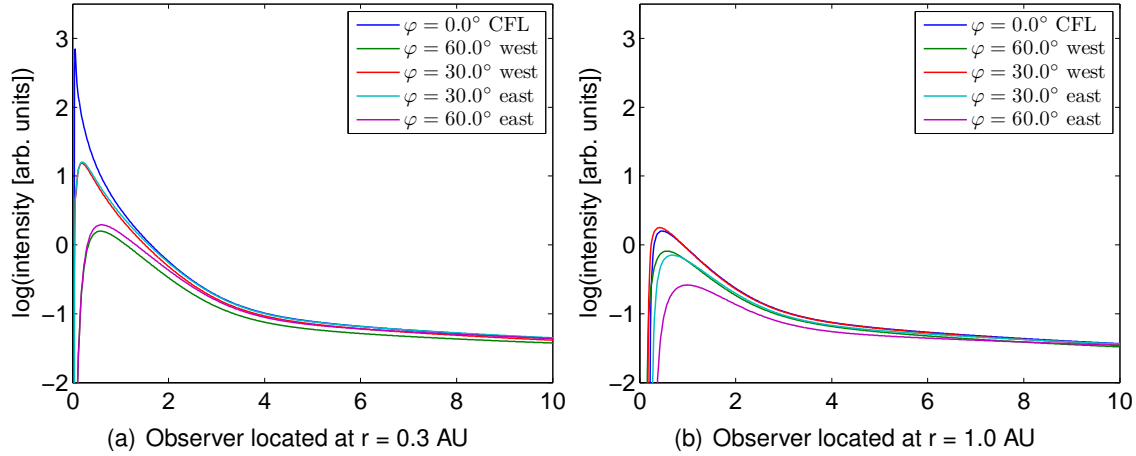


Figure 7.7.: Intensity-time profiles of 0.5 MeV electrons for different azimuthal distances from the CFL. The *standard scenario* with $\gamma = 0.1$ was chosen.

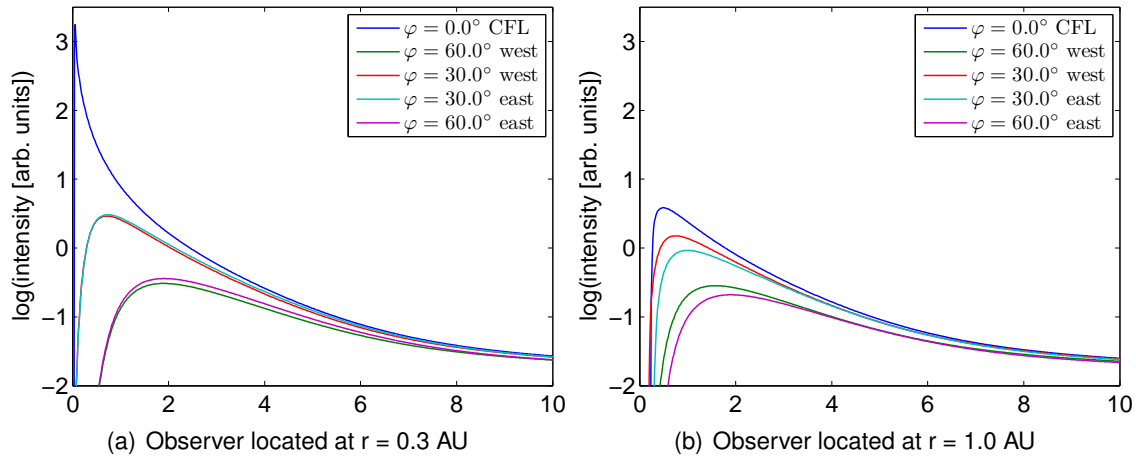


Figure 7.8.: Intensity-time profiles of 0.5 MeV electrons for different azimuthal distances from the CFL. The *standard scenario* was chosen – except for the following parameter: $\gamma = 0.02$.

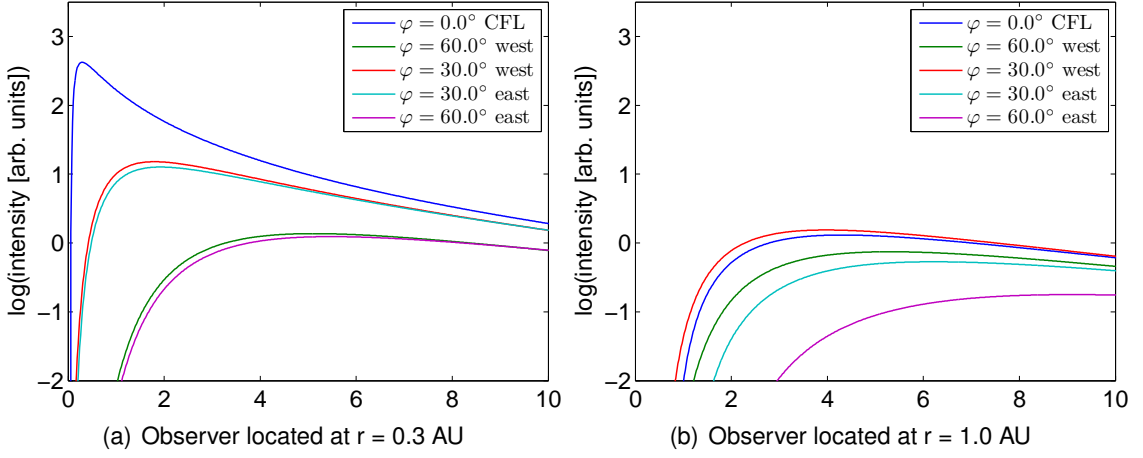


Figure 7.9.: Intensity-time profiles of 0.5 MeV electrons for different azimuthal distances from the CFL. The *standard scenario* with $\gamma = 0.1$ was chosen, except for $\lambda_r = 0.01$ AU (cf. Figure 7.7).

feature is qualitatively the same as in one-dimensional simulations. Enhanced pitch-angle scattering prevents particles from being quickly removed from the observer's site. The time delays mentioned above are even more pronounced than just an increase in γ would provide, since perpendicular losses, as expressed by the diffusion coefficient via

$$\kappa_{\perp} = \gamma \frac{1}{2} v \lambda_{\parallel} = \gamma \frac{1}{2} v \lambda_r \sec(\Psi)^2 \quad \text{, see (5.4), (5.7), and (5.8) ,}$$

cover just a fraction of the overall, from the observer's site removed particle number. Except for these differences, there are many effects that all plots have in common: Let us start with the profiles on CFL. The solution (blue lines) clearly shows the coherent peak early in the event, followed by a slow diffusive decay. Both strong and weak perpendicular transport (Figure 7.7 and 7.8) show almost identical profiles with a coherent peak, but at a lower maximum intensity and with faster decaying intensities than they were detected in the one-dimensional simulation. Since the anisotropies in both cases are almost the same, fits on these profiles neglecting perpendicular diffusion would require larger mean free paths. This could help to overcome the *magnitude problem* emerging from the quasi-linear theory, where the fitted λ s (on 1-D models) were always larger than the ones derived from theory. None of the profiles at $\pm 30^\circ$ or $\pm 60^\circ$ from CFL exhibits the coherent peak, instead profiles become more rounded. The general pattern of variations in intensity and anisotropy profiles is also observed for other choices of the radial dependence of $\kappa_{\perp}/\kappa_{\parallel}$. As a rule of thumb: a more efficient azimuthal transport leads to stronger variation of the profiles on the CFL because more particles are removed to larger azimuthal distances. Simultaneously, profiles at different azimuthal distances are more similar because azimuthal gradients almost vanish.

To sum up this subsection, it can be stated that perpendicular transport is affected efficiently by λ_r : Low values indicate strong pitch-angle scattering along the field lines, which prevents particles from leaving the region very close to the Sun. There, perpendicular diffusion is suppressed by the r^2 scaling. Different combinations of λ_r and γ lead to different propagation fronts – some of them are still confined to the CFL even hours after the injection start, others reveal SEP spreads of up to 180° , comparable to the ones expected

to be caused by traveling shock waves. The center of mass is still associated to the CFL, but particles with speed comparable to the solar wind speed show a slight shift in westward direction. The particle fluxes show that time scales beyond the CFL are higher, and that the profiles become smoother. The anisotropies tend to be reduced for large azimuthal distances, which can be explained by particles following open field lines, then being diffused in azimuth, and finally being back-scattered. Since these involved SEP numbers are very low, they can be attributed to the ambient background plasma. The concept of pitch-angle scattering in field-parallel direction, combined with spatial diffusion perpendicular to it, might help to overcome the *magnitude problem*.

7.2. Comparison to observations in the interplanetary space

In order to study the propagation of solar flare accelerated energetic particles within the ecliptic plane, at least two spacecraft have to be involved simultaneously. The current model has been timely developed according to start of the STEREO mission. Unfortunately, the current solar minimum lasts longer than expected, thus the 30 years old *Helios* data set was used for interpretations. The identical telescopes of *Helios 1* (H1) and *Helios 2* (H2) cover e.g. energies for electrons in the nominal range 0.3 – 0.8 MeV. Both spacecraft perform eccentric orbits around the Sun with distances between 0.3 AU and 0.98 AU and inclinations of up to $\pm 7^\circ$.

In a statistical approach, we will first check the plausibility and validity of the numerical model by comparing the maximum intensities of multi-spacecraft measurements with numerical results (Section 7.2.1). The scatter plots, as they will be presented here, collect numerous events with different propagation conditions, ranging from almost scatter-free (with free mean path of the order of 1 AU) to strongly diffusive. For most events, λ_{\parallel} is expected to be between 0.08 and 0.3 AU (Palmer consensus range, Palmer, 1982).

In Section 7.2.2, the focus is taken on four individual SEP events, where simultaneous fits of the omni-directional intensity- and anisotropy-profiles of first order (McCracken et al., 1967; Schulze et al., 1977) have been made. Fitting only the intensity profiles is not sufficient to interpret the observations: Even under very idealized, interplanetary conditions (no transient disturbances in the magnetic field for example), we can not infer from the given scenarios, that the SEP particles under consideration had to be impulsively released. Different combinations of injection and diffusion could reproduce the same profiles.

Emerging problems and new arising questions about the interplanetary scattering conditions will be discussed in Section 7.2.3.

7.2.1. Intensities varying with connection to the flare site

To illustrate typical observed angular variations in maximum intensity and in times to maximum, the left panel of Figure 7.10 shows maximum intensities from multiple events observed by both *Helios* spacecraft for ~ 0.5 MeV electrons. Each pair of data points, connected by a straight line respectively, is associated with an individual event. The slope of these lines of intensity therefore represents an exponential decay rate depending on angular distance. All intensities are normalized to 1 at the flare site ($\varphi = 0^\circ$). In this context, it should be noted that the exponential dependency is not necessarily implied. Triangles mark those events in which both spacecraft are connected to the flare sector (region of a unipolar magnetic field the flare is located in). Circles mark events in which

only one spacecraft is connected to the flare sector, and squares indicate that both satellites are related to positions outside of the flare sector. We focus on open symbols since we describe the maximum intensities for impulsive events, although there seems to be no indication for systematic differences compared to gradual events (Kallenrode, 1993a).

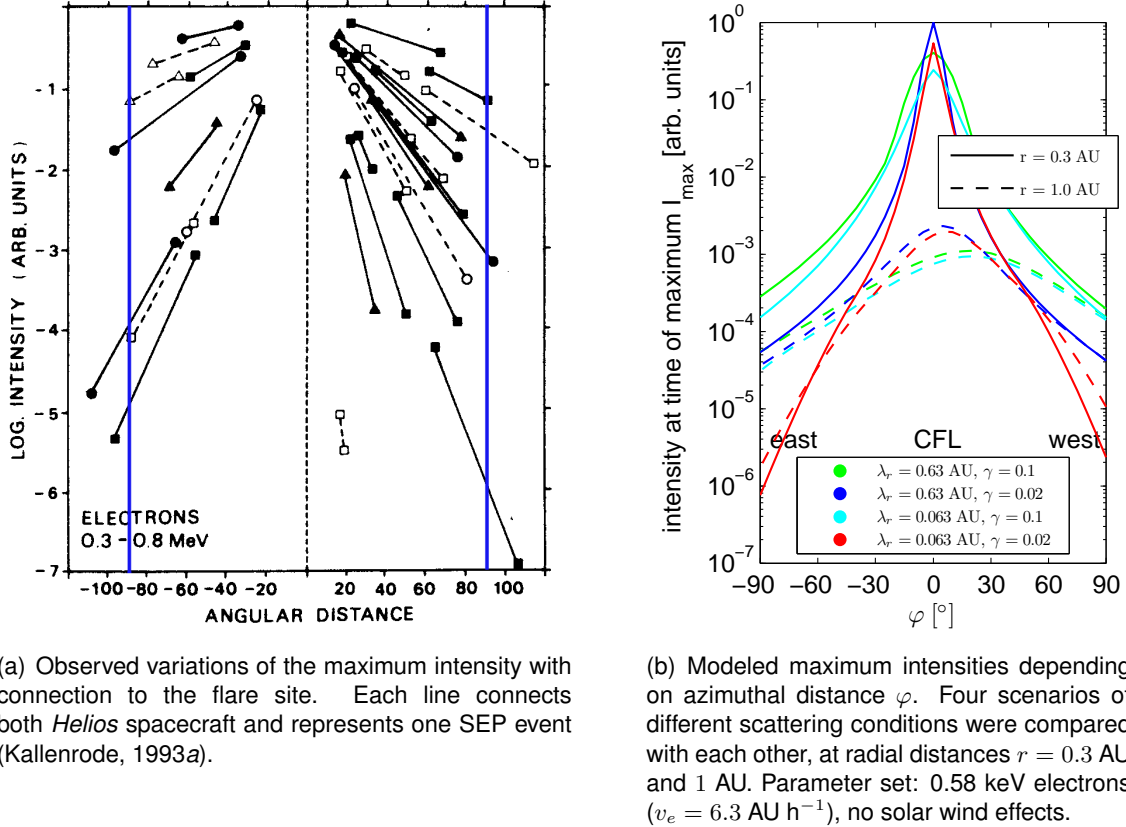


Figure 7.10.: Maximum intensities depending on the connection to the flare site: Angular distance in the right panel coincide with the azimuthal distance because the modeled flare site lies within the ecliptic plane.

The differences in amplitude between the two *Helios* spacecraft are essentially governed by the angular distance, with large variation in the e-folding angle between the events. The mean e-folding angle of 13° – corresponding to a one-order magnitude drop every 29° – fits well to those results obtained from numerical simulations: The maximum intensities of 0.58 keV electrons in right panel of Figure 7.10 show similar drop rates, as seen in particular for the stronger version of perpendicular transport with $\gamma = 0.1$. e-folding angles between a few and up to 20° are also comparable to the ones reported in other multi-spacecraft studies (Kallenrode, 1996; Lario et al., 2006; Wibberenz and Cane, 2006). Note that in contrast to the left panel, intensities are scaled according to normalization factor of the largest maximum intensity (which is for $r = 0.3$ AU, $\lambda_r = 0.63$ AU, $\gamma = 0.01$). We have chosen $r = 0.3$ (solid lines) AU and $r = 1$ AU (dashed lines) for the output locations, since these values approximately correspond to the minimal and maximal solar distances of the *Helios* spacecraft. Thus, we are able to compare to numerical data curves that are expected to be within the domain bordered by solid curves as upper boundary and the dashed curves as lower boundary.

Figure 7.11 illustrates the times to maximum t_{max} for ~ 0.5 MeV electrons versus angular

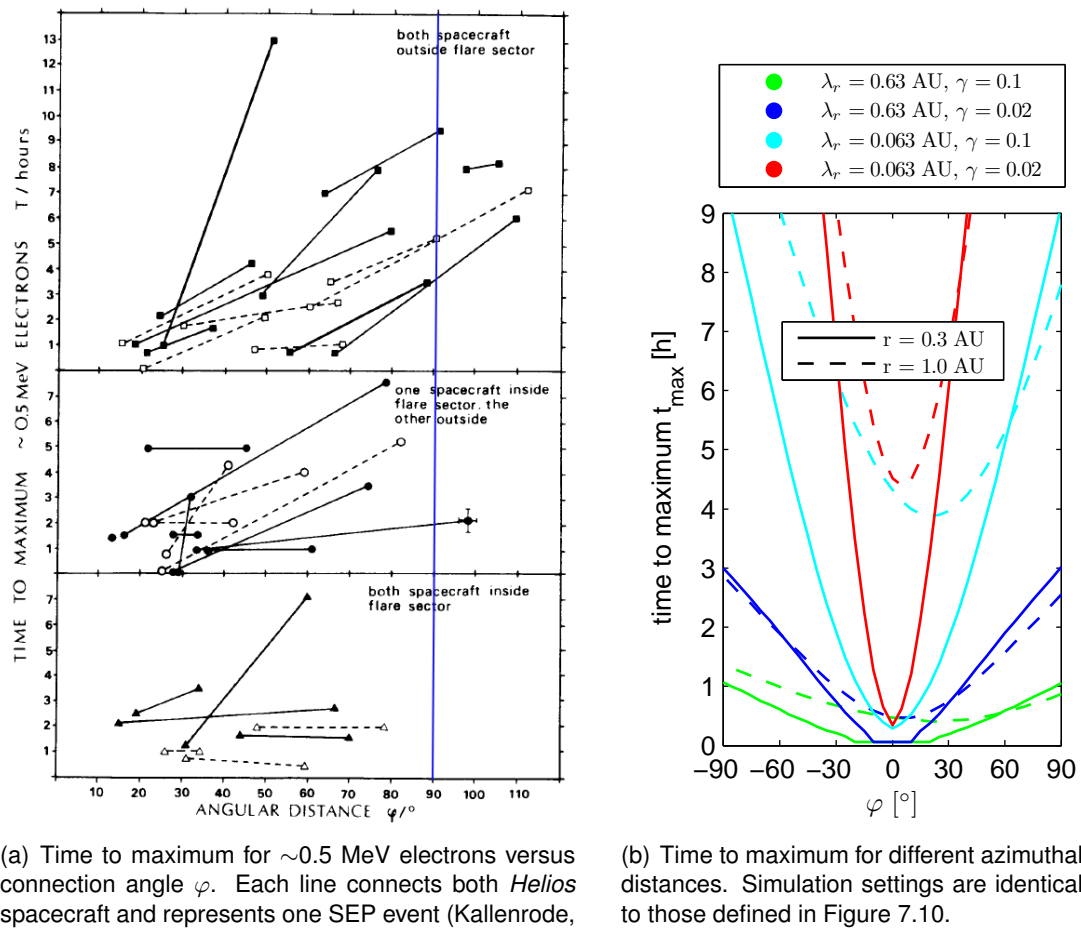
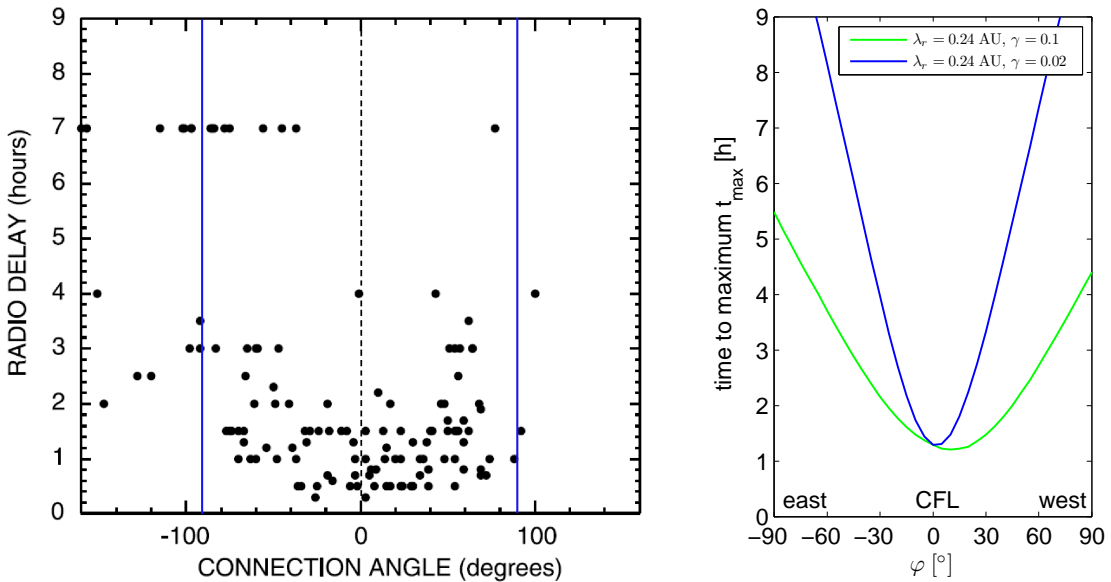


Figure 7.11.: Variation of time to maximum with the connection angle (more details cf. text).

distance. As it has already been done in Figure 7.10, the focus is taken on the same set of events using the same plotting procedure (except for the semi-logarithmic and normalized presentation). The times are separated into three possible categories indicating whether the two spacecraft are connected to the flare sector or not (see description in the upper left of each panel in Figure 7.11). Again, there is a clear indication that the time to maximum increases with increasing angular distance. The slopes become even steeper if one or both spacecraft are separated from the flare site by a neutral line (cf. Section 2.2). Of course, sector boundaries can not be modeled by the current model, but nevertheless there is no problem in finding an adequate parameter set to fit these times to maximum (see right panel in Figure 7.11). Whereas the two-point measurements do not allow any analytical description of the azimuthal variations, all scenarios reveal profiles as described by a parabolic function. Obviously, particles need additional time to travel from a punctual source to the observer, while particles with good magnetic connection to the source propagate in field-parallel direction without any cross-field displacements.



(a) Radio burst delays, shown as a function of the magnetic connection of IMP 8 to the associated flare for >20 MeV proton events. IMP-8 is located at $r = 1$ AU within the Earth's orbit (Cane and Erickson, 2003).

(b) Modeled time to maximum for different azimuthal distances. Parameter set: 30 keV electrons (corresponding to 56 MeV protons with $v = c/3 \approx 2.4 \text{ AU h}^{-1}$), δ -injection in space and time.

Figure 7.12.: Intensity delays varying with connection angle φ .

Concerning the angular variations of *time-to-maximum intensity* of SEP events, Cane and Erickson (2003) also showed that there must be a kind of lateral transport in flaring SEP events. SEP events are preceded by type III radio bursts, caused by flaring 2 – 50 keV electrons that excite Langmuir waves on the background plasma (see e.g. Baumjohann and Treumann, 1986 or Parks, 1991) which themselves emit electromagnetic waves, whose frequencies depend on the local plasma density. The emission drifts to lower ad lower frequencies as the electrons propagate outward with roughly one third of the speed of light. When the electrons reach the spacecraft, no lower emission frequencies are observed. For >20 MeV proton events, Cane and Erickson measured the time from when the burst started at the Sun to when it reached the local plasma frequency at

$r \approx 1$ AU. They plotted these delay times of different events versus the connection angle – the angle between the flare longitude and the footpoint of the field line on which the spacecraft is located (connection angle in the left panel of Figure 7.12).

The right panel shows the modeled azimuthal variation of the time to maximum at $r = 1$ AU for two different scenarios. Both scenarios under consideration simulate identical scattering conditions along the field ($\lambda_r = 0.24$ AU), but they differ in the strength of field-perpendicular diffusive flux. The green line illustrates times for $\lambda_{\perp} = 0.1 \cdot \lambda_{\parallel} \cdot r^2$, whereas the blue line is associated with low perpendicular diffusion (the scaling factor (5.8) is $\gamma = 1/50$ instead). Note that t_{max} has lower values at the western site since cross-field transport additionally shifts particles radially outward. The profiles are still symmetric within $r = 0.3$ AU (not shown in a figure) and resemble those of the simplified, azimuthal model by Lampa and Kallenrode (2009). The times are insignificantly overestimated since the modeled flare site is located at radial distance $r = 0.1$ AU. Flare acceleration is expected to take place in the lower corona at $r \approx 0.01$ AU (within 3 solar radii). Due to numerical reasons, the inner boundary at the CFL was set to $r = 0.1$ (see Section 7.1). For $\gamma = 1/10$ the time of maximum is acquired within less than ten hours for azimuthal distances of 40° around CFL; it increases to values of a day and more for azimuthal distances beyond 30° for $\gamma = 1/50$. For connection angles of $\pm 90^\circ$ delay times up to 4 hours are evident, thus the particles needed additional time to be transported in lateral direction. Using the 2D model, a four hour delay could be reproduced for medium pitch-angle scattering conditions ($\lambda_r = 0.24$ AU), combined with enhanced perpendicular diffusion ($\gamma = 1/10$). Thus, cross-field transport could account for what was formerly known as “open cone of propagation” (Lin, 1970) or fast propagation region (van Hollebeke et al., 1975) and what Cane and Erickson (2003) require for the interpretation of the type III radio bursts.

7.2.2. Fitting both intensity- and anisotropy profiles

As seen in the previous Section 7.2.1, the simulation results can qualitatively good describe the SEP intensities at the time of maximum, and the time of the maximum with respect to the azimuthal distance between the source and the observer. We also have to validate whether pitch-angle diffusion still works in two dimensions. Can the observed distributions confirm that the model assumptions are properly chosen? We therefore looked at four SEP events of relativistic electrons, which have been chosen with respect to the impulsive character. There is no evidence for an interplanetary shock in neither the particle nor the plasma data. We have tried to fit the satellite data with the numerical model as presented here. We always add some isotropic background plasma in order to consider the omnipresent background in interplanetary space and to get a reasonable fit to the pre-flare phase. It should be noted that the values differ by at least one order of magnitude from the maximum intensities. The pitch-angle distribution will be significantly changed only if the additional flux lies in the same order of magnitude. This is the case for the pre-flare phase (the time before any H_{α} s have been detected) as well as for the phase of the first arriving particles at the observer’s site. The amount of added nucleon flux as well as the other fitting values are summarized in Table 7.3 at the end of this section.

Figure 7.13 gives an overview about the first three events. Arrows mark the start of the flare, as it is interpreted in terms of the H_{α} emissions. The spatial configuration of the *Helios* satellites at the measuring time is shown in the insert of each panel in Figure 7.13. The details of the flare and the spacecraft position relative to the flare are given in the table below Figure 7.13 with the column “Fpt” indicating the footpoint of

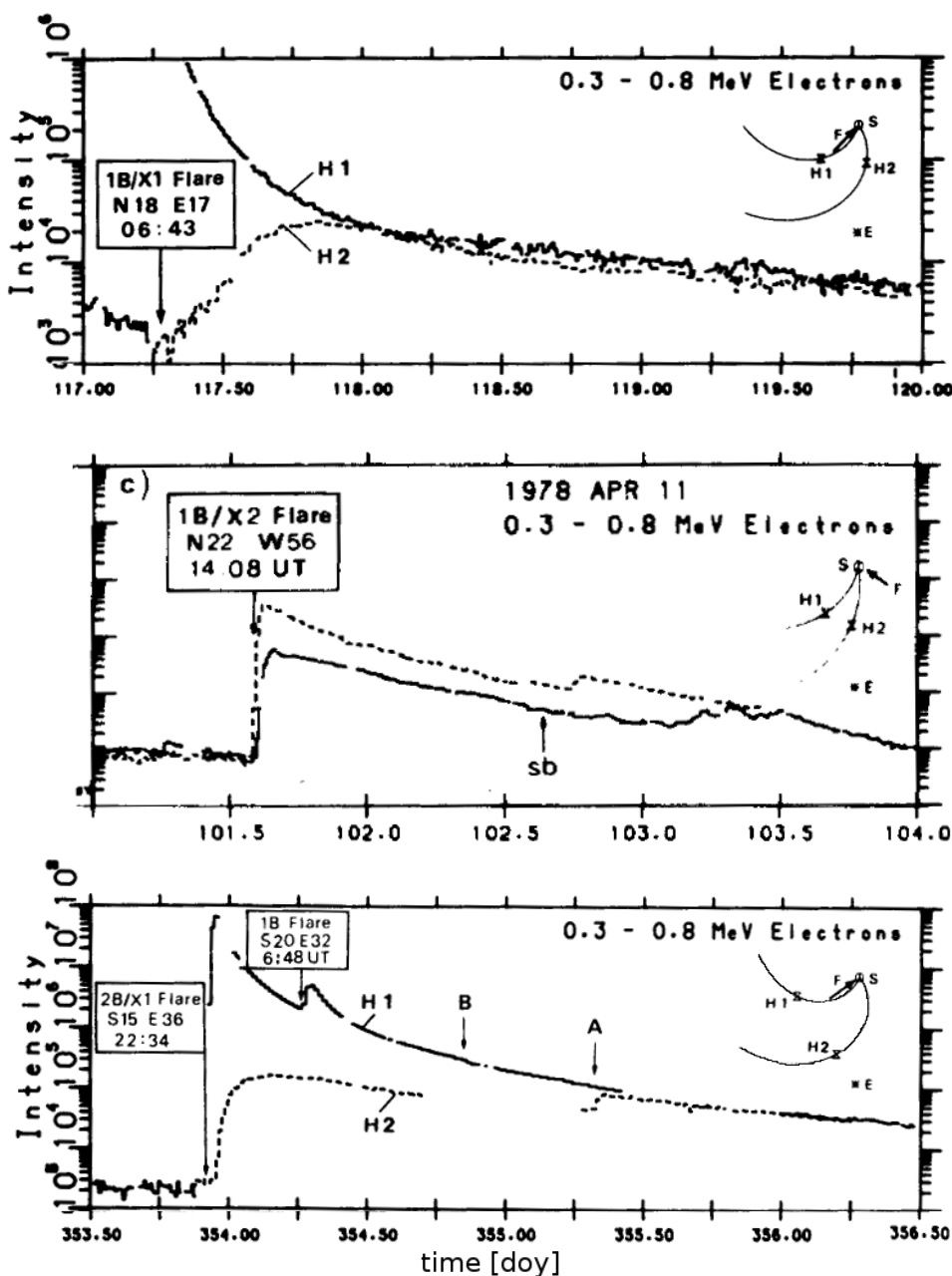


Figure 7.13.: Intensities of ~ 0.5 MeV electrons obtained from *Helios 1* (solid lines) and *Helios 2* (dotted lines) for April 27, 1979; April 11, 1978; and Dec. 19, 1979 (from top to bottom). Intensities are given in $[m^2 \text{ sr s MeV}]^{-1}$ (Kallenrode, 1993a).

Date	Flare	H α	Helios 1	Helios 2					
doy	Location	UT	r/AU	Fpt	$\varphi/^\circ$	r/AU	Fpt	$\varphi/^\circ$	
April 27, 1979	118	N18 E17	0652	0.47	E16	+1	0.36	W30	+47
April 11, 1978	101	N22 W56	1410	0.47	E09	-65	0.49	W22	-34
Dec. 19, 1979	254	S15 E36	2217	0.62	E23	+13	0.75	W46	+82

Table 7.1.: Three particle events observed by both HELIOS spacecraft.

the observer's magnetic field line as calculated from the measured solar wind speed (Kallenrode, 1993a), and φ being the connection angle between the flare site and the footprint. In all three cases, the variation between the spacecraft reflect the combined effects of radial and azimuthal variations, however, the events have been selected such that the radial influences are not very strong.

Like other numerical simulations before, we are confined to the plane of the ecliptic. However, most of the flare sites are located beyond that layer. Consequently, angular distances between the flare site and the observer's magnetic footprint were projected into the observer's plane of $H1$ and $H2$. Table 7.1 therefore lists the "azimuthal distances" φ , which are slightly smaller than the original angular distances.

In all three events, particle intensities at the spacecraft with the smaller angular separation from the flare site (which doubles as the CFL in our model) are much higher and show an earlier and more pronounced maximum as we have already stated in the previous Subsection 7.2.1.

SEP event on April 27, 1979

Concerning the first event on April 27, 1979, it has already been illustrated by Kallenrode (1993a), that both spacecraft are connected magnetically to the flare sector on the solar surface, with one spacecraft almost on the CFL and the other at an azimuthal distance of about 47° . Typical differences in the intensity profiles, that have been found in the previous section, can be re-identified: later and smaller maximum intensities for the spacecraft at the larger angular/ azimuthal distance (dashed curve in the top panel of Figure 7.13), although $H2$ is located slightly closer to the Sun than $H1$. Moreover, in the late phase of the event, intensities become similar, leading to "invariant spectra" (see also Section 3.2). The same features can be also found in the other two events.

Figure 7.14 shows the simulation results as denoted by solid lines. We added some isotropic background plasma by a constant flow of 3000 nucleons per (m^2 s sr MeV). Unfortunately, in the time period around the flare t_{H_α} no particles were detected at $H1$ due to instrumental errors. Thus, we were forced to make a crude estimate of the injection function just on the basis of the onset time t_{H_α} and of the observations of the remote $H2$ satellite.

The event is fitted by a scenario neglecting solar wind effects (see Figure 7.14). The particles' speed was set to $v = 6.3 \text{ AU h}^{-1}$, the ratio of perpendicular-to-parallel diffusion is $\gamma = 0.02$. Since the anisotropies at $H1$ are still non-zero 10 hours after the flare, we chose a slightly gradual injection following the Reid-Axford profile (5.2) with parameters $(t_{diff}, t_{loss}) = (0.5 \text{ h}, 3 \text{ h})$ at the (projected) location of the flare (solid black curve). We assume medium scattering conditions with a mean free path of $\lambda_r = 0.15 \text{ AU}$.

The particle distribution on $H2$ is almost isotropic as a result of both medium pitch-angle scattering in field-parallel direction as well as diffusion perpendicular to it. The fitted curves are in good agreement with the observations, trends and time scales are adequately represented. The fluctuating anisotropy around zero comes from the fact, that there are not enough particles to make statistically relevant averages.

It should be noted that, in general, absolute differences between model and observation data for the remote spacecraft are overstated visually due to the logarithmic scaling.

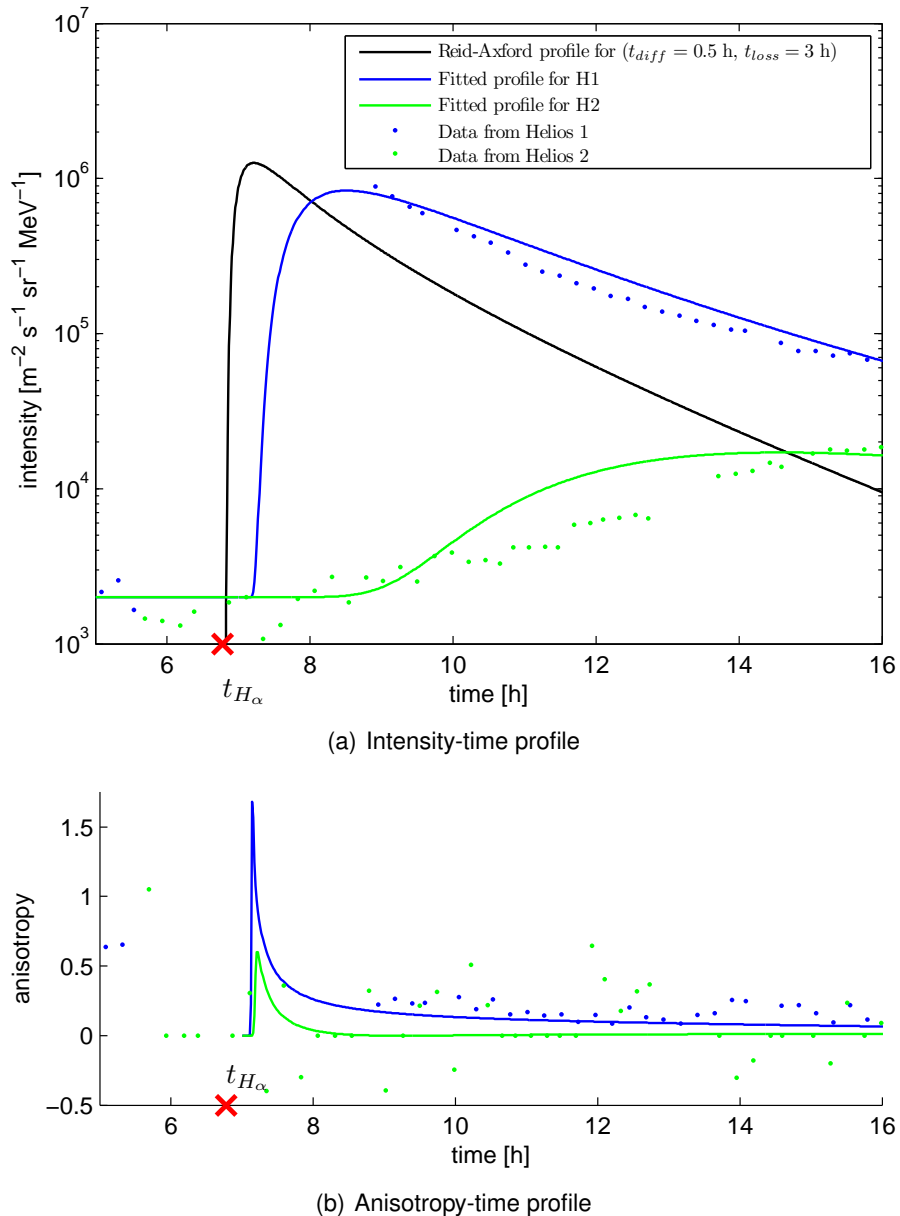


Figure 7.14.: Intensities and anisotropies (lower panel) of 0.5 MeV electrons obtained from *Helios 1* (blue dots) and *Helios 2* (green dots) on April 27, 1979. The corresponding solid curves are the fitted profiles according to the following scenario parameters (for details see text): $\lambda_r = 0.15 \text{ AU}$, $\gamma = 0.02$; and an injection temporally following a Reid-Axford profile with parameters $(t_{\text{diff}}, t_{\text{loss}}) = (0.5 \text{ h}, 3 \text{ h})$.

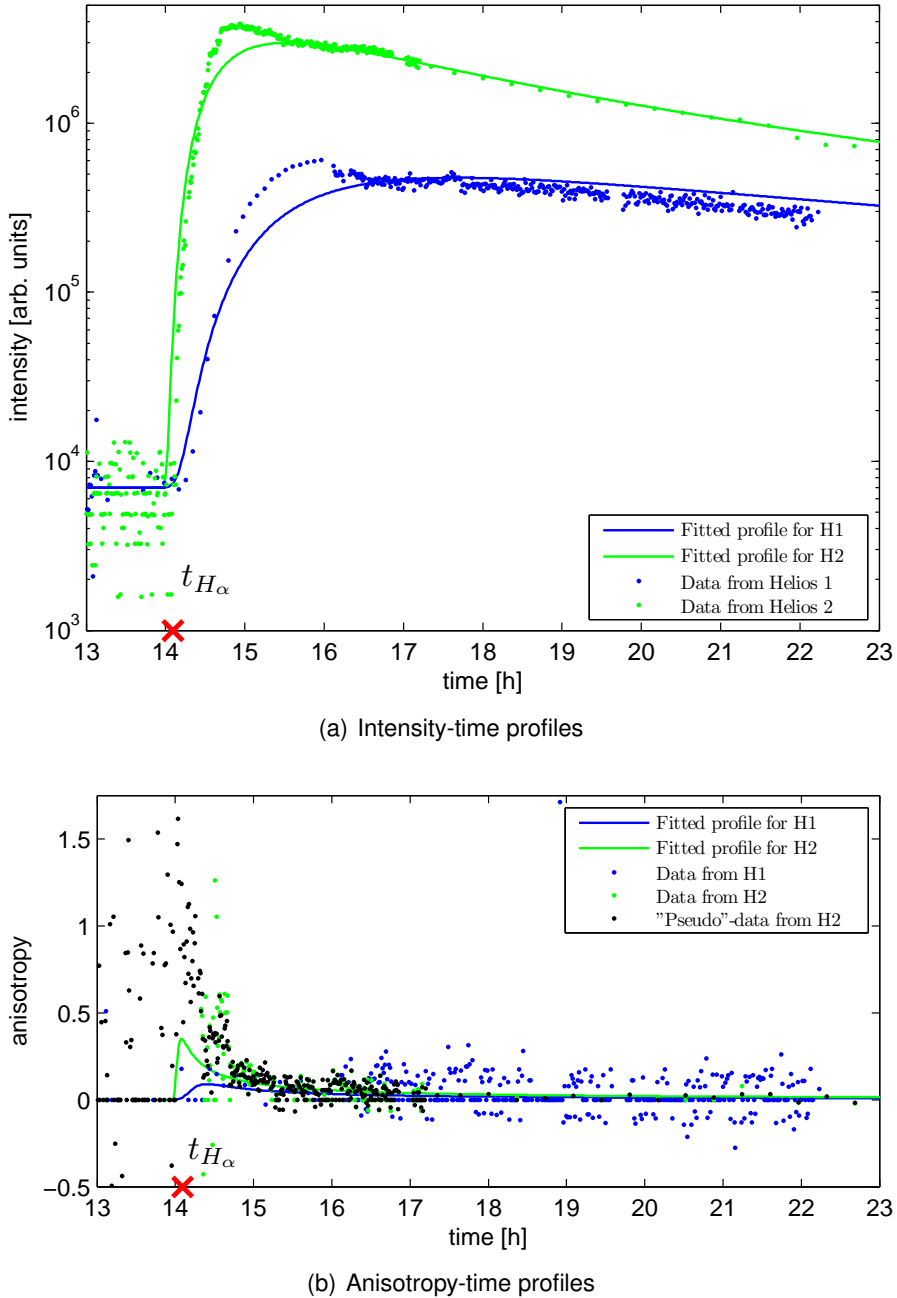


Figure 7.15.: Intensity-time and anisotropy-time profiles on April 11, 1978. Data is taken from the widely separated spacecraft *Helios 1* and *Helios 2*. Fitted profiles are indicated by solid lines. Simulation settings: no solar wind effects, $\lambda_r = 0.3$ AU (for 0.5 MeV electrons, $v = 6.3$ AU h $^{-1}$), $\gamma = 1/10$, δ -injection in time, but spatially extended ($\varphi = \pm 50^\circ$). For details, see text.

SEP event on April 11, 1978

The SEP event in April 11, 1978, is of different nature, although it qualitatively shows the same features as those of other multi-spacecraft observations – such as an earlier onset of the first arriving particles and a more pronounced maximum for a detector being magnetically closer to the flare site. Both *Helios* satellites had almost identical radial distances to the Sun, but were separated by 31° in azimuth (see azimuthal distances in Table 7.1). Kallenrode (1993a) already stated, that the intensities are slightly smaller at the spacecraft with the larger angular distance (as expected from other multi-spacecraft observations). However, the electron profiles on both satellites look very similar. Even after one and half days after the flare start, the differences in intensities between both spacecraft are still significant. The profiles tend to become similar on much larger time scales than in the other two '79 events (see Figure 7.13), where invariant spectra (similar intensities) have already been observed about 12 hours after the start of the flare. On April 11th, the intensities still differ by a factor of ten. Locally confined injections can not reproduce the curves, since even small cross-field diffusion with $\gamma = 0.01$ smears out such strong spatial gradients at ~ 0.5 AU within hours. Neither the pronounced maximum intensities nor the almost identical decay slopes could be simulated. We assume, that both spacecraft must have been located closer to source particles than to the original emission site of the H _{α} s. The SEPs are expected to be transported azimuthally by coronal processes, possibly triggered by reconnection. A larger extent of SEPs can also be explained by the fact, that the flare is located 28° in the north of the ecliptic plane (with the *Helios* satellites being inside this plane). Probably, a formerly peak-like distribution expanded to considerable azimuthal extent until it finally reaches the ecliptic plane.

As a consequence, we assume particles to be uniformly injected inside $\varphi = \pm 50^\circ$ – implying that only *Helios 2* is connected to the source region. In principle, such an extent of a particle source could be interpreted as a hydrodynamic shock wave. But as it is said earlier, a shock can be ruled out because there are no indications neither in the plasma nor the electromagnetic radiation data. Since the anisotropy drops very fast to zero, the diffusion must be very strong: Beeck and Wibberenz (1986) suggested $\lambda_r \sim 0.03$ AU for *Helios 2*. We choose $\lambda_r = 0.06$ AU inside of the injection cone, and a marginally smaller value of $\lambda_r = 0.05$ AU beyond. The abruptly rising intensities suggest an impulsive injection: the source term was set to a δ -function in time. As seen in Figure 7.15, we can prevent particles from being distributed equally in azimuth by reducing perpendicular diffusion by $\gamma = 0.03$ and by increasing the intensity gradient in azimuth by the use of a spatially extended source.

The delay might be explained in terms of stronger scattering (and weak cross-field diffusion) inside the flux tube of *Helios 1*. The assumption of varying scattering conditions in azimuth is supported by the vanishing anisotropies on *Helios 1*.

Note that because of the lack of magnetic field data, anisotropies on *H2* are missing around t_{H_α} . "Pseudo"-anisotropies have been introduced which are computed according to the average field of an Archimedean spiral. These "pseudo"-values should be handled with care or even seriously questioned since they do not consider the variability of the field. If possible, they should be compared with observed anisotropies shortly before and after the time period of missing field data. In particular for this event, the lack of reliable data is complicated by the fact that the intensities of both the electrons and the protons (not shown in a figure) suggest a compressed magnetic field at the time of the first arriving particles: In a more dense field, the gyro radii (2.2) of SEPs decreases, leading to smaller flux tubes and an enhanced particle flux. This might be the reason why

the observed maximum intensities look more pronounced than the modeled ones.

SEP event on December 19, 1979

The SEP event on December 19, 1979, shows the same features as those of the other multi-spacecraft observations. The *Helios* satellites had very similar radial distances to the Sun, but were widely separated (69 degrees in azimuth, see Figure 7.1). In contrast to the first two events, that have been discussed before, both spacecraft are separated by a neutral line (cf. Section 2.2). Source surface maps of equi-potentials of the magnetic field strength with different polarities indicate that only *H1* is connected to the magnetic field sector, in which the flare occurred. The impact of the neutral line on the intensities, especially their extensions down to the photospheric and chromospheric field, may play an important role in particle's propagation: They can escape along regions of opposite polarity very fast by additional drift effects (Roelof, 1974; Roelof and Krimigis, 1973). In addition, Roelof (1973) showed that intensities and their temporal behavior are different in different polarity cells. Kallenrode (1993a) already stated that the time to maximum outside the flare sector increase clearly with angular distance, as seen e.g. in the left panel of Figure 7.11. Gold et al. (1973) interpreted these observations in terms of "fast propagation regions".

And indeed, the assumption of different propagation regions is supported by the fact, that the intensities on December 19, are clearly different in at least one order of magnitude until they abruptly rise and become similar once *H2* encounters the sector boundary about one and half days after the flare (see lower panel in Figure 7.13). The change is marked by arrow "A" in the lower panel of Figure 7.13. Concerning the protons, Reinhard (1975) even suggested that *H2* has encountered a different particle population. This thesis could also be supported by the first order anisotropies, indicated by the 1-minute resolved dots in the lower panel of Figure 7.16. Unfortunately, due to the lack of magnetic field data on *H2*, we again used the "pseudo"-anisotropies (black dots). The profile indicate that the time scales on both spacecraft are very different. On *Helios 1* anisotropy drops very fast to zero, indicating that scattering must be significantly strong. On the other hand, the intensity on *H2* remains stationary over hours with high anisotropies. The *H1* data can be interpreted as a nearly scatter-free and gradual event.

In order to consider these different propagation regions, we introduce a wide cone of 45° around the injection site, with $\lambda_r = 0.3$ AU and an extended injection of 30° temporally following the Reid-Axford profile with parameters $(t_{diff}, t_{loss}) = (0.1 \text{ h}, 0.1 \text{ h})$. Beyond $\varphi \pm 45^\circ$ λ_r is assumed to be three times larger. $\frac{\kappa_\perp}{\kappa_\parallel}(r)$ is scaled by $\gamma = 0.01$. The variation of λ_r in azimuth gives better numerical results, but they are not yet satisfying: While the profiles for *H1* (magnetically connected to the flare sector) properly coincide, the computed anisotropies for *H2* are too small and the intensities are slightly higher. The observation can only be reproduced if one additionally assumes SEPs to be emitted by a different source, which is located magnetically closer to the satellite and which is described by a gradual injection function.

SEP event on May 28, 1980

As an example of leveling gradients, Figure 7.18 shows ~ 0.5 MeV electrons of the SEP event on May 28, 1980, between 15 and 24 UT (universal time). The energetic particles were detected by two spacecraft at different radial distances but closely aligned. *Helios 1* was located at $r = 0.3$ AU, while the *IMP-8* satellite (Interplanetary Monitoring Platform,

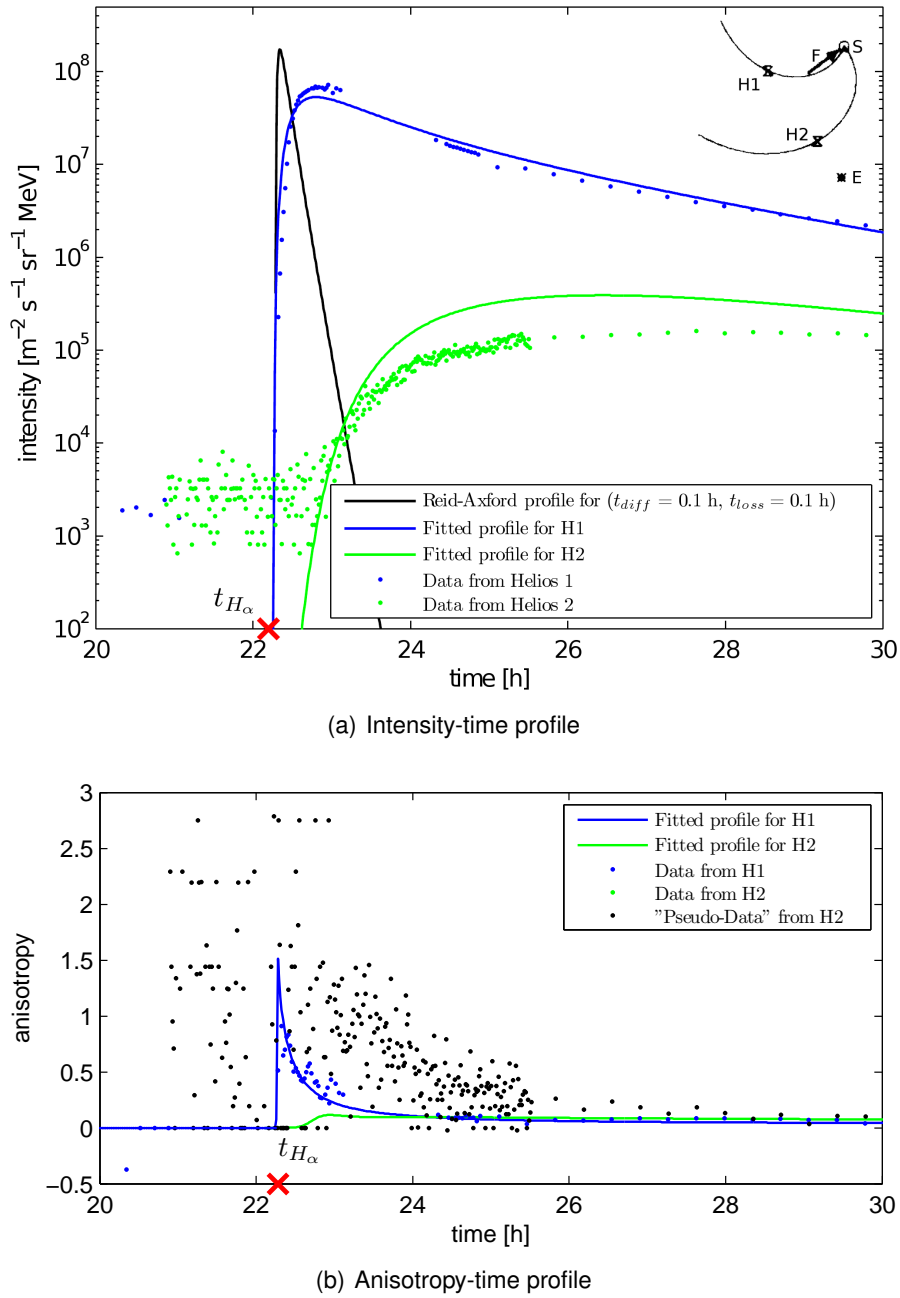


Figure 7.16.: Intensities and anisotropies (lower panel) of 0.5 MeV electrons obtained from *Helios 1* (blue markers) and *Helios 2* (green markers) on December 19, 1979. The corresponding solid curves are the fitted profiles according to the following scenario parameters (for details see text): $\lambda_r = 0.3$ (0.9) AU, $\gamma = 0.01$; and an extended injection of 30° temporally following the Reid-Axford profile with parameters $(t_{diff}, t_{loss}) = (0.1 \text{ h}, 0.1 \text{ h})$.

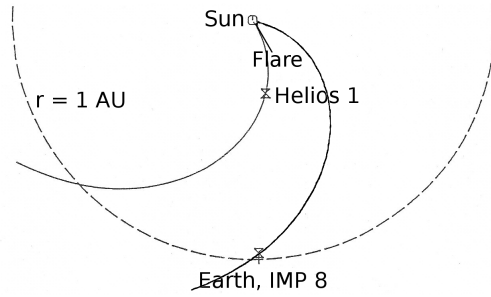


Figure 7.17.: Spatial configuration/ topology of the *Helios 1*, *IMP-8* satellites, and the flare site(s) on May 28, 1980.

IMP 8 MERGE 20sec Resolution Data, 2010) follows a nearly circular orbit around the Earth at a radius of about 35 Earth radii r_E . It spends most of its measuring time outside the magnetosphere within the solar wind ($\sim 60\%$), and thus it has access to energetic particles in interplanetary space. *Helios 1* was magnetically connected to the flare sites near $W40^\circ$ (spatial configuration shown in Figure 7.17), whereas the footpoint of the *IMP-8*-field line lies at about $W105^\circ$. These values were inferred from the measured solar wind speed of approximately 240 km s^{-1} . The corresponding field lines can be traced back to the upper corona by the method of backmapping (Nolte and Roelof, 1973). The particle count numbers of both spacecraft cannot be directly compared. First the data is given in different units: *IMP-8* detects particles with dynamic ranges of 1 to $1E+06$ particles per ($\text{cm}^2 \text{ s sr}$) (*IMP 8 MERGE 20sec Resolution Data, 2010*), whereas the raw data of the first *Helios* satellite is given in units of particles per ($\text{m}^2 \text{ s sr MeV}$) (see e.g. Kallenrode, 1993a). Secondly, the *Helios* energy band for the electrons is much smaller: 0.3 - 0.8 MeV electrons (fraction of the *IMP 8* energy band with 0.22 and 2.5 MeV), with speeds from 5.6 AU h^{-1} up to 6.6 AU h^{-1} . As a consequence, we additionally have to rescale the data. SEP measurements haven given enough evidence for an energy spectrum that follows a power law $f(E, \delta) \propto E^{-\delta}$, with exponent δ ranging between 2 and 4. By integrating over the energy domain, the center of the distribution within the energy domain [0.3 MeV, 0.8 MeV] can be determined by:

$$\bar{E}(\delta) = \left(\int_{0.3}^{0.8} E f(E, \delta) dE \right) / \left(\int_{0.3}^{0.8} f(E, \delta) dE \right).$$

Comparing data sets of different spacecraft including their individual energy bands, the scaling factor is given by:

$$\zeta(\delta) = \left(\int_{0.22}^{2.5} f(E, \delta) dE \right) / \left(\int_{0.3}^{0.8} f(E, \delta) dE \right).$$

Finally, the *Helios* data set can be compared with the *IMP 8* data set via

$$\text{intensity}_{\text{IMP } 8} = \zeta(\delta = 2) \cdot 1E-04 \cdot \bar{E}(\delta = 2) \cdot \text{intensity}_{\text{H1}},$$

with \bar{E} being the particle's energy, averaged over the corresponding energy bin.

The final, scaled result can be seen in Figure 7.18: At 0.3 AU, four different events can be distinguished. All of them are enriched in ${}^3\text{He}$ with ${}^3\text{He}/{}^4\text{He}$ ratios ranging between

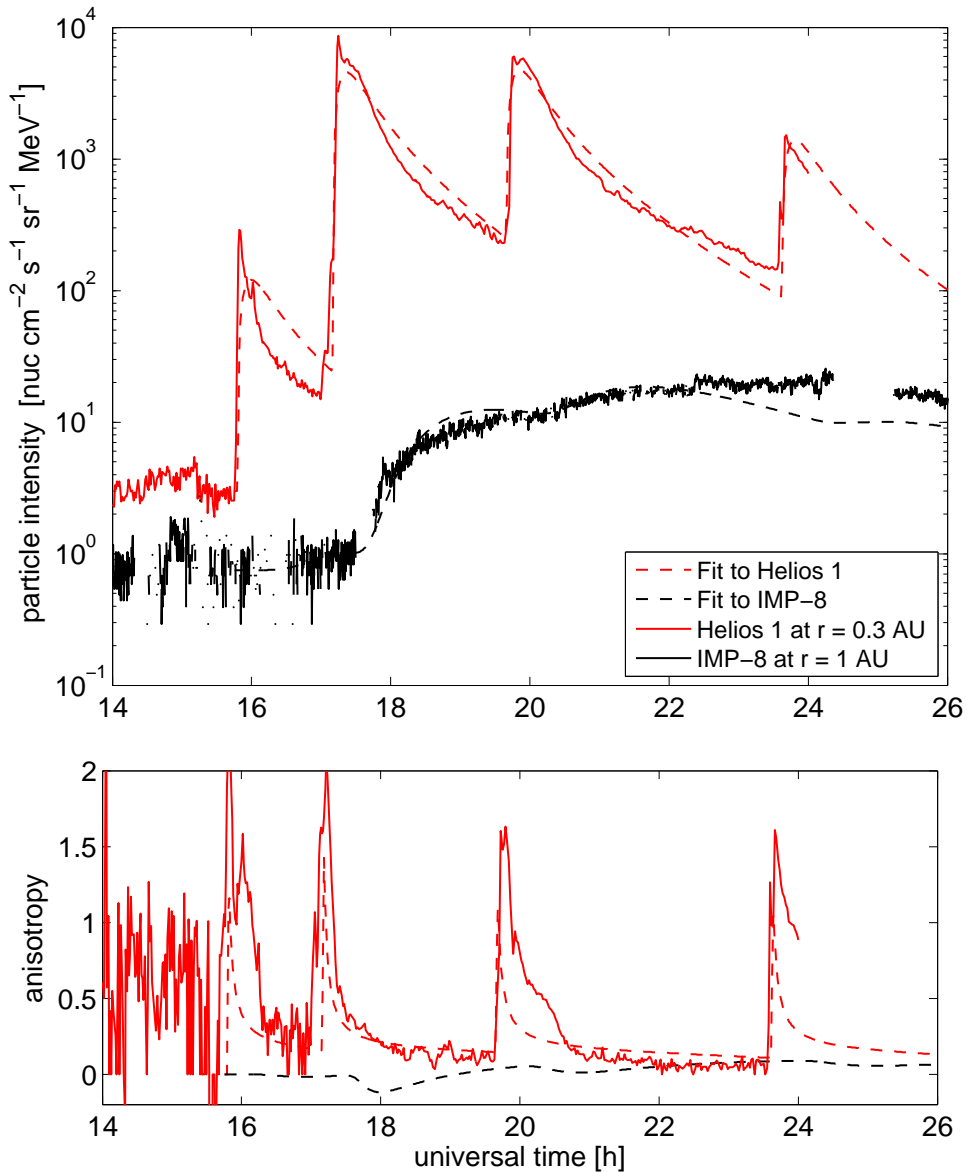


Figure 7.18.: Intensity-time (upper panel) and anisotropy-time profiles (lower panel) on May 28, 1980. Data is obtained from *Helios 1* and *IMP-8* for a sequence of events when the two spacecraft were closely aligned but at different radial distances (0.3 indicated by red lines, and 1 AU indicated by black lines). Fitted profiles indicated by dashed lines. Simulation settings: no solar wind effects, $\lambda_r = 0.3$ AU (for 0.5 MeV electrons with $v = 5.7$ AU h $^{-1}$), $\gamma = 1/50$, injection parameters: ($t_c = 0.01$ h, $t_L = 1.5$ h).

t_{H_α} [h]	1553	1705	1924	2342
r [AU]	0.31	0.31	0.31	0.31
fpt	N00 W37	N00 W41	N00 W38	N00 W43
flare location	S24 W28	S16 W35	S18 W33	N17 W39
φ [°]	9	6	5	4

Table 7.2.: Flare and satellite locations (Kallenrode, 1989) for the May 28, 1980, event. “fpt” indicates the footprint of the observer’s field line, φ denotes the azimuthal distance between the footprint “fpt” and the flare location.

0.1 and 0.2. They are proton poor, and the time scales of the measured soft X-ray and the H_{α} s suggest that energetic particles have been released during an impulsive flare. This is supported by the lack of evidence for a passing shock, that would reveal abrupt changes in plasma density, temperature and magnetic field strength for example. The only, negligible exception from this is a weak shock from an earlier source passing *Helios 1* at 1830 UT (see also p. 89 in Kallenrode, 1989).

The electromagnetic radiation as well as the intensity and omni-directional anisotropies reveal similar time profiles. Since, additionally, the flare sites are almost identical, they support the assumption of the *homology* of the events. In these cases, only part of the energy stored in the magnetic field is released, and the overall field topology is retained (for details see e.g. Gaizauskas, 1983).

A different picture of SEP propagation is drawn at 1 AU from the *IMP-8* satellite: Pitch-angle scattering is stronger than the focusing effect. While at a radial distance of 0.3 AU, the propagation fronts of individual flares are clearly separated from each other, they merge to a single front with larger time and spatial scales at 1 AU. Cane (2005) also made the same comparison and made identical conclusions. This kind of leveling and smoothing of spatial intensity gradients is exactly what numerical simulations already revealed, if the observer is not connected to the flare side anymore. Unfortunately, *IMP-8* gives no information about the angular distributions to support the numerical computed anisotropies. But apart from that: What was formerly explained by a decreasing λ_r with increasing radial distance according to slab turbulence (see e.g. Cane, 2005; Wibberenz and Cane, 2006), can also be interpreted by additional cross-field losses without any radial variability of pitch-angle diffusion.

The interpretations and fits to the *Helios 1* data set by Kallenrode (1989) showed that pitch-angle scattering at $r = 0.3$ AU must be moderate because the anisotropy is high at the time of intensity maximum, and because the anisotropy decays slowly and is still significantly above zero three hours after the H_{α} onsets. Fitting these events by the use of the one-dimensional model of focused transport by Roelof (1969a) gave free mean paths of $\lambda_r = 0.15 \pm 0.05$ AU (Kallenrode, 1989, p. 94). Scenarios of the current two-dimensional model with $\lambda_r \sim 0.3$ AU, an injection onto the CFL following a Reid-Axford profile (5.2) with time parameters $(t_{loss}, t_{diff}) = (0.01 \text{ h}, 1.5 \text{ h})$ and $\kappa_{\perp}-\kappa_{\parallel}$ -ratio being scaled with $\gamma = 1/50$ can qualitatively reproduce the intensity and omni-directional anisotropy profiles (dashed lines) as well. The latter free mean path is even twice as large as the one fitted by the 1D model, although cross-field diffusion leads to a faster removal of particles from the observer's site.

Four separate δ injections were assumed as it is suggested by the measured intensities at 0.3 AU (see also Kallenrode and Wibberenz, 1991b). A comparison of the maximum anisotropies shows an adequate fit, but the numerical values subsequently drop too fast. A more detailed look at the observed anisotropies reveals some subsequent peak-like flares, whose strength (number of emitted particles) consists of just a fraction of the first flare. These additional particles could explain the long-lasting, gradually falling anisotropies. This issue can be best seen for the first of the four, strong flares, where a double-peak structure is evident. It is even more evident in electromagnetic emissions, in particular in X-ray, microwave and radio data (Kallenrode and Wibberenz, 1991b).

SEP simulations at $r = 1$ AU show that the electron anisotropy varies slowly, ranging between 0 and ~ 0.2 . It can even drop below zero. Since only small particle fractions are attributed to that time period, this does not lead to a considerable Sun inward flux. Most of the time, the anisotropies are at 0.1 or 0.2, because "fresh" particles are supplied by the series of homologous events. Combined with moderate pitch-angle scattering, *IMP-8*

detects slowly varying intensities: The particle flux keeps steady over some hours. There is no evidence of separate injections anymore. The numerical results also show that the intensity gradients have almost completely been smoothed.

Date	v [AU h $^{-1}$]	v_{sw} [km s $^{-1}$]	λ_r [AU]			γ	injection		background plasma nuc/(m 2 s sr MeV)
			Helios 1	Helios 2	$\Delta\Phi$ [°]		$q_2(t)$	$q_1(s_{\perp,0})$	
April 27, 1979	6.3	400	0.15	0.15	δ	$\frac{1}{50}$	(0.5 h, 3.0 h)	δ	3000
April 11, 1979	6.3	460	0.05	0.06	45	$\frac{3}{100}$	δ	H 50°	7000
Dec 19, 1978	6.3	400	0.3	0.9	45	$\frac{1}{100}$	(0.1 h, 0.1 h)	H 30°	1875
May 28, 1980	5.7	240	0.3	0.3	δ	$\frac{1}{50}$	(0.01 h, 1.5 h)	δ	3 (H1), 0.75 (H2)

Table 7.3.: Fitting parameters for four ~ 0.5 MeV electron events (for details see text).

To sum up the fits to the four impulsive electron events, Table 7.3 gives an overview about the fitting parameters. $\Delta\Phi$ denotes the azimuthal extent of a certain propagation region around the central field line. The corresponding λ_r is found in the fourth or fifth column, depending on which spacecraft has a better magnetic connection to the injection site. The ambient medium beyond $\pm\Delta\Phi$ is characterized by the second free mean path (related to the other spacecraft). The spatial extent of the source is described by $q_1(s_{\perp,0})$: H 50° e.g. denotes a uniform filling of the field line footpoints within $\varphi \pm 50^\circ$.

Note that due to the lack of sufficient multi-spacecraft data, general conclusions are difficult. But it is evident that SEPs are significantly spread in azimuth on their way to the observer – even close to the Sun at $r = 0.3$ AU. Locally confined injections lead to much higher intensities with a more pronounced maximum if the spacecraft has a smaller separation from the flare site. The leveling of gradients can hide multiple consecutive events. At least for the events as studied here, the occurrence of sector boundaries significantly affects field-perpendicular propagation; they might even separate regions of different propagation properties and different sources. The assumption of λ_r to be constant, κ_\perp to be scaled with r^2 , and a scaling factor γ ranging between 0.01 and 0.1 has been found reasonable in order to get satisfying fits to the multi-spacecraft observations.

7.2.3. Diffusion as the big leveler vs. sudden flux dropouts

The main objection against diffusive interplanetary transport arises from the abrupt flux dropouts of flare accelerated particles, as e.g. observed from the ACE spacecraft at $r \sim 1$ AU. It was impossible to model turbulent or abrupt changes in the intensity profiles with the assumption of λ_r to be constant in azimuth. On the other hand, Mazur et al. (2000) found spatial structures in scales of an hour or less (see e.g. Figure 7.19). Transient disturbances such as shocks and magnetic clouds/coronal mass ejections or corotating interaction regions (CIRs), caused by the solar wind stream structure, may be possible triggers. Indeed, some abrupt decreases of electron fluxes could be explained as signatures of the disconnection of one end of the cloud's magnetic field from the solar corona (Larson et al., 1997). But the observed dropouts occur in such large quantities that magnetic clouds can not explain them solely. Not all dropouts were accompanied by a change in angle of the IMF.

Mazur et al. emphasize that according to the plasma data, other acceleration mechanisms have to be excluded. Dropouts are said to occur simultaneously at all energies, thus the detected particles are not supposed to be accelerated at traveling shocks. This is why Mazur et al. suggested that the spacecraft has changed the position relatively to the

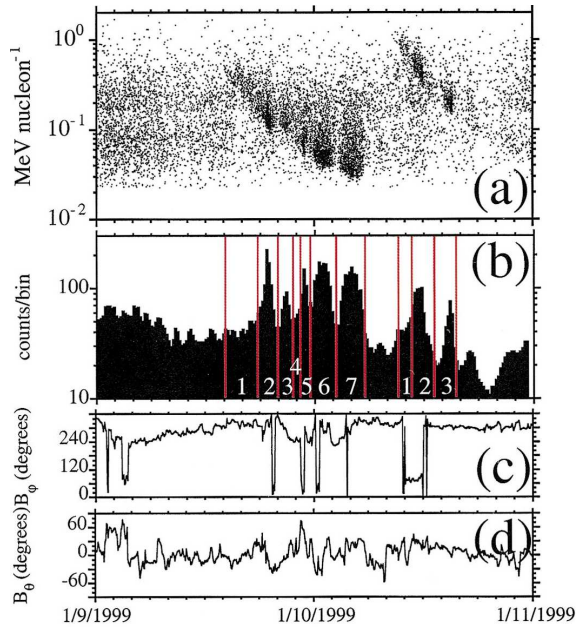


Figure 7.19.: (a) Energy of H-Fe ions (in units of MeV nucleon⁻¹) vs. arrival time at 1 AU for the impulsive flare events of 1999 January 9. (b) H-Fe counts vs. time in smoothed, ~ 14 minute bins. (c) Interplanetary magnetic field angle in the geocentric solar ecliptic (GSE) x-y plane. (d) Interplanetary magnetic field angle normal to the GSE x-y plane. Source: (Mazur et al., 2000)

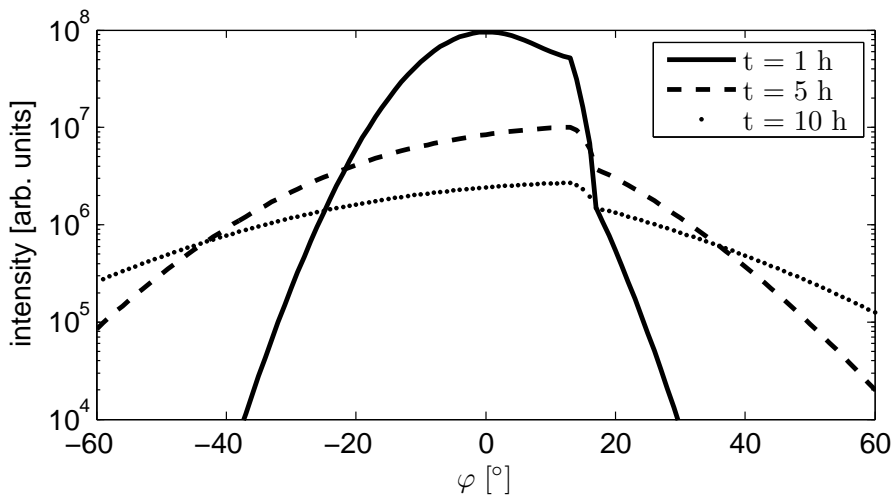


Figure 7.20.: Azimuthal variations of intensity for times $t = 1, 5, 10$ h. The observer is located at $r = 0.3$ AU. The standard scenario (5.1) was chosen, but λ_r has been reduced to $\lambda_r = 0.01$ AU within a cone of 5° in extent around $\varphi = 15^\circ$. Note that the former azimuthal model has been used (see Section 3.2.2).

current flux tube and might be subsequently shifted into a neighboring flux tube, where SEPs are underrepresented. The current model does not allow to change the observer's location at a certain field line within a time-series of intensities or anisotropies. But even if spacecraft motion is involved, the profiles will probably be continuous, since the spatial diffusion term leads to smooth profiles both in time and space. But small changes of the mean free path λ_r with varying azimuthal distance could lead to significant gradients in the transition region of different scattering conditions. We have "produced" such a scenario in terms of the SEP event on December 19, 1979 (Section 7.2.2). Another example is illustrated in Figure 7.20, where a 5° wide cone of enhanced pitch-angle scattering (and consequently reduced perpendicular diffusion) has been introduced west of the CFL. 10 MeV protons, being injected impulsively onto the CFL, are prevented from freely passing the cone – leading to a considerable intensity gradient of one order of magnitude or more over just a few degrees in azimuth.

Note that the scattering conditions are not only determined by local phenomena, but also by frozen-in, "fossil" structures that originate from the solar surface. According to Mazur et al., a possible scenario would be that the footpoint of a flux tube might become mixed with the footpoint of another flux tube which is not magnetically connected to an active region (and consequently still empty). The results would be observed days later by a remote spacecraft at $r = 1$ AU in terms of flux dropouts. Note that field-line mixing was already applied with respect to the field-line-random-walk (FLRW) to estimate the perpendicular diffusion strength with varying radial distance.

We assume that the scattering conditions could vary from one flux tube to another. In literature, this was already discussed in terms of propagation channels (Borovsky, 2008). Consequently, the first approach would be to change the magnitude of λ_r (and/ or κ_\perp). Another approach would be that the flare will not necessarily be a punctual source function, but an extended one with acceleration efficiencies that might spatially vary. Lampa and Kallenrode (2009) already showed that an extended, uniform source would not affect the SEP profiles considerably, "perpendicular diffusion efficiently masks the spatial extend of the injection region". But will this be still true, when initial particles distributions differ from one flux tube to another? Besides the flux tube varying scattering conditions, this could be a possible explanation of the dropouts in the electron fluxes.

8. Conclusions and Outlook

The main goal of this study was to introduce a numerical model that simulates the propagation of solar-flare-accelerated, energetic particles in the inner heliosphere, including solar wind effects. Besides the numerical challenges, we checked whether the azimuthal variations of maximum intensity and time to maximum intensity are of reasonable order to explain the observations. Simultaneous fits to both intensity- and anisotropy-time profiles were made in order to estimate the amount of scattering in μ and the strength of perpendicular diffusion.

Inter-model comparisons and comparison of scenarios with differing spatial resolutions in the validation Chapter 6 have shown, that modeling on varying step sizes lead to good, comparable results. Differences result from inaccuracies in the finite difference terms. Azimuthal resolutions of $\Delta\varphi = 5^\circ$ and below are required for possible data fits to take into account the spatially varying propagation properties. The advantage of increasing step sizes along the magnetic field spiral is found in a better representation of the focusing term. Moreover, even if the outer boundary of the domain is set far beyond a radial distance of 3 AU, this leads to no considerable increase in memory allocation.

The deficiency can be seen in the requirement of continuous, undisturbed transport coefficients. This might complicate the simulation of small-scale turbulence, which is immanent in the perpendicular diffusion coefficient. But we already showed that at least the discretization for diffusive term is identical to the one that has been deduced from *Galerkin finite element method (FEM)*, which uses the alternative integral formulation of the PDE. Discontinuities, suggested by flux dropouts observed in low-energetic protons, or traveling shocks, could be probably better integrated. Anyway, fluctuating quantities, which are smaller than the resolution of numerical grid, are leveled off.

Concerning the comparison to the observations, we can state that perpendicular diffusion leads to efficient particle spread in azimuth with azimuthal variations in time to maximum and intensity at time of maximum strongly depending on the assumption about the ratio $\lambda_\perp/\lambda_\parallel$, its radial and energy dependence.

The assumption of a ratio $\lambda_\perp/\lambda_\parallel$ between 1/50 and 1/10 at $r = 1$ AU, and scaled with r^2 , leads to realistic values for the azimuthal variation of time to maximum and intensity at time of maximum.

Secondly, in particular if azimuthal gradients can be maintained (as suggested by the observations), differences between intensity time profiles on CFL and at some azimuthal distance can be quite pronounced; in particular the CFL profile might be interpreted in terms of weak scattering while the other profiles might be interpreted in terms of diffusive propagation.

Third, the consideration of perpendicular transport in fitting observed intensity and anisotropy time profiles therefore would lead to different combinations of injection and mean free path with larger values of λ on the CFL and smaller values of λ at larger azimuthal distances. Compared to one-dimensional discretized solution, the free mean path λ_r can be chosen lower. Thus, this might help to overcome the *magnitude problem* (see for instance Bieber et al., 1994) in the quasi-linear theory.

The inclusion of cross-field transport leads to azimuthal variations of time to maximum

and intensity at time of maximum comparable with the ones observed in different kinds of particle events.

This has an interesting consequence for our interpretation of acceleration and injection mechanisms: the current paradigm is based on the assumption that intensity time profiles reflect the injection from flare and shock onto that field line. Thus it has been assumed that the shock's acceleration efficiency can be inferred from these profiles and that the shock is a stronger accelerator close to its nose than at its flanks. Efficient cross field transport will also be effective in the case of the shock being a propagating source of particles. Thus profiles at a certain position will be different from the ones expected for negligible cross-field transport. Consequently our interpretation of the observations will be modified – to what extent will only become visible when the shock is included in this model. In addition, cross-field diffusion also might enhance the shock's acceleration efficiency by reducing the injection problem. Cross-field diffusion also could account for the fact that large impulsive events without contribution of a shock can be observed up to $\pm 60^\circ$ around the flare site without invoking coronal shocks or other mechanisms for coronal transport.

It should be noted that for any given $\lambda_{||}/\lambda_{\perp}$ the present version of the model underestimates the influence of cross-field transport, since perpendicular transport in the meridional direction is not considered at all. But a numerical model in a three-dimensional heliosphere has been introduced by Schwan (2009). It is based on the same code, although solar wind effects have not yet been considered.

In addition, the presence of magnetic clouds as large-scale magnetic structures also affects particle propagation as does the presence of structures on smaller scales.

Fits to observed multi-spacecraft time-profiles could be adequately reproduced, but some events as well as the presence of flux dropouts suggest, that scattering conditions might differ from one flux tube to another.

In sum, this approach suggests that a more detailed understanding of SEP profiles from point sources as well as moving sources requires the consideration of this formerly neglected effect. Consequently, it is worth developing the model presented here further in such that both the 3D model and this model including solar wind effect are combined to a single model, that covers the entire inner heliosphere as well as the main propagation processes.

In addition, upcoming multi-spacecraft measurements (e.g. by STEREO) will provide a new set of particle observations at different positions to test the model in more detail in the near future.

A. Appendix

A.1. Physical quantities and acronyms

Symbol	Dimension	Description
α	rad	pitch angle between the particle's velocity and the outward tangent to the average magnetic field
AU	149.6×10^9 m	astronomical unit (distance Sun – Earth)
c	$3 \cdot 10^8$ m s $^{-1}$	speed of light
$c_{l+1/2}$		approximated diffusion coefficient at position $z_{l+1/2}$
CFL		Courant-Friedrich-Levi, or central field line (SEPs are injected symmetrically around the footpoint of the CFL)
$\Delta\varphi$	°	azimuthal distance between two neighboring field lines
ϵ_0	$\frac{1}{\mu_0 c^2}$	electric field constant
$\epsilon_l^{(n)}$		truncation error of a finite difference (FD) scheme with respect to point (t_n, x_l)
FD		finite difference
IMF		interplanetary magnetic field
$\kappa_\mu(r, \mu)$	h $^{-1}$	pitch-angle diffusion coefficient (PADC)
$\kappa_{\parallel}(r)$	AU 2 h $^{-1}$	field-parallel diffusion coefficient
$\kappa_{\perp}(s_{\parallel}, s_{\perp}, \mu)$	AU 2 h $^{-1}$	field-perpendicular diffusion coefficient
λ_{\parallel}	AU	mean free path (mfp) along the field line
mfp		mean free path
μ	$\cos \alpha$	cosine of the pitch-angle α , also known as “pitch-cosine”
μ_0	$4\pi 10^{-7}$ N A $^{-2}$	magnetic field constant
ν	$\in [0, 1]$	reflection coefficient at the outer boundaries in field-perpendicular direction
ω_{\odot}	0.0103 rad h $^{-1}$	solar angular speed
PDE		partial differential equation
Ψ	rad bzw. °	spiral angle (between radial and magnetic field direction of an Archimedean spiral)
PADC		pitch-angle diffusion coefficient

Symbol	Dimension	Description
PADC		pitch-angle diffusion coefficient
q		spectral index of the power density spectrum of magnetic fluctuations
QLT		quasi-linear theory
r_{\odot}	6.955E+08 m 0.004652 AU	= solar radius
SEP		solar energetic particle
σ	$\Omega^{-1} \text{ m}^{-1}$	conductibility (reciprocal of the specific resistance) or dimensionless polarization of the magnetic field fluctuations
s_{ini}	AU	footpoint of the CFL as arc length along the field line (starting from Sun up to the footpoint)
s_{inj}	AU	injection location on the CFL given as arc length along the field line (starting from Sun up to the foot-point)
θ	°	latitude of the Sun
v_{sw}	300 – 800 km s ⁻¹	solar wind speed

A.2. Program details

A.2.1. Structure

The numerical model is based on spatial one-dimensional code by Wong (1982), Schlüter (1985), Hatzky (1996) and others. Most of the additional source code was stored within the module `perpdiff`. Comments about the containing subroutines and the variables can be found in the source code. Additionally, abbreviated information will be given in this section to ease the introduction into this numerical model. Despite of the modularization of the newly introduced source code, `perpdiff` neither is a stand-alone program, nor can it be integrated in the original numerical code of Roelof or Ruffolo model (in contradiction to the former azimuthal scheme by Lampa, 2006). While the former numerical model allows differently shaped field lines, the current model is confined to Archimedean spirals.

SUBROUTINE `gref`

The main program subsequently calls `ginout` (memory allocation and initializations) `gcalc` (numerical scheme) and `intensi` (time-intensity and time-anisotropy profiles).

SUBROUTINE `ginout`

This routine delegates all memory allocation and initializations, that have almost completely outsourced to the modul `perpdiff`. It is a skeleton, without the amount of functionality, that it originally had.

MODULE perpdiff

The largest source code file contains all global variables, that will be allocated and initialized at runtime (static parameters are stored in module parameters). Several subroutines and functions are provided in order to modularize the work flow and to ease a possible expansion of the code. They are invoked by the subroutines ginout and gcalc.

subroutine readInput(infil):

It imports the contents of the configuration file `infil` (see Section A.3) and stores the data.

subroutine checkinputparameters():

It makes plausibility checks to the user's input.

subroutine calcgridpoints():

It computes the numerical grid and its mesh sizes (some essential computations are outsourced to module `perpcalc`).

subroutine calcTransportCoefficients():

It computes the transport coefficients for almost all transport processes (subroutine `ginout` makes some initializations as well).

subroutine init():

It allocates memory needed at runtime; some calculations for the output routines will be done either.

subroutine setfcorr():

It computes the cross sections by numerical integration using the trapezoidal rule; the scheme was improved with regard to varying step sizes along the magnetic field lines (see Section A.4).

subroutine setperpdifffac():

The perpendicular diffusion coefficient is set according to Section 5.3.

subroutine setzinjection(dt):

The source function $Q(t, s_{\parallel}, s_{\perp})$ is set here as a time-varying inner boundary. Its spatial extent around the central field line depends on variable `inj_spacial_type`, which can be either "h" (rectangular function), "d" (δ -injection in space) or "g" (Gaussian distribution).

subroutine setperpadvect():

It determines the advective flows in field-perpendicular direction.

subroutine free():

The routine deallocates memory and closes file streams at the end of the numerical scheme.

The following subroutines provide the numerical scheme for the transport processes in s_{\parallel} , s_{\perp} , μ and p , respectively.

subroutine nextRoelofSStep(kk, t, jmax):

It contains the field-parallel (s_{\parallel}) transport on varying step sizes: The Lax-Wendroff scheme including a flux limiter. Only particles of a fixed energy are involved (denoted by variable kk). t is the current time step index, jmax is the maximal grid index (beyond jmax no advective fluxes are computed).

subroutine nextRoelofMuStepL(kk, jmax):

It contains the pitch-angle transport (in μ). The input parameters are equivalent to those of the above-mentioned subroutine . Compared to the original code, the scheme itself remains unchanged, but all transport coefficients, that hold a spatial dependency, have been computed with respect to the distorted grid (Figure 3.2).

subroutine nextPStep(jmax):

This routine encapsulates the momentum transport scheme (in p). The input parameter is equivalent to those of the subroutine as mentioned above. Again, the scheme itself remains unchanged, but all transport coefficients, that hold a spatial dependency, have been computed with respect to the distorted grid and the solar wind reference frame.

subroutine nextperpstep_sw(kk, jmax):

This routine holds the perpendicular scheme (in s_{\perp}). The input parameter is equivalent to those of the above-mentioned subroutines. The entire ecliptic plane is simulated. An alternative routine without the extension _sw allows cross-field transport with reflecting boundaries.

```

1 DO WHILE (itcount /= kte)
2     itcount = itcount + 1
3
4 !     first half step in time
5     IF (MOD(itcount,2) == 1) THEN
6         ...
7 !$OMP PARALLEL DEFAULT(SHARED) PRIVATE(k, i, z, la)
8 !$OMP DO SCHEDULE(DYNAMIC, max(1,lp/8))
9     DO k = 1, lp
10 !         first step of the s-transport 1/2*L_s
11     CALL nextSStep(k, itcount, jmax)
12 !         first step of the pitch cosine transport 1/2*L_mu
13     CALL nextMuStepL(k, jmax)
14 END DO
15 !$OMP END DO
16 !$OMP END PARALLEL
17
18 !$OMP PARALLEL DEFAULT(SHARED) PRIVATE(k)
19 !$OMP DO SCHEDULE(DYNAMIC, max(1,lp/8))
20 !         first step of the perpendicular transport 1/2*L_perp
21     DO k = 1, lp
22     CALL nextPerpStep_sw(k,jmax)
23 END DO
24 !$OMP END DO
25 !$OMP END PARALLEL
26
27 !         first step of the momentum transport 1/2*L_p
28     CALL nextKStep(jmax)
29
30 ELSE ! second half step in time
31
32 !         2nd step of the momentum transport 1/2*L_p
33     CALL nextKStep(jmax)
34
35 !$OMP PARALLEL DEFAULT(SHARED) PRIVATE(k)
36 !$OMP DO SCHEDULE(DYNAMIC, max(1,lp/8))
37 !         2nd step of the perpendicular direction 1/2*L_perp
38     DO k = 1, lp
39     CALL nextPerpStep_sw(k,jmax)
40 END DO
41 !$OMP END DO
42 !$OMP END PARALLEL
43
44 !$OMP PARALLEL DEFAULT(SHARED) PRIVATE(k, i, z, la)
45 !$OMP DO SCHEDULE(DYNAMIC, max(1,lp/8))
46     DO k = 1, lp
47 !         2nd step of the pitch cosine transport 1/2*L_mu
48     CALL nextMuStepL(k, jmax)
49 !         2nd step of the s-transport 1/2*L_s
50     CALL nextSStep(k, itcount, jmax)
51 END DO
52 !$OMP END DO
53 !$OMP END PARALLEL
54 ...
55 END IF
56
57 END DO

```

Figure A.1.: Source code excerpt of subroutine gcalc: Complete numerical scheme.

The final part of the subroutine collection in `perpdiff` are those routines responsible for the output production:

`subroutine getcrossprofile(txt,timestamp,kk):`

Saves the formatted data of azimuthal intensity- and anisotropy-time profiles at the given time `timestamp` and momentum p_k (`kk`). `txt` contains a textual message that will be written into the header of each output file.

`subroutine getGridData(txt,timestepno,timestamp,kk):`

Saves the unformatted data of pitch-angle distributions for the entire grid (or for those points that correspond to a lower resolution) at the given time `timestamp` and momentum p_k (`kk`). `txt` contains a textual message that will be written into the header of each output file. The writing process occurs during runtime.

`subroutine plot3d(timestepno,kk):`

The routine is invoked at the end of the numerical scheme. It performs some post processing steps to the data, that had been produced by the routine `getGridData`. Intensities and anisotropies are computed and are written to a formatted file.

SUBROUTINE `gcalc`

It contains the complete numerical scheme, the subroutine `nextRoelofSStep(kk,t,jmax)`, `nextRoelofMuStepL(kk,jmax)`, `nextPStep(jmax)` and `nextperpstep_sw(kk,jmax)` are called consecutively, the order is given by the summarized approximation method (see Section 4). Moreover, the output data will be produced here.

SUBROUTINE `intensi()`

This routine is called after all numerical computations in `gcalc` have been done (end of the simulation). The temporal evolution of the omnidirectional intensity and first-order anisotropy will be saved for user-defined locations in file `???PLT.DAT`, where `???` denotes the three-digit scenario number. The calculations are based on binary raw data of the pitch-angle distribution that has been written out during runtime of the numerical scheme.

A.2.2. Installation

The decision was made to apply the *OpenMP API* specification for parallel programming (OpenMP Architecture Review Board, 2009) in order to still have proper run times for this extended 2-dimensional model.

The current compiler `g95` does not support this standard, thus the open source compiler `gfortran` as part of the GNU compiler collection (GCC) was chosen (GNU Compiler Collection, 2010) – even though `g95` provides a larger variety of options, better debugging and more stable compilation results.

Whereas the installation under UNIX systems can be done without any severe problems (the GCC is one of the standard libraries), installing under Windows (XP) is not that easy. Again, `cygwin` as Linux-like environment for Windows systems was applied. It should be

noted that the `gmp` and `mpfr` packages must be installed for `gfortran` to work – besides `make` to ease the compilation process.

The simulation results might differ when two scenarios run at different platforms since floating point numbers and integers are represented by different numbers of bits. By additionally setting the flags `-fdefault-real-8` and `-fdefault-integer-8` during the compilation, all numbers are set to double precision.

This prevents (at least in parts) under- and overflow errors of floating point numbers. These errors occur if not enough bits are provided to represent very high/ low or close-to-zero values.

very low values cannot be represented anymore if not enough bits are provided. But it is also up to the program developer to be aware of multiplication/ divisions of large/ small values. For example: Concerning the computation of transport coefficients in perpendicular direction the order of multiplier had to be chosen properly to get reasonable values.

After having installed the *Cygwin* environment including all essential packages as mentioned above, the following command:

```
tar -xjvf gfortran-X.X-Cygwin-i686.tar.bz2 -C
```

will install `gfortran` in `/usr/local/gfortran`. Note that the `X` stands for the current version of `gfortran`. Another decompressing, probably graphical user interface (GUI) based tool like WINRAR could do this job as well.

To make this compiler globally reachable, you can then either set `/usr/local/gfortran/bin` to be in the search path or set up a link in your local `/bin` directory with this command as an example:

```
ln -s /usr/local/gfortran/bin/gfortran.exe ~/bin/gfortran
```

Assuming `/bin` is in your search path, you can invoke `gfortran` with:

```
gfortran --version
```

If the version details of this compiler are shown, the installation is expected to be completed successfully.

In order to activate the features of *openMP*, the additional flag `-fopenmp` has to be set during the compilation and the execution process as well. The `make` utility – that has been applied here – automatizes these processes. Thus, the user must just execute some short commands that have been defined in the accompanying *Makefile*.

To invoke the compilation process which would build all the object files, go into the root directory of the program (e.g. `nperpgref/`), and then type

```
make
```

as bash shell command. These files are linked together to the executable `gref.exe`, which will be started by

```
make run
```

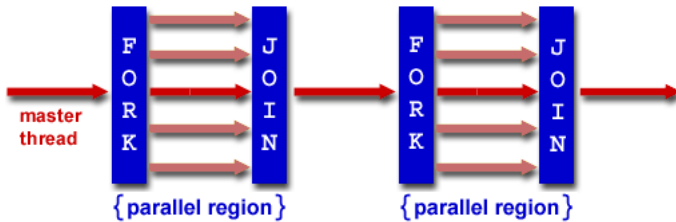


Figure A.2.: Fork-Join model of parallel execution, OpenMP Architecture Review Board (2009).

All the results from the compilation process will be stored in the sub-folder `bin/`. The simulation results can be found at `dat/`. All these outputs can be deleted by the command

```
make clean ,
```

whereas

```
make dclean
```

would delete the simulation data only. Note that the files are irreversibly deleted and cannot be restored.

The configuration input file can be manipulated by the separate program *para*.

```
make para
```

The resulting executable is *para.exe*. Note that the additional parameters for 2-dimensional transport can not be restored, but they can be appended manually by the corresponding lines that have been saved in a separate copy file. Normally, it is more comfortable to do changes in this config file by hand. Changes with respect to the PADC should be done with this tool with priority.

A.2.3. Parallelization

The *OpenMP API* may be used to direct multi-threaded, shared memory parallelism explicitly. OpenMP (**Open** specifications for **M**ulti-**P**rocessing) provides a portable, scalable model. The API supports C/C++ and Fortran on multiple architectures, including UNIX and Windows NT.

The original program was serial, so there was always one *single* execution step after another and all steps were executed consecutively. Giving up serialization in terms of this multi-dimensional summarized approximation method is not easy since – during a definite transport process – all other variables of the phase space density have to be kept constant.

This is why the regions, where multiple threads can work (parallel regions, see Figure A.2), have to start/end where these individual transport process start/end. Since OpenMP is an explicit (not automatic) programming model, the programmer has to decide where to fork the master thread and where to join it.

```

1 !$OMP PARALLEL DEFAULT(SHARED) PRIVATE(k, i, z, la)
2 !$OMP DO SCHEDULE(DYNAMIC, max(1,lp/8))
3   DO k = 1, lp
4 !     first step of the s-transport 1/2*L_s| -----
5     CALL nextSSStep(k, itcount, jmax)
6 !     first step of the pitch cosine transport 1/2*L_mu
7     CALL nextMuStepL(k, jmax)
8   END DO
9 !$OMP END DO
10 !$OMP END PARALLEL
11
12 !$OMP PARALLEL DEFAULT(SHARED) PRIVATE(k)
13 !$OMP DO SCHEDULE(DYNAMIC, max(1,lp/8))
14 !   first step of the perpendicular transport 1/2*L_perp
15   DO k = 1, lp
16     CALL nextPerpStep_sw(k,jmax)
17   END DO
18 !$OMP END DO
19 !$OMP END PARALLEL
20
21 !   first step of the momentum transport 1/2*L_p
22   CALL nextKStep(jmax)

```

Figure A.3.: Source code excerpt of subroutine gcalc: The first half step of the summarized approximation method is illustrated.

The compiler would be responsible for automatically parallelizing such loops across the symmetric multiprocessing (SMP) processors. The compiler can neither check itself whether the most efficient use of shared memory was made, nor it is not required to check for data dependencies, data conflicts, race conditions, or deadlocks.

As the name API says, the developer does not need to know in detail how parallelization will be done. Instead, a simple and limited set of directives for programming shared memory machines has to be established. Significant parallelism can be implemented by using just 3 or 4 directives.

Figure A.3 shows an abbreviated excerpt of the source code. It is part of the first half step in subroutine gcalc where all transport processes (see Section A.2.1) are executed consecutively from the top to the bottom. All lines beginning with the !\$OMP sentinel indicate openMp directives that will be evaluated as long as the -fopenmp flag is set during the entire compilation process. Otherwise they will be treated as comment lines. Note that one has to be aware of additional constraints if the source code is not written in free form.

Some Fortran OpenMP directives come in pairs and have the form shown below. The “end” directive is optional but advised for readability.

```

!$OMP directive
[ structured block of code ]
!$OMP end directive

```

In this study, only two directives were applied. First, PARALLEL which defines parallel regions as block of code that will be executed by multiple threads. This is the fundamental OpenMP parallel construct. Secondly, the DO directive specifies that the iterations of the loop immediately following it must be executed in parallel by a team of threads. Consequently, in case of several nested loops and a single PARALLEL directive around them

(parallel region has already been initiated), the inner loops will be treated as serial code.

The `DEFAULT` clause allows the user to specify a default scope for all variables in the lexical extent of any parallel region. Here, as default, all variables will be shared. The `PRIVATE(...)` statement lists all variables that are private to each thread; each thread will have its own unique copy. Besides the private declarations, other possible read/write conflicts have been resolved explicitly by extending all writable variables or array within parallel regions to an extra dimension – with each additional entry being related to a specific thread.

The `SCHEDULE(type,chunk)` clause describes how iterations of the loop are divided among the threads in the team. The default schedule is implementation dependent. As `type`, `DYNAMIC` was chosen: Loop iterations are divided into pieces of size `chunk`, and scheduled dynamically among the threads; when a thread finishes one chunk, it is dynamically assigned to another. According to the source code, the default chunk size is `1p/8`.

As seen in the source code in Figure (A.1) both field-parallel transport in s and pitch-angle scattering in μ will be executed in parallel with respect to momentum/ particle speed (`1p` grid points). The reason for this single parallel region is that both transport schemes do not depend on velocity.

The cross-field transport had to be parallelized separately since the transport direction changes. Otherwise, a complete parallelization would lead to read/write conflicts when both parallel and perpendicular transport schemes try to get access to identical phase space density cells $\xi_{j,l}$.

The numerical scheme for momentum transport `nextKStep(jmax)` has been parallelized according to number of field lines `1long` (even if it is not indicated in Figure A.1). All particle velocities have to be computed for the next (half) time step before the new positions due to parallel advection along the IMF lines can be set.

A.3. User interfaces

The configuration file contains all parameters needed for a complete setup of the numerical model. The first 40 lines are identical to those of the original configuration file, that is used for the one-dimensional models of the Roelof's and Ruffolo's equation. In contrast to the former models, the parameter choice lacks in some alternatives, which will be illustrated in this section. The standard user will not be forced to make direct changes in the source code, but if he wants to, Section A.2.1 will give some insight into the program structure.

Line 1 denotes a 56-character-long string of a simple comment that will be written into the output files. Their names are given in the following three lines. The first three characters of each file should be identical (and a number), because they correspond to the scenario number. The first file records almost all parameter settings including additional comments. The second contains time-series of pitch-angle distributions at different locations. The third is filled with coefficients up to fourth order of Legendre polynomials, that will be fitted to the pitch-angle distributions along the central field line (CFL). The data will be saved at the end of the simulation.

Each of the two characters in line 5 has its own relevance: The first letter can be "S" or "W". By the use of "S", the numerical value of the pitch-angle diffusion coefficient (PADC) will be determined by the theory of slab turbulence (see Section 2.4.2). The

corresponding parameters are located in the following line: with the number of pitch-angles mmu , the spectral index q , the resonance gap H and the polarization σ . If the first letter in line 4 is set to “W”, the user has to define the PADC manually. The second letter in line 4 will be a flag for the program to decide how the PADC should be adapted to the numerical

scheme. If it is “J” and the user decides to take the slab-PADC, the Integro-interpolation will be applied (see Section 4.3). Manually defined PADCs will be changed by a simple linear interpolation. In case of an “N” (instead of “J”) no adjustments to the PADC will be done.

The next two following parameters are the simulation period in hours (line 7) and the particle speed given in AU h $^{-1}$. Note that this parameter becomes redundant if the momentum transport is explicitly switched on (for details see comments to line 52).

The letter “a” in line 9 determines the IMF’s shape to be Archimedean (Parker) spiral. The shape depends on both inclination of the ecliptic plane and the solar wind speed given in km s $^{-1}$; these values can be found at line 38. The solar angular speed $\omega_{\odot} = 0.0103$ rad h $^{-1}$, which is also responsible for the shape, is assumed to be independent of the latitude. The parameter “a” is not allowed to be changed, since there is no alternative to the Archimedean spiral at present. Changes would lead to malfunctions of the program.

Lines 10-17 contain the discretized PADC. Lines 18-26 also contain the interpolation values for the PADC, but they are computed according to a pitch-angle grid, that is shifted by half step size. This results in an additional PADC value defined within the interval $\mu \in [-1, +1]$.

Line 27: The first location at the CFL given in arc length along the field line. Additional locations can be specified in

lines 46 – 49: Line 46 is set to 1 by default. Thus, at least a single observation point is necessary for a valid run. The following line denotes the arc length of additional locations, line 48 names the azimuthal distances of the observation points (the CFL is located at $\varphi = 0^\circ$) and line 49 gives the latitudinal information. Here, the latitudes are set to 0° – indicating that interplanetary transport is confined to the ecliptic plane only.

Line 28 gives the spatial dependency ns of the PADC. By default, $ns = 2$ is chosen such

```
jEdit - configfile.dat
1 1.0 MeV Protons lambda = 0.1 AU
2 001GRF.DAT
3 001BIN.DAT
4 001BO1.DAT
5 SJ
6      40   1.600000    0.000000E+00  0.000000E+00
7     10.0
8     1.0
9   a
10  0.1013138   0.2870357   0.4506869   0.5928327   0.7140370
11  0.8148608   0.8958582   0.9575721   1.000528    1.025222
12  1.032111    1.021586   0.9939403   0.9493110   0.8875782
13  0.8081763   0.7096978   0.5889324   0.4378706   0.2276414
14  0.2276414   0.4378706   0.5889324   0.7096978   0.8081763
15  0.8875782   0.9493110   0.9939403   1.021586   1.032111
16  1.025222    1.000528   0.9575721   0.8958582   0.8148608
17  0.7140370   0.5928327   0.4506869   0.2870357   0.1013138
18  0.0000000E+00  0.1969471   0.3715382   0.5243405   0.6559151
19  0.7668259   0.8576279   0.9288723   0.9810895   1.014791
20  1.030455    1.028496   1.009257   0.9729536   0.9195790
21  0.8487823   0.7595488   0.6495001   0.5127925   0.3293884
22  9.1113508E-02  0.3293884   0.5127925   0.6495001   0.7595488
23  0.8487823   0.9195790   0.9729536   1.009257   1.028496
24  1.030455    1.014791   0.9810895   0.9288723   0.8576279
25  0.7668259   0.6559151   0.5243405   0.3715382   0.1969471
26  0.0000000E+00
27  0.3
28      2
29     7.5
30     4
31  5.0000001E-02  0.7000000   0.8000000   0.9000000   1.15000
32  1.57000   60.00000
33  -0.5000000   0.5000000   1.000000   0.5000000   2.142857
34  2.142857
35  1.000000
36  0.0000000   0.0000000   0.0000000E+00
37     1
38  1.5708    400.0000
39  0.00000E+00  0.0000000E+00
40      1
41      0.01          # ds
42  1E+11   d  10.0          # mass0, inj_spacial_type, inj_spacial_param
43
44  5.0   1  72  1.0  5.0  # dz, llatt, llong, zfrac, dz_resolution
45  1          # projection_type
46  2          # nout
47  0.30
48  -90.00
49  0.00
50  11          # twatch
51  0.1  1.0  2.0  3.0  4.0  5.0  6.0  7.0  8.0  9.0  10.0 # t
52  6          # rn
53  0.1  0.3  1.0  1.5  2.0  3.0          # routs
54  32          # lp
55  0.1
```

Figure A.4.: Configuration file

that $\lambda_r = \text{const.}$ is fulfilled. Other choices are possible, for example such that the spatial dependencies are given by the 7 spatial nodes in line 31 – 32 and the corresponding strength of the PADC (lines 33 – 34). It should be noted that the latter node (line 32, last number) also denotes the outer boundary of the CFL. When the simulated particles reach the outer boundary in field-parallel direction, they are allowed to be reflected towards the Sun. The reflection coefficient is located in line 35 and is set to 1 by default (full reflection).

The magnetic field can be modified locally to realize a magnetic bottle. Its strength and extent parameters can be found at line 36.

Line 37: The number 1 indicates that all the output data (pitch-angle distributions) will be written for each time, higher values, e.g. 100, means that only each 100th data value will be written.

So far, all parameters have been elucidated that have already found their application in former models. The additional parameters are:

At line 41: The spatial step size Δ_s along the field lines. Note that constant step sizes are not allowed anymore. Any value of Δ_s will be ignored by the program. However, this parameter has been preserved, so that the configuration file can be still applied to both the original program gref and the azimuthal model quergref.

Line 42: Source parameters: Total mass of particles m_0 , injection type (“d”: δ -injection, “h”, rectangular injection, “g”, Gaussian injection) and the spatial extent of the source.

Line 44: From left to right: Azimuthal resolution given in degrees, number of field lines in latitudinal direction (only “1” will be accepted), number of field lines in azimuthal direction, reflection coefficient in field-perpendicular direction (see also Section 4.6) and the azimuthal resolution for the output data (given in degrees).

Line 45: The integer is relevant to the cross-field profiles. “1” denotes slices through the ecliptic plane; “2” is expected to be slice perpendicular to it, with the CFL placed in the center. The parameter becomes important when spatial 3D interplanetary transport will be simulated in the near future.

Line 50 – 51: Number of snapshots of the ecliptic plane and the azimuthal profiles, as well as a list of times when these snapshots will be taken.

Lines 52 – 53: Azimuthal cross-field profiles: The first parameter denotes the number of slice through the plane, and the list in the following line gives the corresponding radial distances.

Line 52: Number of nodes for momentum transport $1p$. If $1p=0$, momentum transport will be switched off, and particles will have the speed as defined in line 8. Otherwise, the velocities will be computed according to (4.31).

Line 55: Ratio between the perpendicular and parallel diffusion coefficient γ , scaled with r^2 .

In order to manipulate the pitch-angle diffusion coefficient values, it is recommended to use the stand-alone program para (Section A.2.2), because these numbers need to be processed further to be well tolerable to the numerical scheme (Section 4.3). The remaining scalar values can be changed by hand as well.

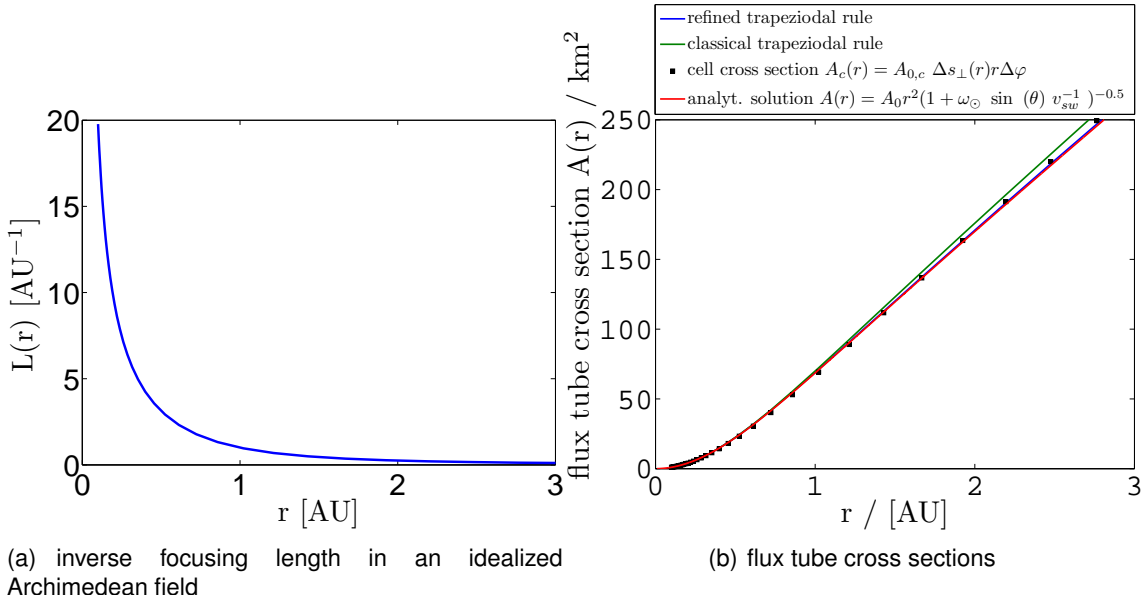


Figure A.5.: Numerical computation of the flux tube cross sections by means of the focusing length.

A.4. Cross sections of flux tubes and their numerical treatment

Both, the computational implementation of the Roelof's equation and the Ruffolo equation calculate the cross sections numerically by using the simple trapezoidal rule for equally spaced abscissas (Press et al. (1992), p. 124-129).

Applying a numerical treatment was necessary since the above-mentioned integration scheme is not accurate enough to describe the cross sections satisfactorily - especially when step sizes become too large. Since $L(s)^{-1}$ is a monotonously decreasing function (see left panel in Figure A.5), an numerical integration over the inverse focusing length would be overestimated compared to a possible analytical solution (right panel in Figure A.5). As in all numerical integration schemes, the truncation error sums up along the integration path. Consequently, the computed cross sections already show a significant deviation beyond 1 AU compared to the analytical solution.

Thus we refined the scheme by introducing virtual grid points between the already existing grid points. Thus we made an adoption from the extended formula of the trapezoidal rule (Press et al. (1992), p. 127), but used varying step sizes instead.

Note that these virtual points themselves do not contribute to the numerical transport scheme but are solely computed in order to get accurate flux tube values.

Cross sections are determined this way:

$$A(s) = A_0(s) \exp \left(\int \frac{1}{L(s)} ds \right), \quad (\text{A.1})$$

with $A_0(s)$ being the cross section at the footpoint of the field line, and $L(s)$ being the focusing length (3.7). The relation is a direct consequence of the fact that particles for a flux rope length unit are conserved and also of the Gaussian Law (the magnetic flux has

to be conserved within a flux tube, valid for the both transport equations, see also Hatzky (1996), p. 42). In case of the idealized, IMF forming Archimedean spiral field (constant solar wind and no further magnetic disturbances are assumed), the analytical solution of the cross section is:

$$A(r) = \frac{A_0 r^2}{B_0 \sqrt{1 + \omega_\odot r \sin \theta v_{sw}^{-1}}}, \quad (\text{A.2})$$

which is the multiple of the inverse of the magnetic field strength. In these studies, the cross sections at the footpoint of each field line have been set to:

$$A(r = r_0) = \Delta s_\perp(r).$$

Consequently, we have not made any assumption about the geometry in meridional direction. Any other cross sections beyond r_0 are directly computed according to the local magnetic field strength $B(r)$. They differ solely in a constant whose value is given by cross section size and the magnetic field strength at the footpoints. Note that the cross sections could alternatively be calculated by simply taking the product of $\Delta s_\perp(r) \cdot r\Delta\theta$. The second factor approximately describes the "height" of a cell in meridional direction, which is simply the arc-length on a circle with radius r and angular displacement $\Delta\theta$ to the neighboring field line. As it is shown on the right hand side of Figure A.5, these cell cross sections are well fitted to the red-colored analytical solution (in this case, θ and φ are identical). But nevertheless, we decided to work the refined trapezoidal rule in order to accommodate magnetic disturbances ranging from the stream structure of the interplanetary medium over transient disturbances such as shocks and magnetic clouds/coronal mass ejections.

A.5. Various intensity-time profiles for ~ 0.5 MeV electrons

For a parameter study, the mean free path λ_r has been varied by $\lambda_r = 0.063, 0.63$ and 6.3 AU. Moreover, the ratio of the perpendicular to the parallel diffusion was set to $\gamma = 0.02$ and 0.1 at $r = 1$ AU, and scaled with r^2 as it is assumed in the standard scenario. The resulting six intensity-time- and anisotropy-time profiles are plotted and arranged side-by-side in this subsection to get a more detailed look into the dynamics of the modeled two-dimensional diffusion. All the features such as vanishing gradients, negative anisotropies, variations in azimuth together with some of these figures have already been discussed in Section 7.1. The focus is taken on ~ 0.5 MeV electrons whose data was obtained at different radial distances ($r = 0.3$ and 1.0 AU) as well as different azimuthal distances from the central field line. SEPs are injected impulsively onto the footpoint of the CFL, described formally as a Dirac-delta function. The simulation results do not provide any new features but they add 10-hour-data for wide domain of parameter sets.

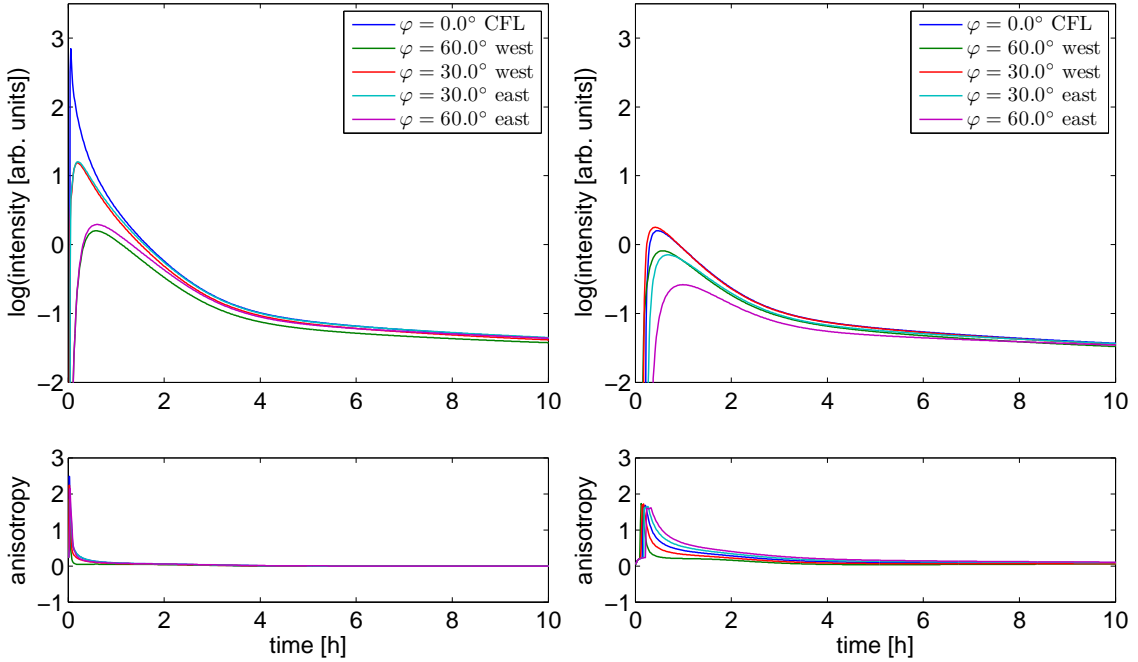


Figure A.6.: Intensity- and anisotropy-time profiles of 0.5 MeV electrons obtained from the *standard scenario* ($\lambda_r = 0.63$ AU, $\gamma = 0.1$). Left panels correspond to $r = 0.3$ AU, right ones to $r = 1$ AU.

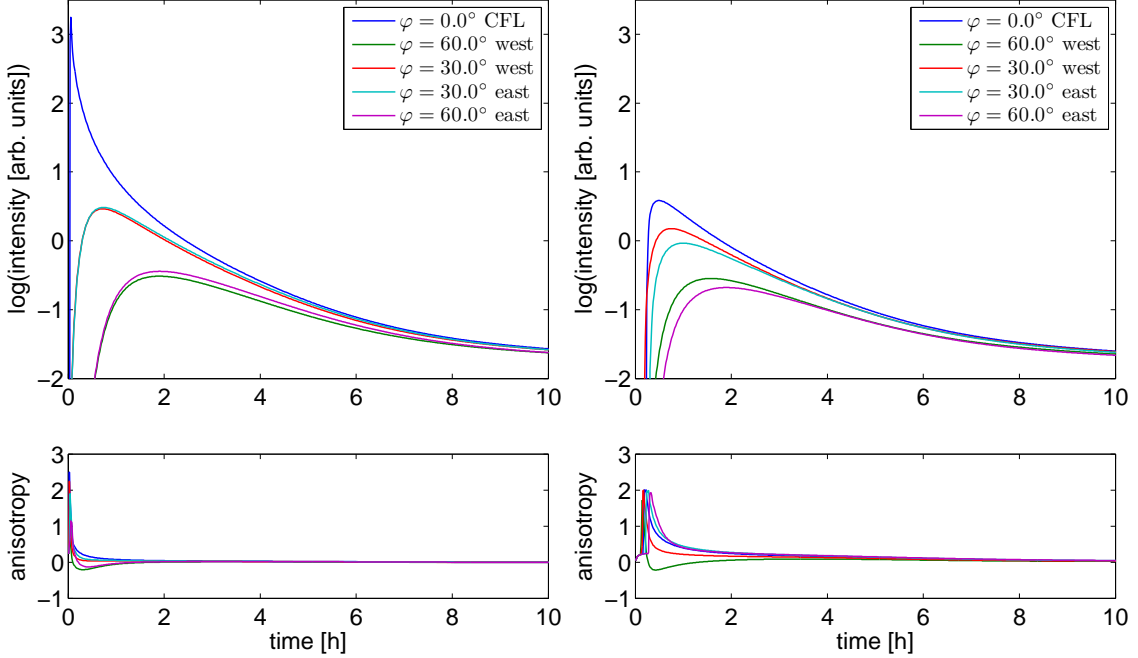


Figure A.7.: Intensity- and anisotropy-time profiles of 0.5 MeV electrons obtained from the *standard scenario*, but γ changed ($\lambda_r = 0.63$ AU, $\gamma = 0.02$). Left panels correspond to $r = 0.3$ AU, right ones to $r = 1$ AU.

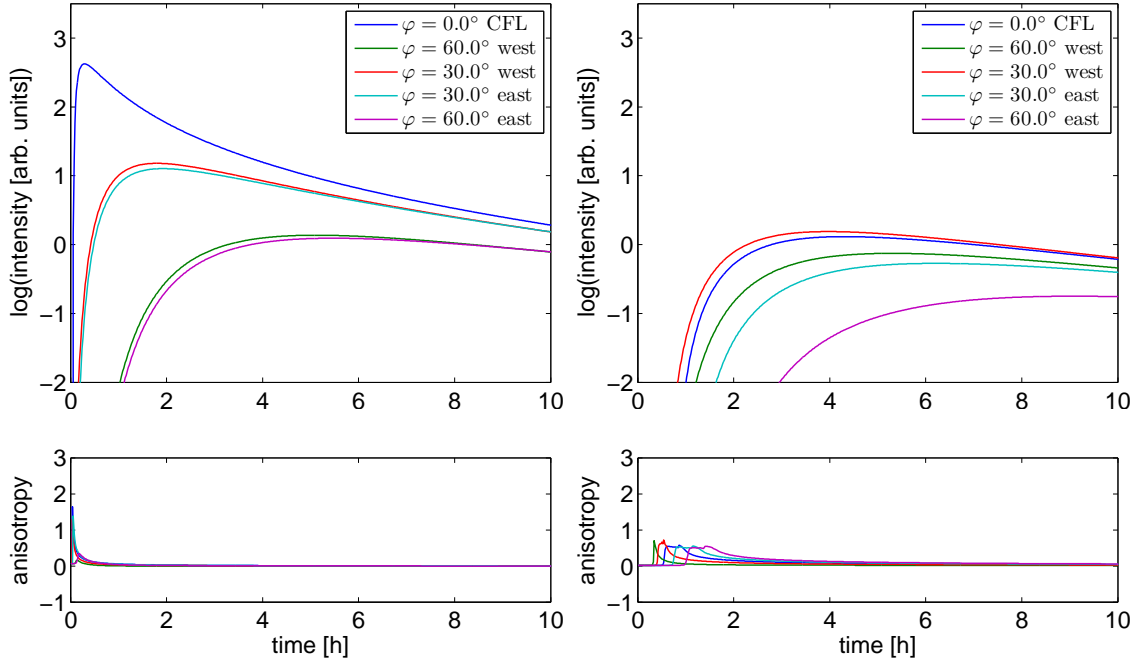


Figure A.8.: Intensity- and anisotropy-time profiles of 0.5 MeV electrons obtained from the *standard scenario*, but λ_r changed ($\lambda_r = 0.063$ AU, $\gamma = 0.1$). Left panels correspond to $r = 0.3$ AU, right ones to $r = 1$ AU.

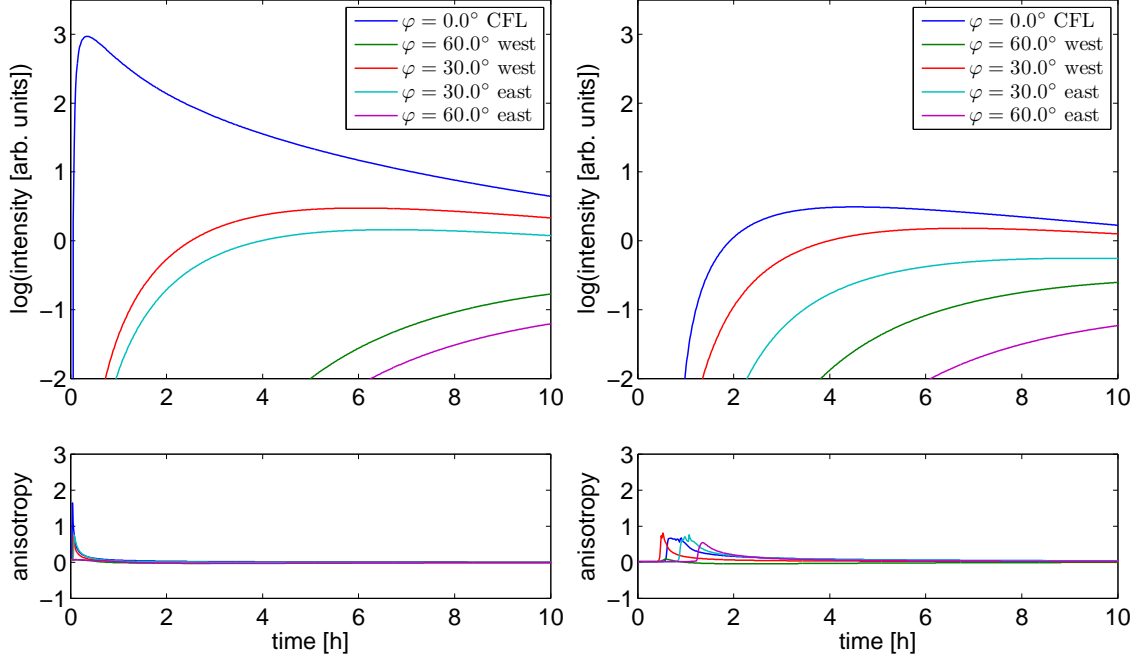


Figure A.9.: Intensity- and anisotropy-time profiles of 0.5 MeV electrons obtained from the *standard scenario*, but λ_r and γ changed ($\lambda_r = 0.063$ AU, $\gamma = 0.02$). Left panels correspond to $r = 0.3$ AU, right ones to $r = 1$ AU.

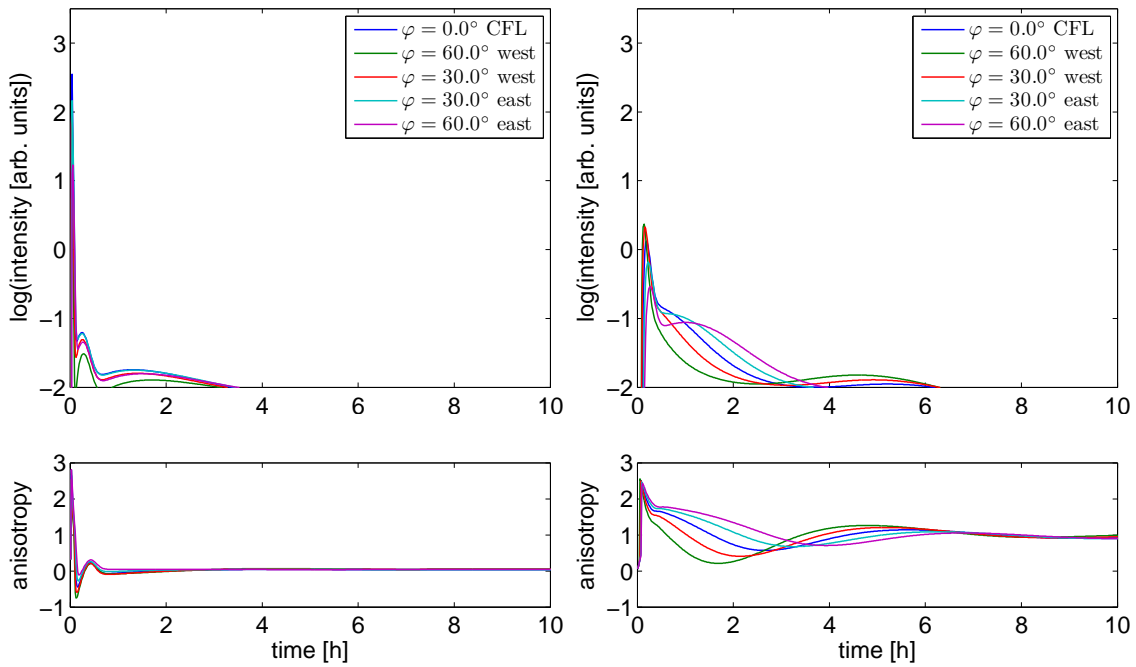


Figure A.10.: Intensity- and anisotropy-time profiles of 0.5 MeV electrons obtained from the *standard scenario*, but λ_r changed ($\lambda_r = 6.3$ AU, $\gamma = 0.1$). Left panels correspond to $r = 0.3$ AU, right ones to $r = 1$ AU.

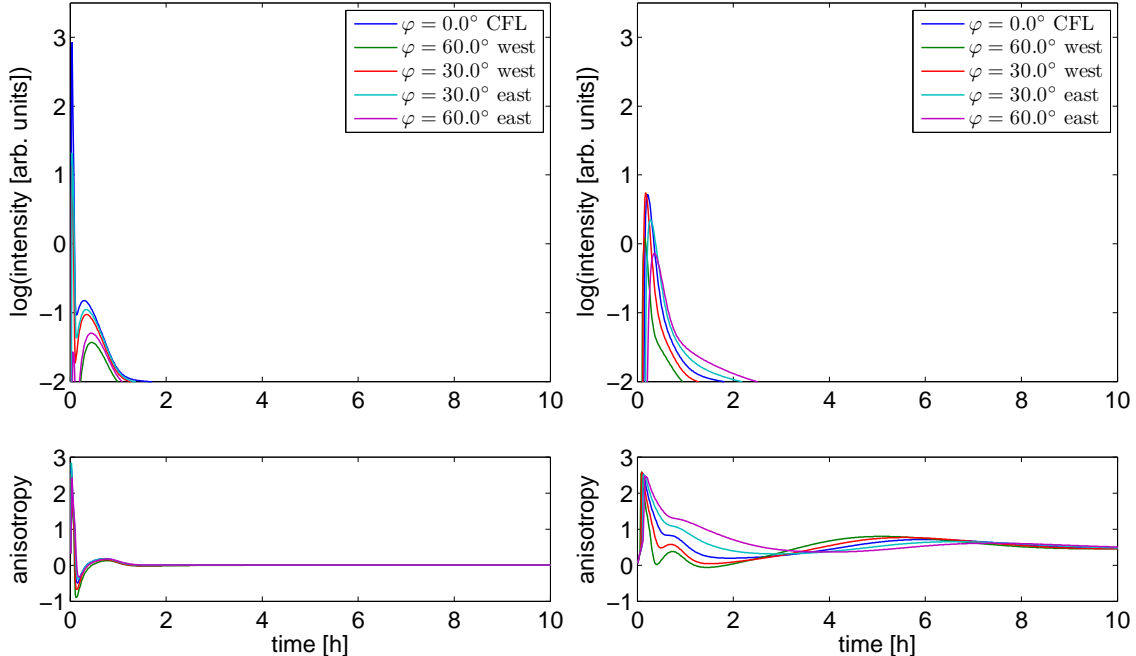


Figure A.11.: Intensity- and anisotropy-time profiles of 0.5 MeV electrons obtained from the *standard scenario*, but λ_r and γ changed ($\lambda_r = 6.3$ AU, $\gamma = 0.02$). Left panels correspond to $r = 0.3$ AU, right ones to $r = 1$ AU.

Bibliography

- Alfvén, H. (1976), "On frozen-in field lines and field line reconnection", *J. Geophys. Res.*, Vol. 81, pp. 4019–4021.
- Anderson, D., Tannehill, J. and Pletcher, R. (1984), *Computational Fluid Dynamics and Heat Transfer*, Series in Computational Methods in Mechanics and Thermal Sciences, Hemisphere Publishing Corporation, pp. 27–28, 159.
- Baumjohann, W. and Treumann, R. (1986), *Basic space plasma physics*, Imperial College Press, London.
- Beeck, J., Mason, G., Hamilton, D., Wibberenz, G., Kunow, H., Hovestadt, D. and Klecker, B. (1987), "A multospacecraft study of the injection and transport of solar energetic particles", *Astrophys. J.*, Vol. 322, pp. 1052–1072.
- Beeck, J. and Wibberenz, G. (1986), "Pitch angle distributions of solar energetic particles and the local scattering properties of the interplanetary medium", *Astrophys. J.*, Vol. 311, p. 437.
- Bieber, J., Earl, J., Green, G., Kunow, H., Müller-Mellin, R. and Wibberenz, G. (1980), "Interplanetary pitch angle scattering and coronal transport of solar energetic particles: New information from helios", *J. Geophys. Res.*, Vol. 85, p. 2313.
- Bieber, J., Matthaeus, W., Shalchi, A. and Qin, G. (2004a), "Nonlinear guiding center theory of perpendicular diffusion: General properties and comparison with data", *Geophys. Res. Lett.*, Vol. 31, p. L10805.
- Bieber, J., Matthaeus, W., Shalchi, A. and Qin, G. (2004b), "Nonlinear guiding center theory of perpendicular diffusion: General properties and comparison with observation", *Geophys. Res. Lett.*, Vol. 31, p. L10805.
- URL:** <http://www.agu.org/pubs/crossref/2004/2004GL020007.shtml>
- Bieber, J., Matthaeus, W., Smith, C., Wanner, W., Kallenrode, M.-B. and Wibberenz, G. (1994), "Proton and electron free mean paths: The palmer consensus revisited", *Astrophys. J.*, Vol. 420, p. 303.
- Borovsky, J. (2008), "Flux tube texture of the solar wind: Strands of the magnetic carpet at 1 AU?", *J. Geophys. Res.*, Vol. 113, p. A08110.
- Bronstein, I., Semendjajew, K., Musiol, G. and Müling, H. (1993), *Taschenbuch der Mathematik*, Harri Deutsch, Frank am Main.
- Burlaga, L. (1991), Magnetic clouds, *in* R. Schwenn and E. Marsch, eds, 'Physics of the Inner Heliosphere', Vol. 2, Springer, Berlin, p. 1.
- Cane, H. (2005), Are there direct flare particles in large solar particle events ?, *in* H. Lacoste, ed., 'Solar Wind 11 – SOHO 16 Connecting Sun and Heliosphere', Vol. ESA SP-592, ESA Publications Division, pp. 71–74.

- Cane, H. and Erickson, W. (2003), "Energetic particle propagation in the inner heliosphere as deduced from low-frequency (< 100 kHz) observations of type III radio bursts", *J. Geophys. Res.*, Vol. 108, p. 1203.
- Chattot, J.-J. (2002), *Computational Aerodynamics and Fluid Dynamics*, Springer-Verlag Berlin Heidelberg.
- Compton, A. and Getting, I. (1935), "An apparent effect of galactic rotation on the intensity of cosmic rays", *Phys. Rev.*, Vol. 47, p. 817.
- Crank, J. and Nicolson, P. (1947), "A practical method for numerical evaluation of solutions of partial differential equations of the heat-conduction type", Vol. 43, Proc. Camb. Phil. Soc., pp. 207–226.
- Dalla, S., Balogh, A., Krucker, S., Posner, A., Müller-Mellin, R., Anglin, J., Hofer, M., Marsden, R., Sanderson, T., Tranquille, C., Heber, B., Zhang, M. and McKibben, R. (2003), "Properties of high heliolatitude solar energetic particle events and constraints on models of acceleration and propagation", *J. Geophys. Res.*, Vol. 30, p. 8035.
- Denskat, K., Beinroth, H. and Neubauer, F. (1983), "Interplanetary magnetic field power spectra with frequencies from $2.4 \cdot 10^{-5}$ Hz to 470 Hz from Helios-observations during solar minimum conditions", *J. Geophys. Res.*, Vol. 6, p. 2215.
- Diehl, R., Parizot, E., Kallenbach, R. and von Steiger, R., eds (2002), *The astrophysics of galactic cosmic rays*, Kluwer, Dordrecht.
- Dröge, W. (1993), "Transport of solar energetic particles", *Ap. J. S.*, Vol. 90, pp. 567–576.
- Dwivedi, B. (2003), The solar corona, in H. Antia, A. Bhatnagar and P. Ulmschneider, eds, 'Lectures on Solar Physics', Vol. ESA SP-592, Springer, Berlin, Heidelberg, p. 281.
- Dwyer, J., Mason, G., Mazur, J., Jokipii, J., von Rosenvinge, T. and Lepping, R. (1997), "Perpendicular transport of low energy corotating interaction region - associated nuclei", *Astrophys. J.*, Vol. 490, p. L115.
- Eddington, A. (1926), *The internal constitution of the stars*, Cambridge University Press.
- Farlow, S. (2003), *Partial Differential Equations for Scientists and Engineers*, Dover Publications, Inc, New York.
- Fisk, L. and Axford, W. (1968), "Effect of energy changes in solar cosmic rays", *J. Geophys. Res.*, Vol. 73, p. 4396.
- Fisk, L. and Axford, W. (1969), "Anisotropies of solar cosmic rays", *Sol. Phys.*, Vol. 7, p. 486.
- Forbush, S. (1946), "Three unusual cosmic ray increases possibly due to charged particles from the Sun", *Phys. Rev.*, Vol. 70, p. 771.
- Gaizouskas, V. (1983), "The relation of solar flares to the evolution and proper motion of magnetic fields", *Adv. Space Res.*, Vol. 2, p. 11.
- Giacalone, J. and Jokipii, J. (1999), "The transport of cosmic rays across a turbulent magnetic field", *Astrophys. J.*, Vol. 520, pp. 204–214.

- GNU Compiler Collection (2010), ‘The OpenMP API specification for parallel programming’.
- URL:** <http://gcc.gnu.org/wiki/GFortranBinaries>
- Gockel, A. (1911), “Messungen der durchdringenden Strahlung bei Ballonfahrten”, *Physikalische Zeitschrift*, Vol. No. 14, 12. Jahrgang, pp. 595–597.
- Gold, R., Nolte, J., Roelof, E. and Reinhard, R. (1973), “The influence of coronal magnetic structures on low energy solar proton events”, *Proc. Conf. Cosmic Rays, 13th*, Vol. 2, p. 1367.
- Goldstein, H. (1959), *Classical Mechanics*, Addison-Wesley: Reading MA.
- Gosling, J. (1992), In-situ observations of coronal mass ejections in interplanetary space, in Z. Svestka, B. Jackson and M. Machado, eds, ‘Eruptive solar flare’, Springer, Berlin, p. 258.
- Gosling, J., Asbridge, J., Bame, S., Feldman, W., Zwickl, R., Paschmann, G., Sckopke, N. and Hynds, R. (1981), “Interplanetary ions during an energetic storm particle event – The distribution function from solar-wind thermal energies to 1.6 MeV”, *J. Geophys. Res.*, Vol. 86, p. 547.
- Green, G. (1992), Pitchwinkelverteilungen energiereicher geladener Teilchen: Ihre Rekonstruktion aus sektorisierten Intensitätsmessungen und ihre Bedeutung für die Untersuchung interplanetarer Ausbreitungsmechanismen, PhD thesis.
- Grossmann, C. and Roos, H.-G. (1994), *Numerik partieller Differentialgleichungen*, Teubner.
- Gurnett, D. and Bhattacharjee, A. (2005), *Introduction to Plasma Physics*, Cambridge University Press.
- Hamilton, D. (1977), “The radial transport of energetic solar flare particles from 1 to 6 AU”, *J. Geophys. Res.*, Vol. 82, p. 2157.
- Hasselmann, K. and Wibberenz, G. (1968), “Scattering of charged particles by random electromagnetic fields”, *Z. Geophys.*, Vol. 34, p. 353.
- Hasselmann, K. and Wibberenz, G. (1970), “A note of the parallel diffusion coefficient”, *Astrophys. J.*, Vol. 162, p. 1049.
- Hatzky, R. (1996), Winkelverteilungen energiereicher geladener Teilchen und die Streueigenschaften des interplanetaren Mediums, PhD thesis.
- URL:** <http://ifkki.kernphysik.uni-kiel.de>
- Hatzky, R. and Kallenrode, M.-B. (1999), “Numerics of interplanetary transport”, *Proc. 26th Int. Cosmic Ray Conf.*, Vol. 6, p. 320.
- Hess, V. (1912), “Beobachtungen der durchdringenden Strahlung bei sieben Freiballionfahrten”, *Mitteilungen aus dem Institut für Radiumforschung, Sitzungsberichte der mathematisch-naturw. Klasse der kaiserlichen Akademie der Wissenschaften*, Vol. Band CXXI, Abteilung IIa, Heft VIII bis X, zweiter Halbband, pp. 2001–2032.
- Hucke, S., Kallenrode, M.-B. and Wibberenz, G. (1992), “Propagation conditions for relativistic electrons in the inner heliosphere”, *Astrophys. J.*, Vol. 394, pp. 351–356.

IMP 8 MERGE 20sec Resolution Data (2010), ‘Description of the four IMP 8 instruments whose data are included in the MERGE data set’.

URL: http://spdf.gsfc.nasa.gov/imp8/imp8_merged.html

Jahns, K. (2007), Querdiffusion geladener Teilchen im interplanetaren Raum, Master’s thesis.

Johnson, C. (1987), *Numerical solution of partial differential equations by the finite element method*, Studentlitteratur, Lund.

Jokipii, J. (1966), “Cosmic ray propagation. I. Charged particles in random magnetic field”, *Astrophys. J.* , Vol. 146, p. 480.

Jones, F. and Ellison, D. (1991), “The plasma physics of shock acceleration”, *Space Sci. Rev.* , Vol. 58, p. 259.

Kallenrode, M.-B. (1989), Injektion energetischer Teilchen in solaren Flares - Möglichkeiten der Bestimmung der Injektion unter verschiedenen Bedingungen der interplanetaren Ausbreitung und Beispiele für das Injektionsverhalten unter Berücksichtigung der Klassifikation in impulsive und graduale Ereignisse, PhD thesis.

Kallenrode, M.-B. (1993a), “Neutral lines and azimuthal transport of solar energetic particles”, *J. Geophys. Res.* , Vol. 98, pp. 5573–5591.

Kallenrode, M.-B. (1993b), “Particle propagation in the inner heliosphere”, *J. Geophys. Res.* , Vol. 98, pp. 19.037–19.047.

Kallenrode, M.-B. (1996), “A statistical survey of 5 MeV proton events at transient interplanetary shock”, *J. Geophys. Res.* , Vol. 101, pp. 24.393–24.410.

Kallenrode, M.-B. (2003), “Current views on impulsive and gradual solar energetic particle events”, *J. Phys.* , Vol. 29, p. 965.

Kallenrode, M.-B. (2004), *Space Physics*, Springer-Verlag Berlin Heidelberg.

Kallenrode, M.-B. (2005), Radial dependence of solar energetic particle events, *in* B. Fleck, T. H. Zurbuchen and H. Lacoste, eds, ‘Proc. Solar Wind 11 – SOHO 16’, Vol. SP-592, ESA, Noordwijk.

Kallenrode, M.-B. and Wibberenz, G. (1990), “Influence of interplanetary propagation on particle onsets”, Vol. 5 (SH Sessions), Proceedings of the 21st International Cosmic Ray Conference, p. 229.

Kallenrode, M.-B. and Wibberenz, G. (1991a), “Particle injection following solar flares on 1980 May 28 and June 8: Evidence for different injection time histories in impulsive and gradual events?”, *Astrophys. J.* , Vol. 376, pp. 787–796.

Kallenrode, M.-B. and Wibberenz, G. (1991b), “Particle injection following solar flares on 1980 may 28 and june 8: Evidence for different injection time histories in impulsive and gradual events?”, *Astrophys. J.* , Vol. 376, pp. 787–796.

Kallenrode, M.-B., Wibberenz, G. and Hucke, S. (1992), “Propagation conditions for relativistic electrons in the inner heliosphere”, *Astrophys. J.* , Vol. 394, p. 351.

- Krimigis, S., Roelof, E., Armstrong, T. and Allen, J. V. (1971), "Low-energy (≥ 0.3 MeV) solar-particle observations at widely separated points (> 0.1 AU) during 1967", *J. Geophys. Res.*, Vol. 76, pp. 5921–5946.
- Laasonen, P. (1949), "Über eine Methode zur Lösung der Wärmeleitungsgleichung", *Acta Math.*, Vol. 81, p. 309.
- Lampa, F. (2006), Numerik des 2-D Transports in fluktuierenden Magnetfeldern, Master's thesis, Universität Osnabrück, Barbarastrasse 7, 49076 Osnabrück.
- Lampa, F. and Kallenrode, M.-B. (2009), "Perpendicular transport in the inner heliosphere: A quick and dirty approach", *Sol. Phys.*, Vol. 260, pp. 423–440.
- Lario, D., Kallenrode, M.-B., Decker, R., Krimigis, S., Roelof, E. and Aran, A. (2006), "Radial and longitudinal dependence of solar 4–13 MeV and 27–37 MeV proton peak intensities and fluences: Helios and IMP-8 observations", *Astrophys. J.*, Vol. 653, pp. 1531–1544.
- Larson, D., Lin, R., McTiernan, J., McFadden, J., Ergun, R., McCarthy, M., Rème, H., Sanderson, T., Kaiser, M., Lepping, R. and Mazur, J. (1997), "Tracing the topology of the October 18 – 20, 1995, magnetic cloud with 0.1 - 10^2 keV electrons", *Geophys. Res. Lett.*, Vol. 24, pp. 1911–1914.
- Lin (1970), "The emission and propagation of 40 keV solar flare electrons II: The electron emission structure of large active regions", *Sol. Phys.*, Vol. 15, p. 453.
- MacLennan, C., Lanzerotti, L. and Gold, R. (2003), "Low energy charged particles in the high latitude heliosphere: Comparing solar maximum and solar minimum: Ulysses observations at solar maximum (ULYSSES)", *Geophys. Res. Lett.*, Vol. 30, pp. ULY7.1–ULY7.5.
- Marchuk, G. (1975), *Applications of Mathematics*, Vol. 2, Springer.
- Matthaeus, W., Qin, G., Bieber, J. and Zank, G. (2003), "Nonlinear collisionless perpendicular diffusion of charged particles", *Astrophys. J.*, Vol. 590, pp. L53–L56.
- Maxwell, J. (1865), "A dynamical theory of the electromagnetic field", *Philosophical Transactions of the Royal Society of London*, Vol. 155, pp. 459–512.
- Mazur, J., Mason, G., Dwyer, J., Giacalone, J., Jokipii, J. and Stone, E. (2000), "Interplanetary magnetic field line mixing deduced from impulsive solar flare particles", *Astrophys. J.*, Vol. 532, pp. L79–L82.
- Mazur, J., Mason, G. and Mewald, R. (2002), "Charge states of energetic particles from corotating interaction regions as constraints on their source", *Astrophys. J.*, Vol. 566, p. 555.
- McCracken, K. G., Rao, U. R. and Bukata, R. P. (1967), "Cosmic ray propagation processes, 1, A study of cosmic ray flare effect", *J. Geophys. Res.*, Vol. 72, p. 4293.
- McKibben, R. (1972), "Azimuthal propagation of low-energy solar-flare protons as observed from spacecraft very widely separated in solar azimuth", *Geophys. Res. Lett.*, Vol. 77, pp. 3957–3984.

- McKibben, R. B., Connell, J. J., Lopate, C., Zhang, M., Anglin, J. D., Balogh, A., Dalla, S., Sanderson, T. R., Marsden, R., Hofer, M., Kunow, H., Posner, A. and Heber, B. (2003), "Ulysses COSPIN observations of cosmic rays and solar energetic particles from the south pole to the north pole of the Sun during solar maximum", *Ann. Geophys.* , Vol. 21, pp. 1217–1228.
- McKibben, R., Lopate, C. and Zhang, M. (2001), "Simultaneous observations of solar energetic particle events by IMP 8 and the Ulysses Cospin high energy telescope at high solar latitudes", *Space Sci. Rev.* , Vol. 97, p. 257.
- Müller-Mellin, R., Heber, B., Kallenrode, M.-B., Kunow, H. and Wibberenz, G. (1993), "Solar energetic particles in the intermediate region of the heliosphere", *Adv. Space Res.* , Vol. 13(6), p. 85.
- Ng, C. and Wong, K.-Y. (2005), "Solar particle propagation under the influence of pitch-angle diffusion and collimation in the interplanetary magnetic field", *16th International Cosmic Ray Conference* , Vol. 5, p. 252.
- Nolte, J. T. and Roelof, E. C. (1973), "Large-scale structure of the interplanetary medium", *Sol. Phys.* , Vol. 33, pp. 483–504.
- Northrop, T. G. (1963), *The adiabatic motion of charged particles*, Intersciences, New York.
- OpenMP Architecture Review Board (2009), *The OpenMP API specification for parallel programming*.
- URL:** <http://openmp.org/wp/>
- Pallavicini, R., Serio, S. and Vaiana, G. S. (1977), "A survey of soft X-ray limb flare images: The relation between their structure in the corona and other physical parameters", *Astrophys. J.* , Vol. 216, pp. 108–122.
- Palmer, I. (1982), "Transport coefficients of low energy cosmic rays in interplanetary space", *Rev. Geophys. Space Phys.* , Vol. 20, p. 335.
- Parker, E. (1958), "Dynamics of the interplanetary gas and magnetic fields", *Astrophys. J.* , Vol. 128, p. 446.
- Parker, E. (1965), "The passage of energetic charged particles through interplanetary space", *Planet Space Sci.* , Vol. 13, pp. 9–49.
- Parks, G. (1991), *Physics of space plasmas - an introduction*, Addison-Wesley, Redwood City, CA.
- Patterson, J. and Armstrong, T. (2003), "Steady-state event-excluded proton spectra at solar minimum at all heliolatitudes", *Geophys. Res. Lett.* , Vol. 30, p. 8037.
- Peiro, J. and Sherwin, S. (2005), *Finite difference, finite element and finite volume methods for partial differential equations*, Vol. I: Methods and Models, Springer-Verlag Berlin Heidelberg.
- Pizzo, V. (1985), Interplanetary shocks on the large scale: a retrospective on the last decades theoretical efforts, *in* B. Tsurutani and R. Stone, eds, 'Collisionless shocks in the heliosphere: reviews of current research', Vol. Geophysics Monogr. 35, American Geophysical Union, Washington, DC, p. 51.

- Press, W., Flannery, B., Teukolsky, S. A. and Vetterling, W. (1992), *Numerical Recipes in FORTRAN 77: The Art of Scientific Computing*, Cambridge University Press.
- Proctor, M. and Gilbert, D. (1994), *Lectures on solar and planetary dynamos*, Cambridge University Press.
- Qin, G. (2007), "Non-parallel diffusion of charged particles: Extension to the non-linear guiding center theory", *Astrophys. J.*, Vol. 656, p. 217.
- Reames, D., Barbier, L. and Ng, C. K. (1996), "The spatial distribution of particles accelerated by coronal mass ejection-driven shocks", *Astrophys. J.*, Vol. 466, p. 473.
- Reames, D., Barbier, L., Rosenvinge, T. V., Mason, G., Mazur, J. and Dwyer, J. (1997), "Energy spectra of ions accelerated in impulsive and gradual solar events", *Astrophys. J.*, Vol. 483, pp. 515–522.
- Reames, D., Dennis, B., Stone, R. and Lin, R. (1988), "X-ray and radio properties of solar (He-3) rich events", *Astrophys. J.*, Vol. 327, p. 998.
- Reames, D., Kahler, S. and Ng, C. (1997), "Spatial and temporal invariance in the spectra of energetic particles in gradual solar events", *Astrophys. J.*, Vol. 491, p. 414.
- Reid, G. (1964), "A diffusive model for the initial phase of a solar proton event", *J. Geophys. Res.*, Vol. 69, pp. 2659–2667.
- Reinhard, R. (1975), Die solare Ausbreitung flare-erzeugter Protonen im Energiebereich 10-60 MeV, PhD thesis.
URL: <http://ifkki.kernphysik.uni-kiel.de>
- Richtmyer, R. and Morton, K. (1967), *Difference Methods for Initial Value Problems*, Wiley-Interscience.
- Roach, P. (1982), *Computational fluid dynamics*, Hermosa Publishers.
- Roe, P. (1986), "Characteristic-based schemes for the Euler equations", *Annual Reviews of Fluid Mechanics*, Vol. 18, pp. 337–365.
- Roederer, J. (1970), Physics and chemistry in space, *in* J. Roederer and J. Zähringer, eds, 'Dynamics of geomagnetically trapped radiation', Vol. 2, Springer, Berlin, Heidelberg, New York, p. 20.
- Roelof, E. (1969a), Effect of adiabatic deceleration on the focused transport of solar cosmic rays, *in* H. Ögelmann and J. Wayland, eds, 'Lectures in high energy astrophysics', Vol. NASA SP-a99, p. 111.
- Roelof, E. (1969b), Propagation of solar cosmic rays in the interplanetary magnetic field, *in* H. Ögelmann and J. Wayland, eds, 'Lectures in high energy astrophysics', Vol. NASA SP-199, Scientific and Technical Information Division, p. 111.
- Roelof, E. (1973), Coronal propagation of energetic charged particles, *in* T. Russel, ed., 'Symposium on High Energy Phenomena on the Sun', Vol. SP-199, NASA Spec. Pub., p. 486.
- Roelof, E. (1974), Coronal structure and the solar wind, *in* T. Russel, ed., 'Solar Wind III', Univ. of California, Los Angeles, p. 98.

- Roelof, E., Gold, R., Simnett, G., Tappin, S., Armstrong, T. and Lanzerotti, L. (1992), "Low energy solar electrons and ions observed at Ulysses February-April 1991: The inner heliosphere as a particle reservoir", *Geophys. Res. Lett.*, Vol. 19, p. 1243.
- Roelof, E. and Krimigis, S. (1973), "Analysis and synthesis of coronal and interplanetary energetic particle, plasma, and magnetic field observations over three solar rotations", *J. Geophys. Res.*, Vol. 78, p. 5375.
- Roos, H. (1994), "Ten ways to generate the II'in and related schemes", *J. Comput. and Appl. Math.*, Vol. 53, pp. 43 – 59.
- Rossi, B. and Olbert, S. (1970), *Introduction to the Physics of Space*, Vol. International series in Pure and Applied Physics, New York: McGraw-Hill Book Company.
- Ruffolo, D. (1994), "Effect of adiabatic deceleration on the focused transport of solar cosmic rays", *Astrophys. J.*, Vol. 442, pp. 861–874.
- Samarskij, A. (2001), *The Theory of Difference Schemes*, Marcel Dekker, Inc.
- Schatten, K., Wilcox, J. and Ness, N. (1976), "A model of interplanetary and coronal magnetic fields", *Sol. Phys.*, Vol. 6, p. 442.
- Schlüter, W. (1985), Die numerische Behandlung der Ausbreitung solarer flareinduzierter Teilchen in den magnetischen Feldern des interplanetaren Raumes, PhD thesis, Mathematisch-Naturwissenschaftliche Fakultät der Christian-Albrechts-Universität Kiel.
- Schulze, B. M., Richter, A. K. and Wibberenz, G. (1977), "Influence of finite injections and of interplanetary propagation on time-intensity and time-anisotropy profiles of solar cosmic rays", *Sol. Phys.*, Vol. 54, p. 207.
- Schwan, C. (2009), 3D interplanetarer Transport – Meridionales Gitter für FD-Schema, Master's thesis, Universität Osnabrück.
- Schwarz, H. R. (1997), *Numerische Mathematik*, B. G. Teubner Stuttgart.
- Shalchi, A., Bieber, J., Matthaeus, W. and Qin, G. (2004), "Nonlinear parallel and perpendicular diffusion of charged cosmic rays in weak turbulence", *Astrophys. J.*, Vol. 616, pp. 617–629.
- Smith, E., Tsurutani, B. and Rosenberg, R. (1978), "Observations of the interplanetary sector structure up to heliographic latitudes of 16° : Pioneer 11", *J. Geophys. Res.*, Vol. 83, p. 717.
- Stevens, M. and Kasper, J. (2007), "A scale-free analysis of magnetic holes at 1 AU", *J. Geophys. Res.*, Vol. 112, p. A05109.
- Stone, R. and Tsurutani, B. (1985), Interplanetary shocks on the large scale: A retrospective on the last decades theoretical efforts, in R. Stone and B. Tsurutani, eds, 'Collisionless shocks in the heliosphere: A tutorial review', Vol. Geophysics Monogr. 34, American Geophysical Union, Washington, DC.
- Struminsky, A., Heber, B., Kallenrode, M.-B., Müller-Mellin, R., Klassen, A. and Kunow, H. (2006), "Injection and propagation of solar protons to high heliospheric latitudes: Ulysses KET observations", *Adv. Space. Res.*, Vol. 38(3), pp. 507–515.

- Tichonov, A. and Samarskij, A. (1961), "Homogeneous difference schemes", *USSR Computational Mathematics and Mathematical Physics*, Vol. 1, pp. 5–63.
- Van Allen, J. and Frank, L. (1959), "Radiation around the earth to a radial distance of 107,400 km", *Nature*, Vol. 183.
- van Hollebeke, M. I., MaSung, L. and McDonald, F. (1975), "The variation of solar proton energy spectra and size distribution with heliolongitude", *Sol. Phys.*, Vol. 41, pp. 189–223.
- van Leer, B. (1977), "Towards the ultimate conservative difference scheme IV. A new approach to numerical convection.", *J. Comput. Phys.*, Vol. 23, pp. 276–299.
- Vlasov, A. A. (1938), "On vibration properties of electron gas", *J. Exp. Theor. Phys.*, Vol. 8 (3), p. 291.
- Webb, G. and Gleeson, L. (1975), "On the equation of transport for cosmic-ray particles in the interplanetary region", *Astrophys. and Space Sci.*, Vol. 60, pp. 335–351.
- Wibberenz, G. and Cane, H. (2006), "Multi-spacecraft observations of solar flare particles in the inner heliosphere", *Astrophys. J.*, Vol. 651, pp. 211–236.
- Wibberenz, G., Kunow, H., Müller-Mellin, R., Sierks, H., Heber, B., Kallenrode, M.-B., Raviart, A., Ferrando, P. and Ducros, R. (1992), "Solar energetic and shock accelerated particles observed between 1 and 4 AU by the Kiel electron Telescope (KET) on board Ulysses", *Geophys. Res. Lett.*, Vol. 19.
- Wong, K. (1982), Interplanetary transport of solar particles in the presence of focusing and pitch-angle diffusion, PhD thesis, Department of Mathematics University of Malaya, Kuala Lumpur, Malaysia.
- Zhang, M., Jokipii, J. and McKibben, R. (2003), "Perpendicular transport of solar energetic particles in heliospheric magnetic fields", *Astrophys. J.*, Vol. 595, p. 493.
- Zhang, M., Qin, G. and Rassoul, H. (2009), "Propagation of solar energetic particles in three-dimensional interplanetary magnetic fields", *Astrophys. J.*, Vol. 692, p. 109.
- Zhang, M., Qin, G., Rassoul, H., McKibben, B., Lopate, C. and Heber, B. (2007), "Ulysses observations of Jovian relativistic electrons in the interplanetary space near Jupiter: Determination of perpendicular particle transport coefficients and their energy dependence", *Planet. Space Sci.*, Vol. 55, p. 12.
- Zhang, T., Russell, C., Baumjohann, W., Jian, L., Balikhin, M., Cao, J., Wang, C., Blanco-Cano, X., Glassmeier, K.-H., Zambelli, W., Volwerk, M., Delva, M. and Vörös, Z. (2009), "Characteristic size and shape of the mirror mode structures in the solar wind at 0.72 AU", *Geophys. Res. Lett.*, Vol. 35, p. L10106.
- Zwickl, R. and Webber, W. (1977), "Solar particle propagation from 1 to 5 AU", *Sol. Phys.*, Vol. 54, p. 457.

Acknowledgments

I would like to express my deep gratitude to my research supervisor Prof. Dr. May-Britt Kallenrode for her goal-oriented guidance and support in solving scientific problems.

I am thankful to Klaus Brauer who gave me the numerical background for solving partial differential equations in various lectures and also during my master's thesis phase.

And finally, I would like to thank all the persons who gave me emotional support and help during my Ph.D study, including my girl-friend Heike, family and friends.

Statutory/ Eidesstattliche Erklärung

Ich erkläre hiermit, dass ich die vorliegende Arbeit ohne unzulässige Hilfe Dritter und ohne Benutzung anderer als der angegebenen Hilfsmittel angefertigt habe. Die aus anderen Quellen direkt oder indirekt übernommenen Daten und Konzepte sind unter Angabe der Quelle gekennzeichnet.

Die Arbeit wurde bisher weder im In- noch im Ausland in gleicher oder ähnlicher Form einer anderen Prüfungsbehörde vorgelegt.

(Ort, Datum)

(Unterschrift)